

Atmospheric Models and Aircraft Measurements: Representativeness and Model Validation

Zur Erlangung des akademischen Grades eines
DOKTORS DER NATURWISSENSCHAFTEN
von der Fakultät für Physik des
Karlsruher Instituts für Technologie (KIT)

genehmigte

DISSERTATION

von

Dipl.-Met. Johannes Eckstein
aus Augsburg

Tag der mündlichen Prüfung:	21. Juli 2017
Referent:	Prof. Dr. Peter Braesicke
Korreferent:	Prof. Dr. Johannes Orphal

Zusammenfassung

Die Atmosphäre ist ein komplexes System, in welchem Dynamik, Thermodynamik und Chemie zusammenkommen. Atmosphärenmodelle sind eine Abbildung all der Prozesse, die dieses System antreiben. Um diese Modelle zu validieren, ist ein Vergleich mit Messungen unabdingbar. Andererseits stellen Modelle den vollständigen Zustand der (modellierten) Atmosphäre bereit, was für die Interpretation von Messungen hilfreich sein kann.

Diese Doktorarbeit steht an der Schnittstelle zwischen Modellen und Messungen. In drei Kapiteln wird beschrieben, wie verschiedene Modelle und flugzeuggetragene Messungen des Projekts IAGOS-CARIBIC von einander profitieren können, um ein vertieftes Verständnis der Atmosphäre zu erlangen.

Im ersten Kapitel werden die IAGOS-CARIBIC Messdaten verwendet, um das Chemie-Klima Modell EMAC zu validieren. Klimatologien der Messdaten werden verglichen mit solchen aus Modelldaten, die zuvor auf den Ort der Messungen interpoliert wurden. Die Mittelwerte von O_3 , CH_4 und CO werden vom Modell gut wiedergegeben, während der Vergleich von Aceton Unzulänglichkeiten aufzeigt.

Das nächste Kapitel widmet sich weiterhin den Klimatologien, die aus den Messdaten heraus erstellt werden können und untersucht, ob diese für den mittleren Zustand der Atmosphäre repräsentativ sind. Die Abbildung des Messdatensatzes in einer Simulation von EMAC wird mit dem mittleren Modellzustand verglichen. Es werden verschiedene Definitionen für Repräsentativität getestet und dann motiviert, dass die Schlussfolgerungen aus den Modelldatensätzen auf die Wirklichkeit übertragen werden können. Die klimatologische Repräsentativität der Messdaten wird für Spurengase verschiedener Variabilität diskutiert. Die Beschränkungen in Druck und geographischer Länge, die dem Messdatensatz eigen sind, werden sodann auf ihren Einfluss auf die Repräsentativität hin untersucht.

Das letzte Kapitel verlegt den Fokus von Atmosphärenchemie auf den hydrologischen Kreislauf. Messdaten aus IAGOS-CARIBIC werden verwendet, um das Modell ICON-ART-Iso mittels einer Fallstudie zu validieren. ICON-ART-Iso ist eine Erweiterung des Atmosphärenmodells ICON, das dem Modell die Möglichkeit beigibt, auch die stabilen Wasserisotope und andere Wasserdiagnostiken zu simulieren. Die Entwicklung von ICON-ART-Iso war Teil dieser Doktorarbeit. Daher beschreibt die Arbeit auch die Physik und deren Implementierung in das Modell. Auf der saisonalen Skala werden IASI Satellitendaten verwendet, um das Modell zu validieren. Die in situ Messungen von IAGOS-CARIBIC kommen dann in einer Fallstudie zum Einsatz, die auch die Vorteile der verschiedenen Wasserdiagnostiken demonstriert.

Für ein erweitertes Verständnis der Atmosphäre ist es notwendig, Messungen aus Projekten wie IAGOS-CARIBIC mit Modellsimulationen zusammenzuführen. Diese Doktorarbeit demonstriert, wie flugzeuggetragene Messungen auf klimatologischer wie auch auf lokaler Skala verwendet werden können, um Modellsimulationen zu validieren. Sie zeigt auch, wie eine klimatologische Modellsimulation zur Interpretation der Messdaten beitragen kann. Die Arbeit zeigt also auf, wie Modelle und Messungen voneinander profitieren können, ein zentraler Aspekt der modernen Atmosphärenwissenschaft.

Abstract

The atmosphere is a complex system of dynamics, thermodynamics and chemistry. Atmospheric models are an integrated description of the different processes that drive this system. To validate these models, it is necessary to compare with measurements. On the other hand, models provide the full (modeled) atmospheric state which can aid in the interpretation of measurements.

This thesis is situated on the interface between models and atmospheric measurements. In three different chapters, it describes how different models and IAGOS-CARIBIC aircraft measurements can benefit from one another to come to an increased understanding of the atmosphere.

In a first chapter, the IAGOS-CARIBIC measurement data are used to validate the chemistry-climate model EMAC. Climatologies generated from the aircraft measurements and from collocated model data are compared. The mean values of O_3 , CH_4 and CO are well reproduced by the model, while the simulation of acetone shows deficiencies.

The next chapter further examines the climatologies that can be compiled from the measurement data and investigates whether these climatologies are representative of the mean atmospheric state. This is accomplished by comparing the model representation of the measurement dataset in a simulation of EMAC to the mean model state. Different definitions of representativeness are tested with these model datasets. Adequate room is given to show that the conclusion about representativeness from the model can be applied to the measurement dataset. The climatological representativeness of the measurements is then discussed for trace gases of different variability. The limitations in pressure and longitude, which are inherent in the measurement dataset, are examined for their influence on the climatological representativeness.

The last main chapter moves from atmospheric chemistry to the hydrological cycle. Data from IAGOS-CARIBIC are used to validate the model ICON-ART-Iso in a case study. ICON-ART-Iso is the new isotope enabled version of the atmospheric model ICON. It adds the possibility to simulate stable water isotopes and other water diagnostics to the model. The development of ICON-ART-Iso was part of this thesis. The isotope physics and their implementation in the model are therefore also described. The model is validated on a seasonal scale with IASI satellite data. The in situ measurements by IAGOS-CARIBIC are then used in a case study, which also demonstrates the advantages of the different water diagnostics.

For an increased understanding of the atmosphere, it is necessary to combine measurements from projects like IAGOS-CARIBIC with model simulations. This thesis demonstrates how aircraft measurements can be used to validate model results on climatological and smaller scales. It also shows how these measurements can gain value from a climatological model simulation by determining the measurement representativeness. Thereby, the thesis develops methods and shows how models and measurements can benefit from one another, which is a central aspect of the science of the atmosphere.

**Atmospheric Models and Aircraft Measurements:
Representativeness and Model Validation**

July 2017

*And if the sun did not travel on wing and foot all the night,
how would the world be illumed at morning-tide?
If the salt water did not rise from the sea to the sky, whence
would the garden be revived by torrent and rain?
When the drop departed from its homeland and returned,
it encountered a shell and became a pearl.*

Jalal al-Din Rumi,
If a tree could move on foot or wing,
translation by A. J. Arberry

Contents

1	Introduction	1
2	Models and aircraft measurement data	3
2.1	Introduction	4
2.2	CARIBIC measurement data	5
2.3	The models used in this thesis	7
2.3.1	The chemistry-climate model EMAC	7
2.3.2	Moving from EMAC to ICON-ART	8
2.3.3	The atmosphere-chemistry model ICON-ART	8
2.4	Interpolation of model output to measurement locations	9
3	Climatological model validation within the ESCiMo project	11
3.1	Introduction	12
3.2	Technical details on measurements and the model simulations	13
3.2.1	Climatologies from CARIBIC data	13
3.2.2	The ESCiMo simulations	13
3.3	Climatological validation of the simulations	14
3.3.1	Climatologies of ozone	14
3.3.2	Climatologies of carbon monoxide	14
3.3.3	Climatologies of methane	15
3.3.4	Climatologies of acetone	15
3.4	Summary and outlook	21
4	Investigation of the climatological representativeness of CARIBIC data	23
4.1	Introduction and literature overview	24
4.2	Model and data	27
4.2.1	The observational IAGOS-CARIBIC dataset	27
4.2.2	The EMAC model simulation	27
4.3	Defining representativeness	29
4.3.1	Representative for what parameter?	29
4.3.2	Representative of which population?	30
4.3.3	Confidence limits of representativeness	33

4.4	Defining a measure for variability	34
4.5	Statistical methods	36
4.5.1	Kolmogorov-Smirnov test	36
4.5.2	Variability analysis	36
4.5.3	Relative differences	38
4.6	Statistical methods applied to random numbers	40
4.6.1	Defining the random number data	40
4.6.2	Variability analysis	40
4.6.3	Relative differences	41
4.6.4	Theoretical considerations	41
4.7	Statistical methods applied to model datasets	43
4.7.1	Applying the Kolmogorov-Smirnov test	43
4.7.2	Sensitivity study on the Kolmogorov-Smirnov test	43
4.7.3	Applying the variability analysis	45
4.7.4	Relative differences	46
4.8	Model and measurement variability	48
4.8.1	Influence of short time scales on the climatological mean	48
4.8.2	Comparing model and measurement variability	49
4.8.3	A conclusion from model data applied to measurements	50
4.9	Representativeness uncertainty of the CARIBIC measurement data	52
4.9.1	Representativeness uncertainty	52
4.9.2	Application to climatologies from CARIBIC measurements	54
4.9.3	Number of flights for representativeness	56
4.9.4	Limitation in longitude: The influence of the Pacific Ocean	57
4.9.5	Limitation in pressure: Aircraft tropopause pressure bias	58
4.9.6	The influence of a strongly reduced measurement frequency	59
4.10	Summary and outlook	61
5	Development and validation of the isotope enabled model ICON-ART-Iso	63
5.1	Introduction	64
5.2	General isotope physics	67
5.2.1	The isotope ratio and the δ notation	67
5.2.2	Fractionation	67
5.2.3	The Rayleigh model	70
5.3	ICON-ART-Iso physics	72
5.3.1	Initialization	73
5.3.2	Surface evaporation	75

5.3.3	Microphysics	77
5.3.4	Saturation adjustment	83
5.3.5	Convection	84
5.4	Technical details on ICON-ART-Iso and the model runs	87
5.4.1	Summary of technical aspects of ICON-ART-Iso	87
5.4.2	Model setup for evaluation and case studies	87
5.5	Simulation of diagnostic H ₂ O	89
5.5.1	Water vapor diagnostics	89
5.5.2	Precipitation diagnostics	93
5.5.3	The distribution of precipitation over land and ocean	95
5.6	Simulation of fractionating isotopes	97
5.6.1	The initialization of the isotopes	97
5.6.2	Different parameterizations for fractionation	99
5.7	Comparison with IASI satellite data	108
5.7.1	IASI retrieval data	108
5.7.2	ICON-ART-Iso simulations and ECHAM5-wiso model data	109
5.7.3	Comparisons for the seasonal and daily cycle	109
5.8	Case study comparison with CARIBIC in situ measurements	117
5.8.1	CARIBIC δ D measurements	117
5.8.2	Two return flights to Caracas	119
5.8.3	Simulation of δ D for the CARIBIC flights with ICON-ART-Iso	121
5.8.4	Tracing the origin of water with ICON-ART-Iso	125
5.8.5	The two cases in a larger context	128
5.8.6	Simulation of the CARIBIC flights with COSMOiso	130
5.8.7	Summary: CARIBIC and ICON-ART-Iso	132
5.9	Summary and outlook	134
6	Conclusions	137
A	Climatological validation within the ESCiMo project: Additional figures	141
B	Technical description of ICON-ART-Iso	151
B.1	Namelist and XML settings	151
B.1.1	Example of settings	151
B.1.2	Namelist overview	153
B.1.3	XML file overview	155
B.2	Technical documentation of ICON-ART-Iso	159
B.2.1	Code structure	159

B.2.2	Code maintenance and testing	168
B.3	Possible future developments	171
B.3.1	Small open issues	171
B.3.2	Larger development projects	171

C	Bibliography	175
----------	---------------------	------------

1. Introduction

The earth's atmosphere is a complex system which is influenced by many different mechanisms. The dynamics and thermodynamics set the stage: A turbulent fluid on a rotating planet is differentially heated depending on the latitude. This fluid contains water in all phases and the hydrological cycle takes its share in recycling the energy. Chemical trace substances also play a crucial role by influencing the radiative balance in the ozone layer or as greenhouse gases.

These mechanisms lead to the atmosphere that is observed today. The atmosphere can be described on different temporal and spatial scales, from very local turbulence to synoptic weather systems and on to climatological implications.

Atmospheric circulation models are an integrated formulation of the current understanding of this complex system. Some are specialized for different scales or completed by an interactive chemistry. These models are used to forecast the development of the atmosphere on scales from a few days to the next century. In case studies, they provide a deeper insight into the atmospheric processes.

But to be developed and validated, these models require the comparison with measurement data. Only if seen in relation to measurements can model results become meaningful for the real atmosphere. On the other hand, it can be difficult to examine measurements without the fields or tools provided by atmospheric models.

This thesis aims at highlighting this intertwined relationship of models and measurements. IAGOS-CARIBIC is a measurement project that has been running since the year 2005. Data on about 100 trace gas and aerosol parameters is collected on four intercontinental flights per month. The thesis demonstrates how the data from this project can be used to validate simulations of very different models on climatological and local scales. Another main chapter shows how a climatological model integration increases the value of this dataset from a climatological perspective.

The thesis is organized as follows: Chapter 2 gives details on the measurement project IAGOS-CARIBIC and on the modeling systems EMAC and ICON-ART. In a first approach, the next chapter then describes how several simulations of the model EMAC can be validated on a climatological time scale with measurements of O_3 , CH_4 , CO and acetone from the IAGOS-CARIBIC project. In this classic approach, climatological mean values of the measurements are compared to mean values from collocated model data.

This leads to Ch. 4, which discusses whether data from the long running IAGOS-CARIBIC project can be used to set up a representative climatology of trace gases in mid latitudes in the tropopause layer. Measured climatologies are an important reference for the atmospheric background state. A

climatological simulation of the model EMAC is sampled along the flight paths of IAGOS-CARIBIC. This model dataset is tested against the mean model state, thereby investigating its representativeness for a climatology. A separate section motivates the application of the conclusions from the model samples to the IAGOS-CARIBIC measurements. The climatological representativeness is discussed depending on the atmospheric lifetime of the different species. After discussing the representativeness in general, the intrinsic limitations of the measurement dataset in pressure and longitude are also investigated.

The last chapter returns to validating model results (Ch. 5). The new, isotope enabled model ICON-ART-Iso is presented. This is an extension to the atmospheric model ICON, which adds the capability to simulate diagnostic water and the stable water isotopes HDO and H₂¹⁸O. After a detailed description of the model physics, it is shown that the model gives consistent results. The model can provide deeper insight into the atmospheric hydrological cycle. But only the comparison with measurements makes the results meaningful. Satellite retrievals from IASI are used for a first seasonal analysis. But it is the high temporal and spatial resolution of the IAGOS-CARIBIC measurements that make these data predestined to validate the new model ICON-ART-Iso. This data is used in a case study to validate the model results.

All three main chapters are presented as self-contained studies, which can also be read independently. Together, they highlight the manifold ways in which model simulations and aircraft measurements can benefit from one another.

Chapter 3 and Ch. 4 deal with the chemical composition of the upper troposphere to lower stratosphere region, a dynamically and chemically very complex region in the atmosphere. Chapter 5, on the other hand, has its focus on the tropospheric water cycle. This way, the different chapters also touch a wide range of meteorological phenomena which make the atmosphere an interesting subject to study.

2. Models and aircraft measurement data

The aircraft measurement project IAGOS-CARIBIC and the models EMAC and ICON-ART are presented. All other chapters use IAGOS-CARIBIC data and compare it to model output of either EMAC or ICON-ART.

The following chapters therefore rely on the technical information provided here. Chapters 3 and 5 use the measurement data to validate EMAC and ICON-ART-Iso model results, while Ch. 4 shows how an EMAC model simulation aids in the interpretation of the aircraft measurements on a climatological scale.

2.1. Introduction

The subject of this thesis is the comparison of measurement data from the IAGOS-CARIBIC project with simulations of atmospheric models. This chapter gives more details on the measurement project IAGOS-CARIBIC (Sec. 2.2) and introduces the models EMAC and ICON-ART that are used in the different chapters (Sec. 2.3).

Chapter 3 discusses how a climatological simulation of EMAC can be validated with IAGOS-CARIBIC data, while Ch. 4 demonstrates how long simulations can aid in the interpretation of the measurements. Chapter 5 introduces the new modeling system ICON-ART-Iso which is validated in a case study with data from IAGOS-CARIBIC. All these studies rely on a software that interpolates the model data onto the location of the aircraft. Section 2.4 gives a short introduction to the software that was developed for this purpose.

2.2. CARIBIC measurement data

IAGOS-CARIBIC (Civil Aircraft for Regular Investigation of the Atmosphere Based on an Instrument Container), is a project within the framework of IAGOS (In-service Aircraft for a Global Observing System, Petzold et al. (2015)). An instrumented container is mounted in the cargo bay of a Lufthansa passenger aircraft during typically four intercontinental flights per month (see Brenninkmeijer et al. (2007) and www.caribic-atmospheric.com). The aircraft flies two return flights from Frankfurt, Germany (Munich, Germany, since August, 2014) to destinations mostly in North or South America or Asia. The Project started in the year 1997 in its first phase, which continued until 2002. This thesis uses data exclusively from the second phase (CARIBIC II), which started in May 2005 and is still ongoing. Data from this period is called CARIBIC measurement data in the following chapters.

During each CARIBIC flight, about 100 trace gas and aerosol parameters are measured. Some are measured continuously with a frequency between 5 Hz and 1/(5 min) and commonly available every 10s while others (e.g. non-methane hydrocarbons) are taken from up to 32 air samples collected during flight.

Figure 2.1 shows the availability of data for each flight for several substances. Not all substances are available from all flights. In addition to those gaps visible in the figure, different instruments have different sampling frequencies and available data may only cover parts of flights. All this leads to different amounts of data that is actually available for a certain substance.

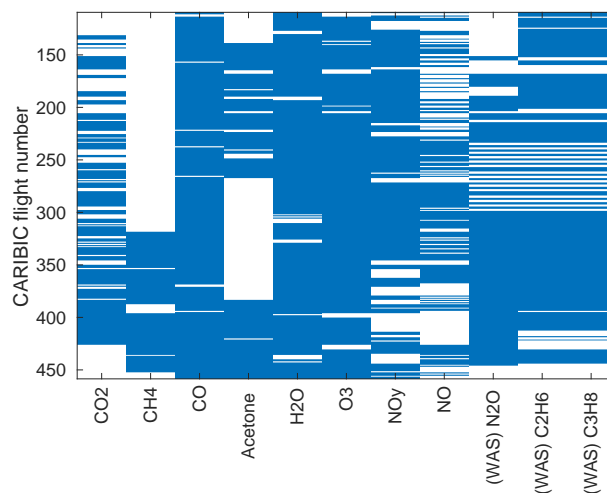


Fig. 2.1.: Availability of data indicated for each flight, in blue where data is available. WAS indicates that the variable is taken from air samples. Note that data may not be available for the whole flight due to lower measurement frequencies or instrument problems.

Figure 2.2 shows all the flight tracks of CARIBIC. All flights start or end either in Frankfurt or Munich, Germany. The majority of flights is directed towards South or North America, Asian destinations coming

second. Destinations in South Africa are only rarely on the flight schedule. This leads to an inhomogeneous distribution of measurement time in latitude and longitude. The distributions of measurements are shown in Fig. 2.3.

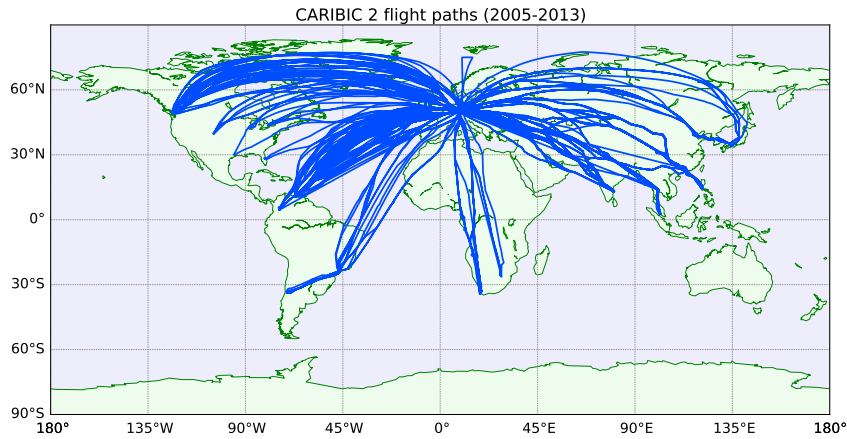


Fig. 2.2.: Flight routes of the CARIBIC aircraft during the project phase CARIBIC II, which started in the year 2005.

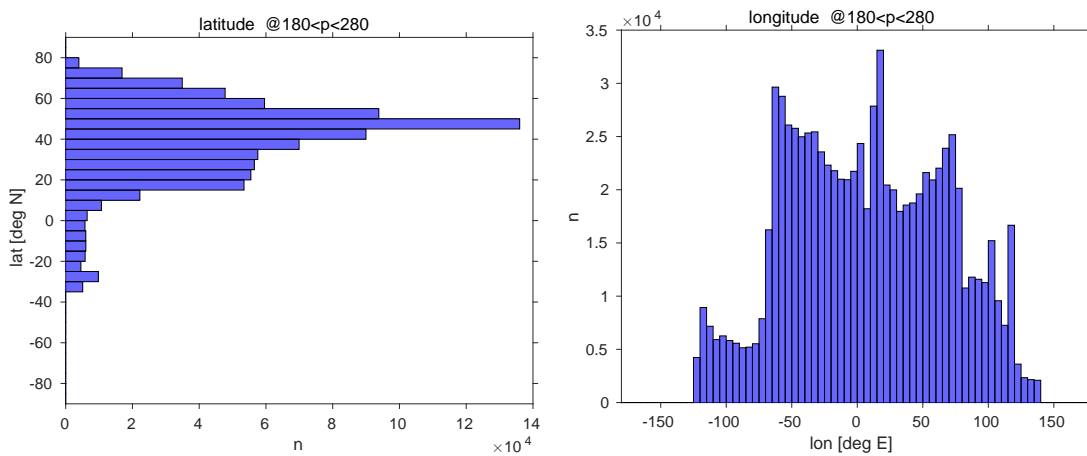


Fig. 2.3.: Latitude (left) and longitude (right) distributions calculated for all CARIBIC II data.

In this thesis, CARIBIC data plays an important role. Chapter 3 uses measurements of four substances to validate model simulations of the model EMAC. Chapter 4 shows how a similar simulation can add value to the measurements by investigating whether they are representative of a mid-latitude climatology. As part of Ch. 5, CARIBIC data is used to validate the newly developed model ICON-ART-Iso in a case study.

2.3. The models used in this thesis

This section presents the two atmospheric chemistry models that are used in this thesis, EMAC (Sec. 2.3.1) and ICON-ART (Sec. 2.3.3). Section 2.3.2 discusses the technical and physical differences. Climatological simulations of EMAC are validated with CARIBIC data in Ch. 3 and used to evaluate the representativeness of CARIBIC data for a climatology in Ch. 4. Chapter 5 presents a newly developed variant of ICON-ART, which is validated with CARIBIC data in a case study.

2.3.1. The chemistry-climate model EMAC

EMAC (ECHAM5/MESSy Atmospheric Chemistry model, Jöckel et al. (2006)) is a combination of the general circulation model ECHAM5 (Roeckner et al., 2006) and different submodels combined through the Modular Earth Submodel System (MESSy, Jöckel et al. (2005)). Being an atmospheric chemistry model, EMAC simulates the chemical composition of the atmosphere in addition to the physical state.

To describe the chemistry, EMAC includes modules capable of simulating gaseous trace substances as well as aerosols. The chemical interactions and the feedback mechanisms on the physical state of the atmosphere are also covered by the different modules, which are combined through the MESSy interface. The sources at the earth's surface are included as the lower boundary. A relatively coarse horizontal resolution is commonly used, reaching up to about 1° , approximately 111 km at the equator. In order to describe stratospheric or even mesospheric processes, the model top is commonly set at 80 km or above.

Generally, EMAC is used for climatological or seasonal investigations at the global to continental scale. Hegglin et al. (2010) performed an extensive inter-model comparison including EMAC (with the same horizontal resolution as the setups used in this thesis). Dynamical as well as chemical metrics were used in this study, focusing on the UTLS. Overall, they find EMAC performs well within the range of the models that were tested. The reader is referred to the study for further details.

From a technical perspective, EMAC (or rather the atmospheric base model ECHAM5) is a spectral model. The physical equations that describe the state and evolution of the atmosphere are expressed in spherical harmonics (Roeckner et al., 2003). The truncation level of the series of harmonics also indicates the horizontal resolution. In this thesis, EMAC is used at a resolution of T42. The output is regridded onto a regular grid with a resolution of 2.8° , which corresponds to 312 km at the equator, less towards the poles.

All the EMAC simulations used in this thesis are nudged model integrations. This means the model dynamics are drawn towards meteorological observations at every model timestep using different meteorological fields, taken from ERA-Interim data (Dee et al., 2011) in this thesis. For example, divergence, vorticity, temperature and ground pressure are nudged for the simulation used in Ch. 4. A nudged model simulates a realistic meteorology that resembles true historical states of the atmosphere. It is therefore more suitable to compare with measurements.

2.3.2. Moving from EMAC to ICON-ART

The chemistry climate model EMAC - built on the atmospheric model ECHAM5 - is a state of the art model, but it has intrinsic limitations. The atmospheric base model is formulated in hydrostatic approximation. This reduces the equation of vertical motion to a diagnostic relationship - the hydrostatic equation - which relates the vertical pressure decrease to density and gravity only. The model can therefore only simulate the atmosphere to a resolution where this approximation is valid, approximately to the order of 10 km.

The formulation in spherical harmonics make it computationally expensive to run a simulation at high resolution. The fields have to be transformed to the spherical harmonics at every time step, which requires much communication between the computational cores on which the model is run (Zängl et al., 2015). This limits the number of cores and makes a higher horizontal resolution difficult from a numerical perspective.

Models that are formulated in grid point space are better suited with future supercomputers relying on heavy parallelization (Zängl et al., 2015). This allows a higher horizontal resolution, for which a non-hydrostatic dynamical core is necessary. The next generation model ICON (Zängl et al., 2015) fulfills these requirements. It is presented in the following section, along with the extension ICON-ART, which simulates aerosols and reactive trace gases.

2.3.3. The atmosphere-chemistry model ICON-ART

The modelling system ICON-ART builds on the non-hydrostatic global circulation model ICON (ICOsahedral Nonhydrostatic) to simulate Aerosols and Reactive Trace Gases (ART). Technical details are given by Zängl et al. (2015) for ICON and by Rieger et al. (2015) for ICON-ART. This section gives a short introduction to ICON-ART.

ICON is a global atmospheric model formulated on an unstructured grid. Basis for the setup of the grid is an icosahedron, the basic triangles of which are subsequently divided into smaller triangles to reach a higher horizontal resolution. The resolution can also be increased in a limited area in so called nests. At the time of writing this thesis, this functionality was implemented for the extension ICON-ART, but it has not been tested for ICON-ART-Iso and is therefore not treated here. The formulation in grid point space makes it possible to split up the globe into separate parts, each of which is then treated by one processing unit. This reduces the communication overhead compared to a spherical model like ECHAM.

As the name implies, ICON is a non-hydrostatic model. This allows the grid to be subsequently refined to resolutions smaller than 1 km. At the moment, ICON is run operationally at the German weather service (DWD) in a global setup with 13 km horizontal resolution and a regional nest over Europe with 7.5 km resolution.

ICON-ART extends ICON to simulate aerosols and reactive trace gases. The modeling system builds on the framework of ICON to simulate water mass and number densities, adding a flexible interface to

simulate more trace substances. The model is introduced by Rieger et al. (2015) and a first update is given by Weimer et al. (2017). The new version will be presented by Schroeter et al. (2017) (in preparation).

Chapter 5 of this thesis presents the extended version ICON-ART-Iso, capable of simulating diagnostic water and the stable water isotopes HDO and H₂¹⁸O. CARIBIC data is used to validate ICON-ART-Iso at the end of Ch. 5.

2.4. Interpolation of model output to measurement locations

In order to compare model data and measurements, it is important to use the model at locations of the measurements. In this thesis, the gridded model output is interpolated onto the location of the measurement. This was done for all model data presented in this study, using the same software, which was first developed. It reads in measurement data from the CARIBIC or other measurement projects and can interpolate model output of several models to the location of those measurements. A linear interpolation in time, latitude, longitude and logarithm of pressure is applied. In the meantime, the program developed for this task has also been used in three Master theses at the institute (Weimer (2015), Stassen (2015) and Diekmann (2017)), the first of which lead to Weimer et al. (2017).

Figure 2.4 shows an example of the result of this interpolation. Measured temperature and the interpolated model temperature from a nudged EMAC simulation are shown for flight 374 of CARIBIC. The interpolated model temperature corresponds well to the measurements. Model temperature is nudged using ERA-Interim reanalysis data, so it is expected to resemble the measurements. The figure therefore also serves as an example of the functionality of the program developed for the interpolation of model data.

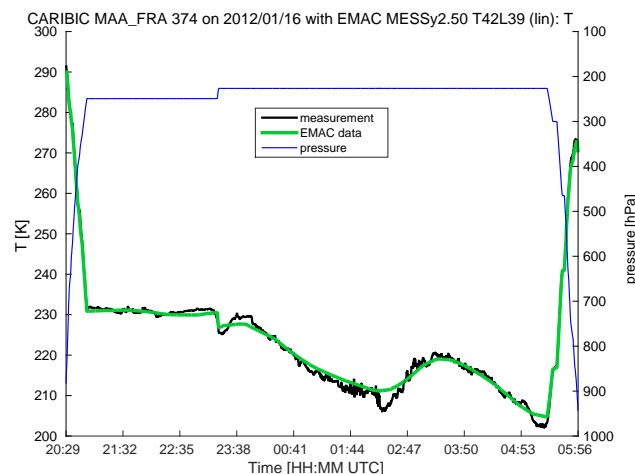


Fig. 2.4.: Measured and interpolated EMAC model temperature for CARIBIC flight 374 from Chennai to Frankfurt using the program developed for this task. Model data is from the EMAC simulation used in Ch.4.

3. Climatological model validation within the ESCiMo project

Several long simulations were performed with the model EMAC within the ESCiMo project to investigate the interaction of atmospheric chemistry and climate. To validate these simulations, IAGOS-CARIBIC data are applied. The output of the nudged simulations is compared with IAGOS-CARIBIC measurement data of ozone, methane, carbon monoxide and acetone in the form of climatologies in the tropopause layer. The study presented in this chapter demonstrates how the data from the long running measurement project IAGOS-CARIBIC can be used to validate model results on climatological time scales. By such a classical application, this chapter is the prelude to Ch. 4 and Ch. 5. These chapters will demonstrate how the measurement data profits from a climatological model run and how a newly developed model can be validated on smaller scales with the IAGOS-CARIBIC data.

3.1. Introduction

The UTLS (upper troposphere/lower stratosphere) is dynamically and chemically very complex and shows strong gradients in temperature, humidity and in many trace gases (Gettelman et al., 2011). As the mid and upper troposphere have a strong influence on the atmospheric greenhouse effect, the UTLS plays an important role in our climate system (Riese et al., 2012). To characterize processes in this area, spatially well resolved data collected on a global scale are required. Aircraft are a suitable platform to carry out these measurements as they are able to probe in situ and at a high frequency.

In order to monitor the current state and predict future changes of the atmosphere, coupled chemistry-climate model simulations are equally important. In order to validate these model simulations, it is necessary to compare the results to measurements for validation. Here again, measurements of long running projects like CARIBIC are of great value.

This chapter presents such a validation study. Several simulations have been performed with the model EMAC within the Earth System Chemistry integrated Modelling (ESCiMo) initiative. Five of these simulations use specified dynamics (i.e. are nudged) and were validated in part with CARIBIC data. Measurements and model results are compared in the form of seasonal climatologies, using data of ozone, methane, carbon monoxide, and acetone ($(\text{CH}_3)_2\text{CO}$).

The following section first discusses a few technical details on the measurements and the model simulation. Section 3.3 then discusses the results in separate sections for the four substances, while Sec. 3.4 summarizes and concludes.

This chapter is part of the study by Jöckel et al. (2016). This publication gives all the details on the model simulations used in this chapter and discusses several other validation studies.

3.2. Technical details on measurements and the model simulations

This section presents technical detail on the measurement data that are used in this chapter and on the model simulation. General information on the CARIBIC project is given in Sec. 2.2, while the EMAC model is presented in Sec. 2.3.1.

3.2.1. Climatologies from CARIBIC data

CARIBIC flies to destinations worldwide, but takes most measurements in the northern hemisphere. In order to obtain meaningful climatologies with good data coverage, latitude was therefore limited to $35^\circ \text{ N} < \text{latitude} < 60^\circ \text{ N}$. Data were also limited by including only values where pressure $p < 280 \text{ hPa}$ to exclude ascents and descents of the aircraft.

Climatologies are presented with a vertical scale relative to the tropopause in kilometers. This information is provided with the measurement data, and derived by linear interpolation to the aircraft position from ECMWF operational analysis data (with a 1° grid resolution) as distance to the 3.5 PVU potential vorticity iso-surface¹. For comparability, i.e., to have the same tropopause definition, a similar calculation was applied to the model data. It is essential to reference data to this height relative to the tropopause (HrelTP), as stratospheric and tropospheric values then become separable when using the data from an aircraft that flies at constant pressure.

3.2.2. The ESCiMo simulations

All the details on the simulations discussed in this chapter are given by Jöckel et al. (2016) and the reader is referred to this publication for further details. In order to compare with CARIBIC data, only nudged simulation could be used. These all use a horizontal resolution of T42, but differ in vertical resolution (L90 vs L47) and the nudging technique. Two simulation also nudge global mean temperature \bar{T} , while the others do not. Table 3.1 summarizes these differences and defines the names of the five simulations used here. In addition, simulation *RCISD-base-10a* includes road emissions, which were not considered in the other simulations. The 10-hourly model output was interpolated to the location of the aircraft by the post-processing tool presented in Sec. 2.

	\bar{T} nudged	\bar{T} not nudged
L90	07	10 and 10a
L47	08	09

Tab. 3.1.: Summary of the simulations used in this validation study. All simulations are referred to by their full name, prepending *RCISD-base-* to the number given here, e.g. *RCISD-base-07*. Simulation *RCISD-base-10a* includes road emissions, different to all the other simulations.

¹description available under http://www.knmi.nl/samenw/campaign_support/CARIBIC/

3.3. Climatological validation of the simulations

This section compares model and measurement climatologies, prepared as specified above, for the four substances investigated in this chapter: ozone, carbon monoxide, methane and acetone. The main figures of all four sections are organized in the same way.

The figures show the climatologies of measurements and of data from the run *RCISD-base-10a* in the top row. The middle row displays their relative differences on the left side. In order to judge upon the significance of the relative differences, a plot of the absolute values of model minus measurements over the sum of the standard deviation of measurements and model is also displayed. The bottom row shows two more climatologies of model differences: *RCISD-base-07* minus *RCISD-base-08*, differing in vertical resolution, and *RCISD-base-07* minus *RCISD-base-10*, differing in nudging of the global mean temperature.

The results of *RCISD-base-10* minus *RCISD-base-10a*, using different road emissions, are discussed, but shown only in App. A. This appendix also includes the climatologies and relevant relative differences of all simulations.

3.3.1. Climatologies of ozone

In the case of ozone (O_3 , Fig. 3.2), the model results compare well with measurements (see Zahn et al. (2012) for instrument specifics). The seasonal cycle is reproduced, but the lower values in the troposphere are generally overestimated by up to 40 % by the model. In the stratosphere, differences are smaller, as the model underestimates measurements by 5 %, reaching 30 % only in summer (June to September), where the elevated ozone levels drop faster in the model than indicated by measurements. This early drop in values is especially noteworthy, the difference being larger than the sum of the standard deviation of model and measurements.

Correcting the road traffic emissions has only a minor influence on the distribution of O_3 (shown in App. A). When nudging global mean temperature, upper tropospheric O_3 levels increase by about 5 %, while stratospheric levels stay constant. Increasing the vertical resolution on the other hand seems to decrease the differences between the seasons, reducing O_3 levels in spring and summer by about 10 % in the simulations with 90 levels and increasing them by up to 5 % in the second half of the year.

3.3.2. Climatologies of carbon monoxide

For carbon monoxide (CO, Fig. 3.3, see Scharffe et al. (2012) for instrument specifics), results mostly mirror those of O_3 . The seasonal cycle is again reproduced by the model, showing a faster drop in the troposphere in spring, which leads to an underestimation of about 35 %. Again, this drop is significant, as the model values deviate more than one standard deviation from the measurements. Stratospheric values are overestimated by about 10 % throughout the year.

Correcting the road traffic emissions has little influence on the results, values increase only by about 5 % in the winter stratosphere (shown in App. A). Nudging global mean temperature has a small effect on CO: for the simulations with 90 levels (*RC1SD-base-07* and *10*), stratospheric spring time values (March to June) increase by about 8 %. Contrary to O₃, it is the increasing vertical resolution that produces differences between stratosphere and troposphere for CO, tropospheric values increasing by 5 % for the simulations with 90 levels and being reduced by up to 10 % in the stratosphere.

3.3.3. Climatologies of methane

Results for methane (CH₄, Fig. 3.4, see Dyroff et al. (2014), for instrument specifics) are similar. Relative differences in general are very small for CH₄, reaching only 5 %, if model results are compared to measurements, and less than 1 % among the different model simulations. The model results are in general too low compared to measurements, with a relative difference of -5 % in the troposphere. The seasonal cycle is correctly reproduced, with slightly overestimated early summer stratospheric values (May to July) by about 2 % and an underestimation of about 4 % during the rest of the year. These differences are almost all larger than the sum of model and measurement standard deviation, indicating their significance. As CH₄ is prescribed by Newtonian relaxation at the surface (see Sec. 3.6 of Jöckel et al. (2016)), the values at the surface always correspond to measurements. This explains why the differences to measurements, even in the UTLS, are so small.

Differences between the model simulations indicate how they differ in vertical transport or in methane lifetime (see Sec. 4.4 of Jöckel et al. (2016)). CH₄ is noticeably affected by the road traffic emissions, decreasing the mean values by about 1 % randomly, not showing any seasonality or stratification (shown in Appendix A). This is consistent with a decreased CH₄ OH lifetime (Fig. 18 of Jöckel et al. (2016)). In contrast, a vertical dependence becomes visible when taking the relative difference of simulations with different vertical resolution, where values are up to 0.2 % in the troposphere and down to -0.5 % in the stratosphere for model simulations with an increased vertical resolution (see Sec. 4.4 of Jöckel et al. (2016)). Nudging of global mean temperature has an interesting effect on the results. Values are practically identical for all seasons, except for late winter (January to March) tropospheric and summer (March to October) stratospheric values, where nudging global mean temperature leads to a relative decrease of up to 0.8 %.

3.3.4. Climatologies of acetone

Acetone ((CH₃)₂CO, Fig. 3.5) shows the largest deviations when comparing model results with measurements (for instrument specifics, see Neumaier et al. (2014)). Tropospheric values are underestimated by about 60 to 100 % and the seasonal cycle of the measurement data is not visible. Again, the large difference to measurements in the troposphere is larger than one standard deviation of model and measurements, making it significant.

The effect of different model simulations is small compared to this difference. Correcting the road traffic emissions has no influence on the results. Nudging global mean temperature increases mean values by about 15 % in the stratosphere during late winter and spring (January to May). Increasing the vertical resolution also increases mean acetone values by 5 % in all seasons and at all heights, except for summer and autumn (May to November) stratospheric values, which are reduced by up to 10 %.

These results are in line with the previous evaluation of Pozzer et al. (2007) (Table 8) who observed an underestimation of $\sim 50 - 35$ % for the same biogenic emissions as used here (55 Tg a^{-1}), which account for ~ 85 % of the total emissions. These results indicate the need for considering oceanic emissions and photochemical production of acetone from monoterpenes, methylbutenol and higher iso-alkanes (Jacob et al., 2002), which were not included. For example Pozzer et al. (2010) showed that *i*-butane and *i*-pentane are responsible for the photochemical production of 4.3 and 5.8 Tg a^{-1} of acetone, respectively.²

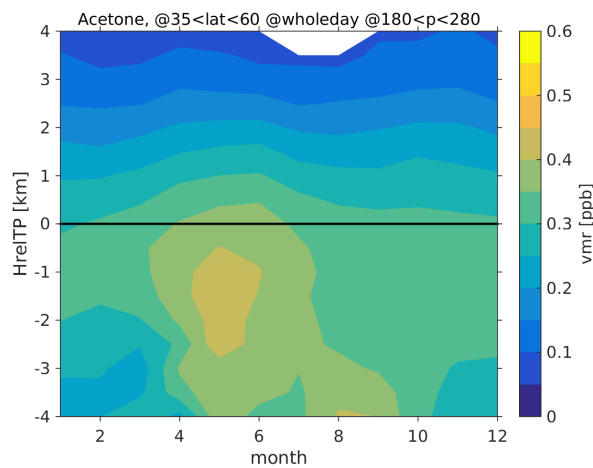


Fig. 3.1.: Climatology of acetone from MOD_{RANDPATH} of Ch. 4, a larger dataset of a similar model setup.

The seasonal cycle is, however, reproduced when taking more model data into account. Figure 3.1 shows the climatology of a larger set of model data (MOD_{RANDPATH} of Ch. 4). The seasonal cycle is reproduced, yet the values remain too low. The underlying model run is also that of Ch. 4, but the setup is very similar to that of *RCISD-base-08*. This also shows that the problem may be related to the distribution of sources in the model, as is indicated by the studies cited in the previous paragraph.

²Author of this paragraph is A. Pozzer, coauthor of Jöckel et al. (2016). It is included here for completeness.

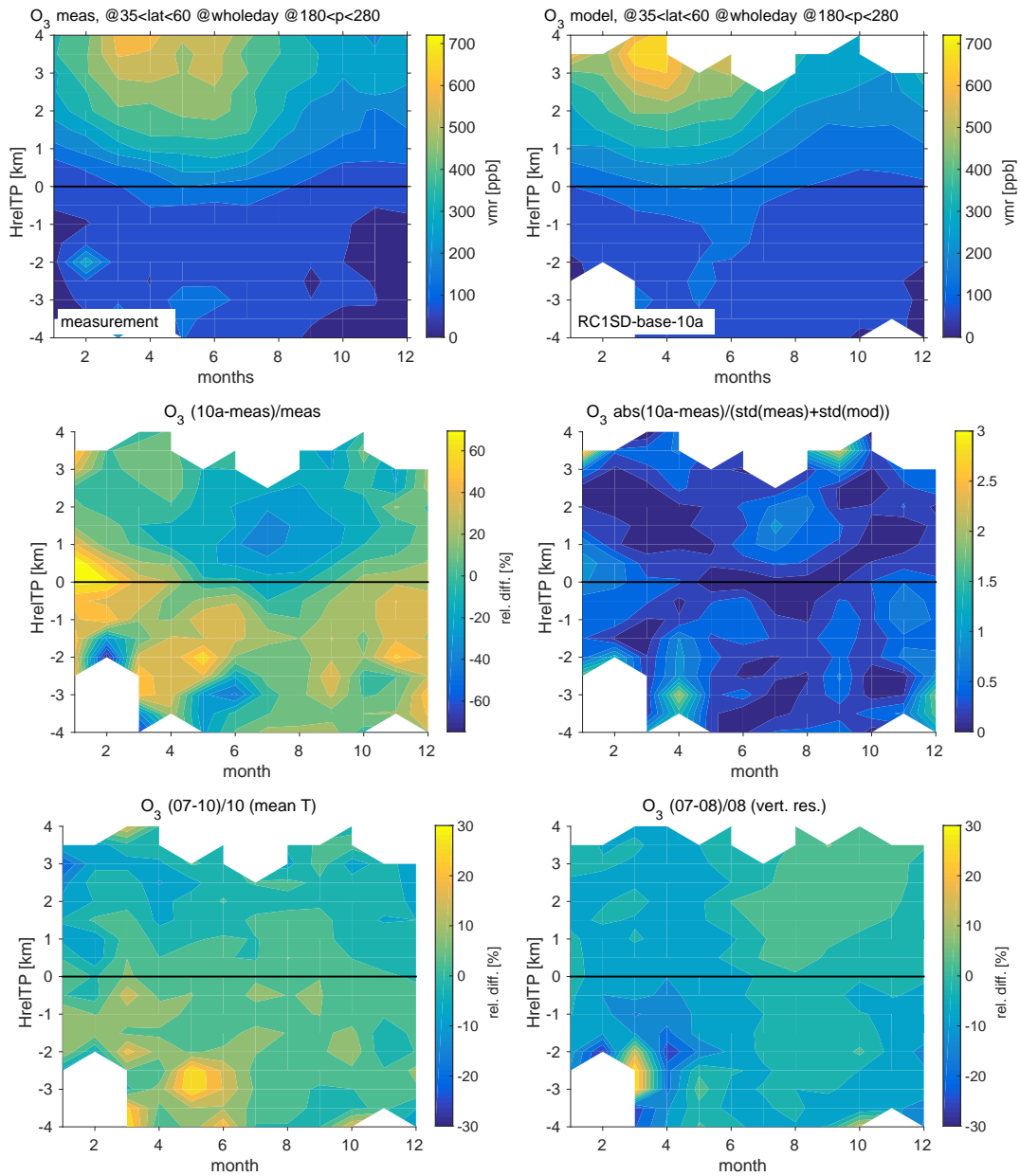


Fig. 3.2.: Results for O₃. The first row shows climatologies of CARIBIC measurements and *RC1SD-base-10a* model data. The second shows the relative difference of model data and measurements and the absolute values of model minus measurements over the sum of the standard deviation of measurements and model. The bottom row shows the relative difference of *RC1SD-base-07* and *RC1SD-base-10*, differing in nudging of global mean temperatures, and the relative difference of *RC1SD-base-07* and *RC1SD-base-08*, with different vertical resolution.

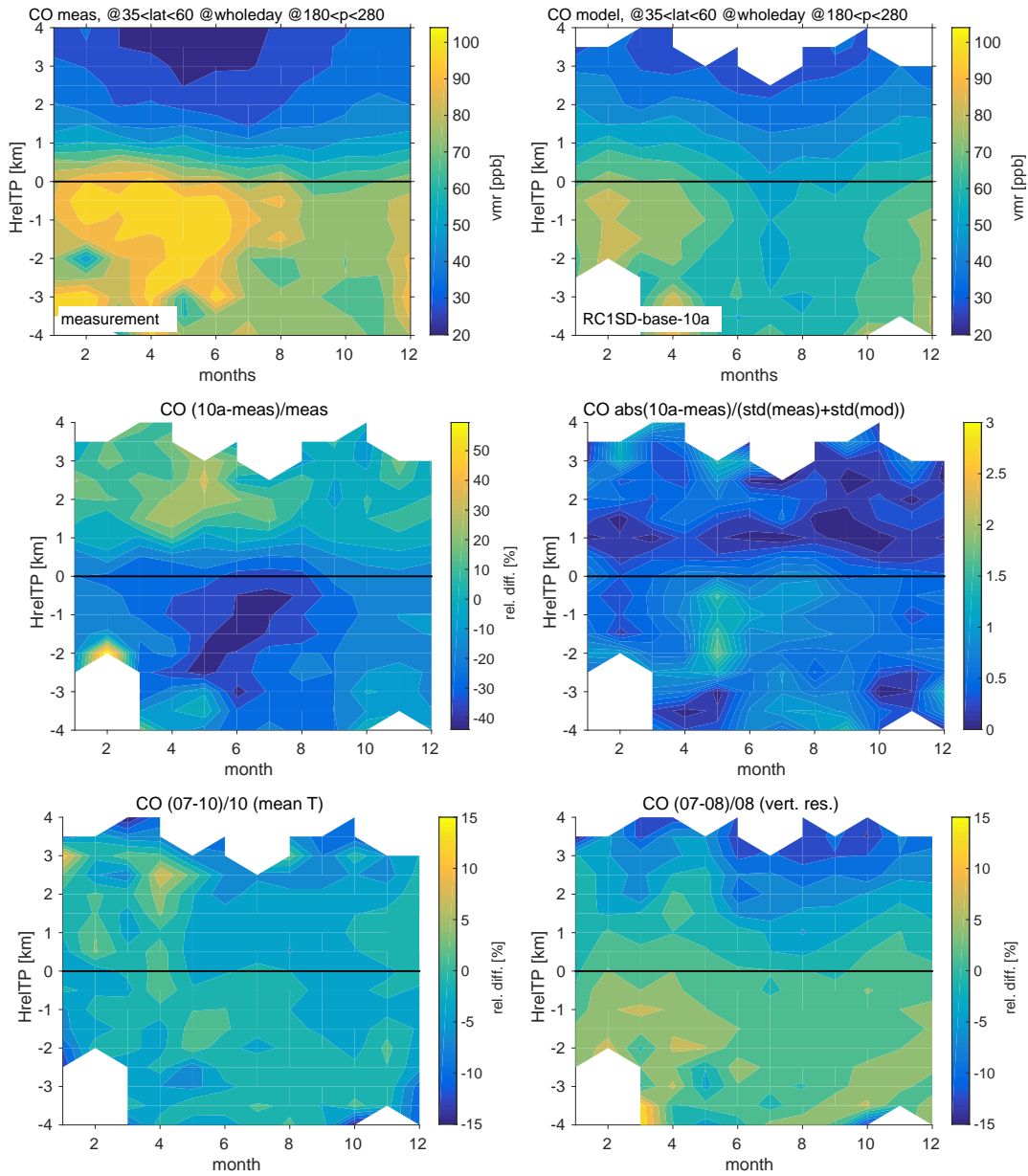


Fig. 3.3.: As Figure 3.2, but for CO.

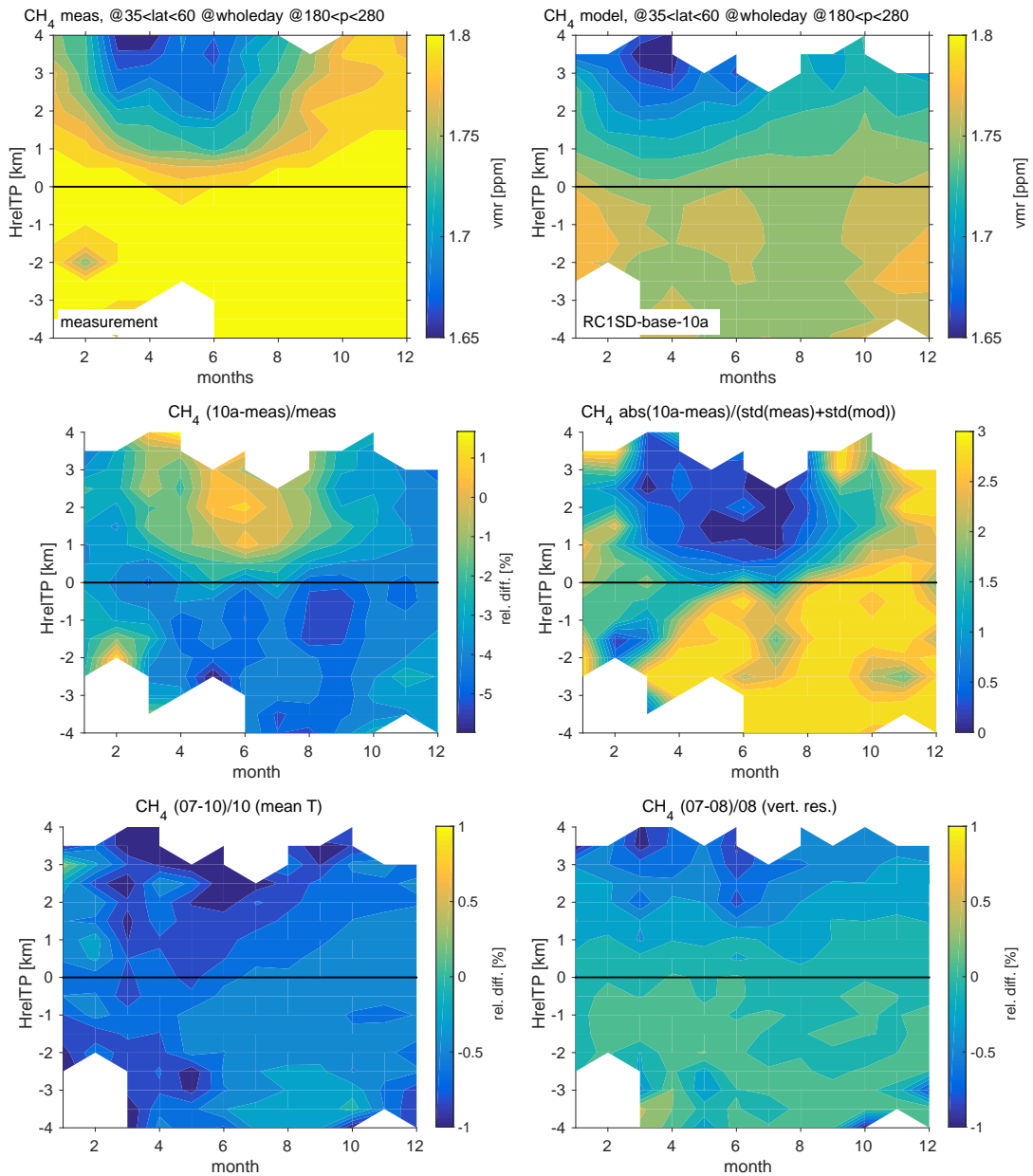


Fig. 3.4.: As Figure 3.2, but for CH₄.

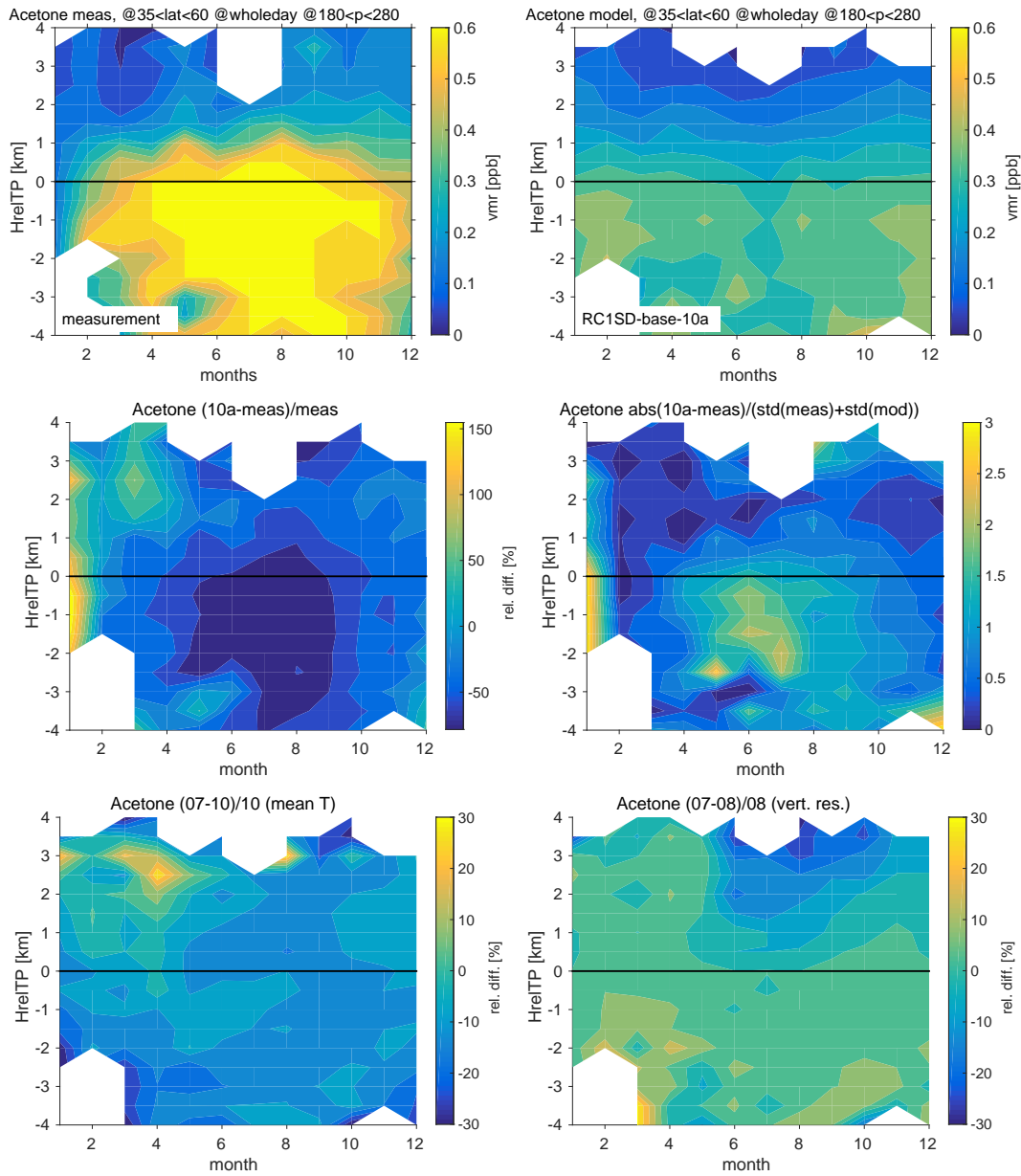


Fig. 3.5.: As Figure 3.2, but for acetone.

3.4. Summary and outlook

By examining the climatologies and their respective relative differences, it has become clear that there exist small but systematic differences between the results of the different model setups. The corrected road emissions have only a minor influence. Increasing the vertical resolution has effects that change mean values by up to 10 %. Different strengths of this influence can be noted for most species between the stratosphere and the troposphere, for O₃ also between different seasons. The effect of nudging global mean temperature is weaker, but it also shifts the seasonal cycle for all species but O₃, leading to relative differences of up to 10 % for selected months.

In comparing to measurements, the model produces realistic values for O₃. Values for CH₄ and CO are slightly underestimated, especially in the troposphere. The model simulations show other small differences along the CARIBIC flight tracks. The largest error is revealed in the distribution of acetone, for which all model simulations show significantly too small values and no annual cycle.

This chapter shows how the CARIBIC data can be applied to validate model simulations on a climatological time scale. While EMAC is a state of the art model, a similar comparison with the same tools has been performed by Weimer et al. (2017), but for a simplified acetone chemistry implemented into the next generation model ICON-ART.

The annual cycle of acetone is reproduced - though with a strong offset - if the model climatology is compiled from a larger, global set of model data. This brings up a new question: Are the climatologies discussed in this chapter representative of the mean atmospheric state? Or are they just mean values of the data? How much data is needed to reproduce the mean state? These questions require a dedicated study, which is the subject of the next chapter, Ch. 4.

4. Investigation of the climatological representativeness of CARIBIC data

Can the data from the long running project IAGOS-CARIBIC be used to create a meaningful climatology for the tropopause level in mid-latitudes? This is investigated with the help of a long integration of the chemistry-climate model EMAC by comparing the representation of the IAGOS-CARIBIC dataset in the model to the mean model state.

Adequate space is given to motivate that the conclusions from the modeled atmosphere can be applied to the real world. The climatological representativeness of the IAGOS-CARIBIC dataset is given a sound mathematical definition and the influence of several limitations of the dataset on the representativeness is discussed.

This chapter thereby demonstrates how a model simulation can add value to such a long running measurement project. It is the central counterpart to the other chapters, which show how model developments can be validated with these measurements on a climatological (Ch. 3) or very local scale (Ch. 5).

4.1. Introduction and literature overview

Measurements taken by commercial aircraft projects like IAGOS (In-Service Aircraft for a Global Observing System, Petzold et al. (2015)) and CONTRAIL (Comprehensive Observation Network for Trace gases by Airliner, Matsueda et al. (2008)) generate large continuous and regular datasets. Research aircraft on the other hand fly for a specific objective on sporadic campaigns. To emphasize the value of the long running projects, these datasets are commonly given the attribute representative. The representativeness of a dataset is a fundamental question that is raised more frequently the longer a project has been measuring. Too often, this adjective is left undefined, while the intent its use is obviously to state the data be used for a certain purpose.

This chapter investigates the climatological representativeness of the IAGOS-CARIBIC dataset for different trace gases and answers the question: For which species is a climatology compiled from CARIBIC data representative of the tropopause region in mid-latitudes? A 20 year nudged simulation of the model EMAC is sampled along the flight paths of CARIBIC. Climatologies compiled from this model data are compared to the climatologies from a larger model sample, which show the mean model state. It is then investigated whether the CARIBIC sampled model data is representative of the larger model dataset by different statistical measures. This demonstrates how a climatological model simulation adds value to this long term measurement project by answering this basic question with a novel method.

Questioning the representativeness of data is not new. Ramsey and Hewitt (2005) give a general introduction to representativeness, coming from soil sciences. As they state, the adjective representative has no meaning of its own, so a definition has to be given and 'it must be asked "representative of what?"'

In the area of meteorology, Nappo et al. (1982) give the following definition: 'Representativeness is the extent to which a set of measurements taken in a space-time domain reflects the actual conditions in the same or different space-time domain taken on a scale appropriate for a specific application.' Representativeness in their understanding 'is an exact condition, i.e., an observation is or is not representative.' Only if 'a set of criteria for representativeness is established, analytical and statistical methods can be used to estimate how well the criteria are met.'

The mathematical definition given by Nappo et al. (1982) is mostly applied to data collected in the boundary layer, where it is used to answer the question whether a flux tower station is representative of the area in which it is positioned (e.g. by Schmid (1997), Laj et al. (2009) or Henne et al. (2010)). This can also be analyzed by means of a cluster analysis with backward trajectories (e.g. by Henne et al. (2008) or Balzani Lööv et al. (2008)). By this method, source regions for measured trace gases can be found and the type and origin of air masses contributing to an observed air mass determined, i.e. the air mass the data are representative of. Köppe et al. (2009) apply this method to aircraft data from the project IAGOS-CARIBIC (Civil Aircraft for the Regular Investigation of the Atmosphere Based on an Instrument container, being part of IAGOS).

Lary (2004) and Stiller (2010) discuss the representativeness error in the field of data assimilation. Lary (2004) uses representativeness uncertainty as a synonym for variability within a grid cell, Stiller (2010) discusses the sampling error, which is considered to be part of the representativeness uncertainty. Larsen et al. (2014) study the representativeness of one dimensional measurements taken along the flight track of an aircraft to the three dimensional field that is being probed. But as they consider single flight tracks, their methods and definitions do not apply here.

The study of Schutgens et al. (2016) is more related to this study. They consider the sampling error on a global scale, comparing normal model means to means of model data collocated to satellite measurements. They find that this sampling error reaches 20 – 60 % of the model error (difference between observations and collocated model values).

This study has been motivated by Kunz et al. (2008). They analyzed whether the dataset of the aircraft campaign SPURT (SPURenstofftransport in der Tropopausenregion - trace gas transport in the tropopause region, Engel et al. (2006)) is representative of the larger MOZAIC dataset (Measurements of Ozone, water vapour, carbon monoxide and nitrogen oxides by in-service Airbus airCRAFT, the precursor of IAGOS-core). Kunz et al. (2008) investigate distributions of two substances (O_3 and H_2O) in two atmospheric compartments (upper troposphere and lower stratosphere). They find that the smaller SPURT dataset is representative on every time scale of the larger MOZAIC set for O_3 , while this is not the case for H_2O . While SPURT O_3 data can be used for climatological investigations, the variability of H_2O is too large to be fully captured by SPURT on the interseasonal time scales.

This is similar to what is done in this study: The representativeness of data for different trace gases from IAGOS-CARIBIC (see Sec. 4.2.1) is investigated for a climatology in the UTLS. Possible mathematical definitions of the word representativeness are first discussed with the help of this data. Then, its representativeness following these definitions is investigated. By using data from the chemistry-climate model EMAC (see Sec. 4.2.2) along the flight tracks of IAGOS-CARIBIC and comparing this to a larger sample taken from the model, it becomes possible to investigate the representativeness of the smaller of the two model datasets. It is also assess whether the complexity of the model is similar to that portrayed by the measurements, using the variability as a measure for the complexity. The variability of the model is high enough and the representativeness of IAGOS-CARIBIC measurement data for a climatology in the UTLS is therefore quantified by using the two model datasets alone.

Section 4.2 gives details on the data from IAGOS-CARIBIC and the model run used in this chapter. The general concept and definition of representativeness is then discussed in Sec. 4.3. This section also gives details on sampling the model. The following section is devoted to the variability, which is used to group results by species (Sec. 4.4). The statistical methods are then explained in Sec. 4.5, namely the Kolmogorov-Smirnov test, a variability analysis following the general idea of Kunz et al. (2008) and Rohrer and Berresheim (2006) and the relative difference of two climatologies. These methods are then applied to random numbers with specific statistical properties in Sec. 4.6 and to the model datasets in Sec. 4.7. Since the study presented here investigates representativeness from model datasets alone and

then applies the conclusion to measurements, it is an important prerequisite to show that this is valid reasoning. Section 4.8 discusses this question by comparing model and measurement variability.

The following Sec. 4.9 discusses the representativeness of the CARIBIC measurement data. Mean values for all species are discussed and the concept applied to three sample climatologies. A separate section answers the practical question how many flights are necessary to achieve a certain degree of representativeness. Three smaller subsections investigate limits inherent in the CARIBIC dataset: The Pacific remains unsampled, which corresponds to a limit in longitude, the aircraft flies on constant pressure levels and some species have a limited sampling frequency. Section 4.10 summarizes this chapter and gives an outlook.

The largest part of this chapter has already been published (Eckstein et al., 2017), either in the main document or in the supplement to this paper. The three final smaller sections go beyond this publication.

4.2. Model and data

This section describes which measurements of the CARIBIC dataset are used in this chapter and gives technical details on the model simulation. A general introduction to the project IAGOS-CARIBIC is given in Sec. 2.2, while the model EMAC is introduced in Sec. 2.3.1.

4.2.1. The observational IAGOS-CARIBIC dataset

Of the many substances measured by IAGOS-CARIBIC, this study considers NO_y , H_2O , O_3 , CO_2 , NO , $(\text{CH}_3)_2\text{CO}$ (acetone), CO and CH_4 from continuous measurements and N_2O , C_2H_6 and C_3H_8 from air samples. NO_y is the sum of all reactive nitrogen species, measured by catalytic conversion to NO (Brenninkmeijer et al., 2007). Data of N_2O , CH_4 and CO_2 were detrended by subtracting the mean of each year from the values of that year and adding the overall mean.

The data of all flights from the year 2005 (beginning of the second phase of CARIBIC) to the end of December, 2013 (end of the model run) are considered in this study. This dataset will be referred to as $\text{MEAS}_{\text{CARIBIC}}$.

As this study investigates representativeness using model data, the geolocation of the CARIBIC measurements at 10s resolution is used. In a second step, the gaps of the CARIBIC measurements and height information (due to technical problems etc.) are mapped onto their representation in the model data to infer the representativeness of the measurement data.

4.2.2. The EMAC model simulation

The model integration of EMAC used in this study simulated the time between January 1994 and December 2013, with data output every eleven hours. Meteorology is nudged up to 1 hPa using divergence, vorticity, ground pressure and temperature from six-hourly ERA-Interim reanalysis (Dee et al., 2011). It includes the extensive EVAL-Chemistry using the kinetics for chemistry and photolysis of Sander et al. (2011). This set of equations has been designed to simulate tropospheric and stratospheric chemistry equally well.

Boundary conditions for greenhouse gases (latitude dependent monthly means) are taken from Meinshausen et al. (2011) and continued to 2013 from the RCP 6.0 scenario (Moss et al., 2010). Boundary conditions for ozone depleting substances (CFCs and halons) are from the WMO-A1 scenario (WMO, 2010). Emissions for NO_x , CO , and non-methane volatile organic compounds are taken from the EDGAR data base¹.

The setup of the model in this study is similar to that made for the run RC1SD-base-08 of the Earth System Chemistry integrated Modelling (ESCiMo) initiative, presented by Jöckel et al. (2016). It differs in vertical resolution (47 versus 39 levels), but horizontal resolution, nudging and the chemistry are the same. The study by Jöckel et al. (2016) gives a detailed description and presents first validation results,

¹see <http://edgar.jrc.ec.europa.eu/index.php>

parts of which are presented in Ch. 3. Tribute to setting up the model simulation used in this study goes to Ole Kirner of SCC, KIT (ole.kirner@kit.edu).

The substances from the model used in this study are the same as those from measurements. NO_y , which is simulated in its components, is summed up from N, NO, NO_2 , NO_3 , N_2O_5 (counted twice because measurements of NO_y are taken by catalytic conversion), HNO_4 , HNO_3 , HONO, HNO, PAN, ClNO_2 , ClNO_3 , BrNO_2 and BrNO_3 . Data of N_2O , CH_4 and CO_2 were detrended, using the same method applied to the measurements.

4.3. Defining representativeness

As noted above and specified by Nappo et al. (1982) and Ramsey and Hewitt (2005), the word representative is meaningful only if accompanied by an object. Ramsey and Hewitt (2005) raise three questions which need to be answered in order to address representativeness: 1. For what parameter is the sample data to be seen as representative: e.g. the mean, a trend or an area? 2. Of which population are the sample data to be seen as representative? 3. To which degree are the data to be seen as representative? To assess the representativeness of CARIBIC data, these three questions have to be answered as well.

4.3.1. Representative for what parameter?

First, it is crucial to define what the CARIBIC data is anticipated to be representative of, since 'the same set of measurements may be deemed representative for some purpose but not other' (Nappo et al., 1982). In this study, it is investigated whether the CARIBIC data can be used to construct a climatology in the UTLS. Monthly binned data in the height of ± 4.25 km are considered around the dynamical tropopause defined at the pressure at 3.5 PVU and in mid-latitudes with $75^\circ\text{N} < \varphi < 35^\circ\text{N}$.

In order to reference data to the tropopause, the geometric height in kilometers relative to the tropopause (HrelTP) is used at each datapoint. For the measurements, this height is provided by the meteorological support of CARIBIC by KNMI² (Koninklijk Nederlands Meteorologisch Instituut), who use data from ECMWF (European Centre for Medium-range Weather Forecast) for their calculation.

From model output, the height relative to the tropopause (HrelTP) can be calculated, as the pressure value of the dynamical tropopause is known at each location, as well as the temperature and pressure profile. This HrelTP value calculated from the model data along the flight tracks of CARIBIC compares well with interpolated values from ECMWF provided by KNMI (Pearson correlation coefficient of $\rho = 0.97$), which is expected as the meteorology of the model is nudged using ERA-Interim data. The distribution of all values of HrelTP from the model is shown in Figure 4.1, showing a maximum right at the tropopause. Data were used within ± 4.25 km around the tropopause in steps of 0.5 km.

Even though all data of trace gases (be it from model or measurements) are sorted into bins of HrelTP, it is important to keep in mind the limits in pressure. These are inherent in the CARIBIC dataset, as the aircraft flies on constant flight levels with $180\text{hPa} < p < 280\text{hPa}$. In addition, pressure is explicitly limited to this range in order to exclude data from ascents and descents of the aircraft. But since data are considered relative to the tropopause, these limits are no longer visible directly from the resulting climatology, even though they can influence it strongly. The reason is that aircraft flying at constant pressure can measure far above (below) the tropopause only if the tropopause is located at high (low) pressure. The properties of many trace substances are not only a function of their distance to the tropopause, but also of pressure. The limits in pressure inherent in the sample therefore also influence the climatology.

²see http://www.knmi.nl/samenw/campaign_support/CARIBIC/

They have to be considered and should be explicitly stated. This effect is illustrated in Sec. 4.9.5 with the help of the methods developed in this chapter.

In addition to limiting in HrelTP and p , it is necessary to apply a limit in latitude φ . The data is limited by including only the mid-latitudes with $75^\circ\text{N} < \varphi < 35^\circ\text{N}$. Tropical data with $\varphi < 35^\circ\text{N}$ are excluded because of the considerably higher dynamical tropopause. Data with $\varphi > 75^\circ\text{N}$ are excluded because of the different chemistry in far northern latitudes, which leads to considerably different mixing ratios for some some species that should not be combined with data from lower latitudes in one climatology. In addition, this latitudinal band is well covered by CARIBIC measurements. Other regions or latitudinal bands can be investigated using the same approach.

Like the limit in pressure, CARIBIC data are also limited in longitude, as the Pacific Ocean is never probed. The effect of this limit on the climatology is discussed in Sec. 4.9.4.

As a summary, the question (Representative for what parameter?) asked in the beginning can be specified: Is a climatology compiled from CARIBIC data representative of the tropopause region in mid-latitudes?

4.3.2. Representative of which population?

When assessing the representativeness of the sample made up by all CARIBIC measurements (called $\text{MEAS}_{\text{CARIBIC}}$, see Sec. 4.2.1), the population is the atmosphere around the tropopause and its composition. For many of the species measured by CARIBIC, there is no other project that takes such multi-tracer in situ measurements as regularly at the same spatial and temporal resolution. IAGOS-core and CONTRAIL sample with much higher frequency, but take measurements of only few substances while satellites do not resolve the small scale structures necessary to disentangle the dynamics around the tropopause. The population is therefore not accessible by the measurement platforms currently available.

This is the reason why the representativeness of the CARIBIC data are investigated by comparing the model data along CARIBIC flight tracks to two larger samples taken from the model. These larger datasets are considered the population, in reference to which the representativeness of the smaller dataset (model along CARIBIC paths) is assessed. Three datasets were created from the model output: the model along CARIBIC paths and two random model samples. All are presented in the following paragraphs, a summary being given in Table 4.1 and Figure 4.1.

$\text{MOD}_{\text{CARIBIC}}^{\text{regular}}$: For the dataset $\text{MOD}_{\text{CARIBIC}}^{\text{regular}}$, the model output was interpolated linearly in latitude, longitude, logarithm of pressure and time to the position of the CARIBIC aircraft, using the location at a resolution of 10s for all species, independent of the time resolution in $\text{MEAS}_{\text{CARIBIC}}$. Figure 4.1 shows the flight paths considered in this study. Since CARIBIC also measures temperature (at 10s resolution), the high pearson correlation coefficient of $\rho = 0.97$ of modelled to measured temperature can serve as an indication that this interpolation leads to reasonable results, despite the coarser resolution in time and space of the model output.

dataset	EMAC on	total sets	per month	duration	p distribution
$MOD_{CARIBIC}^{regular}$	CARIBIC paths (2005-13)	334	up to 4 in 3 days	8-10h	flight levels show up, $\bar{p} = 223.42$ hPa $\sigma(p) = 18.94$ hPa
$MOD_{RANDPATH}$	random paths	1296	12 in 28 days	24h	adjusted gaussian, $\bar{p} = 223.42$ hPa $\sigma(p) = 18.94$ hPa
$MOD_{RANDLOC}$	random loca- tion	864	8 in 28 days	24h	uniform, $\min(p) = 10$ hPa $\max(p) = 500$ hPa

Tab. 4.1.: Summary of the specifications defining the three datasets $MOD_{CARIBIC}^{regular}$, $MOD_{RANDPATH}$ and $MOD_{RANDLOC}$. See the running text for the specifications of $MEAS_{CARIBIC}$, $MOD_{CARIBIC}^{sampled}$ and $MOD_{RANDPATH}^3$.

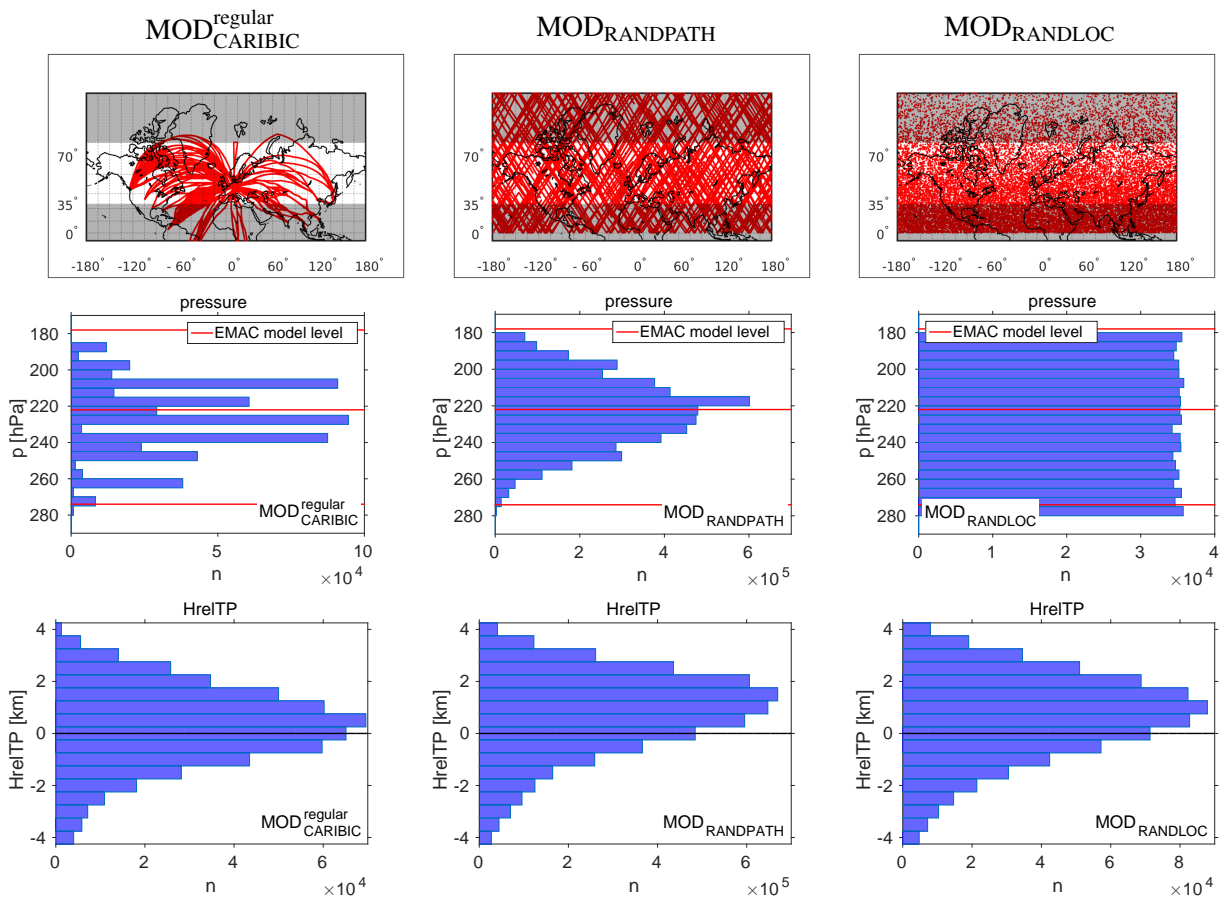


Fig. 4.1.: Flight paths (top), distribution in p (center) and HrelTP (bottom) for the three datasets $MOD_{CARIBIC}^{regular}$ (left), $MOD_{RANDPATH}$ (center) and $MOD_{RANDLOC}$ (right). Only parts of the paths of $MOD_{RANDPATH}$ and $MOD_{RANDLOC}$ are shown in the top row.

MOD_{CARIBIC}^{sampld}: The measurement frequency for some species in MEAS_{CARIBIC} is lower (e.g. those taken by whole air samples), all species contain gaps because of instrument problems at some point and some of the species considered by the model datasets are not measured at all. Sometimes, it is interesting to consider MOD_{CARIBIC}^{regular} reduced to the exact number of measurement points, i.e. reduced by all these measurement gaps. The model dataset along CARIBIC paths that has the same gaps as MEAS_{CARIBIC} will be referred to as MOD_{CARIBIC}^{sampld}.

As is visible in Fig. 4.1 (central column), only three of the model levels lay in the pressure range sampled by CARIBIC. To have comparable statistics, MOD_{CARIBIC}^{regular} was compared to two random model samples.

MOD_{RANDPATH}: The dataset referred to as MOD_{RANDPATH} is a larger set of flight paths used to sample the model. This set was mainly used to investigate the representativeness of MOD_{CARIBIC}^{regular}. From the year 2005 to the end of 2013, 12 random flight paths were generated per month (1296 in total, evenly spaced in each month's first 28 days) and the model fields interpolated onto these paths. The starting point was randomly chosen in the northern hemisphere, as well as the direction taken by the aircraft. The speed was set to 885.1 km h⁻¹, the median of the speed of the true CARIBIC aircraft. The flights start at 0:00 UTC and sample the model for 24h in 10s intervals. They are reflected at the north pole and at the equator and reverse the sign of the increment in latitude direction once during flight. The first 100 of these paths are displayed in Figure 4.1.

The pressure was kept constant for each of the random flights, reproducing the statistics of the pressure distribution for CARIBIC as a whole. For this, a normal distribution centered around 223.42 hPa with a standard deviation of 18.94 hPa was used to choose the pressure value for each of the random flights. All pressure values of $p < 180$ hPa or $p > 280$ hPa were redistributed evenly between 200 hPa and 250 hPa to exclude unrealistically high or low values and sharpen the maximum.

MOD_{RANDPATH}³: The dependency of representativeness on the number of flights is an important part of this study. Each of the random paths was divided into three parts, resulting in 3888 eight hour flights, the duration of a typical intercontinental flight with CARIBIC. Representativeness was then calculated with the different methods for MOD_{RANDPATH} and these subsamples, increasing their size by including more of the 3888 shorter random flights. This dataset of randomized shorter flights will be referred to as MOD_{RANDPATH}³.

MOD_{RANDLOC}: For this sample, latitude and longitude were randomly drawn in the northern hemisphere (not aligned along a route) and the definition of the pressure distribution widened, drawing pressure from a uniform distribution from 500 hPa to 10 hPa for each flight. Again, the datasets start at 0:00 UTC and the separate points are 10s apart, collecting 8640 samples on a sampling day. Eight of these sets are distributed evenly in each month, summing to a total of 864 sets of this type. This set was used to test whether MOD_{CARIBIC}^{regular} is representative of a climatology around the tropopause only within its pressure limits or also when expanding these limits.

As is visible in Figure 4.1, the distribution in HrelTP is very similar for MOD_{RANDPATH} and MOD_{RANDLOC} even though the pressure is prescribed in very different ways (mean of 0.79 km and 0.64 km respectively). The distribution of MOD_{CARIBIC}^{regular} is different (mean of 0.26 km), which is due to the larger amount of data from southern latitudes (not shown). The different regional sampling is one of the reasons why climatologies from MOD_{CARIBIC}^{regular} and MOD_{RANDPATH} differ and this difference also affects the distribution in HrelTP.

4.3.3. Confidence limits of representativeness

When defining representativeness, one more question remains: What are the confidence limits of the representativeness?

Three definitions for representativeness are discussed and applied in this study: The Kolmogorov-Smirnov test, the variability analysis following Kunz et al. (2008) and the relative difference of two climatologies. The first method gives a yes-no answer within a chosen statistical confidence level. The other two approaches are formulated in such a way as to return a score. By (arbitrarily) setting a value for the score, the representative cases can be discriminated from the non-representative cases (see Sec. 4.5 and Sec. 4.7), the score corresponding to a confidence level.

There are two more requirements that are defined as having to be met by representativeness in general:

1. Representativeness has to increase with the number of samples (flights in the case of this study).
2. Representativeness has to decrease with increasing variability of the underlying distribution.

These two assumptions are implicitly also made by Kunz et al. (2008), as they investigate the representativeness of a smaller for a larger dataset and for two species of different variability. The measure for variability used in this study is explained in the following section.

4.4. Defining a measure for variability

Representativeness is expected to differ for different species because of their atmospheric variability, which is also a measure of atmospheric lifetime. This is part of the definition of representativeness given in Sec. 4.3.3. Kunz et al. (2008) also find that O_3 and H_2O are different in their representativeness and attribute this to the variability. It is therefore reasonable to consider results for representativeness relative to the variability of a species. In this study, the relative standard deviation σ_r is used as a measure for variability. It is calculated following Equation 4.1 using the mean μ and standard deviation σ of each species.

$$\sigma_r = \frac{\sigma}{\mu} \quad [4.1]$$

Figure 4.2 shows the sorted values of σ_r for the species considered in this study, using the full time series to calculate σ_r . It is worthwhile to note that in defining variability in this way, the study closely follows Junge (1974), who showed that under certain constraints, the relationship

$$\sigma_r = \frac{\sigma}{\mu} = a \cdot \tau^{-b} \quad [4.2]$$

holds, which links variability and lifetime τ using two species-dependent constants a and b . This relationship has frequently been called Junge relationship in the past (e.g. by Stroebe et al. (2006) or MacLeod et al. (2013)). And indeed, as visible in Figure 4.2, longer lived species like CO_2 or N_2O show lower variability, while shorter lived species show higher variability. This is true almost independent of the data set considered to calculate σ_r .

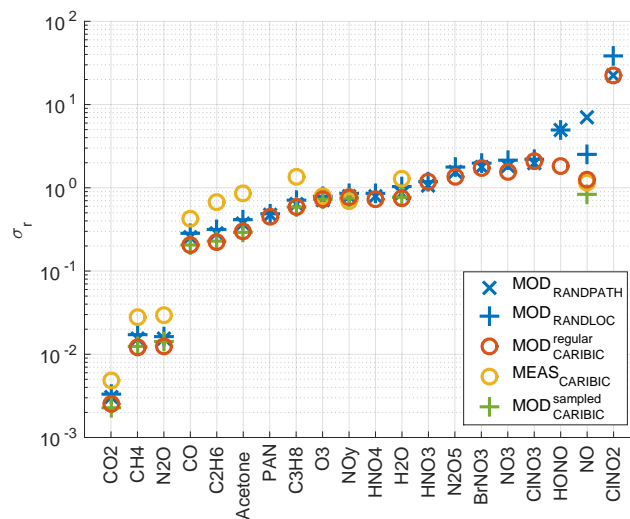


Fig. 4.2.: Variability σ_r calculated for different datasets using Equation 4.1. The species are sorted by σ_r , species with low variability listed to the left, using the values from $MOD_{RANDBATH}$ for sorting. Note that $\log_{10}(\sigma_r) = \tau^*$, see Eq. 4.3.

It is important to note that the values determined from $MEAS_{CARIBIC}$ and shown in Fig. 4.2 are affected by the measurement frequency in case of data sampled by whole air samples (N_2O , C_2H_6 and C_3H_8) and

by gaps due to instrument problems. But the influence of these gaps is small, as can be seen by the small differences of the two values for $\text{MOD}_{\text{CARIBIC}}^{\text{regular}}$ and $\text{MOD}_{\text{CARIBIC}}^{\text{sampled}}$. $\text{MEAS}_{\text{CARIBIC}}$ has a slightly higher variability than the model datasets for most species. The relationship of model and measurement variability is discussed in more detail in Sec. 4.8. The model datasets are very similar, despite their different sampling patterns. They only differ for short-lived species (to the right in Figure 4.2), which have a strong daily cycle, e.g. NO.

In Sec. 4.3.3, representativeness was defined as having to decrease with increasing variability. In order to emphasize the relationship of σ_r with τ and to differentiate this variability (calculated from the complete time series) clearly from other similar terms, τ^* , defined in Equation 4.3, is used in the following sections to test the relationship of representativeness and variability.

$$\tau^* = \log_{10}(\sigma_r) = \log_{10}(a) - b \cdot \log_{10}(\tau) \quad [4.3]$$

Sec. 4.5.2 will take a closer look at variability. It will be discussed how variability depends on the time scale for which it is calculated. The values shown in Figure 4.2 and used for the calculation of τ^* make use of the full time series, and thereby the overall variability. If shorter time scales had been considered, the values for σ_r in Figure 4.2 would change, but not the order of the species that follows from the values.

So including these thoughts on variability in the question formulated at the end of Sec. 4.3.1, the question answered in this study can again be asked more precisely: For which species is a climatology compiled from CARIBIC data representative of the tropopause region in mid-latitudes?

4.5. Statistical methods

Three different methods to evaluate representativeness have been used: the Kolmogorov-Smirnov test, the variability analysis and relative differences. These are presented in the following sections. In a second step, each of the methods has to pass the two requirements set up in Sec. 4.3.3: Being related to the variability and the number of samples. This is investigated for random numbers in Sec. 4.6 and for the different model datasets in Sec. 4.7.

4.5.1. Kolmogorov-Smirnov test

The Kolmogorov-Smirnov two-sample test is a non-parametric statistical test that is used to examine whether two datasets have been taken from the same distribution (e.g. Sachs and Hedderich (2009)). It considers all types of differences in the sample distributions that can be apparent in the mean, the standard deviation, the kurtosis, etc. The test statistic is the maximum absolute difference \hat{D} in the cumulative empirical distribution functions \hat{F}_x of the two samples x :

$$\hat{D} = \max|\hat{F}_1 - \hat{F}_2| \quad [4.4]$$

The discriminating values D_α have been derived depending on the accepted confidence limit α . In this study, the two empirical distribution functions \hat{F}_i were taken from MOD_{CARIBIC}^{regular} and MOD_{RANDPATH} in each height bin and month. In addition to the Kolmogorov-Smirnov test, the Mann-Whitney test for the mean and Levene's and the Brown-Forsythe test for variance (see again Sachs and Hedderich (2009)) have also been used.

4.5.2. Variability analysis

The variability analysis follows Rohrer and Berresheim (2006) and Kunz et al. (2008). Rohrer and Berresheim (2006) introduced a variance analysis for ground-based observations, Kunz et al. (2008) then applied it to aircraft data. A timeseries of data is subsequently divided into ever shorter time slices of increasing number and the variance is calculated for the data within each time slice. By taking the mean over the whole number of slices and doing this for all divisions in time, a line is calculated, which is characteristic for the development of variance in time.

Instead of considering variance in each time slice, the relative standard deviation $\sigma_r = \frac{\sigma}{\mu}$ is used here, which is the definition of variability following Junge (1974). It is calculated in each time slice and the mean gives the value for the corresponding time scale. In the following, time scale therefore refers to the length of the interval in time in which the variability is calculated. By scaling the standard deviation σ with the mean μ , different species become comparable. Being a combination of variability as defined by Junge (1974) and the variance analysis introduced by Rohrer and Berresheim (2006), this method is called variability analysis in the following paragraphs.

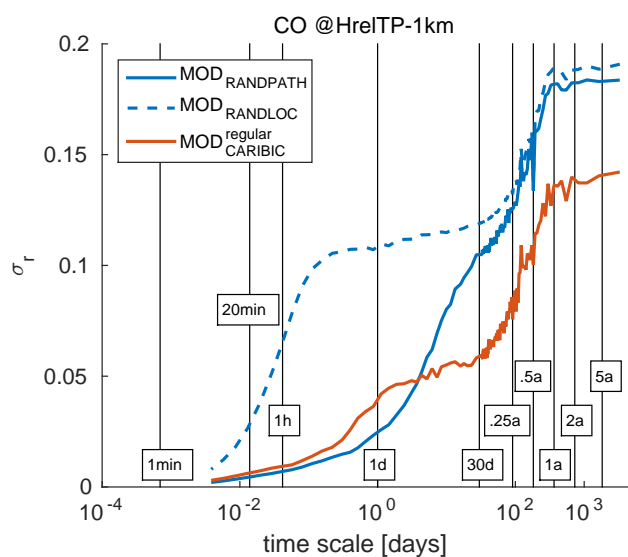


Fig. 4.3.: Variability analysis calculated for CO for $\text{MOD}_{\text{RANDPATH}}$, $\text{MOD}_{\text{RANDLOC}}$ and $\text{MOD}_{\text{CARIBIC}}^{\text{regular}}$ at $\text{HrelTP} = -1$ km (one kilometer below the tropopause). The time scales used to calculate R_{var} using Equation 4.5 are indicated by vertical lines.

Figure 4.3 shows the variability analysis for CO just below the tropopause for $\text{MOD}_{\text{CARIBIC}}^{\text{regular}}$, $\text{MOD}_{\text{RANDPATH}}$ and $\text{MOD}_{\text{RANDLOC}}$. The time scale changes from about 5 min to 5 a along the logarithmically spaced abscissa. As CO is a medium long-lived trace gas with an atmospheric lifetime of 2-3 months and a pronounced annual cycle, the mean variability increases up to time scales of 1 a. The variability of $\text{MOD}_{\text{RANDPATH}}$ and $\text{MOD}_{\text{RANDLOC}}$ is larger than that of $\text{MOD}_{\text{CARIBIC}}^{\text{regular}}$ on almost all time scales. For time scales of 30d and more, however, the lines of all three datasets run in parallel, showing an increase up to 1 a, from when on the variability does not increase. This is consistent with the annual cycle of CO, which is also the cause for the relative decrease sharply at 0.5 a and 1.5 a. For time scales below 30d, the distribution of flights in one month dominates the variability analysis. $\text{MOD}_{\text{CARIBIC}}^{\text{regular}}$ includes only up to four flights on consecutive days, the mean variability does not decrease when going to time scales between 30d and 4d, while in $\text{MOD}_{\text{RANDPATH}}$, continuously less data are included in each time slice, leading to a continuous drop in the variability. For time scales of less than 1 d, the data come from a single flight, showing another drop in variability that is linked to using data from geographic regions that are ever more close in the case of $\text{MOD}_{\text{CARIBIC}}^{\text{regular}}$ and $\text{MOD}_{\text{RANDPATH}}$. Since the variability analysis is so closely linked to the distribution in time and space, the variability analysis of $\text{MOD}_{\text{RANDLOC}}$ shows an almost constant value for time scales shorter than 30d until time scales shorter than one day are reached, from when on the variability also drops.

Kunz et al. (2008) used the variance analysis to investigate whether the smaller SPURT dataset represents the variance present in MOZAIC dataset. Following this thinking, the variability is considered as one possible criterion to judge the representativeness of one dataset for another. A score $R_{\text{var}}^{t,h}$ describing

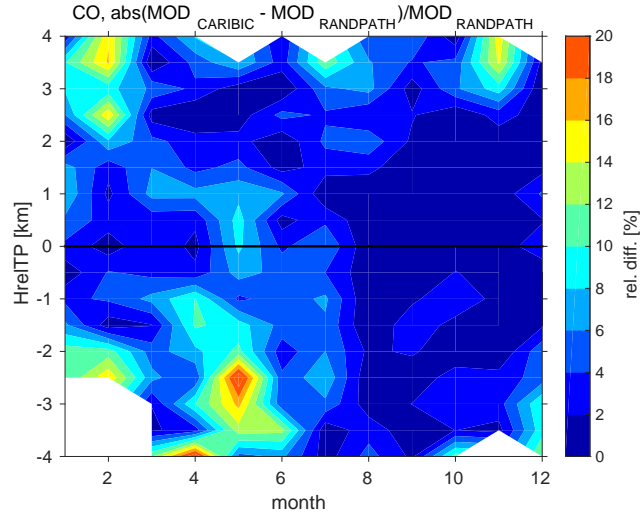


Fig. 4.4.: Relative differences of CO for $\text{MOD}_{\text{CARIBIC}}^{\text{regular}}$ and $\text{MOD}_{\text{RANDPATH}}$. This is the basis used to calculate R_{rel} .

the representativeness is defined from the difference of the values of the variability analysis, using the following equation:

$$R_{\text{var}}^{t,h} = \log_{10} \left(\left| \frac{\overline{\sigma_1^{t,h}}}{\overline{\mu_1^{t,h}}} - \frac{\overline{\sigma_2^{t,h}}}{\overline{\mu_2^{t,h}}} \right| \right) \quad [4.5]$$

where $\sigma_x^{t,h}$ stands for the standard deviation and at $\mu_x^{t,h}$ for the mean in time scale t and height h of the datasets x . The overbar implies that the mean over all time slices corresponding to the time scale t of σ/μ are used. Considering Figure 4.3, the score can be interpreted as the absolute value of the difference of the two lines at certain time scales t .

Decreasing values of $R_{\text{var}}^{t,h}$ mean better representativeness, the value always being negative. Depending on t , the representativeness in different time scales can be evaluated. Here, time scales of 30d, 0.25 a, 0.5 a, 1 a, 2 a and 5 a are used to calculate $R_{\text{var}}^{t,h}$. When applying this method to all height bins, a profile in R_{var}^t is calculated for each species. This is one possible definition for representativeness. Yet it has to pass the two requirements of being related to number of samples and variability outlined in Sec. 4.3.3.

4.5.3. Relative differences

The third approach to assess representativeness is to analyze the relative differences between the climatologies from two differently large datasets. The procedure is summarized in Equation 4.6:

$$R_{\text{rel}}^h = \log_{10} \left(\frac{1}{12} \sum_{m=1}^{12} \frac{|\mu_1^{m,h} - \mu_2^{m,h}|}{\mu_2^{m,h}} \right) \quad [4.6]$$

which was applied to each height bin h . $\mu_x^{m,h}$ stands for the mean of the data in the month m and in height bin h of the datasets x . The logarithm to the basis 10 was applied to the mean relative difference profile to end up with a profile in R_{rel} , similar to the score R_{var}^t calculated from the variability analysis.

Contrary to the Kolmogorov-Smirnov test or the variability analysis, this test statistic does not contain any information on the underlying distribution, because it uses only the mean in each bin.

Figure 4.4 shows an example of relative differences between CO from $\text{MOD}_{\text{CARIBIC}}^{\text{regular}}$ and the larger dataset $\text{MOD}_{\text{RANDPATH}}$. The differences are small, mostly below an absolute value of 0.15. R_{rel} is defined (in Equation 4.6) as the logarithm to the base 10 of the mean over all months (not shown). The score increases towards the top and bottom in Figure 4.4 due to less data there. Like for R_{var}^t , decreasing values in R_{rel} mean better representativeness. And like R_{var}^t , R_{rel} has to be tested for passing the requirements of being related to number of samples and variability (see Sec. 4.3.3) in order to be acceptable as a score for representativeness.

Other than just as a score, the value of R_{rel} can be understood as the average uncertainty for assuming the climatology of $\text{MOD}_{\text{CARIBIC}}^{\text{regular}}$ as a full model climatology. This is more obvious if taken to the power of 10, in which case the uncertainty will take values between 0 and 1. Use of this will be made in Sec. 4.9.1.

4.6. Statistical methods applied to random numbers

All three methods to investigate representativeness were first applied to data created with a random number generator. This random number data (referred to as RAND in the following) can be considered a theoretical abstraction of the model datasets MOD. The following sections are therefore a preliminary study, investigating the principal usefulness of the methods presented in Sec. 4.5.

With RAND defined as in the following section, it is possible to test representativeness using the variability analysis following Rohrer and Berresheim (2006) and Kunz et al. (2008) (see Sec. 4.5.2) and the relative differences (see Sec. 4.5.3). The Kolmogorov-Smirnov test was positive for very few samples (less than fifty numbers, independent of τ^*) and will not be further discussed. Its behavior with aircraft data was subject of a sensitivity study, the results of which are shown in Sec. 4.7.2.

4.6.1. Defining the random number data

To produce the random number data sets, 20 sets of 10^8 numbers were taken from a normal distribution. These 20 sets are referred to as species, well aware of the fact that they are purely artificial. From species to species, the standard deviation σ was set to vary from 10^{-3} to 10^3 , values of the exponent increasing linearly. 20 mean values μ (increasing from 10^4 to 10^8 , with a linear increase in the exponent) were distributed randomly to the 20 species. This results in 20 species with different values for σ and μ . The overall statistics of each species will be indexed by the number 2. For short, this dataset will be called RAND.

The variability τ^* of each species is defined as in Equation 4.3 of the main text: $\tau^* = \log_{10}(\sigma_2/\mu_2)$. The two requirements set up in Sec. 3.3 for representativeness in general also have to hold here: Representativeness has to increase with the number of samples and has to decrease with increasing variability of the underlying distribution.

3000 samples were taken from each of the 20 species. For each sample, 20 numbers were first randomly drawn from each species. These new numbers and all those that had been drawn before then make up this one sample. So the size increases by 20 for each sample. This way, the relationship of the representativeness score with the sample size is directly accessible. Samples are indexed by the number 1.

4.6.2. Variability analysis

The variability analysis (defined in Sec. 4.5.2 and Eq. 4.5) was applied in a simplified manner. As RAND is independent of time, R_{var} is reduced to just a single value containing the absolute difference of variability of each species of RAND and the sample taken thereof: $R_{\text{var}} = |v_1 - v_2|$, where v is the mean variability. Figure 4.5 shows a result. The exact result is a matter of chance, as a random number generator is used. A strong dependence on τ^* and a weak dependence on the number of samples is visible.

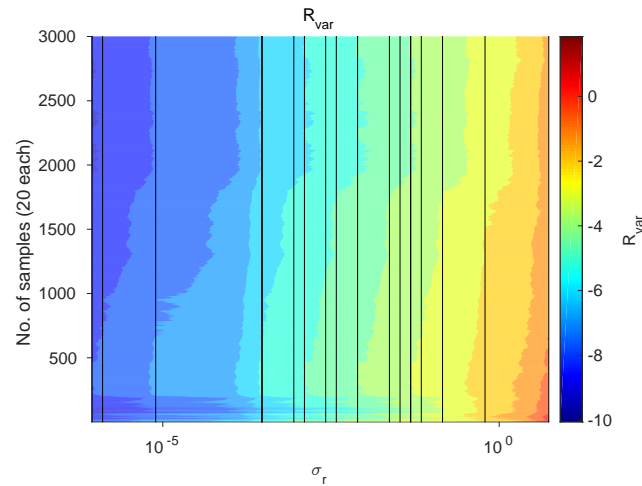


Fig. 4.5.: Representativeness score R_{var} applied to RAND. Vertical lines indicate the values of τ^* of each species.

The variability analysis using RAND meets the two requirements necessary for describing representativeness, which were described in Sec. 4.3.3 and above. This shows that R_{var} can be used as a statistic for describing representativeness.

4.6.3. Relative differences

Similar to R_{var} , R_{rel} is reduced to a simple relative difference when using RAND: $R_{\text{rel}} = |\mu_1 - \mu_2|/\mu_2$, where μ is the mean. Figure 4.6 shows the result when applying R_{rel} to RAND. The dependence on τ^* is strong and linear. The result also depends on the number of samples, showing a slow increase with the number of samples. This dependence is sometimes disturbed by better values which are reached by chance when drawing from RAND.

R_{rel} passes both conditions for a valid description of representativeness: it depends on variability τ^* and on the number of samples. The latter is also being influenced by chance and generally much weaker.

4.6.4. Theoretical considerations

The fact that R_{rel} passes the two conditions for a description of representativeness can be understood with some theoretical considerations. The standard error of the mean is defined by

$$\sigma_{\bar{x}} = \frac{\sigma}{\sqrt{n}} \quad [4.7]$$

where $\sigma_{\bar{x}}$, the standard deviation of a sample, can be given by the following equation (N being the number of samples):

$$\sigma_{\bar{x}} = \sqrt{\frac{1}{N} \sum_{i=1}^N (\bar{x}_i - \mu)^2} \quad [4.8]$$

For $N = 1$, this gives:

$$\sigma_{\bar{x}} = |\bar{x}_i - \mu| \quad [4.9]$$

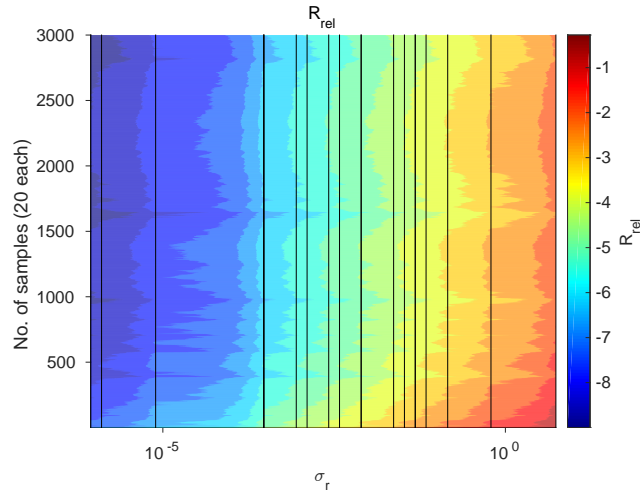


Fig. 4.6.: Like Figure 4.5, but for R_{rel} .

Plugging Eq. 4.9 into Eq. 4.7 gives:

$$\frac{|\bar{x}_i - \mu|}{\mu} = \frac{\sigma}{\mu\sqrt{n}} = \frac{10^{1/\tau^*}}{\sqrt{n}} \quad [4.10]$$

and therefore

$$R_{\text{rel}} = \log_{10} \left(\frac{|\bar{x} - \mu|}{\mu} \right) = -0.5 \log_{10}(n) + \frac{1}{\tau^*} \quad [4.11]$$

So ideally, R_{rel} should depend inversely on τ^* and directly on the logarithm of the number of values. Figure 4.6 shows this is approximately true for RAND.

In the case of RAND, R_{rel} and R_{var} can be used to describe representativeness as they pass the two conditions. Theoretical considerations make the finding for R_{rel} plausible. RAND can be considered a theoretical abstraction of the model datasets MOD, which are investigated in the following section. The findings presented in this section are therefore a first evidence that these two scores can be used to describe representativeness.

4.7. Statistical methods applied to model datasets

This section presents the results of the application of the Kolmogorov-Smirnov test (Sec. 4.7.1), the variability analysis (Sec. 4.7.3) and the relative difference (Sec. 4.7.4) to $MOD_{CARIBIC}^{regular}$ and $MOD_{RANDPATH}$. All have to be related to the number of flights and the variability of the species as discussed in Section 4.3.3. As the results of the Kolmogorov-Smirnov test were unexpectedly negative, a sensitivity study was performed, the results of which are presented in Sec. 4.7.2.

4.7.1. Applying the Kolmogorov-Smirnov test

The application of the Kolmogorov-Smirnov test to $MOD_{CARIBIC}^{regular}$ and $MOD_{RANDPATH}$ yields a first important result. Independent of the trace gas and height considered, the result is always negative. This means that the data in each bin of $MOD_{CARIBIC}^{regular}$ are not representative of the corresponding bin in $MOD_{RANDPATH}$ when defining representativeness by a positive result of the Kolmogorov-Smirnov test. This is also true if the data are not binned in months but only in HrelTP. The result also stays the same for all values of the confidence limit α (using values of 0.001, 0.01, 0.05, 0.1 and 0.2).

A similar finding for aircraft data have already been reported by Kunz et al. (2008). On the one hand side this could mean that $MOD_{CARIBIC}^{regular}$ is simply not representative of $MOD_{RANDPATH}$. But if the other methods presented here are considered, the conclusion seems more appropriate that the Kolmogorov-Smirnov test is simply not the appropriate way to answer the question. It can be considered as too strict for the type of data and the question considered here. This is further investigated in a sensitivity study, which is discussed in the following section.

In addition to binning into twelve months (January to December), $MOD_{CARIBIC}^{regular}$ and $MOD_{RANDPATH}$ have also been tested when first binning into separate months (108 months in nine years) and then using this monthly mean data to compile a climatology. For this monthly mean data, the Kolmogorov-Smirnov test does give a positive result in some heights and months. But no meaningful pattern could be determined from the results. Especially, the result does not depend on τ^* (not shown).

The same is true for the Mann-Whitney test for the mean and Levene's and the Brown-Forsythe test for variance. They give no positive result for data binned directly into months. The result is positive for some months and heights if data are first binned into separate months the monthly mean data used for testing. The positive results seem randomly distributed and no relationship to τ^* could be found. These tests therefore also seem not to be suitable for answering the question of representativeness.

4.7.2. Sensitivity study on the Kolmogorov-Smirnov test

When applying the Kolmogorov-Smirnov test to $MOD_{CARIBIC}^{regular}$, $MOD_{RANDPATH}$ or $MOD_{RANDLOC}$, it returns only negative results. This indicates that $MOD_{CARIBIC}^{regular}$ is not representative of $MOD_{RANDPATH}$ in the definition of the Kolmogorov-Smirnov test. This behaviour was tested in a sensitivity study, the results of which are discussed in this section.

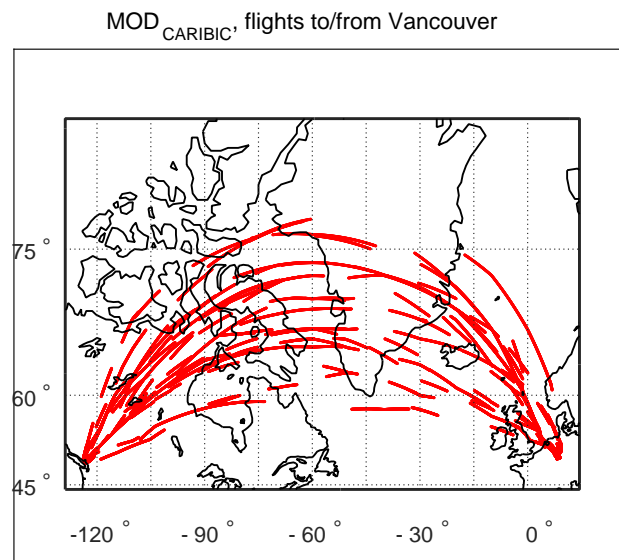


Fig. 4.7.: Flightroutes to Vancouver, Canada, where each flight has been cut into 20 pieces and randomly chosen 30% of those pieces have been plotted. These are tested against the whole data from flights to Vancouver to give one point in Figure 4.8.

One of the most frequent destinations within the CARIBIC project is Vancouver, Canada (near 120°W, 45°N, see Figure 4.7). Only the subset of MOD_{CARIBIC}^{regular} to this destination is considered in this example to minimize effects that may come from different flight routes. Parts of this reduced dataset were tested with the Kolmogorov-Smirnov test against the whole reduced dataset for all variables. To produce these partial datasets, each flight was cut into an increasing number of pieces (corresponding to a certain time) and different percentages of these pieces were used in testing. Figure 4.7 shows an example of applying this method, by cutting each flight into 20 pieces and taking 30% of these by showing the corresponding flightpaths.

Data was not binned in months as only the flights to Vancouver are considered in this section. When applying the Kolmogorov-Smirnov test without binning in months, the result is a profile in HrelTP for each variable. This matrix of height versus species was calculated for each combination of number of pieces and percent of pieces. In each combination, all the profiles of the different variables were averaged to end up with one value between 1 and 0 characterizing the result of the test for this combination of number of pieces and percent of pieces. The result can then give an impression of the strictness of the Kolmogorov-Smirnov test.

Figure 4.8 shows the result of the study. Independent of the number of pieces, the result is positive if all pieces are considered, as the definition of the test prescribes. When removing short pieces (shorter than 20min), the result is also positive if 70% percent of the data is considered. When removing whole flights (at the top of the plot), more than 90% of the data has to be taken into account to achieve a positive result. This result is very similar also for different error probabilities α , taking values of 0.001, 0.01,

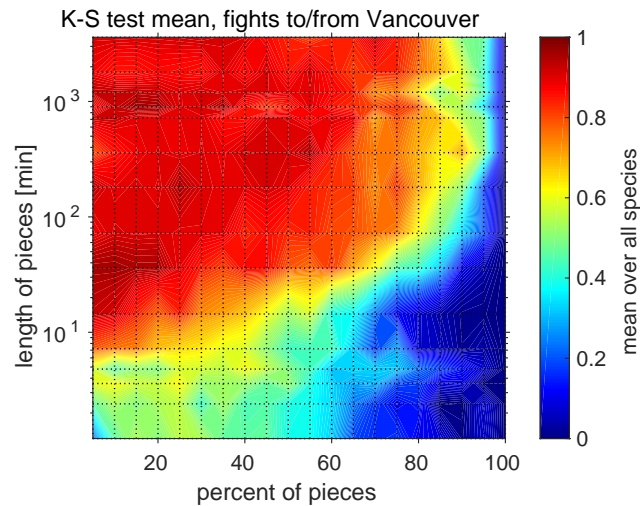


Fig. 4.8.: The Kolmogorov-Smirnov test applied to the flights to Vancouver, Canada, of $\text{MOD}_{\text{CARIBIC}}^{\text{regular}}$ and subsets of these flights. Dotted lines indicate those lengths in time and those percentages that were tested. 0 stands for a passing the Kolmogorov-Smirnov test, 1 for not passing.

0.05 (in the figure), 0.1 and 0.2. The area of failing increases only slightly with the error probability. This showcases the strictness of the test. The Kolmogorov-Smirnov test does not seem suitable to test a dataset measured with aircraft for representativeness of a larger dataset.

4.7.3. Applying the variability analysis

This section presents the results of the application of the variability analysis to $\text{MOD}_{\text{CARIBIC}}^{\text{regular}}$ and $\text{MOD}_{\text{RANDPATH}}$. Equation 4.5 was applied for different time scales (30d, 0.25 a, 0.5 a, 1 a, 2 a and 5 a) to calculate R_{var} . The results are exemplarily discussed for a time scale of 1 a, shown in Figure 4.9. The results are sorted using the values of τ^* displayed in Figure 4.2.

R_{var} shows a strong dependency on τ^* . This is visible from Figure 4.9, in which the results are sorted with decreasing values of τ^* (from Figure 4.2), i.e. with increasingly higher atmospheric variability from left to right. The Pearson correlation coefficient ρ of R_{var} and τ^* is high, $|\rho| > 0.9$ in all height bins, independent of the time scale. R_{var} also shows a strong relationship to the number of samples: The amount of data in both $\text{MOD}_{\text{CARIBIC}}^{\text{regular}}$ and $\text{MOD}_{\text{RANDPATH}}$ decreases below and above the tropopause, and R_{var} follows suit for practically all species.

The relation of R_{var} and the number of flights was also tested by using $\text{MOD}_{\text{RANDPATH}}^3$ defined in Sec. 4.3.3. R_{var} was correlated with the number of flights for each species and height. When investigating a linear relationship, the Pearson correlation coefficient was approximately $|\rho| \approx 0.75$ for the time scale of 5 a, increasing continuously when considering shorter time scales to $|\rho| \approx 0.95$ for the time scale of 30d. Considering a logarithmic relationship increases the goodness of fit for longer time scales, while it decreases that for shorter time scales ($|\rho| \approx 0.85$ for both 5 a and 30d).

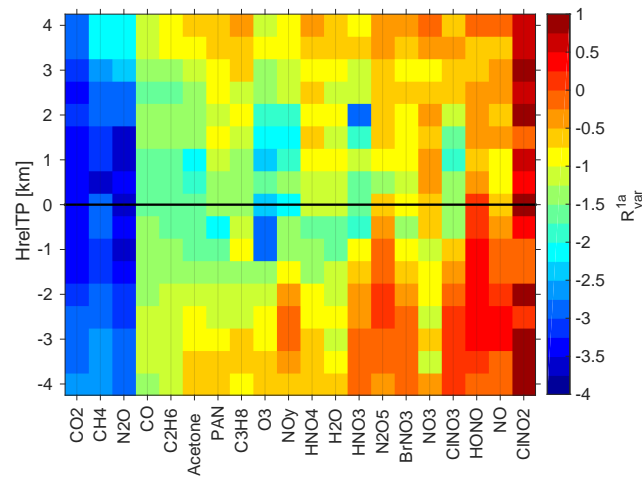


Fig. 4.9.: R_{var} calculated according to Equation 4.5 for a time scale of 1 a for all species in all height bins, using $\text{MOD}_{\text{CARIBIC}}^{\text{regular}}$ and $\text{MOD}_{\text{RANDPATH}}$. Low values indicate small differences in variability.

R_{var} therefore passes the requirements of being inversely related to τ^* and directly to the number of included data points and flights. Figure 4.9 can therefore be used to judge upon the representativeness of $\text{MOD}_{\text{CARIBIC}}^{\text{regular}}$ for $\text{MOD}_{\text{RANDPATH}}$.

This shows that the relative standard deviation (Equation 4.5) can be used to infer representativeness. Kunz et al. (2008) used the variance alone, which proved not to be useful. Rohrer and Berresheim (2006) originally introduced the variance analysis to investigate the sources and time scales of variability in a dataset and for this it remains a valid method. In order to infer representativeness, it is more appropriate to use the relative standard deviation in the analysis instead of the absolute variance.

4.7.4. Relative differences

R_{rel} was calculated for each species in each height bin according to Equation 4.6, results are presented in Figure 4.10.

Figure 4.10 shows how low variability (decreasing to the left, values taken from Figure 4.2), is linked with good representativeness (low values in R_{rel}). R_{rel} decreases linearly with increasing variability τ^* with a high Pearson correlation coefficient greater than 0.95 for all height bins (not shown). As visible in Figure 4.10, R_{rel} also decreases with the number of data points, which maximizes just around the tropopause and decreases above and below it (see Figure 4.1).

This dependence on the number of data points was also tested by using $\text{MOD}_{\text{RANDPATH}}^3$ described in Sec. 4.3.3. The Pearson correlation coefficient ρ between the number of shorter random flights and R_{rel} was $\rho \approx 0.95$ for all species in all heights. Less variable species like CO_2 show a better relationship with the logarithm of the number of flights. This underlines how R_{rel} is well correlated with the number of measurements.

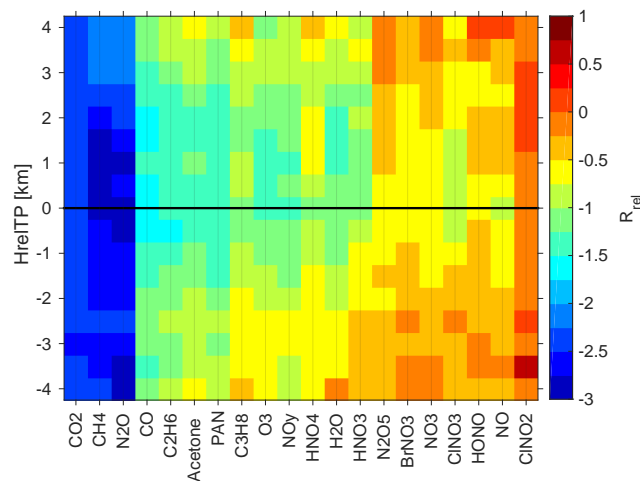


Fig. 4.10.: R_{rel} calculated according to Equation 4.6 for all species in all height bins, using $\text{MOD}_{\text{CARIBIC}}^{\text{regular}}$ and $\text{MOD}_{\text{RANDPATH}}$. Low values indicate small differences in climatological mean values.

Using R_{rel} as a measure passes both conditions: It is directly proportional to the number of flights and indirectly to the variability. In addition to Figure 4.9, Figure 4.10 can therefore be used to judge upon the representativeness of $\text{MOD}_{\text{CARIBIC}}^{\text{regular}}$ for $\text{MOD}_{\text{RANDPATH}}$. R_{rel} can be transformed into a relative difference in percent, by taking R_{rel} to the power of ten. A score of -2 stands for a mean relative difference of 1%.

The score that discriminates representative from the non-representative case has to be arbitrarily chosen (see Nappo et al. (1982) and Ramsey and Hewitt (2005)). R_{rel} gives the uncertainty within which the data are considered representative. If a score of -2 is defined as representative (corresponding to 1% mean relative difference), then representative species and heights can now be separated from those species that are not representative using the results from Figure 4.10. But the score of -2 is arbitrary. If it is reduced to -1.5 (roughly 3% relative difference), $\text{MOD}_{\text{CARIBIC}}^{\text{regular}}$ can be seen as representative for many more species.

4.8. Model and measurement variability

Representativeness is assessed using only model data in this study, yet the final goal is to investigate the climatological representativeness in mid-latitudes of $MEAS_{CARIBIC}$. $MOD_{CARIBIC}^{regular}$ and $MOD_{CARIBIC}^{sampled}$ are used as a placeholder for $MEAS_{CARIBIC}$ and compared to other model datasets ($MOD_{RANDPATH}$ and $MOD_{RANDLOC}$) in the analysis. The results derived from these model datasets will be interpreted for $MEAS_{CARIBIC}$ in Sec. 4.9. This means that conclusions drawn from model data alone will be applied to measurements. This section presents results that justify this reasoning.

For this aim, it is important to investigate the differences between the model and the real atmosphere. It is not crucial that the model reproduces the exact values of the measurements, but rather that the complexity for each species in the model is similar to the real complexity. This will be investigated in the following sections, using the variability of the different datasets as an indicator of the complexity. The influence of the coarse model resolution is the focus of Sec. 4.8.1. Section 4.8.2 then compares the model and measurement variability.

All model datasets have been created from gridded datafiles with a certain resolution (2.8° or about 200km, see Sec. 4.2.2). Considering the median airspeed of the CARIBIC aircraft of 885.1 km h^{-1} , this model resolution corresponds to a time scale of about 20min. $MEAS_{CARIBIC}$ has a time resolution of up to 10s, depending on the instrument. Model data has been linearly interpolated to this high 10s resolution, but this does not introduce the variability that is present in the measurements. The 20min variability is therefore always larger in $MEAS_{CARIBIC}$ than in $MOD_{CARIBIC}^{sampled}$.

In order to work with comparable datasets with respect to the variability, the measurement data are smoothed by interpolating between the 20 min mean values. This smoothed set of measurements will be referred to as $MEAS_{CARIBIC}^{smoothed}$ and applied in the following sections.

4.8.1. Influence of short time scales on the climatological mean

This section investigates to what extent the coarse model resolution influences the climatological mean values. Climatological mean values of $MEAS_{CARIBIC}^{smoothed}$ are compared to mean values from $MEAS_{CARIBIC}$ with the full variability, thereby determining the influence of the reduced 20min variability. A similar influence is expected by the coarse model resolution.

The mean relative difference of the climatologies for different species between $MEAS_{CARIBIC}^{smoothed}$ and $MEAS_{CARIBIC}$ is displayed in Figure 4.11. The differences depend strongly on the species. Those species that are measured by air samples (N_2O , C_2H_6 and C_3H_8) have been shaded in gray, since they contain very little data far above and below the tropopause and are therefore not considered in this section.

The mean relative differences are smaller than 1% for the long lived species to the left and reach 10-20% for the other species at most. Largest values appear where the mixing ratios of the species are small and vertical gradients are strong, i.e. in stratospheric CO, acetone or H_2O and tropospheric O_3 . E.g. H_2O has very low stratospheric mixing ratios, that are reached in small-scale intrusions of stratospheric

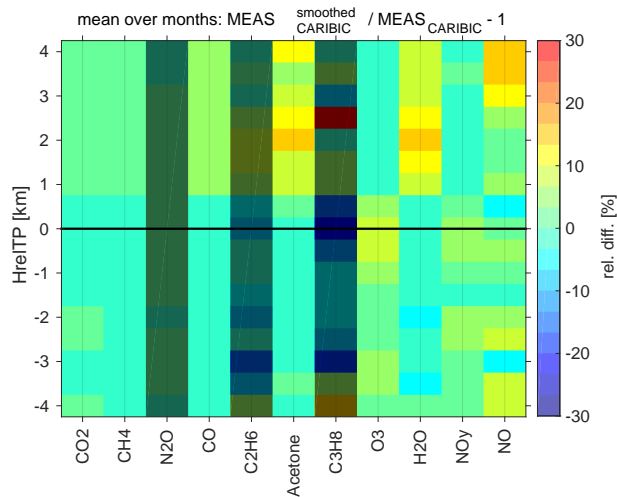


Fig. 4.11.: Mean relative differences of $\text{MEAS}_{\text{CARIBIC}}^{\text{smoothed}}$ and $\text{MEAS}_{\text{CARIBIC}}$. $\text{MEAS}_{\text{CARIBIC}}^{\text{smoothed}}$ has been smoothed by interpolating between the 20min mean values. The relative differences correspond to the error in the climatologies of $\text{MOD}_{\text{CARIBIC}}^{\text{sampled}}$ due to the coarse model resolution. N_2O , C_2H_6 and C_3H_8 are measured by air samples with a low measurement frequency and therefore not considered here.

air encountered during flight. If these small-scale structures are smoothed out, the mean values become larger and the difference of $\text{MEAS}_{\text{CARIBIC}}^{\text{smoothed}}$ and $\text{MEAS}_{\text{CARIBIC}}$ is large and positive.

The relative differences show the small influence of a lower 20min variability on climatological mean values. The time scale of 20 min corresponds to the model resolution. This therefore shows that the coarse model resolution does in principle not lead to very large errors in climatological mean values. Nevertheless, the model could have other deficiencies in the description of the different species. These are made visible in the following section by comparing model and measurement variability directly.

4.8.2. Comparing model and measurement variability

In this section, the variability of $\text{MOD}_{\text{CARIBIC}}^{\text{sampled}}$ is compared directly to that of $\text{MEAS}_{\text{CARIBIC}}^{\text{smoothed}}$. As this study argues completely within the model world, it is important that the model has similar values for the variability, which is used as an indicator of the underlying complexity. If the model cannot reproduce the measurement variability at all, it is not plausible why conclusions on representativeness drawn from model data should also be true for the real atmosphere.

As has been discussed in Sec. 4.5.2, variability depends on the time scale for which it is considered. In order to evaluate the model performance, σ_r is compared on time scales of 30d and 1a. 30d variability includes data from typically 4 flights, so this is a measure for the atmospheric variability on the global, large scale dynamics. 1a variability gives a good impression of the annual cycle, as it includes data from many flights and different years. Figure 4.12 shows $\sigma_r^{\text{MOD}} / \sigma_r^{\text{MEAS}}$ for time scales of 30d (top) and 1a (bottom), using the datasets $\text{MOD}_{\text{CARIBIC}}^{\text{sampled}}$ and $\text{MEAS}_{\text{CARIBIC}}^{\text{smoothed}}$.

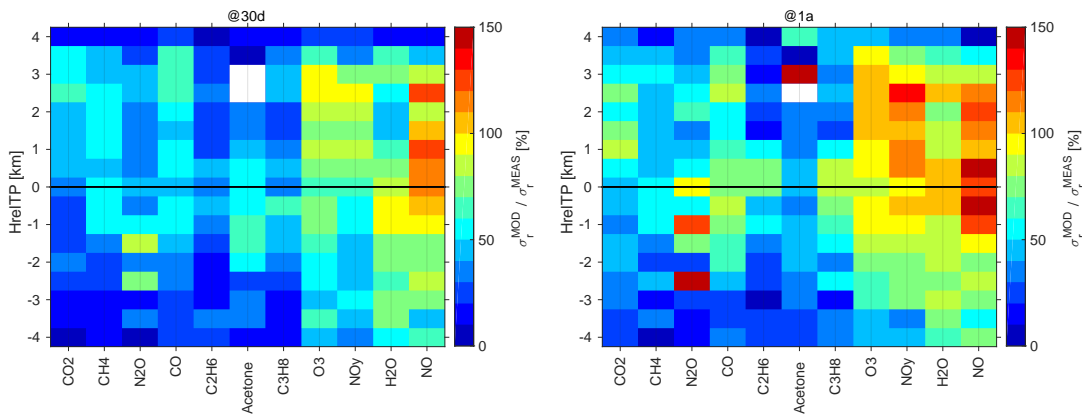


Fig. 4.12.: $\sigma_r^{\text{MOD}} / \sigma_r^{\text{MEAS}}$ given in percent for time scales of 30d (top) and 1a (bottom), where MOD stands for $\text{MOD}_{\text{CARIBIC}}^{\text{sampled}}$ and MEAS stands for $\text{MEAS}_{\text{CARIBIC}}^{\text{smoothed}}$. Values greater than 50% indicate the high model complexity.

Figure 4.12 shows that the variability in the measurements reached by the model differs between species. In general, the variability reached for shorter lived species better fits that of the measurements. Short-lived species also undergo a more complex chemistry in the model, which adds variability. The 30d variability shown in Figure 4.12 (top) reveals to what extent the model is able to capture variability related to the large scale dynamics. Most species reach 40-80%. NO is very short lived and strongly determined by its daily cycle, which is the reason why the variability in the model reaches higher values.

The time scale of 1a shows the variability that represents seasonality. The model does a better job for this time scale than for 30d, short lived species and CO_2 reaching well over 60% of the variability, approaching 100% for some species. Here again, the model chemistry increases the variability for shorter lived species to the right. There are species that are not as well represented, while this also depends on the height considered. N_2O , C_2H_6 and C_3H_8 are also affected by the lower measurement frequency, as they are only measured in air samples.

The model variability is influenced by many factors including the dynamics, the representation of the chemistry and of the sources included in the model. The limited horizontal and vertical resolution also plays a role, even though $\text{MEAS}_{\text{CARIBIC}}^{\text{smoothed}}$ is used as a reference for the comparison. If compared to the original $\text{MEAS}_{\text{CARIBIC}}$, the percentages of variability reached by the model drop by 10-20% (not shown). It is beyond the scope of this study to further disentangle what causes the deficiencies of the model and what leads to the differences between the species.

4.8.3. A conclusion from model data applied to measurements

In the following section, conclusions from an analysis of model data are applied to measurement. This section discussed whether this transfer of conclusions is valid.

Figure 4.11 shows that the influence of the coarse model resolution on climatological mean values is very limited. This shows that it is in principle possible to derive meaningful climatologies from the model data. The coarse resolution has little influence on the mean values.

By considering Fig. 4.12, it was discussed that the model reaches more than 50 % of the variability of the measurements, exact values depending on the species and time scale. In general, the model variability can be increased by using a run with a higher resolution. The variability of the measurements in each bin of HrelTP (height relative to the tropopause) is also influenced by the choice of reference for HrelTP. For this study, HrelTP has been derived from model output fields from ECMWF at a resolution of 1° ($\approx 110\text{km}$), while the measurement data have a much higher resolution ($\approx 2.5\text{km}$, see Sec. 4.2.1). The highly variable measurements are then sorted into bins of coarsely resolved HrelTP. This artificially increases the variability of the measurements in each bin of HrelTP.

The results from the two preceding sections therefore justify to apply results from the model datasets to MEAS_{CARIBIC}.

4.9. Representativeness uncertainty of the CARIBIC measurement data

This section discusses the climatological representativeness of CARIBIC measurement data. The exact definition of this term is given in Sec. 4.3 and is summarized by the question: For which species is a climatology compiled from CARIBIC data representative of the tropopause region in mid-latitudes?

Section 4.5 introduced three statistical measures to test the representativeness and they were applied to random data (Sec. 4.6) and on model data (Sec. 4.7), showing that R_{var} and R_{rel} are both valid measures of representativeness. The previous section then showed that conclusions from the model data are valid also for $\text{MEAS}_{\text{CARIBIC}}$. With this, the stage is set to examine the climatological representativeness of $\text{MEAS}_{\text{CARIBIC}}$.

Section 4.9.1 interprets the results by species as a representativeness uncertainty, while Sec. 4.9.2 shows some sample climatologies. Sec. 4.9.3 answers the question of how many flights are necessary to achieve a certain degree of representativeness. In addition, Sec. 4.9.4 and 4.9.5 discuss the influence of the limitations in longitude in pressure, which are inherent in the CARIBIC dataset. Section 4.9.6 examines the influence of much lower sampling frequencies on climatologies, as in the case of data from whole air samples.

4.9.1. Representativeness uncertainty

The last sections have shown R_{rel} (see Equation 4.6) and R_{var} (see Equation 4.5) to be adequate scores to describe representativeness. After reconsidering the question asked in the Sec. 4.3.1 (Is a climatology compiled from CARIBIC data representative of the tropopause region in mid-latitudes?), R_{rel} will be used in the following. It is more intuitive (compared to R_{var}) as it describes the difference to a larger dataset, e.g. in percent. As noted in Sec. 4.5.3, R_{rel} is also comprehensible as an uncertainty for using the smaller dataset to compile a climatology and will be called representativeness uncertainty correspondingly. Using different wording, R_{rel} in this formulation can also be considered the sampling error of the measurements.

In order to work with a comparable data set with respect to the sampling frequency, $\text{MOD}_{\text{CARIBIC}}^{\text{sampled}}$ is used in the following, see Sec. 4.2. $\text{MOD}_{\text{RANDLOC}}$ (see Table 4.1) serves as reference, as it has a random sampling pattern, represents the full model state and has no relevant intrinsic limits in pressure. Here, data was again used where $180\text{hPa} < p < 280\text{hPa}$. Figure 4.13 shows R_{rel} calculated from these datasets.

This result - deduced from model data only - is also valid for the real world if the complexity of the model is sufficiently high for each species. This has been shown by comparing the variability of $\text{MOD}_{\text{CARIBIC}}^{\text{sampled}}$ and $\text{MEAS}_{\text{CARIBIC}}^{\text{smoothed}}$ for different time scales (see Sec. 4.8). The discussion of the following paragraphs is therefore also valid for the real atmosphere, even though results have been derived from model data alone. Figure 4.13 answers the question: For which species is a climatology compiled from CARIBIC data representative of the tropopause region in mid-latitudes?

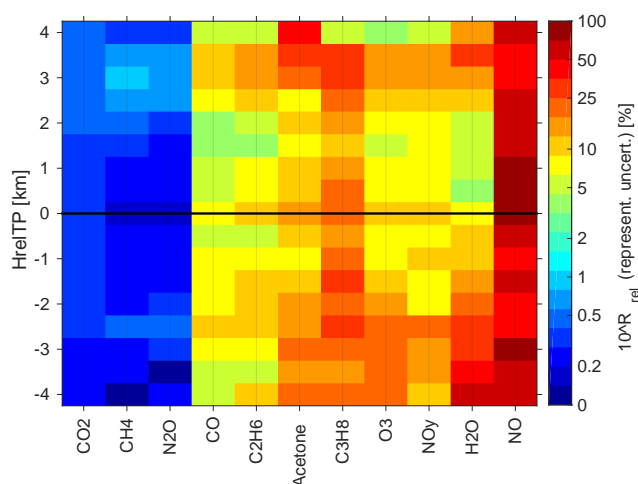


Fig. 4.13.: Representativeness uncertainty for using the CARIBIC data (that is 334 long-distance flights, see Table 4.1) to compile a climatology: $10^{R_{rel}}$ calculated from $MOD_{RANDLOC}$ and $MOD_{CARIBIC}^{sampled}$. Low values indicate small representativeness uncertainties. N_2O , C_2H_6 and C_3H_8 are measured from air samples, which increases the uncertainty, especially for C_3H_8 .

When considering the representativeness uncertainty of a climatology, it is also important to consider the annual cycle of a species. For example, 10% can be a small uncertainty for an abundant species that is more or less constant, while it is little for a species with a strong seasonality. The following paragraphs discuss representativeness by species, not explicitly considering the seasonal variations for each species. The monthly resolved climatologies of CO, CO₂ and O₃ are discussed exemplarily at the end of this section.

Many of the species that sum up to NO_y in the model are not actually measured by CARIBIC and therefore are not displayed in Figure 4.13. In general, the representativeness uncertainty is lowest where there are most measurements, which is just around the tropopause (see Figure 4.1). This effect overlays the physical reasons for the different uncertainties for the considered species.

NO has the highest uncertainty of 90%. There are two possible reasons: On the one hand, there are many gaps in the observations. But NO is also emitted by aircraft in the UTLS (Stevenson et al., 2004), and since CARIBIC flies in the flight corridors heavily frequented by commercial aircraft, it is unrealistic to assume a climatology of these species to be representative of the UTLS on a whole.

H₂O shows a strong gradient in its representativeness uncertainty, which is directly linked to the strong gradient in variability. The dry stratosphere can be described by relatively few measurements, which is why the uncertainty is low, only reaching 25% at most. The humid and variable troposphere influenced by daily meteorology has a higher uncertainty, reaching more than 60%.

NO_y, being a pseudo-species made up of many substances, is more difficult to disassemble. The variability of many components is higher in the troposphere, where the uncertainty is 30% at its maximum. Above, it is smaller than 10% and the climatology therefore quite trustworthy.

It is interesting to note that C_2H_6 and C_3H_8 , both collected in whole air samples still reach uncertainties comparable to those of other species in their range of τ^* . This is due to the fact that these are moderately long-lived species for which only a smaller number of measurements are needed for a representative climatology. The climatology of C_3H_8 comes with an uncertainty of up to 25 %, while that of C_2H_6 is better with an uncertainty of less than 10 %.

The climatology of O_3 is very trustworthy, the uncertainty being smaller than 10 % for most height bins. The higher values in the tropospheric bins should not raise much concern, as O_3 increases strongly with height in the UTLS and an uncertainty of 15 % will be practically unnoticeable compared to the vertical increase.

This is not true for acetone, where the gradient is just opposite to O_3 . The climatology is trustable with an uncertainty only up to 10 % in upper levels, while it increases to 20 % in the lower heights, where the influence of spatially and temporally variable sources at the ground is stronger.

The climatology of CO is very good, the uncertainty in stratospheric height bins being less than 5 %. The troposphere, again stronger under the influence of sources, has a higher uncertainty reaching up to 10 %.

The long-lived trace gases CH_4 , N_2O and CO_2 (all detrended as described in Sec. 4.2.1) all have representativeness uncertainties of less than 0.4 %, which is lower than their seasonal variability. This is interesting especially for N_2O , which is measured only in the whole air samples.

4.9.2. Application to climatologies from CARIBIC measurements

As example and summary, the representativeness uncertainty is applied to climatologies of CO, CO_2 and O_3 , shown in Figure 4.14.

CO is shown for $MOD_{CARIBIC}^{sampled}$ (top left, panel a), $MOD_{RANDLOC}$ (top right, panel b) and CARIBIC measurements ($MEAS_{CARIBIC}$, center left, panel c). The white space in these figures has three possible reasons: the aircraft could have never flown in that bin, there could be measurement gaps in CO or a gap in HrelTP. The measurement gaps of CO and HrelTP from $MEAS_{CARIBIC}$ have been mapped onto $MOD_{CARIBIC}^{sampled}$, but HrelTP differs slightly and therefore also the white space. The representation of CO in the model, comparing top and center left figure (panels a and c), is similar to measurements (in the troposphere more so than in the stratosphere), but was not subject of this study. By comparing the top row ($MOD_{CARIBIC}^{sampled}$ and $MOD_{RANDLOC}$, panels a and b), R_{rel} is found to be a good descriptor for the representativeness of one for the other. By accepting the result from the model to be valid also for measurements, the score calculated from the two model samples can now be used to determine the representativeness uncertainty of $MEAS_{CARIBIC}$.

By again defining $R_{rel} = -1$ (10 % uncertainty, one third of the seasonal variation) as the limit for representativeness, the climatology of $MEAS_{CARIBIC}$ (Figure 4.14, center left, panel c) was shaded in gray where it is not representative. The representativeness uncertainty shown in Figure 4.13 only serves as a first indication of the expected uncertainty when resolving monthwise. The center right panel (panel d)

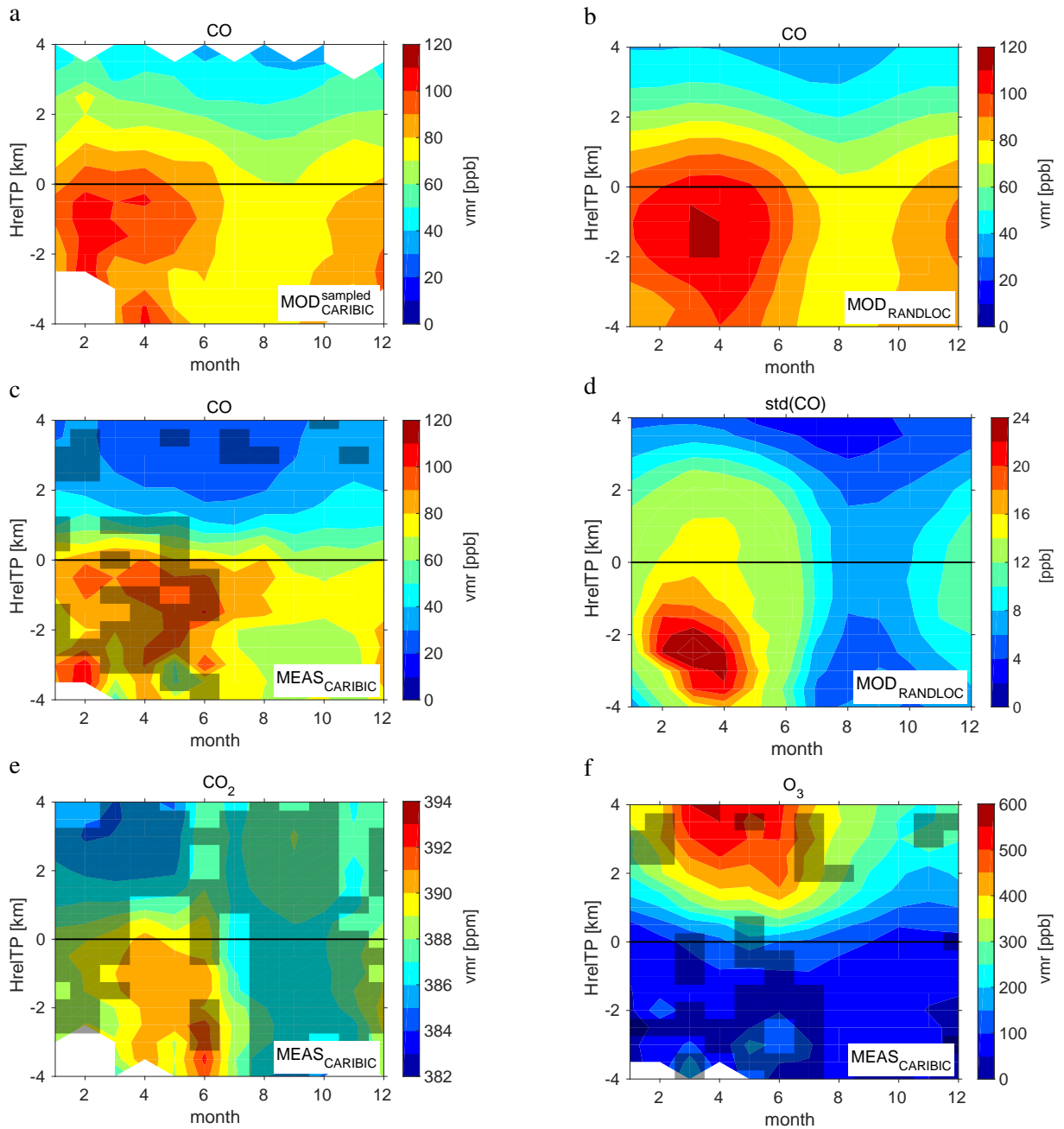


Fig. 4.14.: Climatology of CO, built from MOD^{sampl}_{CARIBIC} (panel a), MOD_{RANDLOC} (panel b) and the CARIBIC measurements (MEAS_{CARIBIC}, panel c). Areas of $10^{\circ}R_{\text{rel}} > 0.1$, calculated from the top row, were used to shade non-representative areas in the climatology of MEAS_{CARIBIC} in grey. Panel d displays the 1σ standard deviation of CO from MOD_{RANDLOC}. The bottom row (panels e and f) displays climatologies from MEAS_{CARIBIC} of CO₂ (left) and O₃, shaded with $10^{\circ}R_{\text{rel}} > 0.003$ and $10^{\circ}R_{\text{rel}} > 0.15$, respectively.

displays the standard deviation of CO from $\text{MOD}_{\text{RANDLOC}}$. By comparing the center panels (c and d), it becomes evident that the variability specific to CO is one of the reasons for the higher representativeness uncertainty in spring, while it cannot explain all the features. The number of flights is a different reason, which explains the higher uncertainty in January, the month with the least flights.

The limit of 10 % should not be applied in general and has to be adapted to the species under consideration. This becomes evident by the bottom row in Figure 4.14 (panels e and f), which shows climatologies of CO₂ and O₃. CO₂ shows a small annual variation around a high background value. So 10 % uncertainty could be easily reached by a single measurement, which would certainly not be representative of the whole year. The shading for CO₂ in Figure 4.14 was set at a threshold of 0.3 %, again just above one third of the seasonal variation. The high values in spring in the upper troposphere show an even lower uncertainty, the uncertainty of all data being less than 0.7 % (not shown). The opposite is true for O₃, for which the threshold was set to 15 % uncertainty (around one fourth of the seasonal variation). Many tropospheric values in spring or at times of high gradients in the stratosphere at the beginning and end of spring have an uncertainty higher than these 15 %.

As the results in Figure 4.13 are sorted by the variability of the species and this is linked to their lifetime in following Junge (1974), conclusions are possible for species even if they have not been explicitly considered in this study. This is true for SF₆, for example, which is measured in whole air samples by CARIBIC but was set to 0 in the model run and could therefore not be included in this study. As it is long-lived in both troposphere and stratosphere (Ravishankara et al., 1993), a climatology from CARIBIC SF₆ measurements can be considered to be representative even though it is measured only by whole air samples.

4.9.3. Number of flights for representativeness

Another question can be answered with the methods developed in this chapter: For those substances not representative yet, how often does one have to fly in order to achieve a representative climatology?

This question can be answered with the help of $\text{MOD}_{\text{RANDPATH}}^3$. Figure 4.15 shows the representativeness uncertainty for some species and different numbers of flights. As has been discussed in Section 4.9.1, the yearly variation of a species is one of the factors that determines the threshold of the uncertainty with which the species can be considered to be representative.

E.g., for (detrended) CO₂, the mean value of $\text{MOD}_{\text{RANDLOC}}$ is 385.7 ppmv with a yearly variation of 2.5 to 3.5 ppmv. A representativeness uncertainty of at least 0.5 % has therefore to be set as the minimum threshold for CO₂. This can be reached with only few flights, much less than those included in $\text{MOD}_{\text{CARIBIC}}^{\text{sampled}}$.

For O₃, on the other hand, the yearly cycle puts an uncertainty of 50 % or more at hand. While this is the minimum value to reproduce the yearly cycle at all, it may still not be sufficient for the application. With the number of CARIBIC flights, the uncertainty in O₃ is low already (< 5 % in this height), while the uncertainty is continuously reduced if the number of flights increases.

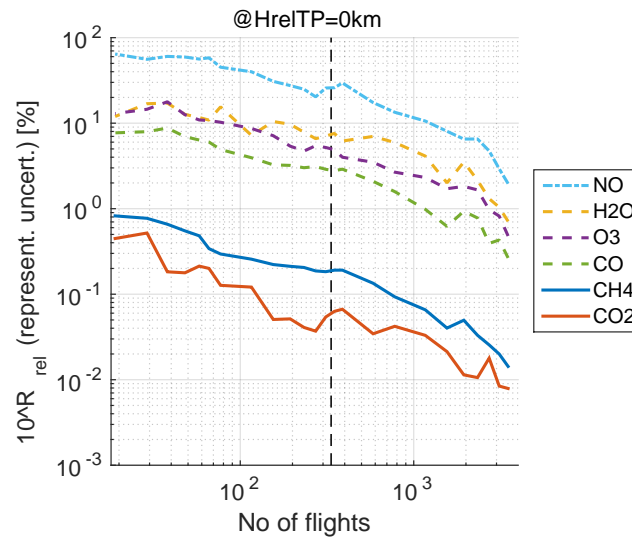


Fig. 4.15.: Representativeness uncertainty for different numbers of flights for some species. The number of flights in MEAS_{CARIBIC} is indicated by the vertical dashed line. Other species can be deduced from their value of τ^* with the help of Figure 4.2.

As is indicated by Figure 4.15, highly variable species like NO need many flights in order for their climatologies to reach low uncertainties. Even 1000 flights, approximately ten more years of flying the CARIBIC observatory, will not reduce the uncertainty below 10 %.

Other species that are not included in Figure 4.15 can be deduced from their value of τ^* with the help of Figure 4.2. Those species measured in air samples need even more CARIBIC flights than indicated by the number in Figure 4.15, as the measurement frequency is much lower.

4.9.4. Limitation in longitude: The influence of the Pacific Ocean

As visible in Fig 4.1, there are no CARIBIC measurements over the Pacific Ocean, while MOD_{RANDLOC} and MOD_{RANDPATH} also cover the Pacific. The uncertainty introduced by taking the Pacific into account in MOD_{RANDLOC} is investigated in this section.

R_{rel} is calculated from MOD_{CARIBIC}^{regular} and MOD_{RANDLOC} in two different setups. R_{rel} is calculated from full MOD_{RANDLOC} and MOD_{CARIBIC}^{regular} (denoted by R_{rel}^A) and compared to R_{rel} calculated with MOD_{RANDLOC} limited in longitude λ to $120^\circ W < \lambda < 120^\circ E$ (denoted by R_{rel}^B). The result is shown in Figure 4.16 as relative differences $|R_{rel}^A/R_{rel}^B - 1|$ between the two uncertainties. The relative differences show the share of the uncertainty inherent in MOD_{CARIBIC}^{regular} because the Pacific is included in the reference dataset MOD_{RANDLOC}.

The importance of the Pacific depends on the species under consideration and whether the stratosphere or troposphere are considered. The influence on stratospheric values is very small for all species. In addition, those heights with less data (top and bottom) are most strongly influenced if the Pacific is not

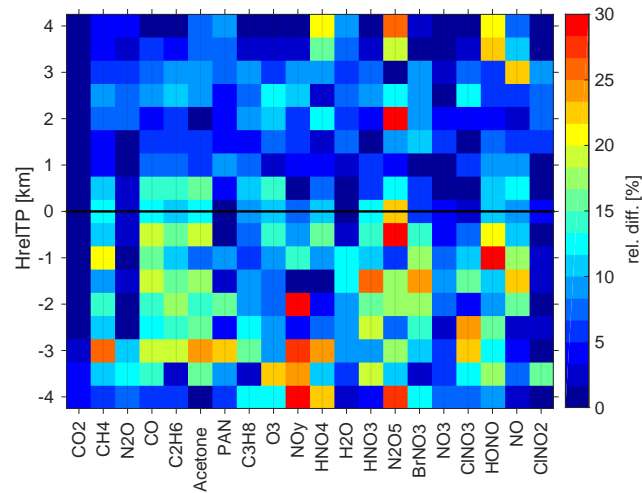


Fig. 4.16.: $|\frac{R_{\text{rel}}^{\text{A}}}{R_{\text{rel}}^{\text{B}}} - 1|$, given in percent. This is the fraction of the representativeness uncertainty introduced in R_{rel} calculated from $\text{MOD}_{\text{CARIBIC}}^{\text{regular}}$ and $\text{MOD}_{\text{RANDLOC}}$ by including the Pacific ocean in $\text{MOD}_{\text{RANDLOC}}$, even though it is not sampled by $\text{MOD}_{\text{CARIBIC}}^{\text{regular}}$. Both, $R_{\text{rel}}^{\text{A}}$ and $R_{\text{rel}}^{\text{B}}$ have been calculated from $\text{MOD}_{\text{CARIBIC}}^{\text{regular}}$ and $\text{MOD}_{\text{RANDLOC}}$, excluding the Pacific in $\text{MOD}_{\text{RANDLOC}}$ in the calculation of $R_{\text{rel}}^{\text{B}}$.

considered. For the long-lived species CO_2 and N_2O , the uncertainty increases only little (less than 3%) if the Pacific is included in the reference climatology of $\text{MOD}_{\text{RANDLOC}}$. But tropospheric CH_4 is more influenced by surface values. Interestingly, ClNO_2 is also not affected, which clearly shows that the effect does not depend on lifetime, but on the source regions and the chemistry. Acetone, CO and C_2H_6 are air pollutants with strong sources in Asia. Parts of these sources are excluded if the Pacific is not considered, which is why the inclusion of the Pacific in $\text{MOD}_{\text{RANDLOC}}$ is responsible for 15-20% of the total uncertainty. The situation is similar for HNO_3 , N_2O_5 , BrNO_3 and HONO . For the other species, the uncertainty introduced by the Pacific is smaller.

4.9.5. Limitation in pressure: Aircraft tropopause pressure bias

By calculating R_{rel} using $\text{MOD}_{\text{CARIBIC}}^{\text{regular}}$ and $\text{MOD}_{\text{RANDLOC}}$, an important fact can be illustrated about data collected with instruments on civil aircraft. As the aircraft flies at constant pressure levels, data are also taken at these pressure altitudes only. If data are then resorted into heights relative to the tropopause (HrelTP), this limit in pressure is no longer visible. Nevertheless, it influences the results as the volume mixing ratios of many trace substances are not only a function of their distance to the tropopause, but also of pressure.

The effect on the climatological values can be illustrated by calculating R_{rel} using $\text{MOD}_{\text{RANDLOC}}$ and $\text{MOD}_{\text{CARIBIC}}^{\text{regular}}$ within $10\text{hPa} < p < 500\text{hPa}$. Figure 4.17 shows the results (right panel). For comparison, the left panel of Figure 4.17 shows R_{rel} of the same datasets when setting $180\text{hPa} < p < 280\text{hPa}$,

the range at which CARIBIC measures. The representativeness uncertainty is much higher in almost all heights in the right hand side ($10\text{hPa} < p < 500\text{hPa}$), except just above the tropopause, where $\text{MOD}_{\text{CARIBIC}}^{\text{regular}}$ contains most data. Only the long lived species CO_2 , N_2O and CH_4 retain their low uncertainties. For the more variable species to the right of the figure, the representativeness uncertainty increases strongly, especially in the troposphere, where the variability increases if data taken at higher pressure are included.

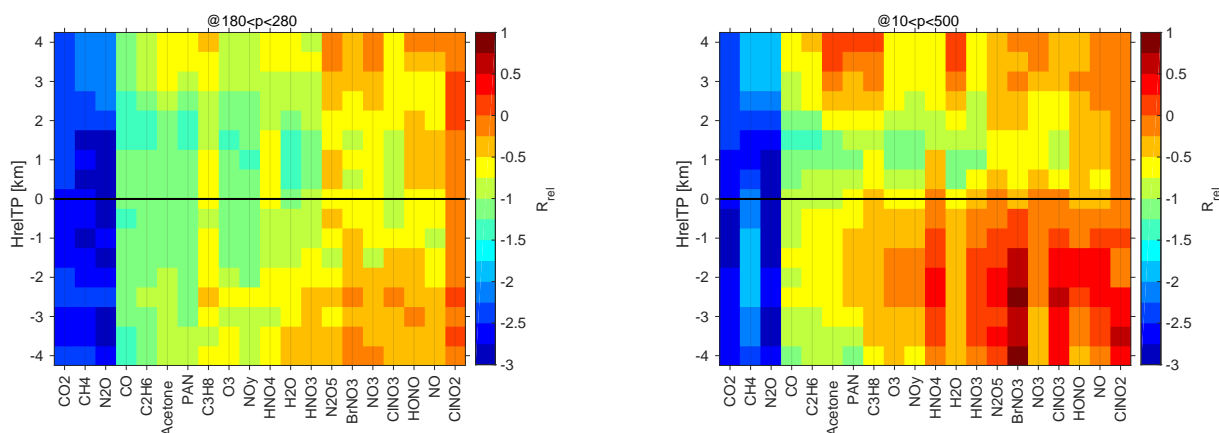


Fig. 4.17.: R_{rel} calculated from $\text{MOD}_{\text{CARIBIC}}^{\text{regular}}$ and $\text{MOD}_{\text{RANDLOC}}$ with the range of p set to $180\text{hPa} < p < 280\text{hPa}$ (left) and $10\text{hPa} < p < 500\text{hPa}$ (right). Low values indicate small climatological differences. The difference between the two panels shows the influence of expanding the limits in p when calculating the climatological mean values with HrelTP used as a vertical coordinate.

The strong increase in representativeness uncertainty is always present in measurement data from commercial aircraft, which can only collect data high above the tropopause when the tropopause is at high pressure and far below when it is at low pressure values. This bias is naturally contained in all data measured at constant pressure and then sorted relative to the tropopause and should be kept in mind when examining climatologies from corresponding platforms.

4.9.6. The influence of a strongly reduced measurement frequency

Many of the species available from the CARIBIC project are not measured continuously but from up to 32 air samples taken during each flight. The instrument collecting the samples is called Whole Air Sampler, abbreviated to WAS. Considering the whole dataset of $\text{MEAS}_{\text{CARIBIC}}$, there is approximately one WAS measurement for every 200 possible measurements from the other instruments. In other words, while continuous measurements reach a time resolution of 10 s, the WAS samples are taken at an average time resolution of 30 min. The effect this much lower sampling frequency has on the climatologies and on the representativeness is investigated in this section with the help of $\text{MOD}_{\text{CARIBIC}}^{\text{regular}}$.

To investigate the influence of WAS sampling, R_{rel} is calculated from $\text{MOD}_{\text{CARIBIC}}^{\text{regular}}$ and the same dataset that has been subsampled. If one WAS value is considered for every 200 values at full time resolution, this is denoted by WAS200 and equivalently for other frequencies. Combining the two ab-

abbreviations, the subsampled dataset will be abbreviated by $\text{MOD}_{\text{CARIBIC}}^{\text{WAS200}}$ accordingly, omitting 'regular'.

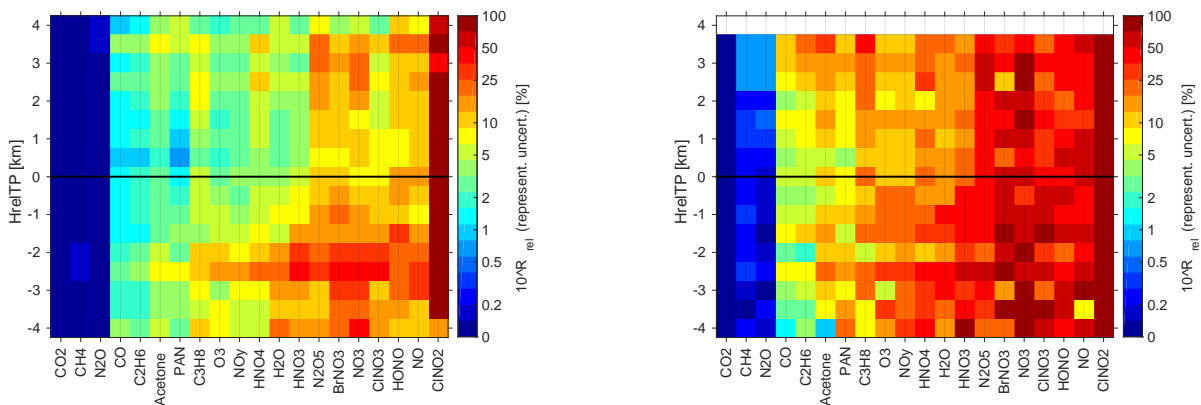


Fig. 4.18.: R_{rel} calculated from $\text{MOD}_{\text{CARIBIC}}^{\text{regular}}$ and $\text{MOD}_{\text{CARIBIC}}^{\text{WAS200}}$ (left) $\text{MOD}_{\text{RANDPATH}}^{\text{WAS2000}}$ (right).

Figure 4.18 shows the representativeness uncertainty ($10^{R_{\text{rel}}}$) calculated from $\text{MOD}_{\text{CARIBIC}}^{\text{regular}}$ and $\text{MOD}_{\text{CARIBIC}}^{\text{WAS200}}$ (left panel) and $\text{MOD}_{\text{CARIBIC}}^{\text{WAS2000}}$ (right panel). In both cases, the influence on shorter lived species (corresponding to higher variability) is stronger, and more so in the troposphere than in the stratosphere.

The left hand panel approximately corresponds to the real WAS frequency. It becomes obvious that the uncertainty introduced to the climatology by considering only WAS data is very small for the long lived species, staying below 0.2 % for all three species. This is especially interesting for N_2O , which is only available from WAS data. The medium short-lived species C_3H_8 and C_2H_6 are also available from WAS data only. Here, the uncertainty is higher already, reaching between 1 % and 10 %. This uncertainty could be reduced with a higher measurement frequency. For shorter lived species, the uncertainty introduced by WAS sampling is increasingly higher, reaching more than 50 % for the nitrogen containing species in the troposphere.

The right hand panel is for reference: What would be the influence of an even lower measurement frequency? The relative distribution among the species is similar to the sampling at WAS200, but increases for all substances. Only the long lived species still reach low values, for all other species this low frequency would render the climatology no longer useful. The white space in the very top shows that there is no longer enough data in this height at this sampling frequency.

The difference between R_{rel} corresponding to the panels of Fig. 4.18 is positive or close to 0 for almost all species and heights (not shown). The uncertainty increases for all species if the frequency is lowered from WAS200 to WAS2000. No clear dependency on the species is visible. It rather seems that all species are affected to the same degree. This fits the results of Sec. 4.9.3, which has also shown that R_{rel} increases linearly for all species. The slope is similar for all species in Fig. 4.15, which corresponds to the similar values shown here for the different species.

4.10. Summary and outlook

This chapter describes and assesses the degree of climatological representativeness of data from the passenger aircraft project IAGOS-CARIBIC. After a general discussion of the concept of representativeness, general rules are applied to investigate whether climatologies from IAGOS-CARIBIC trace gas measurements can be seen as representative. This specific question is answered: For which species is a climatology compiled from CARIBIC data representative of the tropopause region in mid-latitudes?

In order to answer this question, four datasets were created from a nudged model run of the chemistry-climate model EMAC. Two datasets sample the model at the geolocation of CARIBIC measurement data ($\text{MOD}_{\text{CARIBIC}}^{\text{regular}}$ and $\text{MOD}_{\text{CARIBIC}}^{\text{sampled}}$). These datasets are contrasted to the much larger datasets $\text{MOD}_{\text{RANDPATH}}$ (random flight tracks with similar properties as those of $\text{MOD}_{\text{CARIBIC}}^{\text{regular}}$) and $\text{MOD}_{\text{RANDLOC}}$ (random locations).

As a first step, it is demonstrated that these model datasets are appropriate to answer the question, which asks for the representativeness of CARIBIC measurement data. In order to justify that conclusions from model data are applied to measurements, model and measurement variability are compared. The variability is used as an indication of the model's ability to reproduce changes in space and time that are seen in the measurements. To compare like with like, variability on scales smaller than the model resolution is removed from the measurements. With this prerequisite the model reproduces 50-100% of the variability of the measurements, depending on time scale, height relative to the tropopause and species. This is sufficient to transfer the results from the model world to the real atmosphere considering the coarse resolution of the model and that of the data used for binning the measurements into height relative to the tropopause.

Three methods to describe representativeness are developed and applied: (i) the Kolmogorov-Smirnov test (and the Mann-Whitney, Brown-Forsythe and Levene's test), (ii) variability analysis following Kunz et al. (2008) and (iii) a test interpreting the relative difference between two datasets. Two fundamental requirements are essential for representativeness: its increase (i) with the number of measurements and (ii) with decreasing atmospheric variability of the species, which is related to atmospheric lifetime following Junge (1974). By formulating the variability analysis and relative differences as scores (R_{var} and R_{rel} respectively), it is demonstrated that they pass these two requirements, while the statistical tests are all too strict. R_{rel} (describing the representativeness of a climatology) is better suited for answering the question and is therefore used in the remaining analysis.

The score R_{rel} is easily converted to a representativeness uncertainty in percent and this measure is used in the discussion. The results show that CO_2 , N_2O and CH_4 have very low uncertainties (below 0.4%). CO , C_2H_6 , and O_3 reach higher values (5% - 20%), but can still be used to compile representative climatologies around the tropopause. NO_y and H_2O are only usable in the lower stratosphere (uncertainties of 5% to 8% there, higher elsewhere), while NO and C_3H_8 cannot be used for a representative climatology (uncertainties of 25% and more). Naturally, the interpretation of results strongly

depends on the chosen threshold uncertainty and should depend on the seasonal variability of the species under consideration. This is demonstrated by setting different limits for climatologies of CO₂, CO and O₃.

The uncertainty can be translated into a number of flights necessary to achieve representativeness. This is demonstrated for some species by showing the relationship of the number of flights and the representativeness uncertainty. For long-lived species like CO₂ and CH₄, the 334 IAGOS-CARIBIC flights used in this study already provide enough data, while short-lived species like NO need around 1000 flights to reduce the uncertainty to 10 %, sufficient to reproduce the strong annual cycle.

Three sections then discuss the influence of three limits inherent in the CARIBIC dataset: CARIBIC never flies over the Pacific Ocean, which is discussed by a limit in longitude. The error introduced by this limit is not related to the lifetime, but shows signals of the air polluting substances in the Asian emission plume, especially in the tropospheric heights. As CARIBIC flies on constant pressure levels, there is also an intrinsic limit in pressure. Its influence correlates with the variability and increases strongly above and below the tropopause. The reduced measurement frequency for species measured by taking air samples is also investigated, which strongly depends on the variability of a species.

This chapter demonstrates one way in which the CARIBIC project as a whole can profit from model simulations. The question of representativeness quickly appears if the data are sorted into geographical or temporal bins. The study presented in this chapter shows how a long running model integration helps in answering this question, in this case for a broad latitudinal and temporal domain. The same methods could be applied to other questions that go beyond case studies, e.g. regional patterns or trends that are observed. The model takes the role of a statistical database in which a hypothesis can be tested. This adds value to the measurements by demonstrating the amount of information they contain. Where before, *representative* was an adjective with the character of cheap merchandise, it can now be given a sound scientific meaning.

5. Development and validation of the isotope enabled model ICON-ART-Iso

ICON-ART-Iso is the new isotope enabled version of the atmospheric model ICON. It expands the model physics by the possibility to simulate diagnostic H_2O and the stable water isotopes HDO and H_2^{18}O . The newly implemented physics are documented and it is demonstrated how the model can lead to a deeper understanding of the water cycle.

CARIBIC data are compared to model results of ICON-ART-Iso in a case study. This demonstrates how model developments can be validated using aircraft measurements on a small scale and forms the counterpart to Ch. 3, which shows how the full CARIBIC dataset can be applied for a climatological validation study.

The previous Chapter 4 - about the climatological representativeness of CARIBIC data - investigates how value can be added to the CARIBIC measurements by model simulations. This chapter demonstrates the value of the aircraft data for the development of a new modeling system.

5.1. Introduction

Water is one of the characteristic substances of the climate system. The ice caps and snow covered surfaces strongly influence the albedo of the surface (Kraus, 2004), the ocean is an unmatched reservoir to dissolve trace substances (Jacob, 1999) and redistribute heat (Pinet, 1993) and all animal and plant life depends on liquid water. The atmosphere is by mass the smallest compartment of the hydrological cycle, but it is this compartment that serves to transfer water between the spheres of liquid, frozen and biologically bound water on the earth's surface (Gat, 1996). Within the atmosphere, water is again of great importance. It is the strongest green house gas (Schmidt et al., 2010) and distributes energy through the release of latent heat (Holton and Hakim, 2013) and liquid and frozen particles influence the radiative balance (Lange, 2002), to name only three prominent mechanisms.

A correct description of the atmospheric water cycle is therefore inevitable for the understanding and simulation of the atmosphere and the climate system (Riese et al. (2012), Sherwood et al. (2014)). The stable isotopologues of water, henceforth called isotopes, are a unique diagnostic tool that can provide a deeper insight into the water cycle (Galewsky et al., 2016). Because of the larger molar mass of the isotopes, their ratio to standard water is shifted upon phase changes, a process termed fractionation. By considering the isotopes in vapor and precipitation, the isotope ratio therefore provides an entry point to an advanced understanding of the processes that make up the water cycle.

This chapter presents ICON-ART-Iso, the newly developed, isotope enabled version of the general circulation model ICON (Zängl et al., 2015). By equipping this new and flexible model with the capabilities to simulate the water isotopes HDO and H₂¹⁸O, a first step is made to a deeper understanding of the water cycle in the model. After validation with measurements, the model results become transferable to the real atmosphere.

An extensive literature overview on measurements and modeling of the water isotopes is given by Galewsky et al. (2016). Pioneering research starting in the 1950's first examined the isotopes in precipitation (Dansgaard (1954), Dansgaard (1964)). First theoretical advances on the microphysics (Jouzel et al. (1975), Jouzel and Merlivat (1984)) and surface evaporation (Craig and Gordon, 1965) made it possible to consider the isotopes in paleoclimate simulations (Joussaume et al. (1984), Joussaume and Jouzel (1993)). Measurement techniques and modeling of the isotopes has advanced. Cryogenic samplers first measured the isotope content in vapor (Dansgaard, 1954), which has become possible by laser absorption spectroscopy in the last 15 years (Lee et al. (2005), Dyroff et al. (2010)). The isotope content in atmospheric vapor can be derived from satellite measurements (Gunson et al. (1996), Worden et al. (2006), Steinwagner et al. (2007), Schneider and Hase (2011)). Many more global circulation models have been equipped to simulate the atmospheric isotope distribution, further focusing on climatological questions (Risi et al. (2010), Werner et al. (2011)) or with a shift now to process understanding (Blossey et al. (2010), Pfahl et al. (2012)). Despite this progress, the potential of isotopes in improving the under-

standing and physical description of the single processes "remains largely unexplored" (Galewsky et al., 2016).

By design, ICON is a flexible model, capable of simulations on climatological time scales as well as on time scales for numerical weather prediction, see also Sec. 2.3.3. The advection has been designed to be mass consistent (Zängl et al., 2015), which is essential for the simulation of the diagnostic isotopes (Risi et al., 2010). By using the infrastructure of ICON-ART (Rieger et al., 2015), ICON-ART-Iso is flexible to simulate many diagnostic instances of water at once. From the multitude of isotope enabled models (see Galewsky et al. (2016) for an overview), ICON-ART-Iso stands out by its fine horizontal resolution on a global grid which comes with advanced physical parameterizations and the flexibility in design to simulate diagnostic water as well as the isotopes.

CARIBIC (see Sec. 2.2) has taken measurements of the isotope content of vapor in the free troposphere since 2010 (Dyroff et al. (2010), Christner (2015)). Except for Christner (2015), this dataset has remained untouched to date. But the in situ measurements of 100 intercontinental flights are a unique dataset by their geographical coverage and resolution. The data is used in this study to validate model results of ICON-ART-Iso. These high resolution, global scale measurements are a perfect match to the ICON-ART-Iso simulations, which give results of the same scale.

The previous chapter extensively discussed how the large CARIBIC dataset can profit from model simulations by investigating its climatological representativeness with the state of the art model EMAC. This chapter shows how the next generation model ICON in turn profits from the long term project to validate the newly developed system ICON-ART-Iso.

This chapter first discusses some general concepts of the physics of water isotopes in Sec. 5.2. This is followed by a detailed description of the physics special to ICON-ART-Iso in Sec. 5.3, which have been implemented in ICON to simulate the isotopes. Section 5.4 gives a short technical introduction to ICON-ART-Iso and details on the simulations used to evaluate the model. The complete technical documentation is given in App. B.

The following four sections describe model results and first validation studies: Section 5.5 looks at water vapor and precipitation diagnostics. Focus is laid on the source regions - ocean or land - of the water in vapor and precipitation. The next section (Sec. 5.6) demonstrates the flexibility of ICON-ART-Iso by discussing different setups for the simulation of the isotopes. The different parameterizations that have been implemented are evaluated separately and their influence is investigated. A first validation with measurements is made in Sec. 5.7. Retrievals from IASI satellite measurements are compared with ICON-ART-Iso results for two weeks in winter and summer 2014, considering different regions and the daily cycle. The data is also related to results from the isotope enabled climate model ECHAM5-wiso (Werner et al., 2011).

Section 5.8 then comes to the comparison with CARIBIC measurements. Data from four flights are compared with simulations of ICON-ART-Iso. Unlike with the satellite measurements, the model data shows the imprint of different, small-scale processes in the isotope ratio when sampled along CARIBIC

flight tracks. The measurements along the same track make a validation possible. For different reasons, the exact reproduction of the measurements by the model can not be anticipated. The analysis along the flight tracks still reveals that the model is capable of resolving and simulating small scale processes. The simulations of the four flights are also compared with results of the regional isotope model COSMOiso (Pfahl et al., 2012). Section 5.9 summarizes this chapter and gives an outlook to possible future developments of ICON-ART-Iso.

5.2. General isotope physics

This section explains some general principles of the physics of water isotopes. The δ notation is introduced (Sec. 5.2.1) and equilibrium as well as kinetic fractionation are discussed (Sec. 5.2.2). The Rayleigh model of fractionation serves as a reference for the interpretation of results and is explained in Sec. 5.2.3. This section does not explain the different parameterizations implemented in ICON-ART-Iso. These are discussed in Sec. 5.3

5.2.1. The isotope ratio and the δ notation

The mass mixing ratios q of the heavy isotopes (${}^h q$) are commonly reported in relation to that of the main, light isotope H_2O (${}^l q$) in form of the isotope ratio $R = {}^h q_x / {}^l q_x$. The index x refers to the specific water substance under consideration. The reference ratio is the Vienna Standard Mean Ocean Water, abbreviated as VSMOW. Values of R_{VSMOW} are given in Table 5.1.

	literature	H_2O	HDO	H_2^{18}O	H_2^{17}O
molar mass [g/mol]	Mook (2001)	18.015	19.021	20.015	19.015
R_{VSMOW}	Mook (2001)	1.0	$3.12 \cdot 10^{-4}$	$2.01 \cdot 10^{-3}$	$3.80 \cdot 10^{-4}$

Tab. 5.1.: Molar mass and R_{VSMOW} , the isotope ratio in the Vienna Mean Ocean Water standard, given for the three isotopes of water considered in this study, H_2O , HDO and H_2^{18}O , and for H_2^{17}O .

In reporting isotope values, the isotope ratio is again given as relative difference to R_{VSMOW} to form the δ notation, as given in Eq. 5.1. R_{VSMOW} is very close to ocean surface isotope ratio. As more processes act on water in the atmosphere, the local isotope ratio changes. The δ notation is therefore useful to describe this shift in the isotope ratio relative to the main source. By defining δ values in this way, a δ value 0 states that the local ratio is equal to that of R_{VSMOW} while a value of -1000 states the complete absence of the isotope. The δ value of HDO is denoted by δD , while that of H_2^{18}O is denoted by $\delta^{18}\text{O}$. Small positive values can occur, especially in values of the condensed phase.

$${}^h \delta_x = \left(\frac{{}^h q_x / {}^l q_x}{R_{\text{VSMOW}}} - 1 \right) \cdot 1000 \quad [5.1]$$

5.2.2. Fractionation

The isotope ratio is changed by processes involving phase changes in such a way that the heavier isotope is enriched in the condensed phase. The change of the isotope ratio due to such a process is called fractionation. There are two ways of fractionation, which are explained in the following paragraphs: Equilibrium and kinetic fractionation. Both are caused by the different molar masses given in Table 5.1. They rarely act alone in changing the isotope ratio, as will become clear in Sec. 5.3.

5.2.2.1. Equilibrium fractionation

Equilibrium fractionation describes systems in thermodynamic equilibrium or where processes happen fast enough to assume the system to be in equilibrium. Due to their higher mass (see Table 5.1), the chemical binding energies of the heavier isotopes are higher than those of H₂O. This leads to higher vapor pressures over ice and over liquid water (Mook, 2001). This difference is expressed in form of the equilibrium fractionation factor α_{liq} over liquid and α_{ice} over ice. In ICON-ART-Iso and in this text, the values of α are defined as the ratio in vapor R_{vap} over the ratio in the condensed phase R_{cond} . Since the vapor pressures of the heavier isotopes are higher, they condense more readily and evaporate less easily than standard water. The values of α are therefore smaller than 1. This is expressed in Eq. 5.2.

$$\alpha = \frac{R_{\text{vap}}}{R_{\text{cond}}} < 1 \quad [5.2]$$

Different measurements of the equilibrium fractionation have lead to different parameterizations for α . All the measurements have shown α to depend on temperature T , all parameterizations therefore depend on it. In ICON-ART-Iso, the parameterizations by Majoube (1971) and those by Horita and Wesolowski (1994) have been implemented for α_{liq} and those by Merlivat and Nief (1967) for α_{ice} , each for HDO and H₂¹⁸O respectively.

Figure 5.1 shows the values for α_{liq} and α_{ice} for the different parameterizations for HDO and H₂¹⁸O. Equilibrium fractionation is stronger for HDO and stronger over ice than over liquid water. This leads to less negative δ values in H₂¹⁸O compared to HDO. This difference is also the reason why fractionation during ice formation is more effective than during interaction with the liquid phase.

5.2.2.2. Kinetic fractionation

The higher mass of the heavier isotopes (see Table 5.1) leads to a lower diffusion velocity, as the kinetic energy of a molecule, determined by temperature, is defined as $k_B T = \frac{1}{2} m v^2$ (Mook, 2001). Like α , the equilibrium fractionation factor, this is described by considering the ratio of the diffusion constants, defined as ${}^hD/{}^lD < 1$. In contrast to α , the ratio ${}^hD/{}^lD$ is simply a constant value and not a function of T . The different literature values are listed in Table 5.2.

Molecular diffusion is not explicitly resolved by ICON-ART-Iso or considered here. But ${}^hD/{}^lD$ is needed to parameterize many fractionating processes, e.g. evaporation from the ocean surface or vapor deposition on ice. Fractionation that is caused by the different diffusion constants is referred to as kinetic fractionation.

5.2.2.3. Non-fractionating processes

There are also processes that act on water which do not change the isotope ratio, they are non-fractionating. When ice melts to water, for example, the isotope ratio in the ice will be equal to that in the water after melting. From a Lagrangian viewpoint, advection is also a non-fractionating process. For all processes

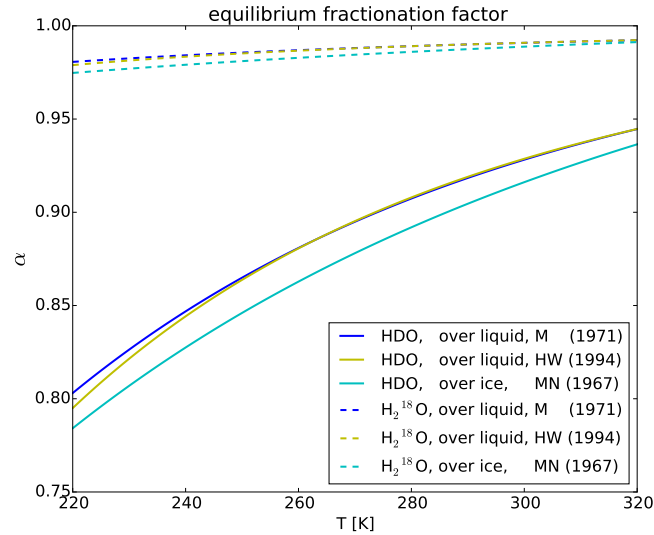


Fig. 5.1.: Equilibrium fractionation factor α over ice and liquid water for HDO and H_2^{18}O for the different parameterizations that have been implemented in ICON-ART-Iso. The abbreviations of the different literature sources are as follows: M (1971) for Majoube (1971), HW (1994) for Horita and Wesolowski (1994) and MN (1967) for Merlivat and Nief (1967).

literature	H_2O	HDO	H_2^{18}O
Merlivat (1978)	1	0.9755	0.9723
Cappa et al. (2003)	1	0.9839	0.9691

Tab. 5.2.: The ratio of diffusion constants $^hD/lD$ of the three isotopes of water considered in this study given for two literature sources. These values are available as options in ICON-ART-Iso.

which act in this way, the same principle applies: The ratio in the source of the process determines the ratio in the tendency. If a certain amount of ice melts to water, the isotope ratio in that amount is equal to the isotope ratio in the ice. This is generalized in Eq. 5.3 for the tendency S , see also Pfahl et al. (2012) or Blossey et al. (2010).

$$h_S = l_S \cdot \frac{h_{q_x}^{\text{source}}}{l_{q_x}^{\text{source}}} \quad [5.3]$$

5.2.3. The Rayleigh model

The Rayleigh model of fractionation is the frame of reference that will be used in Sec. 5.7 and 5.8 to discuss pairs of $\{\delta D, q\}$. Diagrams showing pairs of these values are used to discuss different processes that lead to the depletion of the heavy isotope under consideration. The Rayleigh model of fractionation describes an idealized process, which is discussed in many publications, e.g. by Gat (1996) or Galewsky et al. (2016).

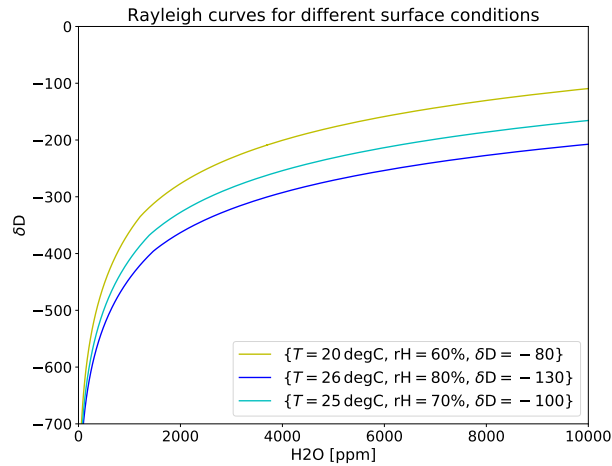


Fig. 5.2.: Pairs of $\{\delta D, q\}$ as calculated by the Rayleigh model for different surface conditions. Starting values at the surface are $\{T = 20^\circ\text{C}, rH = 60\%, \delta D = -80\}$, $\{T = 26^\circ\text{C}, rH = 80\%, \delta D = -130\}$, $\{T = 25^\circ\text{C}, rH = 70\%, \delta D = -100\}$.

An air parcel is assumed to rise from the ground with initial values of δD , q and T . Using a certain profile of T as function of p , the parcel will reach saturation. From then, the excess water is assumed to be removed instantaneously by precipitation while the temperature profile is assumed to remain unchanged by the latent heat release. The heavier isotopes are depleted in the remaining vapor according to equilibrium fractionation as the parcel moves upward along the temperature profile. Equation 5.4 describes the relationship between the isotope ratio R_{vap} and q with the equilibrium fractionation factor α as defined in Eq. 5.2.

$$d \ln(R_{\text{vap}}) = (1 - \alpha) d \ln(q) \quad [5.4]$$

The temperature profile can be assumed to be adiabatic, as discussed by Johnson et al. (2001). This text uses those profiles that have been applied in Christner (2015) and Schneider et al. (2017). They use a quadratic approximation of mean temperature profiles taken by CARIBIC during tropical ascents (Christner, 2015). The equilibrium fractionation factor α is determined by assuming liquid water and the parameterization by Horita and Wesolowski (1994). Figure 5.2 shows the three Rayleigh curves that are given as reference in Sec. 5.8 and 5.7. Starting values at the surface are $\{T = 20^\circ\text{C}, \text{rH} = 60\%, \delta\text{D} = -80\}$, $\{T = 26^\circ\text{C}, \text{rH} = 80\%, \delta\text{D} = -130\}$, $\{T = 25^\circ\text{C}, \text{rH} = 70\%, \delta\text{D} = -130\}$. rH is the relative humidity. These curves represent surface conditions typical of tropical or subtropical latitudes, which are the main areas of interest in model evaluation in this study.

As shown in Fig. 5.2, the Rayleigh model leads to depletion in the heavy isotopes towards lower values of q , i.e. as water vapor is removed by subsequent rainout during the ascent. Since the Rayleigh model describes a very simple atmospheric process of adiabatic ascent, it can serve as reference for measured pairs of modeled or measured pairs of $\{\delta\text{D}, q\}$, which carry information on possibly more complex atmospheric processes.

5.3. ICON-ART-Iso physics

ICON-ART-Iso is the isotope enabled version of the ICON model (Zängl et al., 2015), using its numerical weather prediction physics package. It is a model to diagnostically simulate the heavy isotopes HDO and H₂¹⁸O and other instances of water. Each instance is diagnostically passed through the atmospheric branch of the hydrological cycle of the model and all the processes that act on water in ICON also alter the distribution of each instance simulated by ICON-ART-Iso. The development of ICON-ART-Iso is based in many parts on the code of COSMOiso, see Pfahl et al. (2012), which served as a reference during the development of ICON-ART-Iso. It also builds heavily on the infrastructure provided by ICON-ART (Rieger et al., 2015).

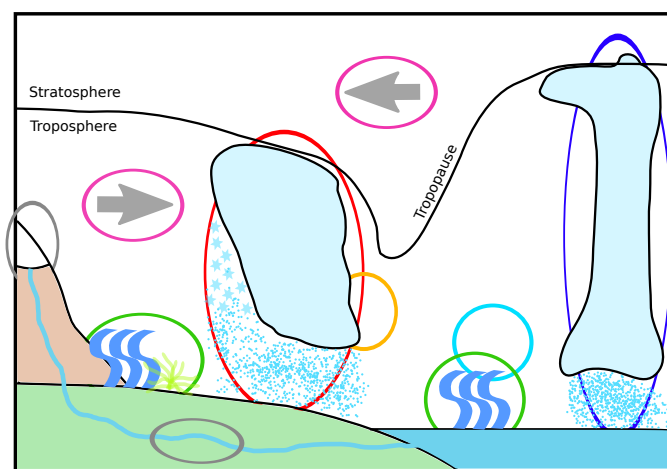


Fig. 5.3.: Schematic diagram of the water cycle in ICON. The different processes are represented by icons and circles of different color. The following processes are included in the model and the diagram: Land surface processes (gray), evaporation from land and ocean surfaces (green), formation of cloud water by saturation adjustment (yellow), formation and interaction of different hydrometeors in microphysics (red) and sub-grid scale convective processes (dark blue). Transport is accomplished by advection for grid scale (pink) and turbulence for sub-grid scale (light blue). The figure is inspired by Fig. 2 of Christner (2015).

A schematic illustration of the water cycle in ICON is given in Fig. 5.3. The water cycle considered by ICON-ART-Iso consists of the following main parts, to each of which this chapter devotes one section: Surface evaporation (Sec. 5.3.2), cloud processes described by microphysics (Sec. 5.3.3), the formation of clouds by saturation adjustment (Sec. 5.3.4), and the convection parameterization (Sec. 5.3.5). The initialization of the isotopes is described in Sec. 5.3.1. ICON-ART-Iso makes use of the 2-moment microphysical scheme by Seifert and Beheng (2006) and the Tiedtke-Bechtold convection scheme by Bechtold et al. (2014). Ground surface processes are not included, as these are treated by a separate submodel of ICON and only give the lower boundary condition for ICON-ART-Iso. How this is approximated is also

explained in Sec. 5.3.2. The advection as well as turbulent diffusion are calculated with the same routines as for all the other trace substances and not explained here, see Zängl et al. (2015) and Rieger et al. (2015) for more details on these parameterizations.

ICON uses mass mixing ratios q to describe the amount of a water substance. Values of the light, abundant isotope will be denoted by the index l , while h will be used for the heavy, rare isotopes. The standard water simulated by ICON is assumed to consist of H_2O only by ICON-ART-Iso, a good approximation also made by Pfahl et al. (2012). As ICON-ART-Iso uses the 2-moment microphysical scheme by Seifert and Beheng (2006), seven substances (and therefore tracers) are used to describe water in the atmosphere: vapor, cloud water, ice, rain, snow, graupel and hail. These will be abbreviated with v , c , i , r , s , g and h respectively. Each instance of water simulated by ICON-ART-Iso consists of these seven substances. The instance and the group of tracers it consists of is referred to as an isotope, abbreviated with q .

This section does not give details on the technical aspects of ICON-ART-Iso. A short introduction on technical details is given in Sec. 5.4 and a detailed documentation is given in App. B. ICON-ART-Iso is part of the ICON-ART project (Rieger et al., 2015) and the flexibility of this system has also been implemented in ICON-ART-Iso. This means that the number of isotopes that is simulated is not fixed but determined during run time. Different parameterizations can be used or processes switched off for different isotopes during one simulation.

The following sections explain the parameterizations implemented in ICON-ART-Iso to describe fractionation during each of the following main processes: surface evaporation, microphysics, saturation adjustment and convection. Table 5.3 gives a summary of the different subprocesses and parameterization options, also listing the corresponding section. First, Sec. 5.3.1 explains the initialization of the isotope fields.

5.3.1. Initialization

The initialization of the model is of great importance, as the initial values give the starting point for a simulation. The ICON fields for initialization are taken from IFS reanalysis or another atmospheric model. Vapor, cloud water, ice, rain and snow are among the variables that are taken from the analysis to initialize ICON. The isotope ratios have to match the location of these fields, because they are only diagnostic values that cannot exist independently. This makes it close to impossible to take the isotope ratios from a different atmospheric model than that which is used for initialization. Therefore, the isotope fields are initialized relative to the initial ICON fields, using climatological relationships. Initialization from another isotope enabled model has not been implemented.

For instances of diagnostic H_2O , the initialization ratio can be a constant factor. But this is not the case for the heavy isotopes. Due to the different processes in the atmosphere, the atmospheric water vapor is generally more depleted of the heavy isotopes with increasing height. The depletion of isotopes of an air parcel that rises, thereby cooling adiabatically and losing all water vapor by condensation and rainout

main process	subprocess	section	option	literature
surface evaporation	-	5.3.2	*3	Pfahl and Wernli (2009)
			4	Merlivat and Jouzel (1979)
microphysics	evaporation	5.3.3.1	*1	Stewart (1975)
			2	Pruppacher and Klett (2012)
			3	Blossey et al. (2010)
	ice formation	5.3.3.2	*1	Blossey et al. (2010)
			2	Pruppacher and Klett (2012)
saturation adjustment	-	5.3.4	*2	Pfahl et al. (2012)
			3	Blossey et al. (2010)
convection	satur. adjust.	5.3.5.1	*1	Pfahl et al. (2012)
			2	Blossey et al. (2010)
	downdrafts	5.3.5.2	*1	Pfahl et al. (2012)
	evaporation	5.3.5.3	*1	Pfahl et al. (2012)

Tab. 5.3.: Summary of the parameterizations implemented in ICON-ART-Iso for the different fractionating processes. Standard setup for a fractionating isotope is marked by *.

is described by the Rayleigh model, see Sec.5.2.3. However, these assumptions are also not suitable to initialize the model, as the initial state of the atmosphere is not formed by adiabatic ascent.

The isotopes of water are therefore initialized using climatological δ values applied to the ICON fields. The parameterization relies on four δ values, three for vapor (ground level, tropopause, and model top) and one for the offset for hydrometeors. The values for HDO and H_2^{18}O are given in Table 5.4. The values are taken from literature only for HDO. All values for H_2^{18}O are defined in accordance with the global meteoritic water line (GMWL), which states that $\delta\text{D} = 8 \cdot \delta^{18}\text{O} + 10\%$ (Craig, 1961). By the four values, profiles are calculated as a function of p . The profiles are related to the tropopause level, following the WMO definition (using the vertical temperature gradient and 2K threshold, Holton et al. (1995)). This insures a minimum adaptation to the state of the atmosphere.

	literature	H_2O	HDO	H_2^{18}O
δ_{bottom}	Gat (2010)	1	-50	-5
$\delta_{\text{tropopause}}$	Steinwagner et al. (2007)	1	-650	-80
δ_{top}	Steinwagner et al. (2007)	1	-400	-48.75
δ_{offset}	Gat (2010)	1	-100	-11.25

Tab. 5.4.: Values for the initialization with climatological δ values. Literature sources give the values for HDO, values for H_2^{18}O have been determined from GMWL: $\delta\text{D} = 8 \cdot \delta^{18}\text{O} + 10\%$ (Craig, 1961).

The values listed in Table 5.4 (all but offset) are used to calculate a profile using Eqs. 5.5–5.10. First, two factors a and b are calculated for the tropospheric and stratospheric part of the profile. Corresponding pressure values p are needed for the lowest and highest level as well as for the tropopause. These factors are then used to determine the local δ values from the local values of p . This results in a linear relationship of δ and p above the tropopause and a relationship with $\log(p)$ in the troposphere.

$$a_{\text{troposphere}} = \frac{\delta_{\text{bottom}} - \delta_{\text{tropopause}}}{\log(p_{\text{bottom}}) - \log(p_{\text{tropopause}})} \quad [5.5]$$

$$a_{\text{stratosphere}} = \frac{\delta_{\text{tropopause}} - \delta_{\text{top}}}{p_{\text{tropopause}} - p_{\text{top}}} \quad [5.6]$$

$$b_{\text{troposphere}} = \delta_{\text{bottom}} - a_{\text{troposphere}} \cdot \log(p_{\text{bottom}}) \quad [5.7]$$

$$b_{\text{stratosphere}} = \delta_{\text{tropopause}} - a_{\text{stratosphere}} \cdot p_{\text{tropopause}} \quad [5.8]$$

$$\delta_{\text{troposphere}} = a_{\text{troposphere}} \cdot \log(p) + b_{\text{troposphere}} \quad [5.9]$$

$$\delta_{\text{stratosphere}} = a_{\text{stratosphere}} \cdot p + b_{\text{stratosphere}} \quad [5.10]$$

Figure 5.4 shows the resulting profile of δ values for p_{bottom} , $p_{\text{tropopause}}$ and p_{top} set to 1000hPa, 200hPa and 1hPa respectively. The figure also shows the initial state of δD of a model simulation as latitudinal cross section. The dependence on the height of the local tropopause shows up strongly, highlighting the importance to consider this parameter.

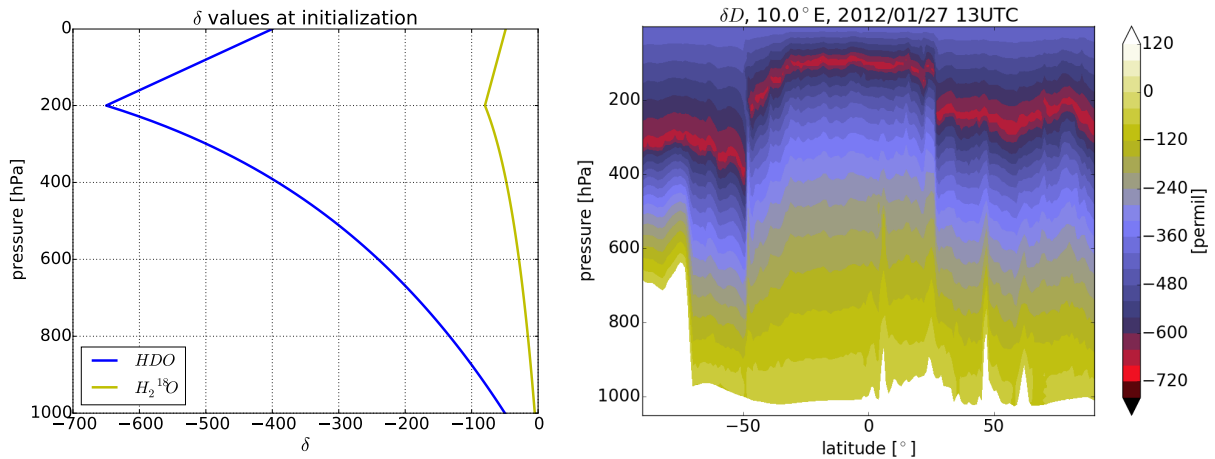


Fig. 5.4.: Profiles of δD and $\delta^{18}\text{O}$ for the values of p_{bottom} , $p_{\text{tropopause}}$ and p_{top} set to 1000 hPa, 200 hPa and 1 hPa respectively, using the δ values given in Table 5.4 (left). The initial state of δD of a model simulation is shown on the right as latitudinal cross section at 10°E .

5.3.2. Surface evaporation

Surface evaporation provides the source term for the atmospheric water cycle and can be considered the counterpart of precipitation. While the source for precipitation is the water contained in the atmosphere,

evaporation from the surface feeds on the water reservoirs in or on the ground or in the ocean. These reservoirs are also simulated to some extent by ICON, but ground and surface waters have not been implemented in ICON-ART-Iso. The isotopic composition of ground and surface waters is therefore also not a prognostic variable.

Simulation of the atmospheric water cycle is still possible. The surface flux ($lq_{v,s}^{fl}$) is calculated by ICON and only the fractionation of this known flux has to be parameterized. For ICON-ART-Iso, $lq_{v,s}^{fl}$ is split up into dewfall ($lq_{v,s}^{dew}$), formation of rime ($lq_{v,s}^{rime}$), evaporation from from water or land ($lq_{v,s}^{evap}$) and transpiration of plants ($lq_{v,s}^{transp}$). Equation 5.11 summarizes how these terms fractionate and sum up to $h q_{v,s}^{fl}$.

$lq_{v,s}^{transp}$ is assumed not to fractionate. Ideally, the ratio in the evaporating water body or soil layer (R_{surf}) would then be used and Eq. 5.3 applied directly. Since the surface ratio is not known, values of R_{VSMOW} (given in Table 5.1) are applied for R_{surf} . $lq_{v,s}^{dew}$ and $lq_{v,s}^{rime}$ are both directed towards the surface, the source is therefore the atmosphere, for which the isotope ratio is known (R_{atm}). These two fluxes follow equilibrium fractionation, using one of the parameterizations for α specified in Sec. 5.2.2.1. Evaporation ($lq_{v,s}^{evap}$) is a fractionating process. Even more so, the flux cannot be assumed to happen in equilibrium, since unresolved turbulence and diffusion is also involved. R_{evap} is therefore parameterized. Two parameterisations for R_{evap} have been implemented in ICON-ART-Iso.

$$h q_{v,s}^{fl} = lq_{v,s}^{evap} \cdot R_{evap} + lq_{v,s}^{transp} \cdot R_{surf} + lq_{v,s}^{dew} \cdot \frac{R_{atm}}{\alpha_{liq}} + lq_{v,s}^{rime} \cdot \frac{R_{atm}}{\alpha_{ice}} \quad [5.11]$$

Both parameterizations for R_{evap} build on the Craig-Gordon model for evaporation, a model for atmospheric resistance (Gat, 2010). Equation 5.12 gives the general expression for R_{evap} . Here, h is the relative humidity with respect to surface temperature and k is the non-equilibrium fractionation factor. In the case of $R_{atm} = 0$, $R_{atm} = R_{evap}$ is assumed for a global closure. Equation 5.12 then changes to Equation 5.13. R_{surf} is again approximated by R_{VSMOW} from Table 5.1.

$$R_{evap} = k \cdot \frac{\alpha_{liq} R_{surf} - h R_{atm}}{1 - h} \quad [5.12]$$

$$R_{evap} = k \cdot \frac{\alpha_{liq} R_{surf}}{1 - h(1 - k)} \quad [5.13]$$

The two parameterizations for R_{evap} use Eq. 5.12 and Eq. 5.13 with different definitions of the non-equilibrium fractionation factor k . Merlivat and Jouzel (1979) give k as a function of wind speed in 10m height (u). The implementation in ICON-ART-Iso follows that by Pfahl and Wernli (2009), applying a linear approximation of the original functions. Depending on two wind regimes, different sets of parameters and functions are used. This is summarized in Table 5.5.

The second parameterization, by Pfahl and Wernli (2009), is simpler. k is parameterized using only the ratio of diffusion constants hD/lD and a constant exponent $\tilde{\kappa}$. In order to use Eq. 5.12, k is defined using Eq. 5.14 in ICON-ART-Iso. $\tilde{\kappa}$ is set to 0.28 in standard setup, but can be set to a different value at run time.

$$k = 1 - \left(\frac{hD}{lD} \right)^{\tilde{\kappa}} \quad [5.14]$$

		HDO	H ₂ ¹⁸ O	$k = \text{fct}(u) =$
$u < 7\text{m/s}$	κ_1	6.10	6.92	$(\kappa_1 - \kappa_2 \cdot u)/1000$
	κ_2	0.13	0.15	
$u \geq 7\text{m/s}$	κ_3	0.45	0.51	$(\kappa_3 + \kappa_4 \cdot u)/1000$
	κ_4	0.28	0.32	

Tab. 5.5.: Values and functions needed for the parameterization of the non-equilibrium fractionation factor k for the parameterization of Merlivat and Jouzel (1979) as used by Pfahl and Wernli (2009).

5.3.3. Microphysics

Thermodynamic processes that lead to phase changes of water and subsequently to the formation of rain and other hydrometeors are summarized under the term microphysics. These processes happen at the resolution of the model, which is why they are abbreviated as *gscp*, grid scale precipitation. The fact that they are explicitly resolved by the model differentiates them from convection, which describes those thermodynamic processes which are not resolved by the model.

Several microphysical schemes have been implemented into ICON and they differ in their complexity and in the number of hydrometeors that are simulated. For ICON-ART-Iso, the 2-moment microphysical scheme by Seifert and Beheng (2006) has been adapted to also consider diagnostic isotope tracers. In its current formulation, the scheme by Seifert and Beheng (2006) describes seven different phases of water (vapor, cloud water, ice, rain, snow, graupel and hail). For all but vapor, it also calculates prognostic number densities. Because the isotopes cannot exist independently of the regular water tracers, the number densities do not have to be doubled. In contrast to the rest of the model, microphysics use mass densities ρ instead of mass mixing ratios q to describe the amount of a substance at a certain grid point. This is reflected by a change in notation in this document, with indexing remaining as before.

The 2-moment microphysical scheme consists of a series of 39 box models that describe 62 processes. Figure 5.5 shows an attempt of visualizing these processes. The evaporation of cloud water and its formation from vapor is not treated by microphysics. It is calculated by saturation adjustment, which is described in Sec. 5.3.4. Most of the 62 processes are non-fractionating, so Eq. 5.3 can be applied directly. For example, this is the case when ice melts to rain or cloud water or when ice and snow collect on graupel. Fractionation happens only if the vapor phase is involved, with the exception that sublimation is assumed not to fractionate. This assumption is also made by Blossey et al. (2010) and Pfahl et al. (2012). So only evaporation of liquid or melted particles and the formation of ice involve fractionation. The different parameterizations for these processes are explained in the following sections. All parameterizations calculate a tendency hS for the heavy isotopes, in part using the corresponding tendency lS from ICON. Vapor mass densities at saturation are denoted by $\rho_{l,v}^*$ over liquid water and $\rho_{i,v}^*$ over ice.

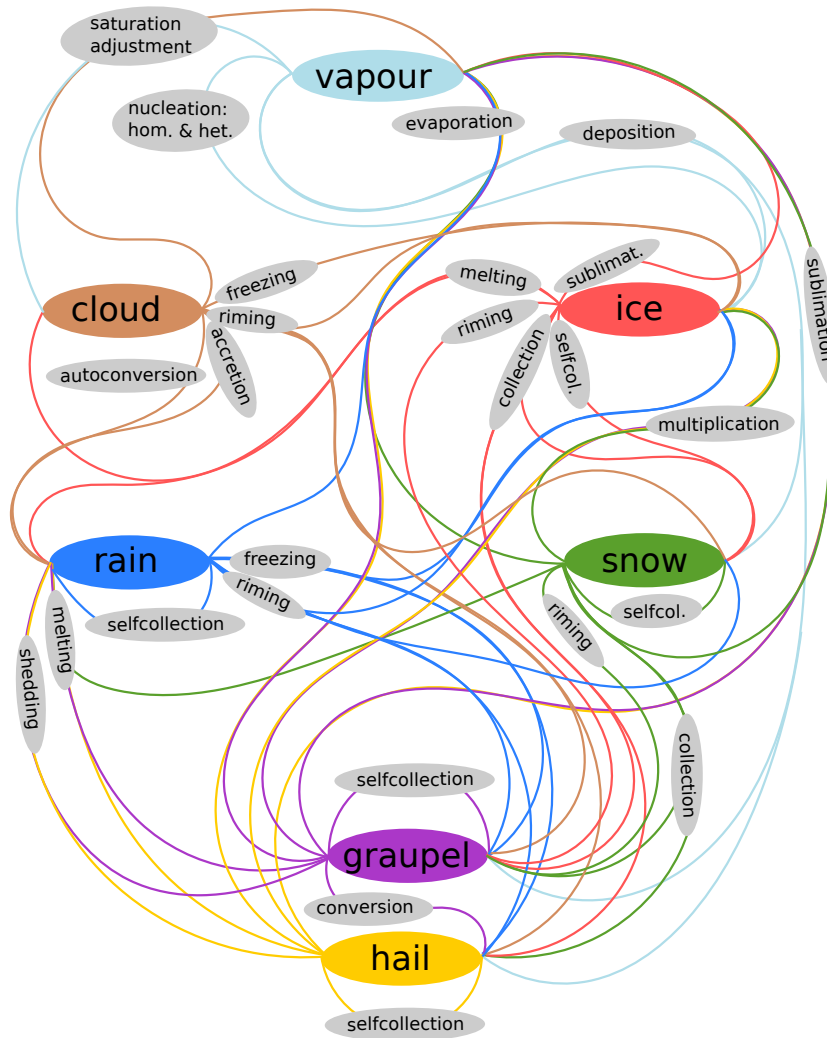


Fig. 5.5.: Schematic diagram showing (most of) the processes that are described by the 2-moment scheme by Seifert and Beheng (2006) in ICON. All processes are marked by a line, the color of which is determined by the source of the process. Only those processes that involve the vapor phase fractionate: homogeneous and heterogeneous nucleation, vapor deposition on the ice classes and evaporation of rain and the melting ice classes. Sublimation is assumed not to fractionate. Saturation adjustment (i.e. the interaction of vapor and cloud water) is not part of microphysics, but treated separately, see Sec. 5.3.4. The diagram is inspired by Fig. 4.1 of Seifert (2002).

5.3.3.1. Evaporation of hydrometeors

Within the 2-moment scheme, rain and the heavier ice classes (snow, graupel and hail) can evaporate. The evaporation of the ice classes happens after melting, sublimation is treated separately and is not considered to fractionate. Three different parameterizations have been implemented that calculate fractionation during the evaporation of hydrometeors, which are explained in the following.

All three approaches build on the same fundamental relationship. For diffusional growth of a droplet of mass ${}^l m$ consisting of standard water, Eq. 5.15 can be applied (Pruppacher and Klett, 2012). ρ_a and ρ_∞ are the mass densities at the droplet surface and in the surroundings, respectively. f is the ventilation factor to consider an increased diffusion due to the movement of the air relative to the droplet. This equation can easily be transformed to Eq. 5.16 by using $m = \frac{4}{3}\pi a^3 \tilde{\rho}_s$ and the ideal gas law $\rho = e/\mathcal{R}_v T$. Here, \mathcal{R}_v is the gas constant of vapor, $\tilde{\rho}_s$ the density of the droplet solution and e the vapor pressure, taken at the droplet surface (e_a) or in the surroundings (e_∞). e_a has already been replaced by the saturation vapor pressure over liquid water $e_l^*(T_a)$ in the reasonable assumption of a saturated droplet surface. The different parameterizations use different approaches to arrive at a tendency for the heavy isotopes $d^h m/dt$.

$$\frac{d^l m}{dt} = -4\pi a {}^l D {}^l f \left({}^l \rho_a - {}^l \rho_\infty \right) \quad [5.15]$$

$$a \frac{da}{dt} = -\frac{{}^l D}{\mathcal{R}_v \tilde{\rho}_s} \left(\frac{e_l^*(T_a)}{T_a} - \frac{e_\infty}{T_\infty} \right) \quad [5.16]$$

Approach following Stewart (1975) The simplest of the parameterizations to calculate fractionation during evaporation is an application of the study by Stewart (1975). This parameterization is also implemented in COSMOiso, see Pfahl et al. (2012). $d^h m/dt$ is calculated from $d^l m/dt$ following Eq. 5.17. Here ρ_x stands for the mass density of either rain, snow, graupel or hail.

$$\frac{d^h m}{dt} = \frac{d^l m}{dt} \left(\frac{{}^h D}{{}^l D} \right)^n \frac{\alpha_{\text{liq}} {}^l \rho_{l,v}^* \frac{{}^h \rho_x}{{}^l \rho_x} - {}^h \rho_v}{{}^l \rho_{l,v}^* - {}^l \rho_v} \quad [5.17]$$

To arrive at Eq. 5.17, Eq. 5.15 is reformulated for the heavy isotopes by replacing ${}^l D$, ${}^l \rho_a$ and ${}^l \rho_\infty$ with the respective variables for the heavy isotopes. By dividing this heavy isotope version of the equation by Eq. 5.15, a preliminary version of Eq. 5.17 is reached. The saturation density of the heavy isotopes is then replaced using the definition of the equilibrium fractionation factor α_{liq} given in Eq. 5.2. The ratio of the diffusion constants is additionally modified by setting the exponent n to account for differences in the ventilation. In a default setup, this parameter is set to $n = 0.58$, following Stewart (1975) and the implementation in COSMOiso by Pfahl et al. (2012).

Theoretical approaches The evaporation tendency of heavy isotopes can also be derived by a theoretical approach (Blossey et al., 2010). The fundamental equations that govern the evaporation of droplets are applied to the heavy isotopes and $d^h m/dt$ is derived directly. Because two different approximations

can be applied at a certain point, two different parameterizations can be derived. The fundamental science is explained in Pruppacher and Klett (2012), while Blossey et al. (2010) give a short summary and apply the equations to heavy isotopes. The following paragraphs summarize the derivation of the parameterizations.

Both parameterizations build on the same relationships which are repeated here for standard water to make clear how to arrive at the equation for heavy isotopes. Starting point is Eq. 5.16. Two unknown variables have to be determined in this equation: T_a and $e_l^*(T_a)$ at the droplet surface. We first turn to T_a . By evaporating, the droplet cools, which is described the equation for latent heat release (Eq. 5.18), where L_e is the latent heat of evaporation. By again substituting $m = \frac{4}{3}\pi a^3 \rho$ and using the equation for conductive heat transfer (Eq. 5.19, with the conductivity k_a), an equation for T_a can be derived (Eq. 5.20). To increase readability, γ is introduced.

$$\frac{dQ}{dt} = -L_e \frac{dm}{dt} \quad [5.18]$$

$$\frac{dQ}{dt} = 4\pi a k_a (T_\infty - T_a) \quad [5.19]$$

$$T_a = T_\infty \left(1 + \frac{L_e \tilde{\rho}_s}{k_a T_\infty} a \frac{da}{dt} \right) = T_\infty (1 + \gamma) \quad [5.20]$$

The saturation vapor pressure at the droplet surface $e_l^*(T_a)$ is determined by integrating the Clausius-Clapeyron equation to yield Eq. 5.21, where $e_l^*(T_\infty) = e_{l,\infty}^*$ has been set for better readability.

$$e_l^*(T_a) = e_{l,\infty}^* \exp \left[\frac{L_e}{\mathcal{R}_v} \left(\frac{T_a - T_\infty}{T_a T_\infty} \right) \right] = e_{l,\infty}^* \exp \left[\frac{L_e}{\mathcal{R}_v T_\infty} \frac{\gamma}{1 + \gamma} \right] \quad [5.21]$$

By using Eqs. 5.20 and 5.21, Eq. 5.16 can be transformed to Eq. 5.22, which contains only variables of the droplet surroundings or constant droplet parameters. This is Eq. 13-26 of Pruppacher and Klett (2012) without solution or curvature effects, formulated for evaporation with the ventilation factor f , see also Eq. 13-64 of Pruppacher and Klett (2012) and Eq. B7 of Blossey et al. (2010).

$$a \frac{da}{dt} = - \frac{D e_{l,\infty}^*}{\mathcal{R}_v \tilde{\rho}_s T_\infty} \left(\frac{1}{1 + \gamma} \exp \left[\frac{L_e}{\mathcal{R}_v T_\infty} \frac{\gamma}{1 + \gamma} \right] - \frac{e_\infty}{e_{l,\infty}^*} \right) \quad [5.22]$$

This equation cannot be solved directly, since γ is a function of ada/dt . Here, Pruppacher and Klett (2012) and Blossey et al. (2010) part by using different approximations.

Evaporation of heavy isotopes using Pruppacher and Klett (2012) Pruppacher and Klett (2012) use $\gamma \ll 1$ and approximate the exponential function by Eq. 5.23. Equation 5.22 can then be solved for ada/dt . The final equation for $d^l m/dt$ is given in Eq. 5.24 where $^l S_l = \frac{e_\infty}{e_{l,\infty}^*}$ has been set as subsaturation

ratio with respect to liquid water. This is the equation that is also implemented in the 2-moment scheme of Seifert and Beheng (2006) in ICON for the evaporation of hydrometeors.

$$\exp\left[\frac{L_e}{\mathcal{R}_v T_\infty} \frac{\gamma}{1+\gamma}\right] \approx 1 + \frac{L_e}{\mathcal{R}_v T_\infty} \cdot \gamma \quad [5.23]$$

$$\frac{d^l m}{dt} = \frac{4\pi a^l f ({}^l \mathcal{S}_l - 1)}{\frac{\mathcal{R}_v T_\infty}{{}^l D e_{l,\infty}^*} + \frac{L_e^2}{k_a \mathcal{R}_v T_\infty^2}} \quad [5.24]$$

In order to consider the evaporation of the heavy isotopes, Eq. 5.24 has to be derived again, using ${}^h D$, ${}^h f$ and ${}^h \rho$ in place of the corresponding variables in Eq. 5.15. ${}^h D$ can easily be determined as ${}^h D/{}^l D = \beta$ is a constant. ${}^h f = {}^l f$ is set for evaporation, so only ${}^h \rho_a$ and ${}^h \rho_\infty$ have to be determined. Following Blossey et al. (2010), Eqs. 5.24 and 5.25 can be applied, where $R_{\text{atm}} = {}^h q_v/{}^l q_v$ has been set for the isotope ratio in the surrounding air and $R_{\text{hyd}} = {}^h q_x/{}^l q_x$ for that in the evaporating hydrometeor.

$${}^h \rho_\infty = {}^l \rho_{l,\infty}^* \cdot {}^l \mathcal{S}_l R_{\text{atm}} \quad [5.25]$$

$${}^h \rho_a = {}^l \rho_a \cdot \frac{R_{\text{hyd}}}{\alpha_{\text{liq}}} \quad [5.26]$$

Applying these two relations and following the steps outlined above for the standard water leads to Eq. 5.27, the tendency of evaporation for the heavy isotopes.

$$\frac{d^h m}{dt} = 4\pi a^h f \frac{\frac{R_{\text{atm}}}{R_{\text{hyd}}} \alpha_{\text{liq}} {}^l \mathcal{S}_l - 1}{\frac{\alpha_{\text{liq}}}{\beta R_{\text{hyd}}} \frac{\mathcal{R}_v T_\infty}{{}^l D e_{l,\infty}^*} + \frac{L_e^2}{k_a \mathcal{R}_v T_\infty^2}} \quad [5.27]$$

Evaporation of heavy isotopes following Blossey et al. (2010) The parameterization by Blossey et al. (2010) has also been implemented. It uses a slightly different approach to approximate Eq. 5.22 by taking $T_a T_\infty \approx T_\infty^2$ and using a Taylor expansion in $T_a - T_\infty$. Therefore, γ does not have to be introduced. The standard tendency then takes the same form as above (Eq. 5.24), but that for the heavy isotopes is slightly different, as given in Eq. 5.28, where b_l is given in Eq. 5.29. Equation 5.28 is another parameterization to describe the evaporation of heavy isotopes from hydrometeors.

$$\frac{d^h m}{dt} = 4\pi a^h f \frac{\left((1+b_l) \frac{R_{\text{atm}}}{R_{\text{hyd}}} \alpha_{\text{liq}} - b_l\right) {}^l \mathcal{S}_l - 1}{\frac{\alpha_{\text{liq}}}{\beta R_{\text{hyd}}} \left(\frac{\mathcal{R}_v T_\infty}{{}^l D e_{l,\infty}^*} + \frac{L_e^2}{k_a \mathcal{R}_v T_\infty^2}\right)} \quad [5.28]$$

$$b_l = \frac{{}^l D L_e^2 \rho_{l,\infty}^*}{k_a \mathcal{R}_v T_\infty^2} \quad [5.29]$$

5.3.3.2. Formation of ice

Ice is formed from the vapor phase during homogeneous and heterogeneous nucleation and during vapor deposition on existing frozen particles, i.e. ice, snow, graupel or hail. In contrast to liquid particles, the isotopic content of the frozen particles is not homogeneous within one particle, but layered (Jouzel et al., 1975). The vapor that is depositing on a particle will interact only with the outermost layer. The layering

is unknown to the model, but the isotope ratio of the outermost layer is assumed to be identical to the isotope ratio in the depositing flux, which is in accordance with Blossey et al. (2010).

For standard water, we again follow Pruppacher and Klett (2012) for a derivation similar to that for evaporation in Sec. 5.3.3.1. For a correct parameterization of fractionation, it is important to formulate the following not in terms of $d^l m/dt$ but of $d^l \rho_v/dt$, the mass density of vapor. For standard water, the two are interchangeable of course, except for their sign ($d\rho_v = -dm$). Also different to evaporation, the equilibrium fractionation factor α_{ice} and the subsaturation ratio ${}^l S_i$ have to be calculated relative to ice. The latent heat of fusion L_f has to be considered to give $L_s = L_e + L_f$ for the total latent heat release.

In analogy to Sec. 5.3.3.1, starting point is Eq. 5.30 which is subsequently developed into Eq. 5.31. C is the shape factor and the index i denotes that these values have to be taken for the ice particle, the surface of which is indexed by c .

$$\frac{d^l \rho_v}{dt} = 4\pi C^l D^l f \left({}^l \rho_c - {}^l \rho_\infty \right) \quad [5.30]$$

$$\frac{d^l \rho_v}{dt} = - \frac{4\pi C^l f \left({}^l S_i - 1 \right)}{\frac{\mathcal{R}_v T_\infty}{{}^l D e_{i,\infty}^*} + \frac{L_s^2}{k_a \mathcal{R}_v T_\infty^2}} \quad [5.31]$$

Again, the densities ρ have to be replaced by the corresponding values of the heavy isotopes. For ${}^h \rho_\infty$, Eq. 5.32 is used. Eq. 5.33 gives ${}^h \rho_c = {}^h \rho_{i,c}^*(T_c)$. Here, the fact that the deposition flux interacts only with the outermost layer has been considered by using the ratio in the deposition flux instead of the isotope ratio R_{hyd} as was done in Eq. 5.26. In addition, the fractionation factor α_{ice} is applied directly (and not its inverse value), since we are now considering the ratio in the vapor.

$${}^h \rho_{v,\infty} = {}^l \rho_{i,\infty}^* \cdot {}^l S_i R_{\text{atm}} \quad [5.32]$$

$${}^h \rho_{v,c} = {}^l \rho_c \cdot \frac{d^h \rho_v}{d^l \rho_v} \cdot \alpha_{\text{ice}} \quad [5.33]$$

For ${}^l \rho_c$, an approach similar to Eq. 5.21 can be made by replacing L_e by L_s and calculating saturation relative to ice. Analogous to evaporation, two different approximations can be made for the exponential function. Again, we follow Pruppacher and Klett (2012), while the tendency given by Blossey et al. (2010) is repeated below. By inserting Eq. 5.32, 5.33 and the analogue to Eq. 5.21 for saturation pressure into Eq. 5.30, an equation for $d^h \rho_v/dt$ for the heavy isotopes can be written down, see Eq. 5.34. C is replaced by using Eq. 5.31. The equation can then be analytically solved for $d^h \rho_v/dt$. Equation 5.35 then gives the tendency for deposition of the heavy isotopes. This is the procedure followed by Blossey et al. (2010), but they derive dm/dt and arrive at a different fractionation factor α_k .

$$\frac{d^h \rho_v}{dt} = -4\pi C^l f^l D_v \rho_{i,\infty}^* \left[R_{\text{atm}} {}^l S_i - \frac{d^h \rho_v}{d^l \rho_v} \frac{1}{\alpha_{\text{ice}}} \left(1 + \frac{L_s^2}{4\pi C k_a \mathcal{R}_v T_\infty^2} \frac{d^l \rho_v}{dt} \right) \right] \quad [5.34]$$

$$\frac{d^h \rho_v}{dt} = \alpha_k R_{\text{atm}} \frac{d^l \rho_v}{dt} \quad [5.35]$$

Depending on the approximation of the exponential term in Eq. 5.33, the definition of α_k differs slightly. If the approximation of Pruppacher and Klett (2012) is made, the result is Eq. 5.36, while Blossey et al. (2010) give Eq. 5.37 after a Taylor expansion in ΔT . Both use b_i of Eq. 5.38. ζ is the ratio of diffusion constants defined as ${}^lD_v/{}^hD_v$ (the inverse of β for evaporation used above). Equation 5.37 is also used in COSMOiso (Pfahl et al., 2012). Both parameterizations have been implemented in ICON-ART-Iso. The ventilation factor hf can be set to increase or decrease the influence of ζ . It is set to 1 for ice, graupel and hail and to 0.995 for snow in accordance with Pfahl et al. (2012).

$$\alpha_k = \frac{(1 + b_i) {}^lS_i}{({}^hf\zeta + b_i) ({}^lS_i - 1) + \alpha_{\text{ice}} (1 + b_i)} \quad [5.36]$$

$$\alpha_k = \frac{(1 + b_i) {}^lS_i}{{}^hf\zeta ({}^lS_i - 1) + \alpha_{\text{ice}} (1 + b_i) {}^lS_i} \quad [5.37]$$

$$b_i = \frac{{}^lD_v L_s \rho_{i,\infty}^*}{k_a \mathcal{R}_v T_\infty^2} \quad [5.38]$$

5.3.4. Saturation adjustment

Saturation adjustment describes the interaction of cloud water and vapor at the model scale. Temperature, cloud water content and water vapor are adjusted according to saturation vapor pressure. In ICON, this is done iteratively using a Newton iteration. For isotopes and the diagnostic water, however, this iteration does not have to be redone. Just like equilibration between vapor and cloud water happens fast relative to the model time step, the same can be said about the equilibration of the isotope fluxes. This is also the approach followed by Pfahl et al. (2012) and Blossey et al. (2010).

Adjusting vapor and cloud implies that the vapor is at saturation within a cloud. This can be described by setting ${}^lS_l = 1$. In comparing Eqs. 5.24 and 5.27, this approach can also be adopted for the heavy isotopes by setting the numerator of Eq. 5.27 to zero. R_{hyd} then stands for the isotope ratio in cloud water. The result is a diagnostic relationship for R_{hyd} displayed in Eq. 5.39 from which the mass mixing ratio can be inferred.

$${}^hq_c = {}^lq_c \alpha_{\text{liq}} R_{\text{atm}} \quad [5.39]$$

There is a logical problem if this equation is applied directly. $R_{\text{atm}} = {}^hq_v/{}^lq_v$ depends on hq_v which is determined by the same process. The solution to this problem is to reformulate the equation using the sum of ${}^hq_v + {}^hq_c$, which is equal before and after saturation adjustment. If hq_v is added to Eq. 5.39, the result is Eq. 5.40, in which ${}^hq_v + {}^hq_c$ appears on the right hand side. This sum does not change because of saturation adjustment, so the implementation is no longer a problem. This procedure is also followed by Blossey et al. (2010) and (Pfahl et al., 2012).

$${}^hq_c = \frac{{}^hq_v + {}^hq_c}{1 + \frac{1}{\alpha_{\text{liq}}} \frac{{}^lq_v}{{}^lq_c}} \quad [5.40]$$

For an unknown reason, the code of COSMOiso uses α_{liq} instead of $1/\alpha_{\text{liq}}$ in the denominator. This version of Eq. 5.40 has also been implemented in ICON-ART-Iso.

5.3.5. Convection

The convection parameterization describes those thermodynamic processes that are too small of scale to be calculated on the model grid directly. Nevertheless, the effects these processes have on the state of the atmosphere cannot be neglected. Prominent examples of such processes are heavily precipitating thunderstorms, but non-precipitating convection makes up a non-negligible part of cloud cover that influences the radiation balance, for example. In ICON, the Tiedtke-Bechtold scheme has been implemented as only choice in the numerical weather prediction physics package (Tiedtke (1989), Bechtold et al. (2014)). As convective processes are an important branch of the atmospheric water cycle, this parameterization has also been adapted for ICON-ART-Iso. The Tiedtke-Bechtold scheme will simply be referred to as convection in the following paragraphs.

Convection calculates tendencies of vapor, cloud water and ice in default setup, tendencies for rain and snow can also be simulated. It also calculates precipitation rates for rain and snow. Convection is an implicit scheme and therefore differs from microphysics and saturation adjustment, which work on the model grid directly. Convection does not run as a box model but uses the whole atmospheric column and also depends on turbulent, advective and surface fluxes of vapor. The latent heat released during the condensation processes are the main drivers of the dynamics of convection. So water is a driver of convection as well as strongly influenced by it. The diagnostic water species of ICON-ART-Iso on the other hand are only affected by the processes that change the distribution but do not themselves influence dynamics.

Fractionation happens during three subprocesses of convection: Saturation adjustment at initialization and during ascents, adjustment of fluxes in saturated downdrafts and during evaporation of rain below cloud base. The parameterizations that have been implemented are explained in the following paragraphs. These are the same parameterizations that are also part of COSMOiso (Pfahl et al., 2012).

One main difference to the grid scale parameterizations described in Sec. 5.3.3 and 5.3.4 is that those implemented in convection consider mixed phase clouds. Ice and liquid cloud water content is not treated separately by convection but only total condensed water is known to convection (the different hydrometeors are only calculated at the very end). The separation into liquid and frozen water is achieved by parameterizing the liquid water fraction as a function of temperature using a parameterization from ICON. The fraction of liquid water will be denoted by ω in the following and $(1 - \omega)$ will be the ice fraction accordingly.

Section 5.3.5.1 describes convective saturation adjustment. The evaporation of hydrometeors is treated differently depending on whether it happens below cloud base (Sec. 5.3.5.3) or in saturated downdrafts (Sec. 5.3.5.2).

5.3.5.1. Convective saturation adjustment

Saturation adjustment happens during initialization to determine cloud base values and in the calculation of cloud ascent. In liquid clouds, the parameterization following Blossey et al. (2010) is again used, see Sec. 5.3.4. For completeness, the final equation is repeated here (Eq. 5.41).

$$h_{q_c} = \frac{h_{q_v} + h_{q_c}}{1 + \frac{1}{\alpha_{liq}} \frac{l_{q_v}}{l_{q_c}}} \quad [5.41]$$

The parameterization applied for grid scale adjustment assumes a fixed mass of $h_{q_v} + h_{q_c}$. This is not valid in mixed-phase or ice clouds. The parameterization therefore has to be expanded in order to be used in convection if the liquid water fraction $\omega < 1$. In case of mixed clouds, the isotope ratio in the vapor is determined separately for ice and liquid. The two are then recombined according to the fraction of liquid water, following Eq. 5.42, with $R_{atm}^{by\ liq}$ and $R_{atm}^{by\ ice}$ subsequently given in Eqs. 5.43 and 5.44. They have been implemented as in COSMOiso (Pfahl et al., 2012), with more details given by Jouzel and Merlivat (1984) and Bony et al. (2008).

$$R_{atm} = (1 - \omega) \cdot R_{atm}^{by\ ice} + \omega \cdot R_{atm}^{by\ liq} \quad [5.42]$$

$$R_{atm}^{by\ liq} = \frac{\alpha_{liq} \cdot l_{q_v}}{l_{q_v}^{before} + l_{q_v} \cdot (\alpha_{liq} - 1)} \quad [5.43]$$

$$R_{atm}^{by\ ice} = \left(\frac{l_{q_v}}{l_{q_v}^{before}} \right)^{\alpha_{eff}} \quad [5.44]$$

The factor α_{eff} which appears in Eq. 5.44 is determined by Eq. 5.45, where $\beta = hD/lD$ is set again. The supersaturation with respect to ice, ξ_{ice} , is calculated from Eq. 5.46, where $T_0 = 273.15$ K is used. The tuning parameter λ is set to 0.004 in standard setup, following Pfahl et al. (2012) and Risi et al. (2010).

$$\alpha_{eff} = \frac{\xi_{ice} \beta}{\xi_{ice} - 1 + \alpha_{ice} \beta} \quad [5.45]$$

$$\xi_{ice} = 1 - \lambda(T - T_0) \quad [5.46]$$

5.3.5.2. Evaporation in saturated downdrafts

Convective downdrafts are assumed to remain saturated by continuously evaporating precipitation. This greatly simplifies the description of fractionation. There is no condensation or formation of hydrometeors, so a steady state as in saturation adjustment would not be the correct assumption here. Instead, the ice fraction is assumed to sublimate without fractionation while equilibrium fractionation is applied for the liquid fraction. This is summarized in Eq. 5.47, where R_{hyd} stands for the isotope ratio in the evaporating hydrometeor. R_{adj} is the isotope ratio in the adjusted precipitation content and used to calculate the isotope rain content.

$$R_{adj} = (1 - \omega) \cdot R_{hyd} + \omega \cdot \frac{1}{\alpha_{liq}} R_{atm} \quad [5.47]$$

5.3.5.3. Evaporation below cloud base

Evaporation of precipitation leads to a drop in the temperature and is therefore an important process in convection, which draws its energy from vertical temperature gradients. This section describes the fractionation during evaporation of precipitation below cloud base, i.e. in an unsaturated environment. For this purpose, the parameterization by Stewart (1975) is again applied to the liquid fraction. In a different form, it is also available as one choice for parameterizing evaporation of hydrometeors in microphysics, see Eq. 5.17. In contrast to microphysics, convection does not calculate a tendency to which a factor could be applied to arrive at the tendency of the heavy isotopes. Instead, Eq. 5.17 must be integrated to arrive at the isotope ratio of the hydrometeors after evaporation, i.e. ${}^h m / {}^l m$ instead of $d^h m / d^l m$.

In following Stewart (1975), the ratio in the liquid part of the general hydrometeor after evaporation $R_{\text{adj}}^{\text{liq}}$ can be given with Eq. 5.48. Here, f is the ratio of the adjusted over the old hydrometeor mixing ratio. $R_{\text{hyd}}^{\text{before}}$ is the isotope ratio in the hydrometeor before adjustment and rH is the relative humidity calculated as the vapor pressure over saturation vapor pressure.

$$R_{\text{adj}}^{\text{liq}} = \gamma R_{\text{atm}} + f^{\beta} (R_{\text{hyd}}^{\text{before}} - \gamma R_{\text{atm}}) \quad [5.48]$$

$$\gamma = \frac{\text{rH}}{\alpha_{\text{liq}} - \mu} \quad [5.49]$$

$$\beta = \frac{\alpha_{\text{liq}} - \mu}{\mu} \quad [5.50]$$

$$\mu = (1 - \text{rH}) \left(\frac{{}^h D}{{}^l D} \right)^{-n} \quad [5.51]$$

Using Eq. 5.48, the isotope ratio in the adjusted hydrometeor can be given with Eq. 5.52. The ice fraction is assumed to sublimate without fractionation, maintaining its isotope ratio.

$$R_{\text{adj}} = (1 - \omega) R_{\text{hyd}}^{\text{before}} + \omega R_{\text{adj}}^{\text{liq}} \quad [5.52]$$

Following Pfahl et al. (2012) (COSMOiso code), an additional equilibration has been implemented to determine the final isotope ratio of the hydrometeor, as given in Eq. 5.53. The parameter ξ_{add} is a tuning parameter that is set to 0.5 in standard setup.

$$R_{\text{adj}}^{\text{final}} = R_{\text{adj}} + \xi_{\text{add}} \cdot \omega \left(\frac{R_{\text{atm}}}{\alpha_{\text{liq}}} - R_{\text{adj}} \right) \quad [5.53]$$

5.4. Technical details on ICON-ART-Iso and the model runs

5.4.1. Summary of technical aspects of ICON-ART-Iso

This section is a summary of the full technical description given in App. B. Technically, ICON-ART-Iso is part of the ICON-ART project. ICON-ART is an extension to ICON model (Zängl et al., 2015) and simulates trace gas and aerosol substances, see Sec. 2.3.3 for more details and Rieger et al. (2015). As ICON-ART-Iso is a regular branch of development of ICON and ICON-ART and under version control by git, it is possible to stay up to date with new developments of ICON and ICON-ART.

ICON-ART provides a flexible way of adding tracers to the model by an XML table that is read during run time. ICON-ART-Iso makes use of this flexibility to set up and simulate groups of tracers called isotopes. Each isotope is defined in the XML table and all settings regarding the processes and fractionation are made in this table. As outlined in Sec. 5.3, there are four main processes that consider fractionation: surface evaporation, saturation adjustment, microphysics and convection. Some of these have subprocesses which are controlled separately and they all contain tuning parameters. In addition, there are some general parameters that can be set. So the number of choices to make for each isotope is large. Appendix B.1 lists all the options for these processes, including tuning parameters. Appendix B.2 then gives technical details of the implementation of the different parameterizations within the model code of ICON-ART. A summary of the parameterizations is given in Table 5.3.

5.4.2. Model setup for evaluation and case studies

All runs discussed in the following sections were performed on an R2B06 grid, which corresponds to approximately 40 km horizontal resolution (Zängl et al., 2015), and with a simulation timestep of 360 s. The simulations were initialized with either ERA-Interim (Dee et al., 2011) or ECMWF analysis data. The initialization date will be given in each section. The output was saved on a $1^\circ \times 1^\circ$ regular grid (approx. 111 km resolution at the equator).

Sea surface temperatures and sea ice cover were kept constant at their value of initialization during all model runs. This is the standard procedure for numerical weather prediction. It is not suitable to simulate climatological or seasonal variations as the ocean is an important driver of some of these variations. Keeping these two parameters constant affects all longer simulations, especially those that try to simulate a yearly cycle. Simulations that are affected by this error in the setup are used in Sec. 5.5.3 and 5.7. Notice is again made there to this flaw.

The standard setup for fractionating HDO or H_2^{18}O is given in the summary table of the physics section, Table 5.3, where it is marked by *. This is the same set of parameterizations that is used in COSMOiso and it is used in the simulations if not specified otherwise. In all simulations, equilibrium fractionation factors were set to use the parameterization by Majoube (1971) and Merlivat and Nief (1967) over liquid water and ice, respectively. The ratio of diffusion constants was set to the values given by Merlivat (1978).

abbreviation	initialization	land evaporation	ocean evaporation	fractionation
0.0001	$R_{\text{init}} = 0.0001$	on	on	off
init	$R_{\text{init}} = 1$	off	off	off
ocn	$R_{\text{init}} = 0$	off	on	off
lnd	$R_{\text{init}} = 0$	on	off	off
ICON	the standard ICON water			

 Tab. 5.6.: Summary of settings for diagnostic H₂O isotopes, which are discussed and used in the following sections.

In addition, the flexibility to turn off fractionation and simulate H₂O opens new perspectives for applications. By setting $R_{\text{init}} = 1$ but turning all evaporation off, the isotope will precipitate out of the model domain as time progresses. This way, the influence of the initialization can be determined (q^{init}). On the other hand, isotopes with $R_{\text{init}} = 0$ and evaporation will progressively accumulate in the model atmosphere and replace q^{init} . This will be demonstrated with the isotopes q^{ocn} and q^{lnd} , which evaporate from ocean and land points only, respectively. This way, q^{init} , q^{ocn} and q^{lnd} form a ternary solution and their mass adds up to the same value as q^{ICON} , the standard water of ICON.

Overall errors - coding or numerical - are explored with an isotope indexed by 0.0001. All processes are turned on, but fractionation is turned off. The isotope is initialized with a ratio of $R_{\text{init}} = 0.0001$. This ratio should always be conserved, so that $R_{\text{init}} \cdot q^{\text{ICON}} = q^{0.0001}$ should always be true for all tracers that make up the isotope.

The settings of these diagnostic H₂O isotopes are summarized in Table 5.6. The indices will be applied to mass mixing ratio of vapor q_v , total precipitation \mathcal{P} , the isotope itself q and the ratio in vapor with respect to q_v^{ICON} , $R^X = q_v^X / q_v^{\text{ICON}}$.

5.5. Simulation of diagnostic H₂O

The capability of ICON-ART-Iso to simulate instances of diagnostic H₂O is an important prerequisite for the simulation of isotopes. Only if the standard water is described correctly can changes in the isotope ratio be attributed to fractionation. If the model does not simulate a diagnostically doubled H₂O correctly, the fractionation of heavier isotopes will be masked by these coding or numerical errors. The definitions of the diagnostic instances of water discussed in the following sections are summarized in Table 5.6.

The three following sections move from technical aspects to a first application of diagnostic H₂O. Section 5.5.1 investigates numerical errors still present in the model that lead to small differences in $q^{0.0001}$ compared to q^{ICON} . But the capability to simulate q^{init} , q^{ocn} and q^{land} are also introduced. Section 5.5.2 takes a closer look at the sink of these three isotopes: precipitation. Section 5.5.3 makes use of two longer runs for a first investigation of the relative amounts of ocean and land evaporated water in precipitation.

5.5.1. Water vapor diagnostics

This section discusses results for q_v of the isotopes presented in Table 5.6. The results are exemplarily shown as horizontal cross sections after 10 days of simulation in Fig. 5.6 and Fig. 5.7. The cross sections are taken from model level 86. Due to the terrain following coordinate system, the height of this level varies, the mean pressure for the specific time step shown in the two figures is approximately 940hPa, which is a few hundred meters above sea level for grid points over the ocean.

Figure 5.6 shows cross sections for q_v^{ICON} , $10000 \cdot q_v^{0.0001}$ and the difference $\Delta = q_v^{0.0001} - 0.0001 \cdot q_v^{\text{ICON}}$. As explained above, it is an important prerequisite that Δ is close to 0. Fig. 5.6 documents that ICON-ART-Iso is very well capable of simulating a diagnostic water cycle. All processes that alter the field of q_v^{ICON} apparently also alter the field of $q_v^{0.0001}$. After 10 days of simulation, the difference is not larger than $\Delta = 10^{-7}$ g/kg, which is 9 orders of magnitude smaller than the actual fields. The error does not grow as the simulation progresses, but the shape changes as the two variables are advected independently.

Not shown is the result of the testing setup of ICON-ART-Iso, see App. B.2.2. In this setup, the values of each water tracer of ICON is passed to the fields of the testing isotopes right before each of the main processes (advection, turbulence, saturation adjustment, microphysics and convection). After each process, the difference of the ICON field and the isotope is saved. This difference is smaller than 10^{-16} for all processes and times, independent of the value chosen for R_{init} . This also shows that ICON-ART-Iso is capable of simulating all the processes of the hydrological cycle in the model and allows to move on to other, less technical results.

Fig. 5.7 shows fields of q_v for q_v^{init} , q_v^{ocn} and q_v^{land} after 10 days of simulation. This demonstrates the basic functionality of ICON-ART-Iso to differentiate source regions and determine the influence of the initialization state. After 10 days, q_v^{init} still makes up about half the water that is present in the

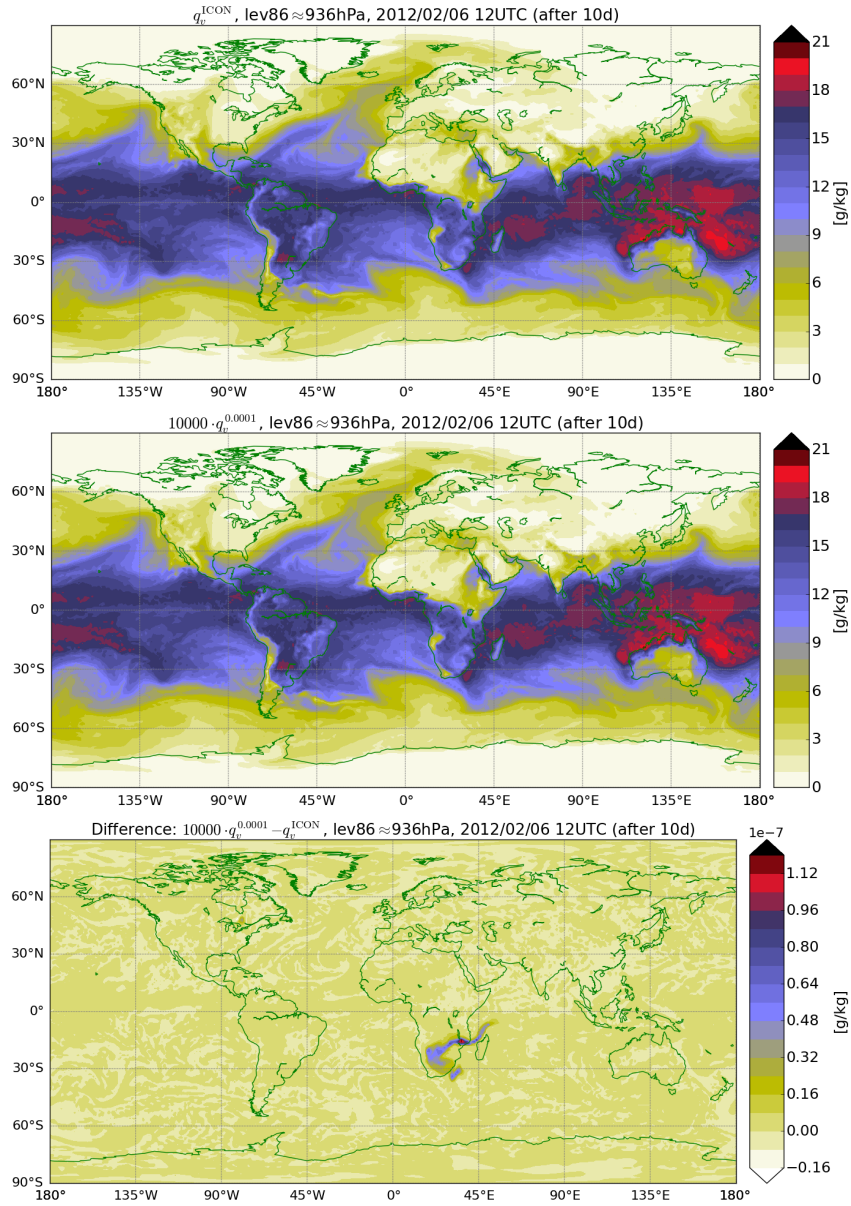


Fig. 5.6.: q_v^{ICON} (top) and $10000 \cdot q_v^{0.0001}$ (middle) and their difference $q_v^{0.0001} - 0.0001 \cdot q_v^{ICON}$ (bottom), all on level 86 (\approx 940 hPa) after 10 days of simulation. $q_v^{0.0001}$ is a diagnostic isotope with no fractionation initialized with $R_{init} = 0.0001$.

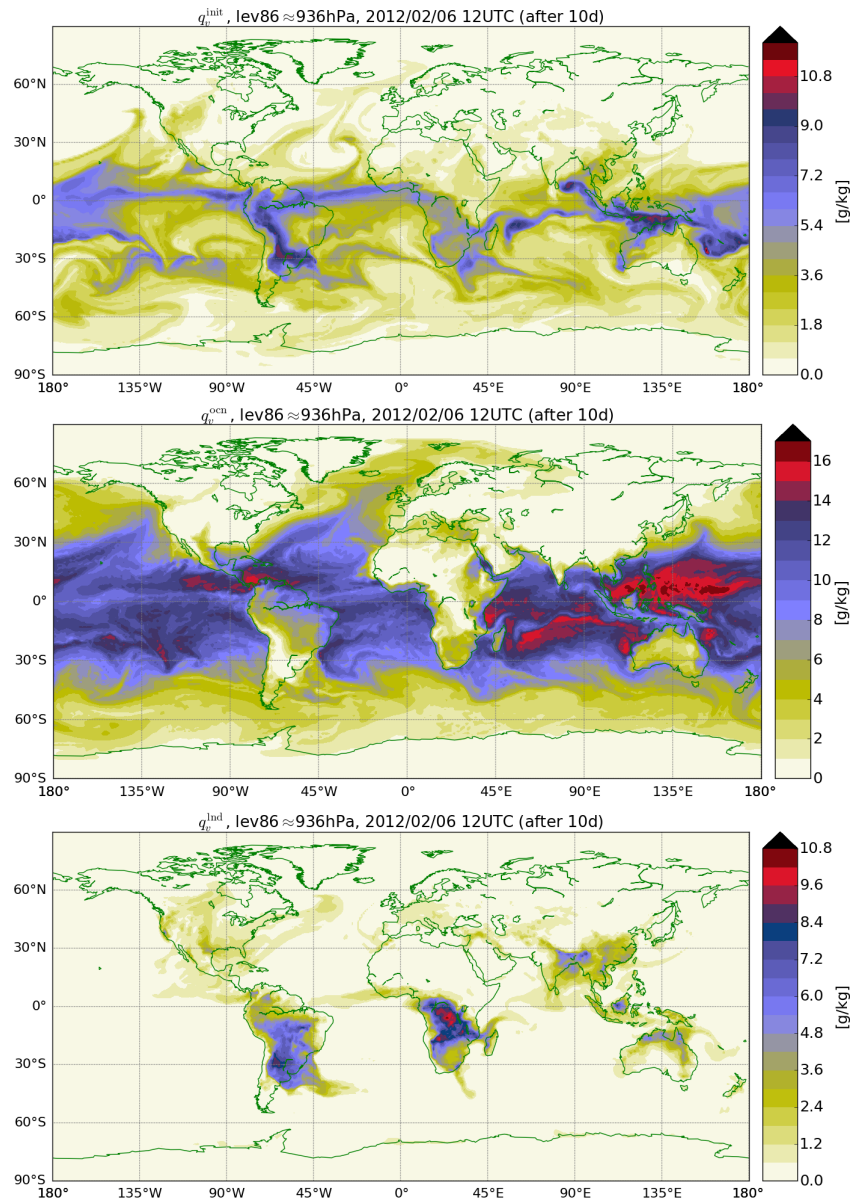


Fig. 5.7.: Three different instances of q_v on level 86 (\approx 940hPa) after 10 days of simulation. From top to bottom: q_v^{init} , initialized with $R_{\text{init}} = 1.0$ and no evaporation (top), q_v^{ocn} , initialized with $R_{\text{init}} = 0.0$ and evaporation only from the ocean surface (middle) and q_v^{lnd} , initialized with $R_{\text{init}} = 0.0$ and evaporation only from land surfaces (bottom). q_v^{init} , q_v^{ocn} , and q_v^{lnd} are diagnostic isotypes with no fractionation.

model troposphere. The overall structure is similar to that of q_v^{ICON} in Fig.5.6 with maximum values in the tropics. q_v^{ocn} and q_v^{land} make up the other half of the vapor. These two fields show complementary structures: maximum values of q_v^{land} are found over tropical land areas in Africa and Southern America. This vapor is not advected far out onto the ocean. The high values of q_v^{land} are complemented by minima of q_v^{ocn} .

5.5.2. Precipitation diagnostics

This section takes a look at precipitation diagnostics after 10 days of simulation. The total precipitation \mathcal{P} of the isotypes summarized in Table 5.6 will be analyzed. Total precipitation is the sum of all precipitated water from grid scale and convective processes.

Figure 5.8 documents $\mathcal{P}^{\text{ICON}}$ and the sum of $\mathcal{P}^{\text{init}} + \mathcal{P}^{\text{ocn}} + \mathcal{P}^{\text{land}}$. As q^{init} , q^{ocn} and q^{land} are the ternary solutions components that sum up to q^{ICON} , the precipitation sum should also be equal to the ICON native precipitation. Figure 5.8 shows that this is very nearly the case. The difference is not available as an output field and would therefore contain interpolation artefacts when shown here.

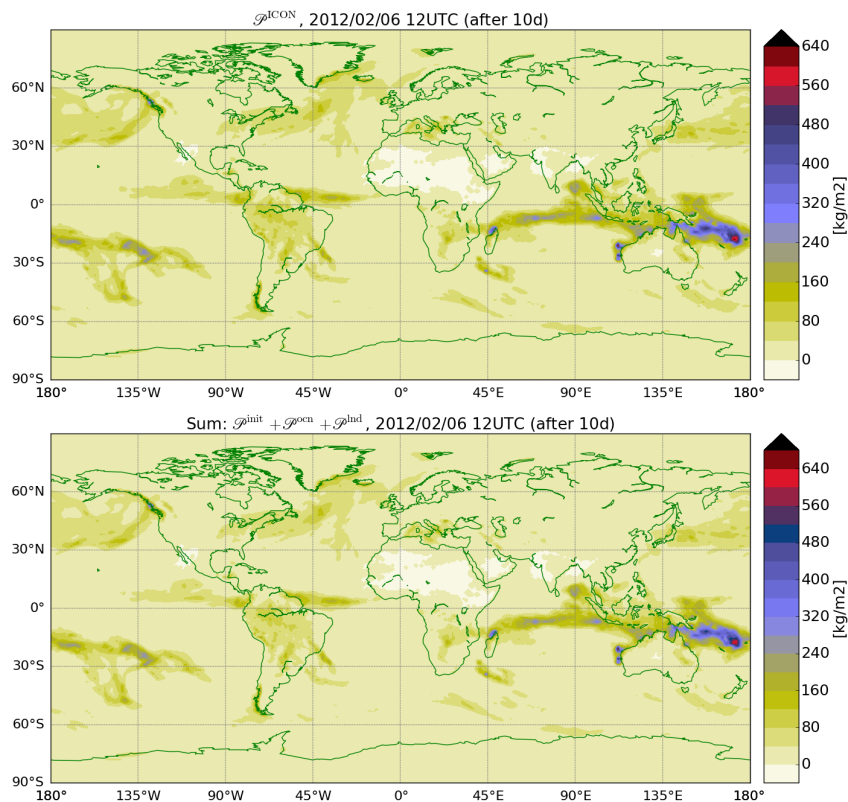


Fig. 5.8.: Total precipitation \mathcal{P} after 10 days of simulation: $\mathcal{P}^{\text{ICON}}$ (top) and the sum $\mathcal{P}^{\text{init}} + \mathcal{P}^{\text{ocn}} + \mathcal{P}^{\text{land}}$ (bottom). The separate fields are displayed in Fig. 5.9.

The possibilities of splitting up q^{ICON} into the three partners q^{init} , q^{ocn} and q^{land} is suitably demonstrated by taking a look at the total precipitation \mathcal{P} of each isotype separately. Figure 5.9 shows \mathcal{P} for each of the isotypes. Initialization water precipitates everywhere where there is precipitation ($\mathcal{P}^{\text{init}}$, top panel). The field resembles that of $\mathcal{P}^{\text{ICON}}$ given in Fig. 5.8. Water that has evaporated from the ocean during the model run also precipitates mostly over the ocean. Only islands and coastal areas are affected by precipitation from ocean evaporate (\mathcal{P}^{ocn} , center panel). The effect is even stronger for land evaporate ($\mathcal{P}^{\text{land}}$, bottom panel). The vapor evaporated from land is advected onto the ocean but quickly precipitates

there. This effect is especially obvious for tropical areas, where the strong evaporation apparent in Fig. 5.7 is complemented by strong precipitation. The next section further explores the distribution of $\mathcal{P}^{\text{init}}$, \mathcal{P}^{ocn} and $\mathcal{P}^{\text{land}}$ in different latitudes over ocean and land points.

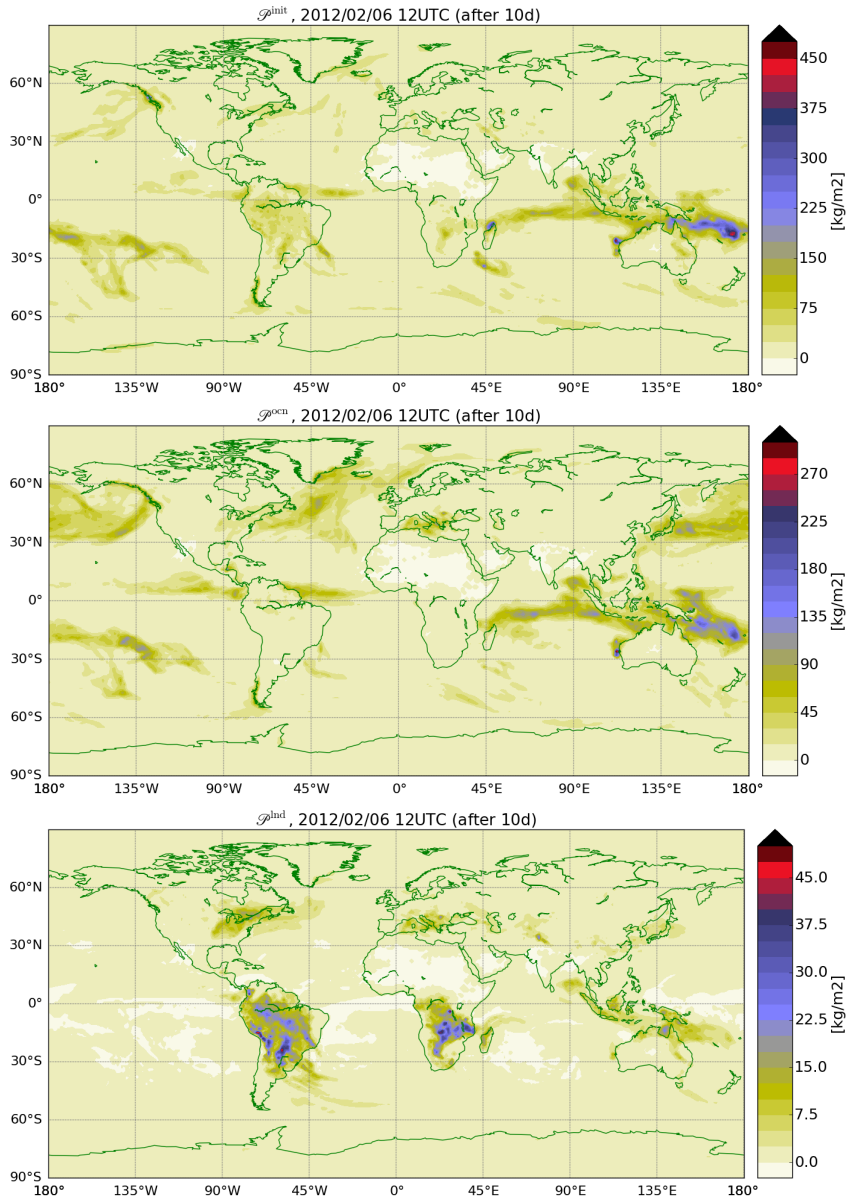


Fig. 5.9.: Total precipitation \mathcal{P} after 10 days of simulation for $\mathcal{P}^{\text{init}}$ (top), \mathcal{P}^{ocn} (middle) and $\mathcal{P}^{\text{land}}$ (bottom). Note the different color scales.

5.5.3. The distribution of precipitation over land and ocean

This section takes a closer look at the different distributions of $\mathcal{P}^{\text{ICON}}$, $\mathcal{P}^{\text{init}}$, \mathcal{P}^{ocn} and \mathcal{P}^{ld} . For this study, use is made of two longer runs that were initialized on November 5, 2013 and May 5, 2014 and simulated four months each (not considering changing sea surface temperatures and sea ice cover, as noted in Sec. 5.4). This section makes use of the data from January and July, respectively, considering values of the total precipitation \mathcal{P} fallen in that month. Figure 5.10 displays the values relative to $\mathcal{P}^{\text{ICON}}$ for all the different latitudes, considering ocean and land points separately. Figure 5.10 also gives the convective sum of each isotype. In addition, the center panels give the fraction of precipitation that has fallen over the ocean relative to the total precipitation and the fractional area of the ocean on each latitudinal band.

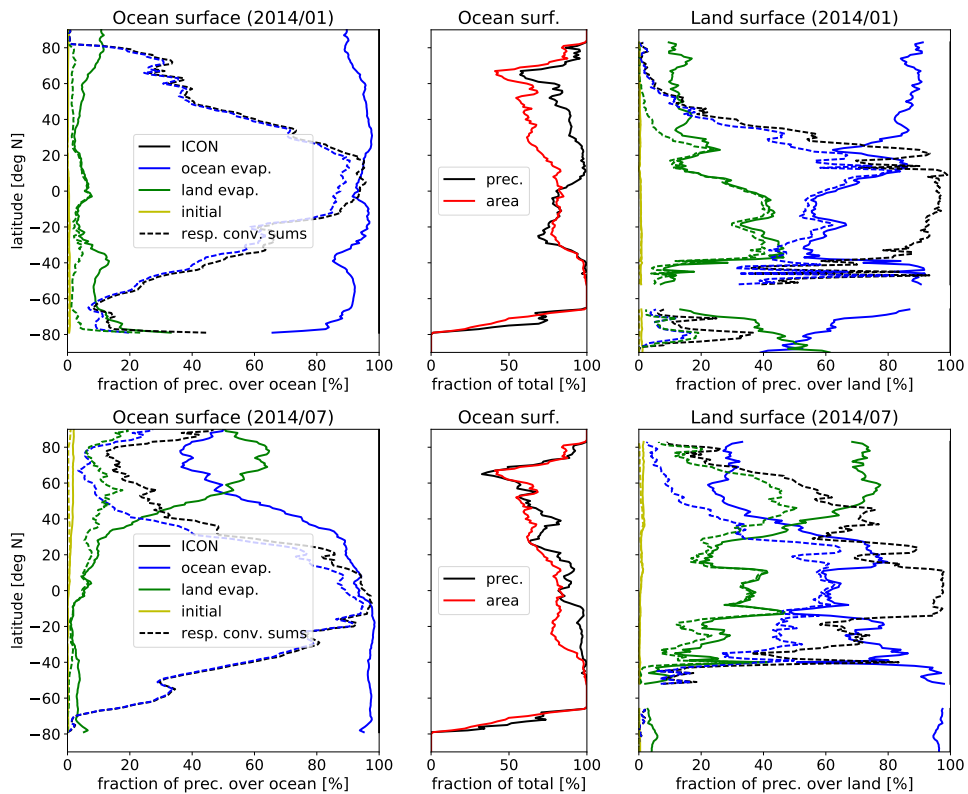


Fig. 5.10.: Latitudinal sums of total precipitation for January (top) and July (bottom), 2014 for q^{ICON} , q^{init} , q^{ocn} and q^{ld} . Left panels show sums over the ocean surface, right panels those over land surface, both as fraction of the total precipitation over these areas in each latitude. Dashed lines indicate the sum of convective precipitation for each source of the vapor. Center panels display the fraction of precipitation fallen over the ocean as fraction of the total precipitation (over land and ocean) and the fraction of the area covered by ocean.

Figure 5.10 shows the model state two months after initialization. At this time, the tropospheric moisture has almost completely been replaced by water that has evaporated during the model run. This

is demonstrated by the very low values of $\mathcal{P}^{\text{init}}$ in all four panels. Technically, this means that the ternary solution of q^{init} , q^{ocn} and q^{land} that makes up q^{ICON} is practically reduced to a binary solution of only q^{ocn} and q^{land} . q^{init} does not have to be considered in the troposphere two months after initialization.

The area covered by ocean is not equally distributed over different latitudes (center panels of Fig. 5.10). Despite the different characteristics of the different seasons which will be discussed in the following paragraphs, this distribution in latitude dominates the overall fraction of rain that falls over the ocean. This is why the other panels display values of \mathcal{P} relative to the sum over each compartment, not to the total sum.

During northern hemisphere winter over the ocean (top left panel of Fig. 5.10), the precipitation is strongly dominated by ocean evaporated water. Land evaporated water hardly reaches the ocean. The situation is almost opposite over land (top right): In the northern and southern hemisphere mid latitudes, more than 70% of the precipitated water comes from the ocean. Only the tropics receive up to 40% of precipitation from land evaporated water. Most precipitation in tropical and subtropical latitudes originates from convection (indicated by dashed lines). This process is resolution dependent. If the same simulation had been performed at a higher resolution, more convective processes could have been directly resolved. The amount of precipitation from convection therefore does not point at atmospheric processes but says more about the importance of the convection parameterization in the model.

The situation is markedly different in northern hemisphere summer (bottom row of Fig. 5.10), especially in the northern hemisphere. In summer (bottom right), the northern hemisphere land areas supply themselves a major part of the moisture that then precipitates. The importance of convection is also increased in the northern hemisphere summer. Despite the larger moisture availability over the ocean, the northern hemisphere land areas also supply the larger part of moisture that precipitates over the ocean in July. With this strong effect clearly visualized, a similar tendency is also observable for southern hemisphere summer (top row) for the southern hemisphere on a smaller scale. The influence of land evaporated water for the ocean is stronger in summer while ocean evaporated water supplies almost all moisture in winter. The influence of land areas is weaker over the southern hemisphere due to the different distribution of land masses.

This short study demonstrates the capabilities of ICON-ART-Iso to tackle questions regarding the general water cycle. Note that for final conclusions, the analysis should be redone with simulations that consider changes in sea surface temperatures and sea ice cover. The effects of land and ocean evaporate on the respective other compartment could be expanded by looking at smaller areas, resolving the interaction between land and ocean points on a regional scale. It could also be expanded by a finer resolution of the source areas. E.g., the Mediterranean, Black Sea, Red sea and remaining ocean could be treated separately to study the influence of the different water bodies on the precipitation in the middle east. All this is not possible with ICON but needs the expansion to ICON-ART-Iso.

5.6. Simulation of fractionating isotopes

The main goal of developing ICON-ART-Iso is the simulation of the isotopes of water. This section uses first simulations to examine the models functionality to do so. Comparisons with other isotope enabled models as well as in situ and satellite measurement data follow in Sec. 5.8 and 5.7.

Section 5.6.1 first discusses the initialization of the isotopes, showing how its influence diminishes over time. Section 5.6.2 then takes a look at the different parameterizations that have been implemented into ICON-ART-Iso to describe fractionation at phase changes.

5.6.1. The initialization of the isotopes

Section 5.3.1 describes how the isotopes are initialized relative to the values of the ICON water: Mean δ values at the tropopause level, the lowest model level and the model top are used to determine the initial state of the tracers that make up the isotope. This section shows how this initial state evolves in time.

A model run initialized on January 27, 2010 is examined after five, 20, 60 and 120 days. The result is shown in Fig. 5.11 as vertical cross sections taken along $10^\circ E$ latitude. The left hand column shows fields of a HDO isotope initialized with the mean δD values described in Sec. 5.3.1 while the right hand column shows the same location for a HDO isotope initialized with zero. Both isotopes are set to fractionate with the same set of standard settings summarized in Table 5.3.

Figure 5.11 shows four instantaneous snap shots. Nevertheless, the left hand panels resemble one another. There are patches in the tropopause layer with values for δD reaching -760, surface values retain higher values of about -50. The stratospheric values retain their values of approximately -350 from the initialization. This is a first hint that initialization is a good approximation of the model state.

This hypothesis is underlined by comparing the left to the right hand column of Fig. 5.11. HDO of the right hand side is initialized with zero, so $\delta D = -1000$ at the start of the model simulation. After 5 days, only the lowest model layers and areas of strong upward motion have been reached by this isotope. After 20 days, the troposphere has been filled up and the values are of a magnitude comparable to that of the left column while the differences remain obvious. After 60 days, most of the differences have disappeared and even the lowest values on the left hand side are also found on the right side. This is still true after 120 days, where the whole troposphere has been filled with δ values of HDO even if it initialized with zero.

The difference after 120 days is also displayed in Fig. 5.12. To highlight the area of the differences, the ordinate axis has been set to a log scale. As becomes clear from this figure, the differences in the tropospheric layers are negligible. There remain large differences in the stratosphere. But these are also constant, showing that the δD values of the isotope with a realistic initialization have not changed much in these layers. The tropopause layer is therefore marked by a strong gradient. In the atmosphere, the increase in q_v and δD in the stratosphere is caused by the oxidation of methane (Moyer et al., 1996). This

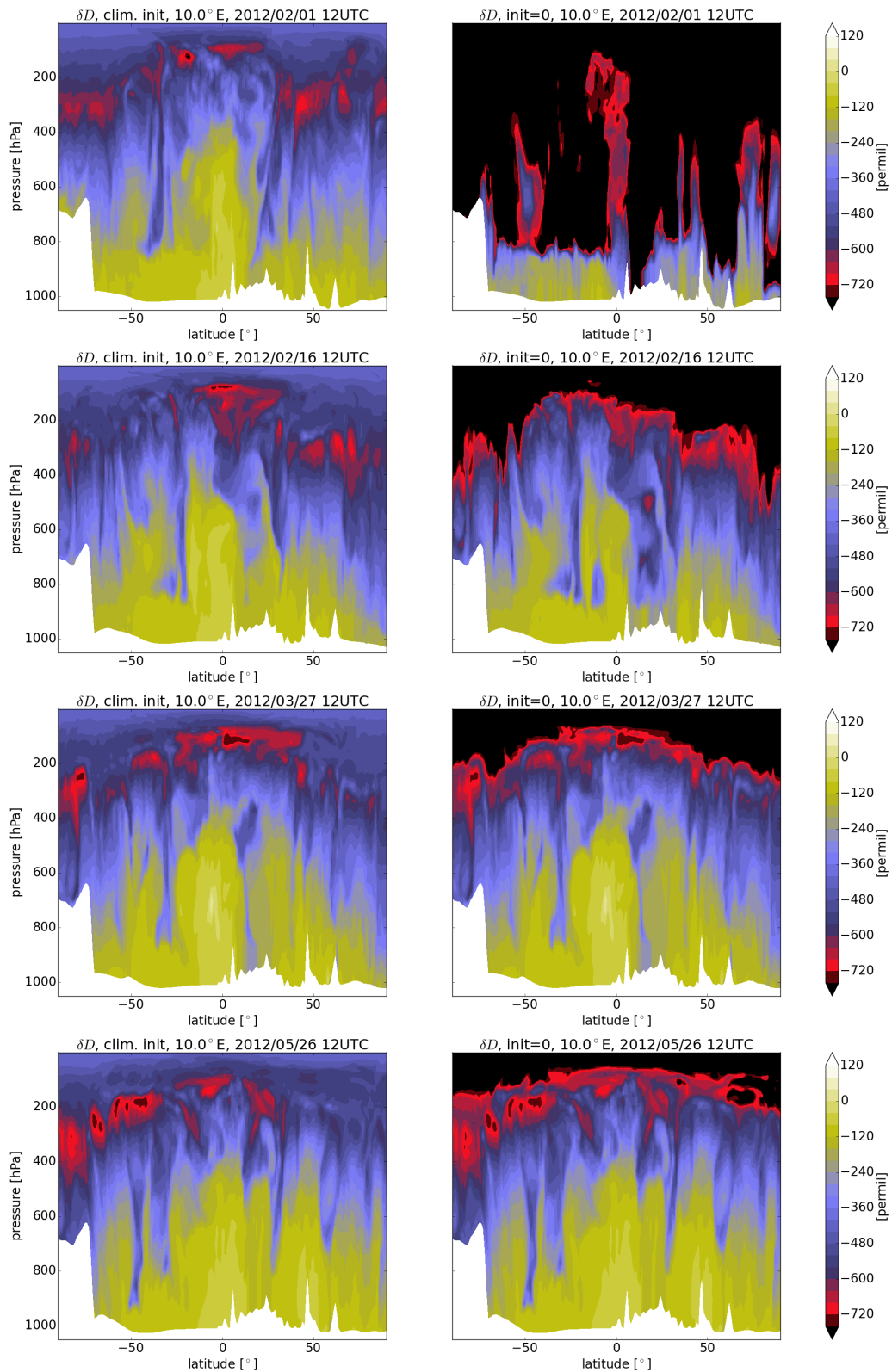


Fig. 5.11.: Vertical cross sections of δD at $10^\circ E$ latitude 5, 20, 60 and 120 days after initialization (from top to bottom) for HDO initialized with mean values (left, see Sec. 5.3.1) and initialized with 0 (right). Note that $q_v^{\text{HDO}} = 0 \text{ kg/kg}$ corresponds to $\delta D = -1000$. The difference after 120 days is displayed in Fig. 5.12.

is included for neither H_2O nor the isotopes. The stratospheric increase can therefore not be reproduced without an additional parameterization.

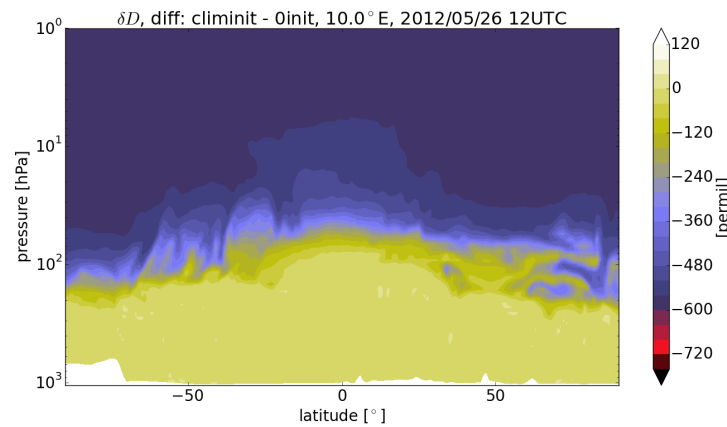


Fig. 5.12.: Vertical cross section at 10°E of the difference of δD values after 120 days of simulation for HDO initialized with climatological values minus HDO initialized with 0. The two fields are displayed separately in the last row in Fig. 5.11.

Figure 5.13 displays the zonal mean values of δD 1 day and 120 days after initialization for the isotope initialized with mean measurements. After 1 day, the field is still very close to the initialization and the field is a smeared out version of what is shown in Fig. 5.4 for the first timestep. After 120 days, the zonal mean has changed. The tropical values have remained virtually unchanged. The southern hemisphere tropopause is more depleted of HDO. This can be attributed to the cold temperatures in winter, which probably lead to the formation of ice clouds, an important process that leads to a strong drop in δD . The influence of the different processes on δD will be discussed in Sec. 5.6.2. Northern hemisphere tropopause values have also adapted, while the minimum is retained. Zonal mean surface values have remained unchanged except over Antarctica, where vapor deposition quickly leads to a strong drop in δD , as will also be discussed in Sec. 5.6.2.

Overall, the results presented in this section show that the initialization of the isotope fields with mean measurement values is reasonable. Tropospheric values are reproduced by the model if the isotopes are initialized with zero. The initialization adapts locally with changes naturally occurring due to the different fractionating parameterizations. In order to reproduce the stratospheric increases in δD , methane oxidation would have to be included. Nevertheless, the model does take some time to adjust the mean values from initialization to an intrinsic model state. The influence of the initialization can be grasped by also using a diagnostic isotope of H_2O , as has been shown in the previous section.

5.6.2. Different parameterizations for fractionation

This section discusses the results of the different parameterizations for fractionation for each fractionating process: grid scale ice formation, grid scale evaporation, saturation adjustment, convective processes

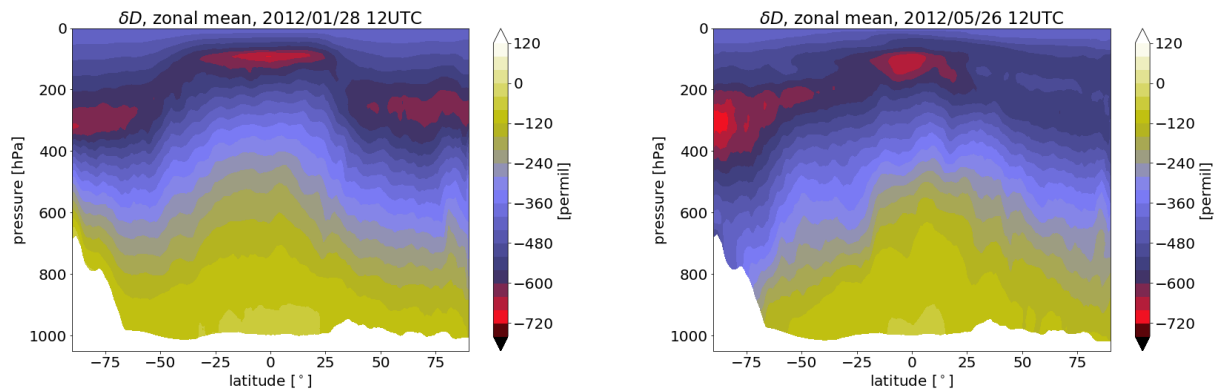


Fig. 5.13.: Zonal mean of δD 1 day (left) and 120 days (right) after initialization for a HDO isotope initialized with mean values of measurements as described in Sec. 5.3.1.

and surface evaporation. The physics of each parameterization have been explained in Sec. 5.3. In addition, to comparing the parameterizations for each process, the importance of the different processes for the depletion of HDO will be discussed. This section makes use of a model run started on January 27, 2012 set up with many different HDO isotopes. For each isotope, only one parameterization was turned on. These are compared with one another and with an isotope using the standard set of parameterizations. Another important reference is the non-fractionating isotope, which is initialized like the others but considers all processes in a non-fractionating setup. The different fields will be compared after 10 days of simulation on level 70, which corresponds to approximately 610 hPa.

Figure 5.14 gives the reference fields. Standard HDO (top panel) shows a strong meridional gradient with maximum values in the tropics. Lowest values in δD reach -760 in northern mid-latitudes. Maximum values in the tropics are greater than -100. This gradient disappears when all fractionation is turned off (bottom panel). Of course the field is not constant, as the vertical gradient has not been completely removed. One of the main processes that leads to the meridional distribution is shown in the middle panel: This is the result for an HDO isotope with standard fractionation, except that the formation of ice has been set to be non-fractionating. This brings the standard HDO isotope much closer to the completely non-fractionating isotope. This is especially true in non-tropical latitudes and therefore shows the importance of this process for the formation of the meridional gradient. The following sections will discuss the influence of each parameterization separately, considering only one process at a time. Of course, the sum of all processes is not equal to the result with all processes turned on, as the impact of fractionation of one process depends on the field that is also determined by the other processes.

5.6.2.1. Fractionation during grid scale ice formation

Fractionation during grid scale ice formation is one of the main processes that lead to the depletion of HDO. This is due to the strong influence of the equilibrium fractionation factor α , which is smaller over ice than over liquid water, see Sec. 5.2.2.1. Grid scale ice formation happens during deposition of

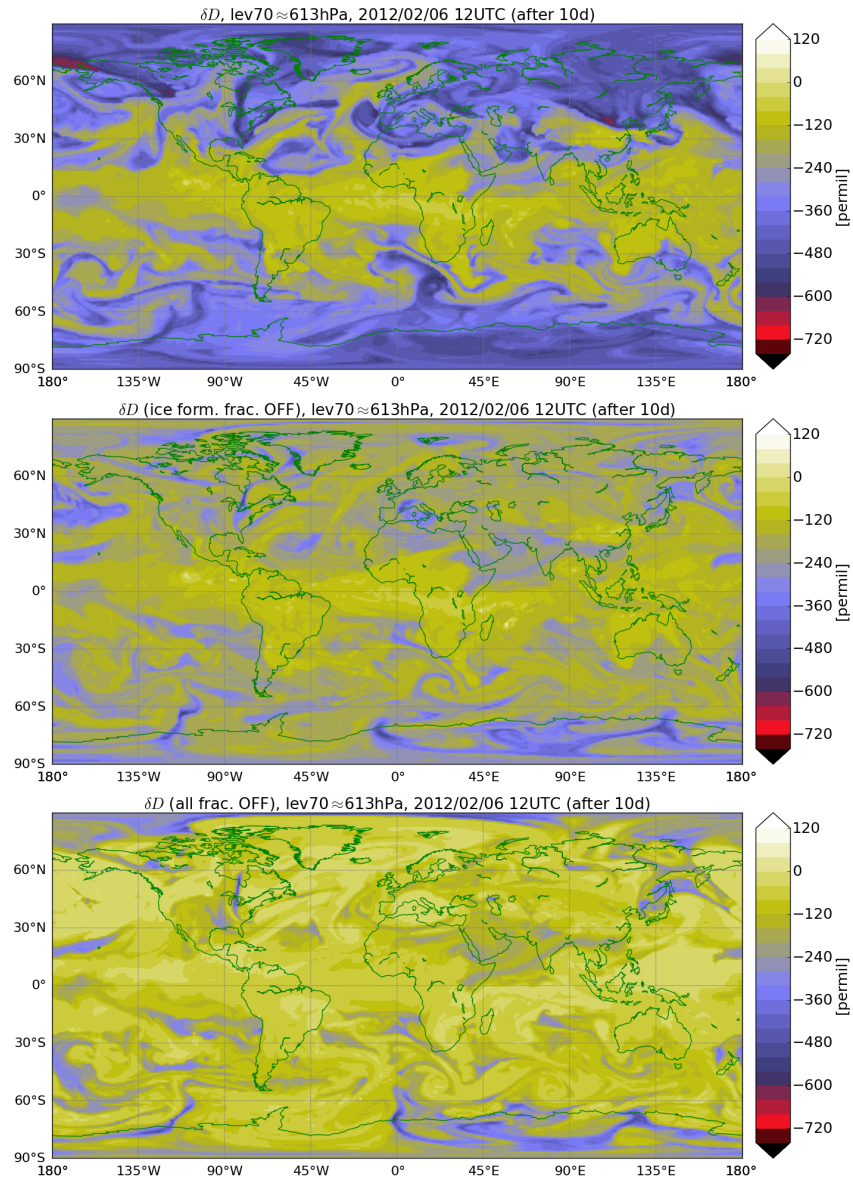


Fig. 5.14.: Horizontal crosssections of δD at level 70 (≈ 610 hPa) with different setups for the simulation of HDO, listed from top to bottom: standard setup (top), fractionation at ice formation turned off (middle) and all fractionation turned off (bottom).

vapor on existing ice particles as well as during formation of new particles. Two parameterizations for fractionation have been implemented in ICON-ART-Iso, which are described in Sec. 5.3.3.2.

Figure 5.15 shows the result for two HDO isotopes which use these two parameterizations. The two fields are practically identical. This is not surprising, as the two parameterizations build on the same basic principles. They differ only in the exact definition of the fractionation factor α_k . Nevertheless, it is important to compare these panels with the standard full fractionating HDO isotope displayed in the top panel of Fig. 5.14. They are not identical - i.e. the other processes do play a role - but Fig. 5.15 again underlines the importance of this process. To a first approximation, this is the main process that leads to the meridional structure of δD .

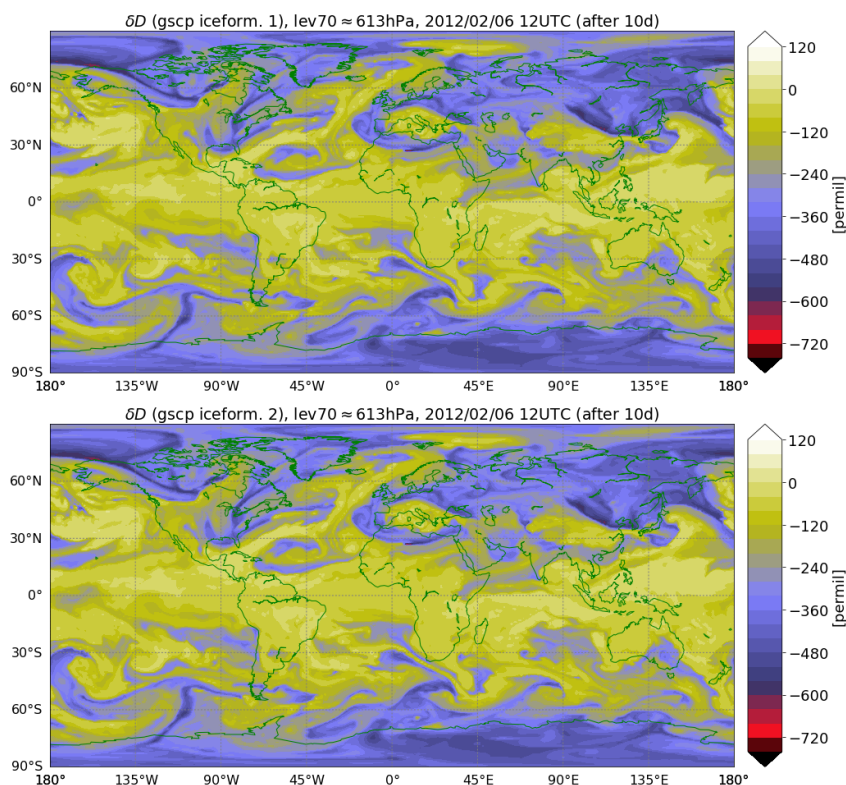


Fig. 5.15.: Horizontal cross sections of δD at level 70 (≈ 610 hPa) with fractionation turned on only for grid scale formation of ice (see Sec. 5.3.3.2), using the parameterization by Blossey et al. (2010) (top) and that following Pruppacher and Klett (2012) (bottom).

5.6.2.2. Fractionation during grid scale evaporation of hydrometeors

Grid scale evaporation of hydrometeors encompasses the evaporation of rain as well as ice phase particles (ice, snow, graupel and hail in case of the 2-moment scheme) that have melted. The parameterization implemented for fractionation differ as one is a bulk scheme (Stewart, 1975), while the others build on a theoretical approach. The implementation of the new parameterization following (Pruppacher and Klett,

2012) proved to be unstable. It is therefore not further considered in this section. Figure 5.16 therefore presents cross sections after 10 days for the scheme by Stewart (1975) in the top panel and by Blossey et al. (2010) in the bottom panel.

The depletion by evaporation by evaporation is weaker than by ice formation, which is mainly due to the higher equilibrium fractionation factor (see Sec. 5.2.2.1). The parameterization by Stewart (1975) in fact has little effect on the overall result, which becomes clear by comparing with the non-fractionating isotope in the lower panel of Fig. 5.14. The parameterization by Blossey et al. (2010) is stronger, especially in the tropics and in the southern hemisphere (compare values west and north of Australia). The effect of the parameterization by Stewart (1975) can be tuned by setting the exponent n that modifies the ratio of the diffusion constants. This can be done via the XML file.

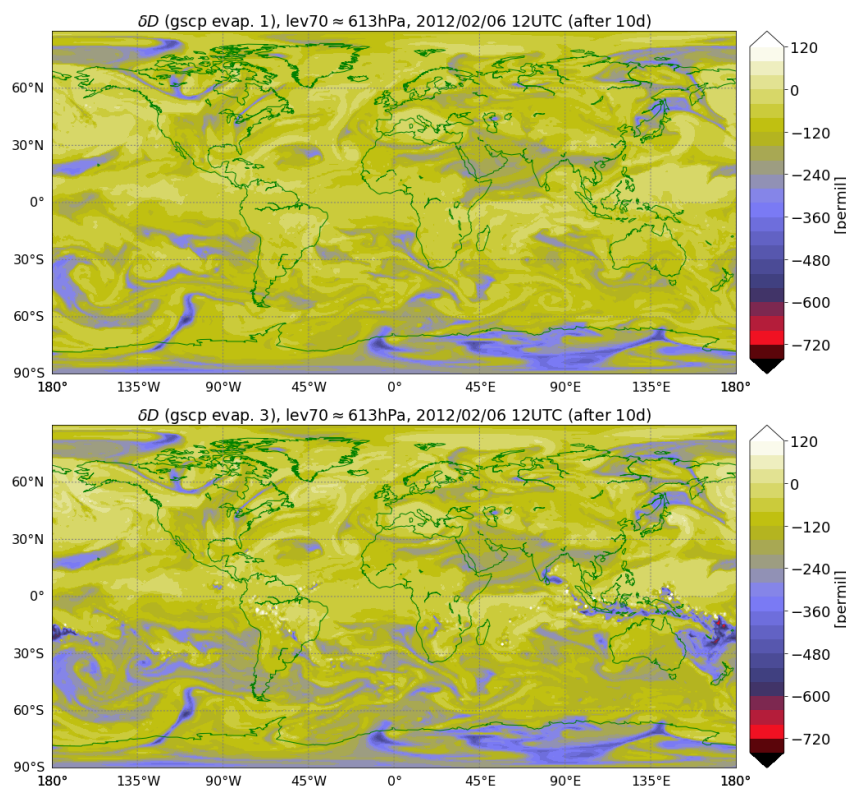


Fig. 5.16.: Horizontal cross sections of δD at level 70 (≈ 610 hPa) with fractionation turned on only for grid scale evaporation of hydrometeors (see Sec. 5.3.3.1), using the parameterization by Stewart (1975) (top) and by Blossey et al. (2010) (bottom).

5.6.2.3. Fractionation during saturation adjustment

The interaction of clouds and vapor are described by saturation adjustment in ICON, which is independent of microphysics or convection. The parameterization that describes fractionation is described in Sec. 5.3.4. Again, two parameterizations have been implemented, which differ only slightly. Figure 5.17

shows the result for the parameterization by Pfahl et al. (2012) (top panel) and by Blossey et al. (2010) (bottom panel).

The influence of this process is small, which becomes apparent when comparing to Fig. 5.14. The parameterization following Blossey et al. (2010) lead to higher δD values. These seem to even become higher than those of the non-fractionating isotope. Because of this behaviour, the parameterization by Pfahl et al. (2012) was used in the standard setup.

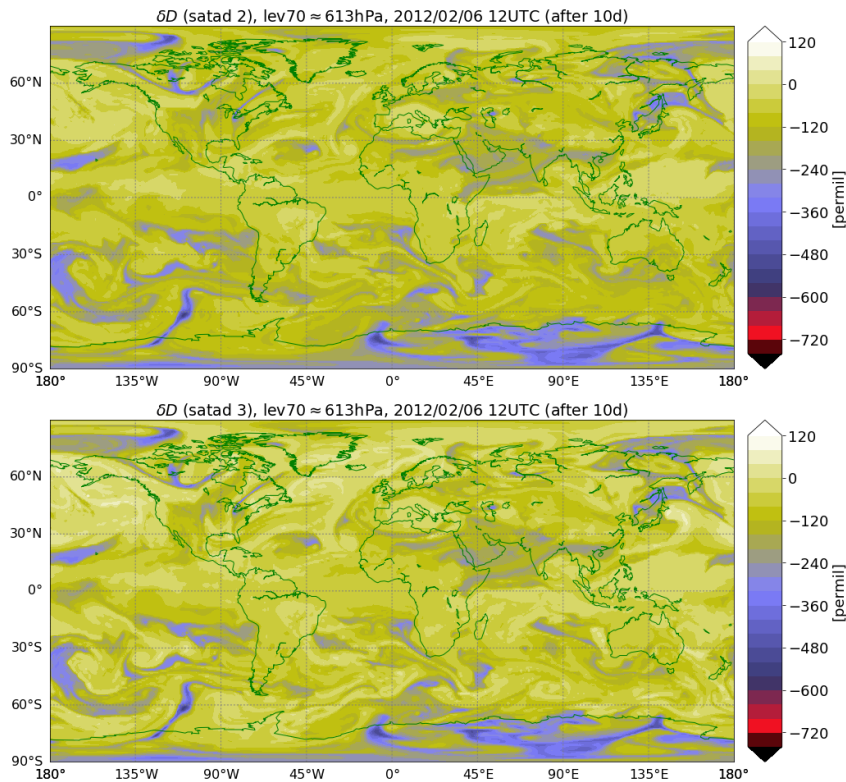


Fig. 5.17.: Horizontal cross sections of δD at level 70 (≈ 610 hPa) with fractionation turned on only for saturation adjustment (see Sec. 5.3.4), using the parameterization by Pfahl et al. (2012) (COSMOiso, top) and by Blossey et al. (2010) (bottom).

5.6.2.4. Fractionation during convection

Convection is different to the three processes discussed to here insofar as it does not describe processes that are resolved on the model grid. Instead, it considers each column separately and describes sub-grid scale thermodynamic processes which lead to clouds and precipitation. Phase changes are described by saturation adjustment for the initial state and for convective updrafts, i.e. the formation of cloud water. In addition, the evaporation of hydrometeors below cloud base is an important process. The isotope ratio also changes in convective downdrafts, which are assumed to be in saturated equilibrium. This is explained in more detail in Sec. 5.3.5.

For each of these three subprocesses, one parameterization to describe fractionation has been implemented. Figure 5.18 gives the result for each of these processes separately set to be fractionating. Convective saturation adjustment (top panel) leads to depletion of HDO. As is natural for convection, the effect is very localized. It can be strong, as is seen over the northern Pacific, the Mediterranean and east of Madagascar, for example. The exchange in convective downdrafts (middle panel) has very little effect on the overall result, again compare to Fig. 5.14. While the evaporation below cloud base is an important process again. It actually leads to higher values of δD . This is caused by hydrometeors (enriched in δD) which evaporate completely and thereby increase the value of δD in the vapor phase. This reevaporation process is also considered by Risi et al. (2010).

5.6.2.5. Fractionation during surface evaporation

Surface evaporation is the sum of several processes that lead to the exchange of water between the atmosphere and the ground, be it over the ocean or over land. In ICON-ART-Iso, these are separated and recombined into evaporation (from bare soil and water), transpiration from plants and dew and rime formation. While transpiration is assumed not to fractionate, dew and rime formation happen in equilibrium, applying the equilibrium fractionation factor directly. Only evaporation is parameterized, using either the scheme by Merlivat and Jouzel (1979) or by Pfahl and Wernli (2009). Section 5.3.2 explains this and the parameterizations in more detail. But it is important to keep in mind that only a part of evaporation is actually effected when choosing a different parameterization, as only the evaporative part is effected by it.

Both parameterizations lead to comparable results. The influence on the free troposphere is visible, but small. The effect of the two parameterizations is much stronger close to the surface, which is why Fig. 5.19 presents results for the lowest model level. It also give results for the non-fractionating and the standard HDO isotope.

As is shown in Fig. 5.19, the difference between the two parameterizations is also small close to the surface. The parameterization by Pfahl and Wernli (2009) leads to slightly lower values in δD . There remain small patches of high positive δD over land areas. These are hints to an error in the model code, which has not been found. These patches remain very small and their overall influence is negligible. This becomes clear when comparing to the other two panels. The non-fractionating HDO shows much higher δD values, especially so over the oceans. This highlights the importance of including this process. The top panel shows the standard setup of HDO in the same level. The values over the tropical and mid-latitude oceans resemble those when setting fractionation only during surface evaporation. But higher latitudes - and more so land areas - show that there is a strong influence of the other processes on these areas, even if they take place in the free troposphere and not mainly on the ground. Figure 5.19 also nicely shows that δD quickly drops to low values over the colder land masses, which was already indicated by the zonal mean values in Fig. 5.13.

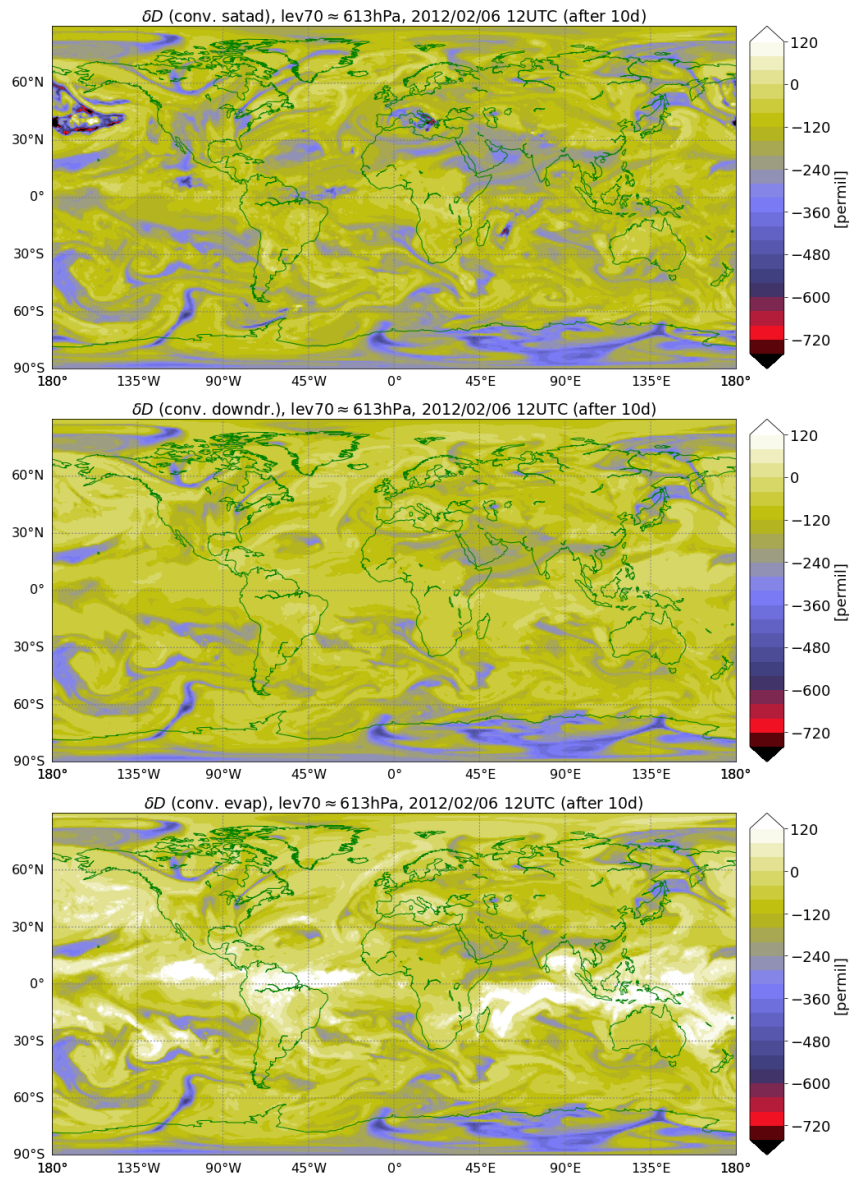


Fig. 5.18.: Horizontal cross sections of δD at level 70 ($\approx 610\text{hPa}$) with the different processes of convection set to be fractionating: saturation adjustment (top), exchange in convective downdrafts (middle) and evaporation below cloud base (bottom), see Sec. 5.3.5. All parameterizations have been taken from Pfahl et al. (2012), where evaporation is described following Stewart (1975).

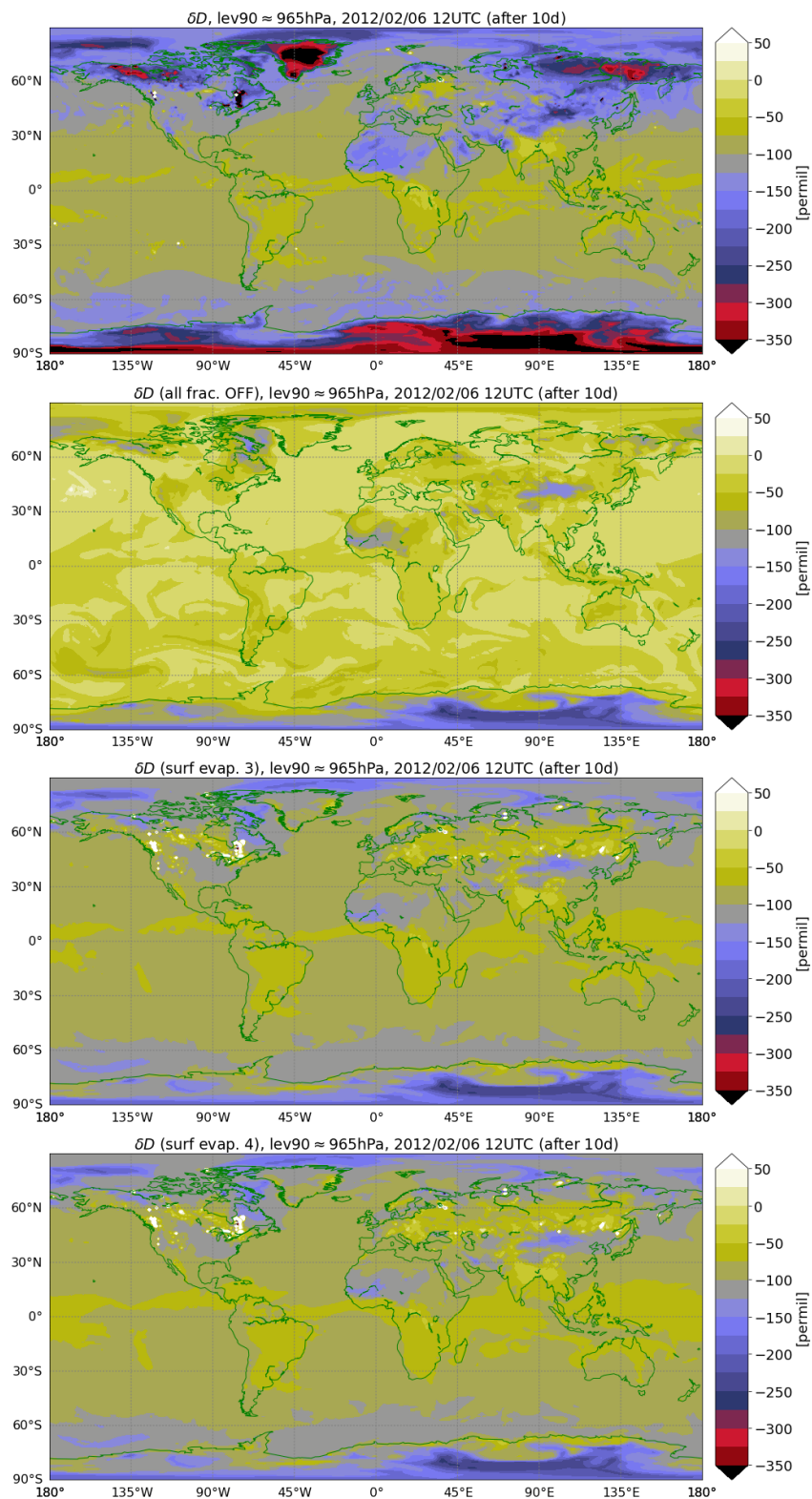


Fig. 5.19.: Horizontal cross sections of δD at level 90 (the lowest level, ≈ 970 hPa) with different sets of parameterizations turned on for HDO, listed from top to bottom: standard set of fractionation parameterizations, non-fractionating HDO, fractionation turned on only for surface evaporation (see Sec. 5.3.2), using the parameterization by Merlivat and Jouzel (1979) (third from top) and that by Pfahl and Wernli (2009) (bottom). Note the different color scale to the other figures showing δD .

5.7. Comparison with IASI satellite data

This section presents a first comparison of ICON-ART-Iso simulations with measurement data. Pairs of $\{H_2O, \delta D\}$ retrieved from MetOp/IASI measurements will be compared with data from two ICON-ART-Iso simulations and data from an ECHAM5-wiso simulation (Werner et al., 2011). In doing so, the section closely follows the case studies presented by Schneider et al. (2017), who compare IASI and ECHAM5-wiso data.

First, Sec. 5.7.1 introduces IASI satellite data and discusses their most important characteristics. Section 5.7.2 briefly introduces the model data and the retrieval method applied to models. Results of the comparison are presented in Sec. 5.7.3. Section 5.7.3.1 discusses signals of the seasonal cycle over the central Pacific in pairs of $\{H_2O, \delta D\}$, while Sec. 5.7.3.2 looks at the daily cycle in the tropics and subtropics. Section 5.7.3.3 takes into account the ocean and land evaporate diagnostics of ICON-ART-Iso to discriminate ocean and land affected air masses.

5.7.1. IASI retrieval data

IASI (Infrared Atmospheric Sounding Interferometer) A and B are instruments on board the MetOp-A and MetOp-B satellites (Schneider et al., 2016). It measures thermal infrared spectra in nadir view from which profiles of $\{H_2O, \delta D\}$ can be derived. As the satellites circle the earth in polar, sunsynchronous orbit, each IASI instrument can take measurements twice a day at local morning (approximately 9:30) and evening (approximately 21:30) hours. The retrieval method is presented by Schneider and Hase (2011) and Wiegele et al. (2014) with updates given in Schneider et al. (2016).

In order to get meaningful results, model data have to be processed to make them comparable with IASI measurements. The instrument does not take direct measurements, of the atmosphere instead it measures spectral radiances that depend on the atmospheric state. Radiances are emitted from the surface and emitted and absorbed by the atmosphere. The remote sensing retrieval process estimates the atmospheric state from the measured radiances. In order to correctly interpret such remote sensing data the averaging kernels are decisive. These kernels reveal how the actual atmospheric state is observed by the remote sensing system, i.e. they contain information on the transformation of the atmospheric state to the final data.

Therefore, data retrieved from satellites are not directly comparable with in situ measurements. It is very important to consider the averaging kernel for each measurement. If the analysis made here will state that it has been done for 4.9 km altitude, this does not mean that the information comes only from this height. The data is also influenced by the layers above and below and the averaging kernel contains the information from where and how strong it is influenced, see Schneider et al. (2017). The height of 4.9 km means that most information contained in the value comes from this height. This is a fundamental difference to in situ measurements as taken by CARIBIC, for example. For the retrieval, an a priori value has to be given, which is indicated in all figures for reference.

Schneider et al. (2017) present a software that simulates the averaging kernels using the atmospheric state of models. That way, the model data can be transformed to give modeled satellite measurements in an analogy to the data retrieved from the real atmosphere. This Retrieval Simulator has been applied to ICON-ART-Iso and ECHAM5-wiso simulations for this section.

5.7.2. ICON-ART-Iso simulations and ECHAM5-wiso model data

In order to compare ICON-ART-Iso measurements with IASI data, two simulations of four months will be used, which were initialized on November 5, 2013, and May 5, 2014 (the same simulations have been used in Sec. 5.5.3). As in Schneider et al. (2017), two target time periods will be investigated from February 12-18 and August 12-18, respectively. As has been shown in Sec. 5.5.3, the model has reached an intrinsic state in the troposphere for these dates, the amount of water remaining from initialization is negligible. This was the intent of giving three months lead time from the initialization to the evaluation time period. The simulations are, however, strongly affected by the constant sea surface temperatures and sea ice cover, as the evaporation from the ocean surface strongly depends on the temperature of surface waters. For this study, model output was considered on a $0.36^\circ \times 0.36^\circ$ grid, which is close to the 40 km (R2B06) resolution of the native ICON grid close to the equator. Output was written for every hour of simulation.

IASI observations are only available at cloud free conditions. In order to exclude cloud affected grid points, the total cloud cover `c1ct` by ICON was used. As this parameter is quite strict - 100% are reached quickly - all points with `c1ct` > 90% were excluded. Surface emissivity E_{srf} is a necessary input parameter for the Retrieval Simulator. In this first study, E_{srf} was set to 0.96 over land and 0.975 over the ocean. This is in accordance with mean values as given by Seemann et al. (2008). In addition, Schneider et al. (2017) show in a sensitivity study that errors on the order of 10% in this value have only a limited influence on the results. From the output of the Retrieval Simulator, values were only used where the sensitivity metric $s_{\text{err}} < 0.05$, as recommended by Schneider et al. (2017).

The phenomena investigated with the ICON-ART-Iso simulations are the same that were discussed by Schneider et al. (2017). The ECHAM5-wiso data is used for reference. ECHAM5-wiso (Werner et al., 2011) is the isotope enabled version of the hydrostatic general circulation model ECHAM5 (Roeckner et al., 2003). The model was nudged to ERA-Interim data (Dee et al., 2011) and the simulation considered changing sea surface temperatures and sea ice cover, both of which it makes difficult to compare the results directly with those of ICON-ART-Iso. The setups are by far not equivalent and the data can therefore only serve as a general reference.

5.7.3. Comparisons for the seasonal and daily cycle

Two phenomena are investigated with the ICON-ART-Iso, IASI and ECHAM5-wiso data in $\{\text{H}_2\text{O}, \delta\text{D}\}$ space: the seasonal and the daily cycle. The seasonal cycle is discussed for different regions over the

central Pacific Ocean, see Sec. 5.7.3.1 for results. The daily cycle is considered in the tropics and subtropics. Here, differences over land and ocean areas are also investigated, see Sec. 5.7.3.2 for results. Section 5.7.3.3 shows how the additional information from ICON land and ocean evaporate can be used. The investigation uses data from August and February, 12-18, of 2014. The exact latitudinal and longitudinal limits of the different areas is given in Table 5.7. All investigations on the following subsections are done for mid-tropospheric values in 4.9 km height.

cycle	region	area	limits in λ		limits in φ		daytime	season
			east	west	south	north		
seasonal Sec. 5.7.3.1	Pacific	by φ	140°E	-140°E	-65°N	-45°N	morning	Feb. vs. Aug.
					-40°N	-20°N		
					-10°N	10°N		
					20°N	40°N		
					45°N	65°N		
daily Sec. 5.7.3.2	Tropics	land	-180°E	180°E	-10°N	10°N	morning vs. evening	Feb. & Aug.
		ocean						
	Subtrop.	Sahara	-10°E	50°E	-22.5°N	35°N	morning vs. evening	Aug.
		Atlant.	-50°E	-30°E				

Tab. 5.7.: Limits in latitude φ and longitude as well as choices for daytime and season for the different regions used in the investigation of the seasonal and daily cycle of $\{H_2O, \delta D\}$ in ICON-ART-Iso ECHAM5-wiso and IASI data.

The scatter of $\{H_2O, \delta D\}$ is not shown directly as the figures would be too cluttered. Instead, the data is binned in $\log_{10}(H_2O)$ and δD on a grid of 0.05×5 (for $\log_{10}(\text{ppm}) \times \text{permil}$) and histogram counts are interpolated onto a 1000 by 1000 grid. This is smoothed with a Gaussian filter with a standard deviation of 15 (30 in case of ECHAM5-wiso due to fewer data). This smoothed data is then normalized by the sum of all value pairs and then normalized by the maximum value. For this probability density, contours are drawn at 0.2, 0.6 and 0.9 for all considered regions. This method is slightly different from Schneider et al. (2017). For reference, the Rayleigh curves of Sec. 5.2.3 are shown in all figures. Schneider et al. (2017) also show Rayleigh curves in their figures, but for different surface values, which is another reason why the figures are different.

5.7.3.1. Results for the seasonal cycle

This section examines the seasonal cycle in pairs of $\{H_2O, \delta D\}$ as seen in morning overpass data retrieved from IASI satellite measurements in February and August, 2014 over the Pacific Ocean. The different latitudinal slices for this investigation are indicated in Table 5.7. The same period is examined with output of ICON-ART-Iso. Data from the model ECHAM5-wiso is given as reference. Both model

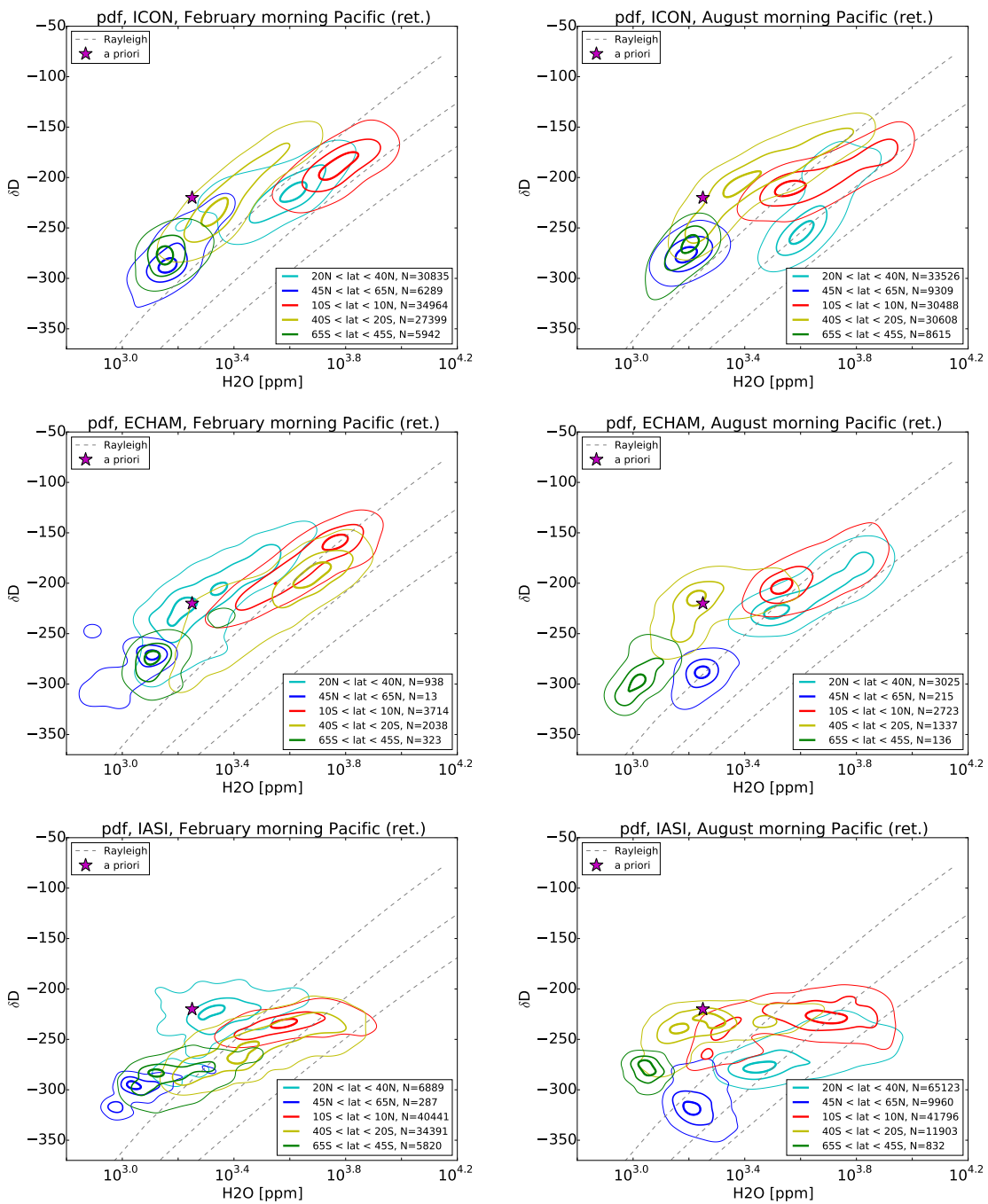


Fig. 5.20.: Pairs of δD and H_2O after processing model data with the IASI Retrieval Simulator of Schneider et al. (2017), top row: ICON-ART-Iso data, middle row: ECHAM5-wiso data, bottom: IASI data for the same time. Data from to morning overpasses in 12 to 18 February (left) and August (right), 2014 for different latitudinal bands over the Pacific Ocean ($\lambda < -140^\circ E$ or $\lambda > 140^\circ E$). Contour lines are indicated at 0.2, 0.6 and 0.9 of the pdf.

datasets have been processed with the Retrieval Simulator of Schneider et al. (2017). See the preceding sections for more details and the exact procedure on how to arrive at the probability contours shown in this section. Figure 5.20 shows the results. IASI data (bottom panels of Fig. 5.20) shows specific characteristics of the different regions. Content in H_2O is highest for tropical air masses and lowest for the highest latitudes in February and August. At the same time, tropical air is least depleted in HDO, while the highest latitudes show the lowest values of δD , i.e. are more depleted. Upon comparing February and August values in each latitude, a clear signal appears everywhere but in the tropics: During summer of the corresponding hemisphere, the air is more humid and more depleted in HDO. The distributions seem to change place from season to season, moving along a line perpendicular to those of the Rayleigh model. The distribution in the tropics shows a broadened shape in August.

Data taken from ECHAM5-wiso (middle panel of Fig. 5.20) shows a similar latitudinal distribution with highest H_2O values in the tropics and lowest δD in the highest latitudes. Tropical and subtropical δD is higher than in IASI data. There is also a seasonal cycle in the non-tropical latitudes. But it stems more from changes in H_2O , the seasonal signal in δD being weaker than in IASI data. The distributions from ECHAM5-wiso data lie approximately parallel to Rayleigh curves. This is not the case for the IASI retrievals, the distributions of which cross the Rayleigh lines. Schneider et al. (2017) interpret this to indicate too strong vertical mixing in the model.

The simulations of ICON-ART-Iso are shown in the top panels of Fig. 5.20. The latitudinal dependence is similar to IASI and ECHAM5-wiso: high H_2O and δD in the tropics and the opposite for mid-latitudes. The range of values is also very similar. This is a first important result and shows that the model shows values within the same range as the satellite data and the ECHAM5-wiso simulations.

The annual cycle, on the other hand, is not reproduced. This is not surprising, as sea surface temperatures were kept constant for both simulations. As sea surface temperatures strongly affect evaporation rates, the seasonal cycle in mid-troposphere H_2O is directly influenced. The same is true for the fractionation at evaporation of the heavy isotopes. If the seasonal cycle is to be the focus of a future study, it should be reexamined in a simulation with changing sea surface temperatures and sea ice cover.

In this first look at the performance of the model, the result of the model reproducing latitudinal dependence of $\{\text{H}_2\text{O}, \delta\text{D}\}$ is the important result. Discrepancies that show in the seasonal dependence can be examined in more detail in a future study.

5.7.3.2. Results for the daily cycle

This section examines the daily cycle in pairs of $\{\text{H}_2\text{O}, \delta\text{D}\}$ of IASI satellite data as well as in model data that has been processed with the Retrieval Simulator of Schneider et al. (2017). Values over land and ocean for the tropics and subtropics are examined separately, with exact definitions of the regions given in Table 5.7. Figure 5.21 shows the probability contours, produced with the method explained in the preamble to this section.

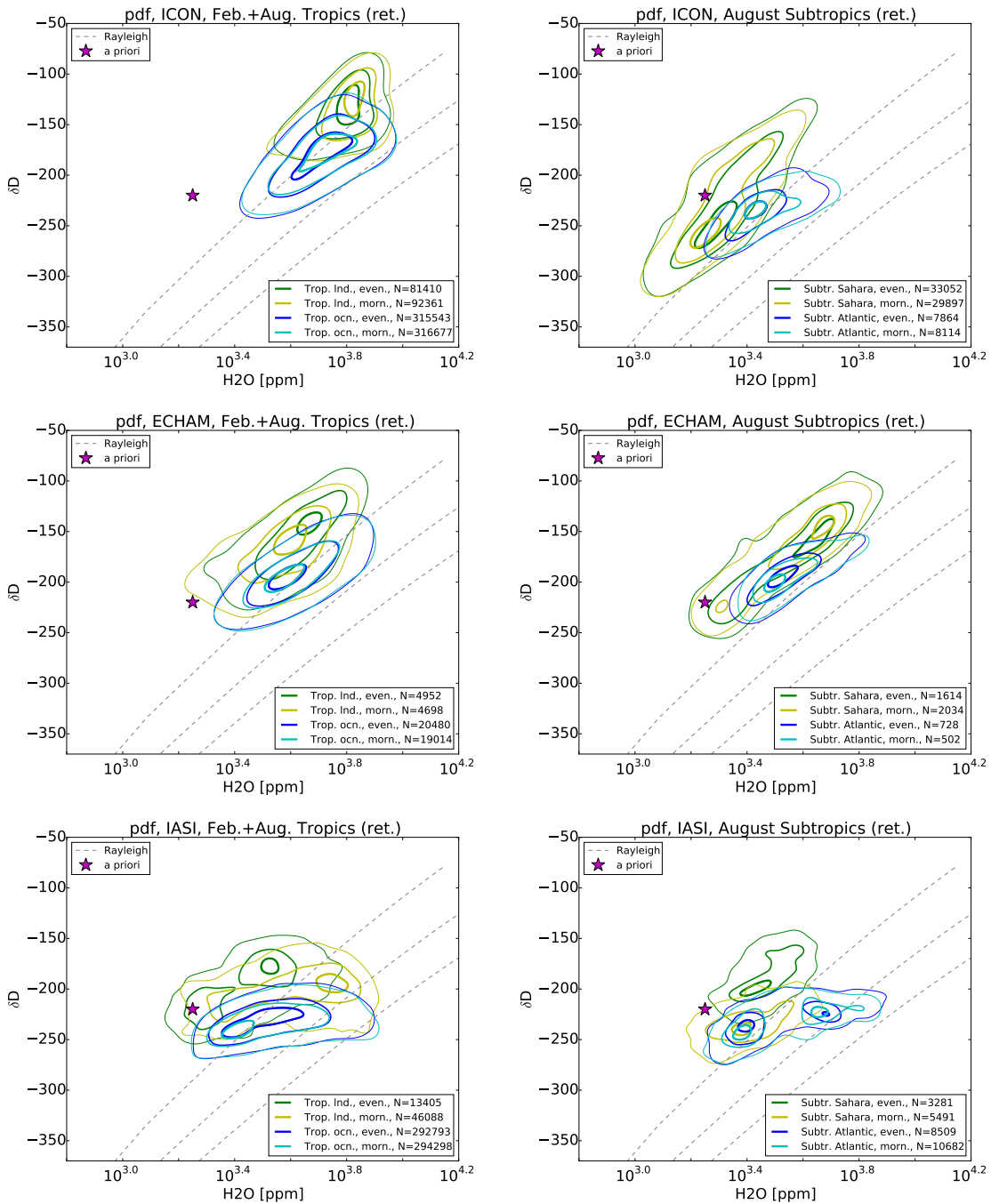


Fig. 5.21.: Pairs of δD and H_2O after processing model data with the IASI Retrieval Simulator of Schneider et al. (2017), top row: ICON-ART-Iso data, middle row: ECHAM5-wiso data, bottom: IASI data for the same time. Left: Data corresponding to morning and evening overpasses for the tropics over land and over the ocean. Right: Morning and evening overpasses for subtropics over land (Saharan desert region) and Atlantic Ocean, see Table 5.7 for the exact definitions of the regions. Contour lines are indicated at 0.2, 0.6 and 0.9 of the pdf.

IASI shows a clear signal of the daily cycle for both the tropics and subtropics over land (bottom panels of Fig. 5.21). There is no such signal over the ocean, morning and evening curves being almost identical. Over land, the tropics and subtropics show air more depleted of HDO in the morning. There is also a daily cycle in H₂O: During morning overpasses, the tropics show higher H₂O values than in the evening. Schneider et al. (2017) argue that this is due to the cloud filter, which removes areas of heavy convection in the evening. In the morning, the cloud has disappeared, but high humidity remains, especially in the lower troposphere. This is partly due to evaporation of rain drops, which explains the enhanced depletion in HDO. Over the Sahara (the subtropical land area considered), the daily cycle is different: While mixing ratios of H₂O rise only slightly during the day, there is a strong increase in the content of HDO. This behavior can be attributed to vertical mixing (Schneider et al. (2017) and references therein).

In ECHAM5-wiso driven retrieval data (Fig. 5.21 middle panels), the mixing ratios of H₂O and values of δD are comparable to IASI data over the ocean for tropics as well as for the subtropics. Like in IASI data, there is also no daily cycle over the ocean. However, in contrast to IASI, there is also no daily cycle observable over land. In the tropics, the model shows higher mixing ratios in H₂O. There is a small shift towards more humid and less depleted air in the evening. In the subtropics over land, ECHAM5-wiso is significantly more humid than IASI and there is no daily cycle. Schneider et al. (2017) again attribute these differences between modeled and measured diurnal cycles to excessive vertical mixing in the model.

The data retrieved from ICON-ART-Iso model simulations is shown in the top panels of Fig. 5.21. Tropical air over the ocean shows higher mixing ratios for H₂O than IASI or ECHAM5-wiso. Tropical land areas are even more humid. The difference in δD is even stronger, being higher than in any other region. A daily cycle does not show in the tropics for ICON-ART-Iso.

The subtropical mixing ratios of H₂O over the ocean are smaller than in the tropics and more similar to those retrieved from IASI or ECHAM5-wiso. The δD values are closer to those shown by IASI. Over land, the values retrieved from ICON-ART-Iso do not show a daily cycle, which is in contrast to IASI data, but similar to ECHAM5-wiso results. ICON-ART-Iso shows signals of a much drier troposphere than ECHAM5-wiso, which is also more similar to IASI data. Values of δD are lower in ICON-ART-Iso than what is retrieved from IASI.

As for the seasonal cycle, results here are also affected by the constant sea surface temperature and sea ice cover values. While this directly manifests itself in relative differences between the seasons in Sec. 5.7.3.1, it probably influences the absolute values here. As tropical and subtropical areas are considered, the effect is not as strong. The results presented here should be understood as a first test and can serve as a first reference, but they can only be the starting point to an in-depth analysis to come.

5.7.3.3. Considering land and ocean evaporate water

The preceding section has shown the influence of land and ocean on the daily cycle and the general distribution of pairs of $\{H_2O, \delta D\}$ for values retrieved from IASI satellite measurements and ECHAM5-wiso and ICON-ART-Iso simulations. The setup of ICON-ART-Iso allows to use an additional parameter to discriminate land and ocean. In addition to simulating HDO, two additional instances of water have been included in the two simulations of ICON-ART-Iso. These instances were both initialized with 0 and set to evaporate only from the ocean or only from land. With three months of lead time to the investigation period in these model runs, the tropospheric water can be described by the sum of these two instances, called ocean and land evaporate respectively. This has already been discussed in Sec. 5.5.3.

In addition to masking data purely on the land-sea mask, ICON-ART-Iso allows to use this additional information. The analysis of the daily cycle of Sec. 5.7.3.2 is repeated here, additionally setting $R^{ocn} > 0.8$ over the ocean $R^{lnd} > 0.5$ over land to determine ocean and land points respectively. R is the ratio of the ocean or land evaporate vapor to ICON standard vapor. The two thresholds are set to these values because - especially over the Sahara - R^{lnd} is rather low. Values of ocean and land evaporate have not been processed with the retrieval simulator, this should be done in an in-depth analysis. Instead values interpolated to 4.9 km were directly used.

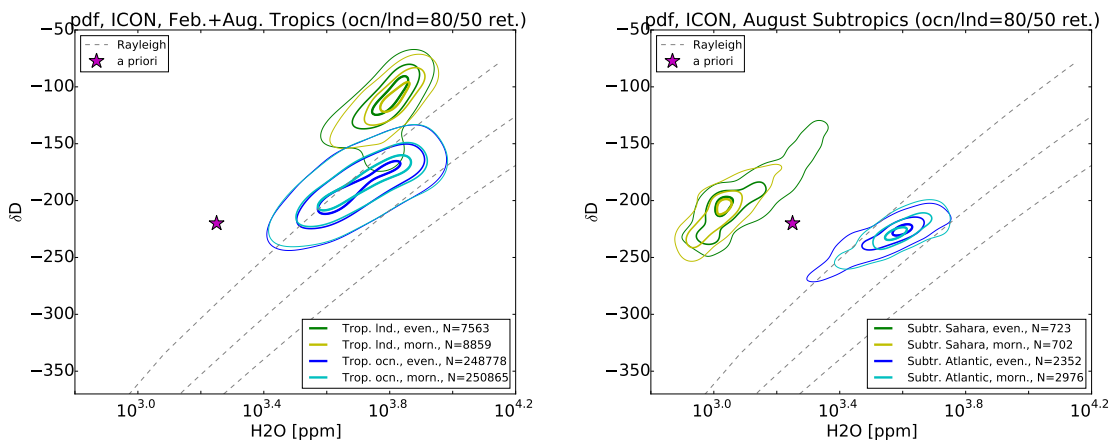


Fig. 5.22.: Pairs of δD and H_2O after processing ICON-ART-Iso data with the IASI Retrieval Simulator of Schneider et al. (2017). Morning and evening overpasses for tropics (left) and subtropics (right) for land and ocean points as in Fig. 5.21. In addition to the land-ocean mask, land data must pass the condition $R^{lnd} > 0.5$ and ocean data must pass $R^{ocn} > 0.8$.

The result is shown in Fig. 5.22 for tropics and subtropics, using the same method as for Fig. 5.21. The characteristics of the different regions show up much more clearly. For the tropical ocean, this means lower mixing ratios in H_2O (the center is shifted to lower values) and more depletion in HDO, removing that end of the distribution that apparently has a strong influence by land evaporate. The distribution of pairs attributed to the land surface is also shifted to slightly lower mixing ratios in H_2O , while δD is shifted to higher values. The latter might be due to the signal of plant evapotranspiration, which is

considered a non-fractionating process. Overall, the most humid points over land and ocean are those with a strong influence of the other domain. With these stricter limits, there is also a small signal of a daily cycle over land, while it is by far not as strong as in the IASI data.

In the subtropics, the effect is even stronger. The two distributions are completely separated. Comparing the number of samples attributed to the land surface, it becomes clear that the remaining part of the distribution is really an extreme. 50% land evaporate over the Saharan desert implies very low mixing ratios in H_2O . The values in δD on the other hand are not so intuitive, being relatively high (with respect to the full subtropical land distribution shown in Fig 5.21, not so with respect to the tropical values). The distribution for the subtropical ocean on the other remains relatively unchanged, becoming slightly more elongated with lower values in δD .

This demonstrates the added value to pairs $\{\text{H}_2\text{O}, \delta\text{D}\}$ by using more instances of water in ICON-ART-Iso. Of course this information is not available from IASI measurements. But in the future, it can be developed into a diagnostic tool to help understand processes happening in the model.

5.8. Case study comparison with CARIBIC in situ measurements

This section returns to the overall subject of the study: The comparison of model and CARIBIC measurement data. In situ measurements are used to validate ICON-ART-Iso in a case study using four flights in August and September, 2010. Simulations of the time periods of these flights will be used to further evaluate the model performance.

The chapter is organized as follows: Section 5.8.1 gives an introduction to measurements of δD by CARIBIC, considering technical aspects and the measurement uncertainty as well as thoughts on the variability and representativeness of the data. Section 5.8.2 describes the meteorological situation during the four flights and discusses their representation in the ICON-ART-Iso simulations.

Results for δD from the ICON-ART-Iso simulation are then discussed and compared with the measurements in Sec. 5.8.3. Section 5.8.4 investigates the origin of the water in the model that was sampled along the flight paths of CARIBIC, which is informative of the model performance on small scales. Section 5.8.5 discusses the model and measurement samples in the context of larger samples. A short Sec. 5.8.6 then turns to simulation results of the regional, isotope enabled model COSMOiso (Pfahl et al., 2012), which served as the basis of the development of ICON-ART-Iso. Section 5.8.7 summarizes and concludes.

5.8.1. CARIBIC δD measurements

Measurements of δD are taken on board the CARIBIC aircraft (see Sec. 2.2) with the instrument ISOWAT (Dyroff et al., 2010). The instrument is a tunable diode-laser absorption spectrometer that takes simultaneous measurements of HDO and H₂O to derive δD , using spectral absorption lines near 3765 cm⁻¹. The instrument is calibrated in flight every 30 minutes Christner (2015).

The lower detection limit for δD is at approximately 40 ppm H₂O. While the precision of the instrument is very good, it is not very accurate. The measurement uncertainty reaches 100 in δD . This uncertainty is not random, but depends on the humidity. As the real δD also depends on the humidity, it is often difficult to assign the observed variability to either cause. The uncertainty increases with lower H₂O mixing ratios, so that stratospheric measurements of δD are not possible (personal communication by Emanuel Christner, KIT, and Christner (2015)).

Figure 5.23 shows all CARIBIC δD measurements that are available from CARIBIC flights in the years 2010 to 2014. These were taken during 75 flights in different months and are limited to areas with high mixing ratios of H₂O. The figure also shows locations with measurements of H₂O for the same flights. H₂O is measured with different instruments on board CARIBIC (Zahn et al., 2014) and there are more measurements, also from before 2010. The CARIBIC data is the largest dataset of in situ δD measurements in the upper troposphere (Christner, 2015).

Despite the relatively large number of measurements (compared to other datasets), the δD dataset is not representative on a climatological time scale, even if the instrument limitations are not considered.

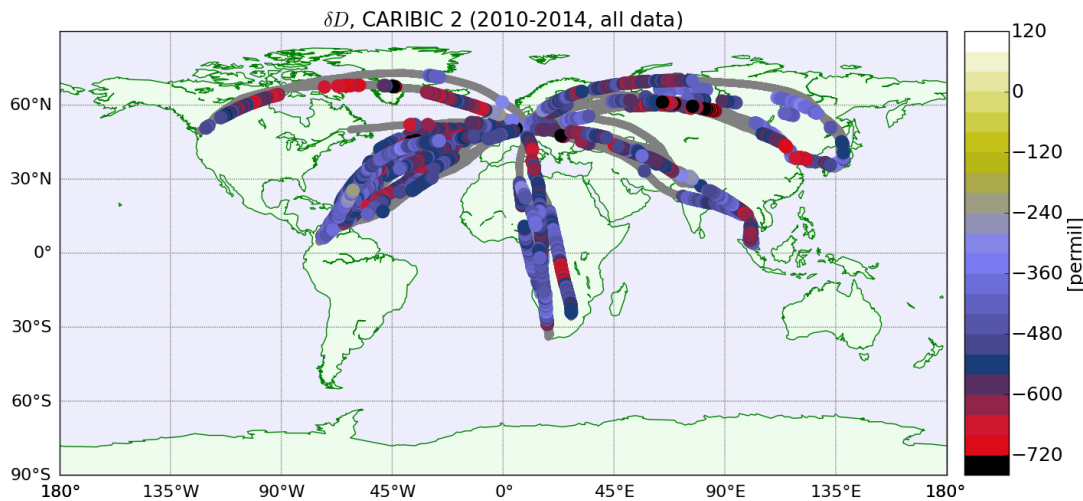


Fig. 5.23.: All CARIBIC δD measurements between 2010 and 2014. The locations of measurements of H_2O from the same flights are marked in gray.

Climatological representativeness of CARIBIC data is discussed in detail in Ch. 4. The variability $\sigma_r = \sigma/\mu$ of Eq. 4.1 for δD is 0.15, while that of H_2O is slightly larger with 0.7. Considering Fig. 4.15, this would mean that data from about 250 flights would be needed for a representative climatology if an uncertainty of 10% is accepted.

In addition to this gap in sheer size of the dataset, there is the problem that the lower detection limit of 40 ppm H_2O of ISOWAT for δD is within the range of values which are actually encountered during flight, especially in stratospheric heights. This makes it impossible to derive a climatology of δD for the lower stratosphere and is the reason why this chapter uses CARIBIC measurements for a case study. A first impression of the performance of ICON-ART-Iso on a seasonal time scale is given in Sec. 5.7 by comparing with IASI satellite data.

The fact that CARIBIC measures in situ makes it very interesting for the analysis of processes on small scales. δD measurements are available as mean over one minute, which translates to a spatial scale of less than 15 km. This is better than the horizontal resolution of ICON-ART-Iso and therefore very well suitable for validation in form of a case study. But because of the low instrument accuracy, it is difficult to use single flights. Mean values or distributions from several flights are used to minimize the influence of this problem.

Similar to Sec. 5.7, data of δD will partly be discussed relative to H_2O . Figure 5.24 shows all pairs of $\{H_2O, \delta D\}$ by CARIBIC, grouped into tropical and northern hemisphere extratropical data points. Data from ascents and descents have been excluded by setting a limit in pressure ($p < 280$ hPa). Figure 5.24 shows the scatter and the corresponding probability contours. To transform the scatter into the contours, the scatter was first binned on a 5×5 ppm grid in δD and H_2O , interpolated onto a 1000 by 1000 matrix and then smoothed with a Gaussian filter of standard deviation 20. The data was then normalized by the

sum of all measurements and by the maximum value. Contours give the probability at 0.1, 0.4 and 0.9. With both scatter and contours given, Fig. 5.24 demonstrates this method. The Rayleigh curves are given for reference, they are the same that have been introduced in Sec. 5.2.3.

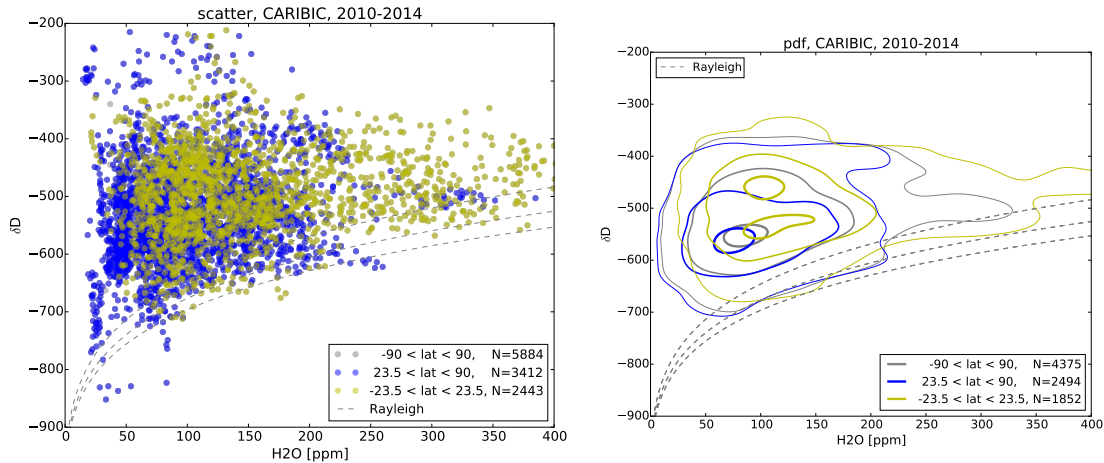


Fig. 5.24.: Measurements of pairs of δD and H_2O taken by CARIBIC for all locations, tropical ($-23.5^\circ < \varphi < 23.5^\circ$), northern hemisphere extratropical ($23.5^\circ < \varphi < 90^\circ$) and for all locations. The left panel is the pure scatter. The right panel indicates contour lines at 0.1, 0.4 and 0.9 of the pdf.

Figure 5.24 shows the characteristics of the different latitudinal bins. Almost all data lie above the Rayleigh curves, the air is less depleted in HDO than after seeing a pure Rayleigh process. Tropical air masses tend towards more humid and less depleted states than mid-latitude air. The mid-latitude data is strongly influenced by the detection limit of 40 ppm, which clearly shows up in the scatter plot. The difference in the two distributions is evidence of the different processes that control the relationship of δD and H_2O in the tropics and mid latitudes.

5.8.2. Two return flights to Caracas

In the subsequent sections, measurements from two return flights from Frankfurt to Caracas of late summer 2010 are analyzed in detail. All four flights sampled air influenced by tropical storms.

Two flights (nrs. 305 and 306) crossed the track of Hurricane Danielle on August 25 and 26, 2010. Hurricane Danielle was a tropical depression that reached storm intensity from August 21 to 30 (Kimberlain, 2010). It formed southwest of the Cape Verde Islands and moved westward, reaching hurricane strength on August 23. It then turned northwest, reaching peak intensity with 943 hPa minimum surface pressure on August 28. Figure 5.25 shows the best track position of the hurricane as well as the flight tracks. The flights crossed the track of Hurricane Danielle west of the storms core but within the outflow region (Christner, 2015).

The other two flights (nrs. 309 and 310), on September 21 and 22, 2010, crossed the Atlantic approximately two days after Hurricane Igor. Christner (2015) shows by back trajectories that the air masses

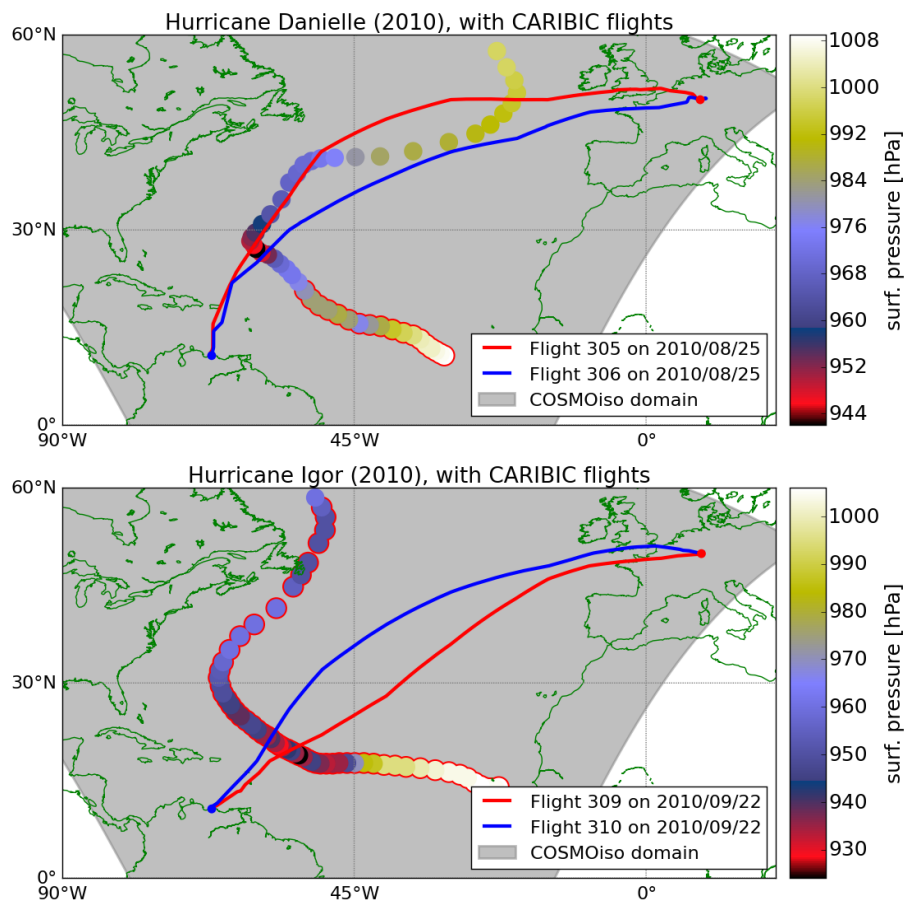


Fig. 5.25.: Surface pressure for the best track position of Hurricanes Danielle (top) and Igor (bottom) of the hurricane season 2010. Flight tracks of CARIBIC flights during the same time are also indicated. The scatter points of surface pressure are circled in red for dates before the date of CARIBIC flights. The model domain of COSMOiso used for the simulation of the storms is marked in gray. Best track positions of the hurricanes are taken from National Hurricane Center reports, Kimberlain (2010) and Pasch and Kimberlain (2011).

sampled by CARIBIC in tropical latitudes where directly influenced by the Hurricane. Hurricane Igor was the strongest tropical storm of the 2010 hurricane season (Pasch and Kimberlain, 2011). It developed on September 9 just south of Cape Verde Islands. Moving east and northeastward, the depression reached major hurricane strength on September 13, which persisted until September 18. The storm then quickly moved northeastward and made landfall in Newfoundland, where it caused severe damage. Figure 5.25 shows the best track position and surface pressure of the Hurricane as well as the flight tracks. The two flights sampled heavily processed air. The high humidity allowed many measurements to be taken in the tropical latitudes.

At the moment, ICON-ART-Iso can only run in forecast mode. No nudging towards meteorological analysis or reanalysis fields has been implemented. Neither of the storms were therefore exactly reproduced by ICON-ART-Iso. Different disturbances are part of the model simulation. But they are not collocated with the observations of the storms Danielle and Igor. The simulations had to be initialized early during the development of the storms in order to give the model the time to develop its own state of δD at the time of the flights. A detailed analysis of the thermodynamic processes in the storms and their influence on the δD distribution is therefore postponed to a later study.

On the other hand, an exact reproduction of the measurements would also be difficult because of their high uncertainty, which is again discussed in Sec. 5.8.3. Section 5.8.5 discusses the distribution of $\{\delta D, H_2O\}$ pairs from the flights and compares these samples to larger datasets. By combining these measurements of a similar characteristic, the influence of the measurement uncertainty is minimized.

5.8.3. Simulation of δD for the CARIBIC flights with ICON-ART-Iso

As has been noted above, ICON-ART-Iso can only run in forecast mode at the moment. In order to investigate the influence of this technical shortcoming, two simulations were started per pair of flights, using different initialization dates. The model output was then interpolated onto the flight paths of the different CARIBIC flights. Cross sections of δD , overlaid with measurement values, are discussed in this section. Sections 5.8.4 and 5.8.5 delve into a more detailed analysis, while Sec. 5.8.6 takes a look at COSMOiso simulation results.

The two simulations for flights 305 and 306 were initialized on August 18 and 21. Results are shown in Fig. 5.26 as vertical cross sections of δD , also indicating the measurements. As the flights started on August 25, the initialization corresponds to a forecast lead time of seven and four days, respectively. Figure 5.26 shows a strong dependence on the initialization date. The results for the simulations are very different for both flights. They do agree in the overall distribution of δD , e.g. the very low, topical δD values close to South America in high altitudes (destination of 305 and start of 306). Measurements are not very well reproduced by either simulation, while this remains hard to analyze in detail in this view.

The difference between the simulations is even more drastic for flights 309 and 310, see Fig. 5.27. In the attempt to simulate Hurricane Igor, the lead time for the forecasts was increased to 14 and 12 days. Of course a forecast of this length cannot be expected to reproduce the very localized measurements

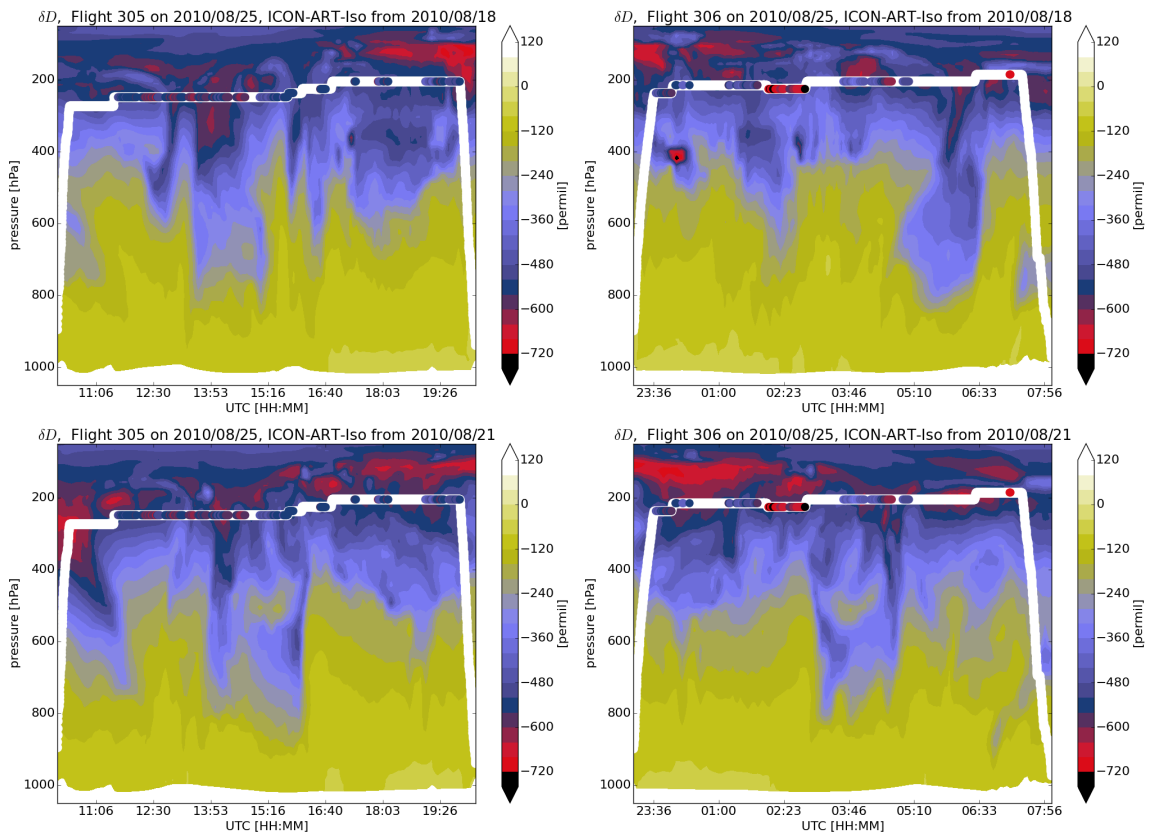


Fig. 5.26.: Cross sections of δD from two different ICON-ART-Iso simulations initialized on August 18, 2010 (top) and August 21, 2010 (bottom). The output is interpolated onto the flight track of CARIBIC flight 305 (left column) and 306 (right column, both on August 25, 2010). Flight altitude is indicated in white, colored values inside the white line represent measurements.

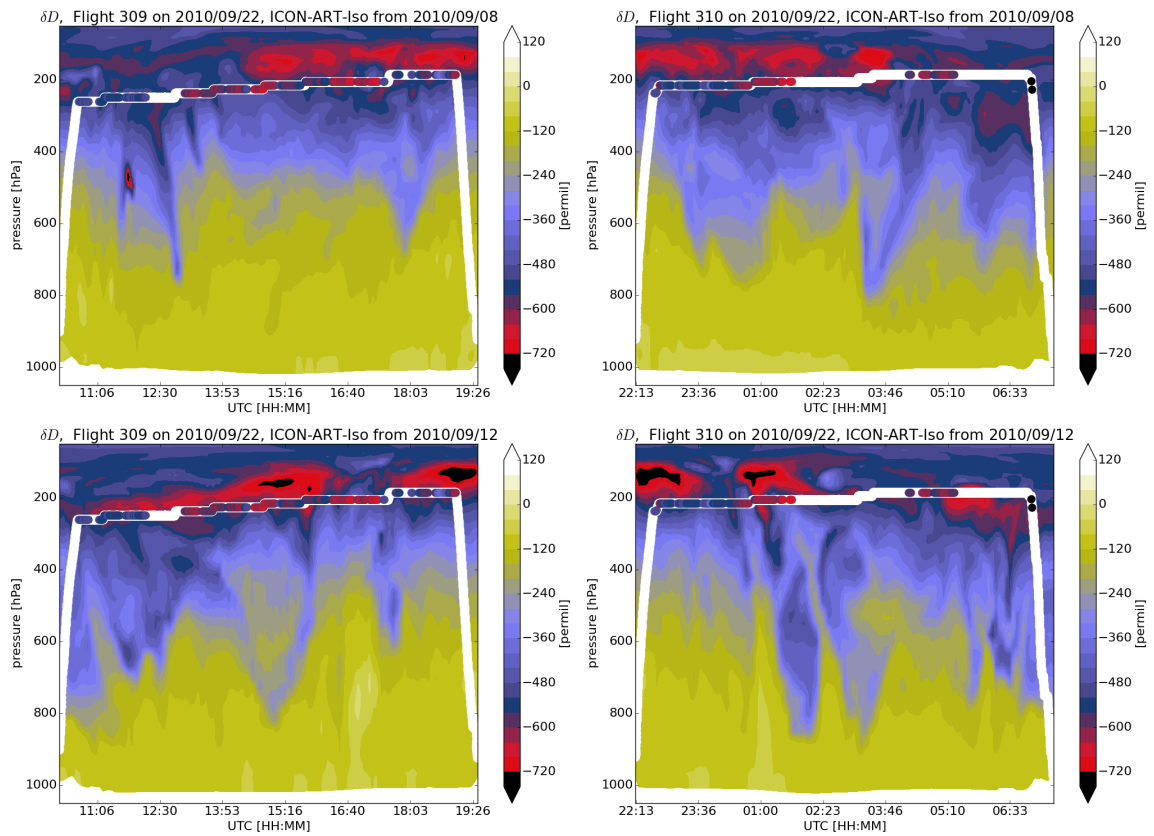


Fig. 5.27.: Cross sections of δD from two different ICON-ART-Iso simulations initialized on September 8, 2010 (top) and September 12, 2010 (bottom). The output is interpolated onto the flight track of CARIBIC flights 309 (left column) and 310 (right column, both on September 22, 2010). Flight altitude is indicated in white, colored values inside the white line represent measurements.

of CARIBIC. But starting later was also not an option, as the model starts from mean values for the isotopes. The cross sections for the two flights again depend on the initialization date. This is true for large and small scale structures alike.

Figure 5.28 shows the scatter plot of modeled over measured δD values. Values for the different simulation start dates (early and late) are indicated, as well as the different flight sets (305 and 306 versus 309 and 310). What has been shown above for the cross sections manifests itself even more so in Fig. 5.28: The measurements are not reproduced by the model, independent of the start date of set of flights. As has been pointed out, the reason for this is twofold: The model is calculating a forecast, which makes an exact reproduction of the in situ measurements close to impossible. But the measurements themselves also have a high uncertainty. Considering a possible uncertainty of up to 100 in δD , the scatter in Fig. 5.28 can be just as well explained by the measurement uncertainty.

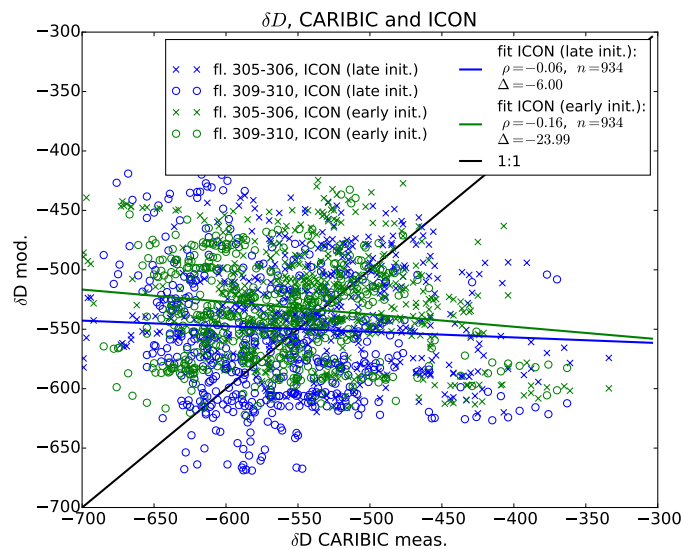


Fig. 5.28.: Scatter plot of modeled over measured δD for CARIBIC flights 305, 306, 309 and 310 using the simulations of Hurricanes Danielle and Igor of ICON-ART-Iso and COSMOiso started on August 21 and September 12, 2010. Open circles represent values of ICON-ART-Iso at those locations where the regional model COSMOiso also has values. Statistics indicated are the Pearson correlation coefficient ρ , the number of values n and the mean offset Δ (measurements minus model values).

The small mean offset between model and measurements can be seen as a positive result. The data in the model may not be locally correct, but the overall range is similar. The meagerly depleted values are not reproduced by the model and values of δD are slightly too high in general, at least for this series of measurements. But the fact that the range is reproduced by both sets of simulations shows that the main processes that lead to fractionation have been correctly implemented into the model. As has been pointed out by Risi et al. (2012) and Field et al. (2014), upper tropospheric δD shows a high sensitivity

to various parameterizations in isotope enabled models. The small mean offset is therefore a promising result.

This sections has shown that it is difficult to use ICON-ART-Iso for case studies as long as nudging has not been implemented. A forecast of the model fields will not simulate fields that resemble exactly the true state of the atmosphere. This has become obvious by comparing simulations with different lead times to CARIBIC measurement data. But the measurements themselves also a high uncertainty, which is why a high correlation coefficient cannot be anticipated. While the model falls short of reproducing the measurements exactly, the mean offset between modeled and measured values of δD is small.

5.8.4. Tracing the origin of water with ICON-ART-Iso

The preceding section attempted to compare CARIBIC δD measurements directly with simulations of ICON-ART-Iso. For different reason by both model and observations, this proved difficult. This section returns to using ICON-ART-Iso alone and investigates the origin of the water that is sampled along the CARIBIC flight paths in the model.

In addition to δD , use is now made of three other isotopes (instances of doubled water): The initialization water q^{init} and the ocean and land evaporate, q^{ocn} and q^{land} . Their definition is summarized in Table 5.6. The water in ICON can be considered a ternary solution of water that is present at initialization and water that evaporates either from land or ocean points during the model run. This is implemented with these three separate isotopes. Their water vapor mixing ratios are considered relative to the total ICON water vapor, q_v^{ICON} , with $R^X = q_v^X / q_v^{\text{ICON}}$.

flight nr.	initializ. water	ocean evap.	land evap.
	R^{init}	R^{ocn}	R^{land}
305	85.23	14.02	3.36
306	86.21	14.72	1.79
309	47.21	54.47	3.66
310	53.93	44.77	5.75

Tab. 5.8.: Ratio R of q_v^{init} , q_v^{ocn} and q_v^{land} in percent of q_v^{ICON} for flights 305 and 306 (during Hurricane Danielle, four days lead time) and flights 309 and 310 (during Hurricane Igor, 12 days lead time).

For this investigation, use is made of the model simulations that start on August 21 and September 12, 2010. The data along the flight paths of CARIBIC flights 305, 306, 309 and 310 is again considered. This means that the lead time of the simulations are quite different: four days for flights 305 and 306 and 12 days for flights 309 and 310. Table 5.8 gives mean values for the ratios of q_v^{init} , q_v^{ocn} and q_v^{land} for the different flights. There is a clear difference in relative amounts of the different constituents depending on the lead time. While flights 305 and 306 are contain more than 85% water from initialization, this value has dropped to approximately 50% for flights 309 and 310. These have a lead time of about 12 days,

compared with four days for flights 305 and 306. Most of this water is replaced by q_v^{ocn} for the September flights, while q_v^{ld} reaches only about 3-5% for both pairs of flights.

From these mean values, it appears that the water sampled along the flight routes can be considered almost a binary solution of q_v^{init} and q_v^{ocn} . Figure 5.29 shows the ratio in vapor as cross sections for all three partners along each flight.

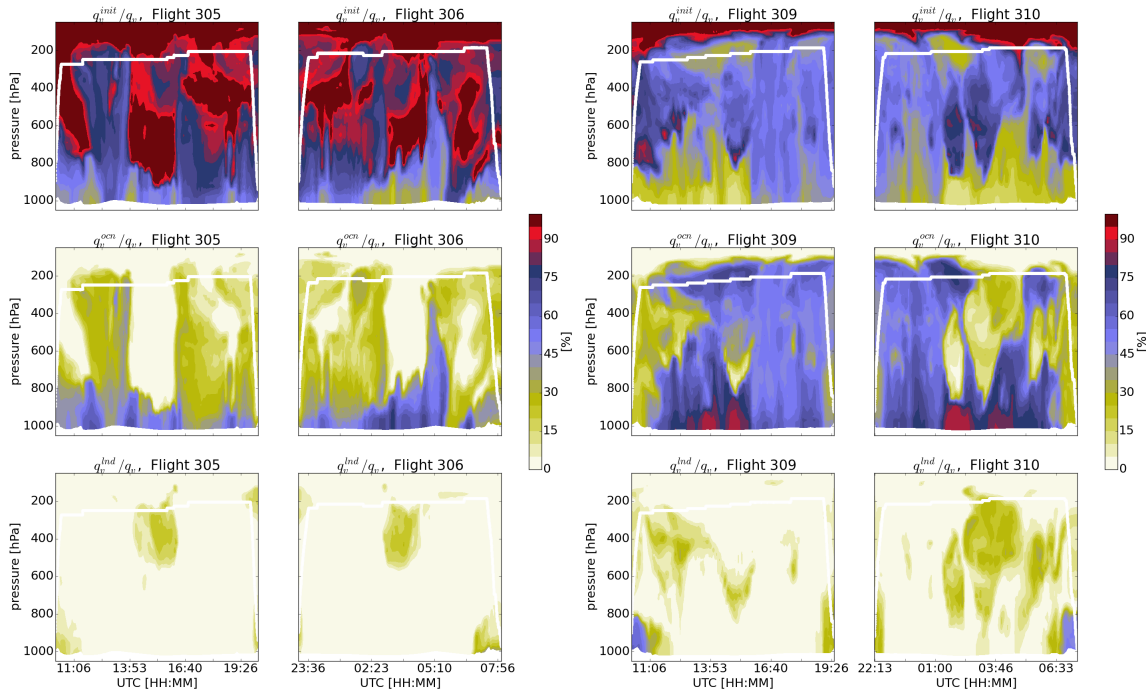


Fig. 5.29.: Ratios of q_v^{init} (top), q_v^{ocn} (middle) and q_v^{ld} (bottom) relative to q_v^{ICON} from two model simulations of ICON-ART-Iso interpolated onto the flight paths of four CARIBIC flights. Left: CARIBIC flights 305 and 306 on August 25, 2010 with ICON-ART-Iso initialized on August 21, 2010. Right: CARIBIC flights 309 and 310 on September 22, 2010 with ICON-ART-Iso initialized on September 12, 2010. See Fig.5.25 for the flight tracks.

For flights 305 and 306 (four days lead time, left panels of Fig. 5.29), q_v^{init} is still present throughout the troposphere, while there are regions of strong vertical ascent that show up as high ratios of q_v^{ocn} , reaching 40% at flight level. After 12 days lead time (right panels of Fig. 5.29), q_v^{init} has withdrawn to higher altitudes and the ocean has expanded its influence. q_v^{ocn} now reaches more than 60% for a substantial time of flight. It is also worthwhile to take a look at q_v^{ld} . The mean value of approximately 5% is not determined only during start and landing times. But all flights also encounter water that contains a non-negligible part of land evaporate. These swaths of vapor are encountered in the middle of flight - just in the center of the Atlantic Ocean (compare Fig. 5.25 for the flight tracks). This translates to a long transport pathway of the air and heavy processing of the contained water.

Figure 5.30 combines values of δD and H_2O along the flight paths with information on the origin of the water that is sampled. The scatter of δD over H_2O is color coded with R^{init} . Because R^{ind} is very low during the longer parts of the flights, $R^{\text{ocn}} = 1 - R^{\text{init}}$ is a good approximation. Green colors indicate $R^{\text{ind}} > 10\%$, where the approximation of a binary solution is not valid.

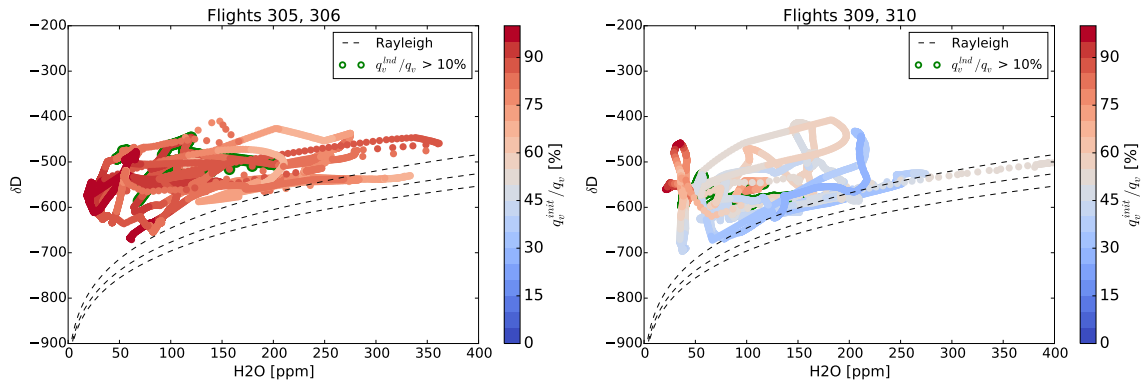


Fig. 5.30.: Scatter of δD over H_2O from two simulations of ICON-ART-Iso interpolated onto the paths of CARIBIC flights 305 and 306 (on August 25, 2010, four days lead time, left panel) and flights 309 and 310 (on September 12, 2010, 12 days lead time, right panel). Color coding indicates the ratio of $q_v^{\text{init}}/q_v^{\text{ICON}}$ in percent. Locations with $q_v^{\text{ind}}/q_v^{\text{ICON}} > 10\%$ are marked in green. Values are considered where $p < 280\text{hPa}$.

As has been discussed above, flights 305 and 306 sample mostly vapor from water set at the initialization (left panel of Fig. 5.30). This water has been processed by microphysics and convection, but the initial state has not been created by the model itself. Generally, the driest air that is encountered also contains the highest amount of q_v^{init} . Those samples that show a relatively high ratio of q_v^{ind} do not have characteristic values of δD and H_2O . The long transport history and the processes during this transport may have diluted a signal that may once have been present.

Flights 309 and 310 (right panel of Fig. 5.30) show a much stronger influence of the ocean, as $R^{\text{ocn}} \approx 1 - R^{\text{init}}$ makes up more than 50% of the sampled vapor. The sampled air is generally drier and slightly more depleted in HDO than for flights 305 and 306. Again, the water with high ratios of q_v^{ind} does not show a special characteristic.

A characteristic signal is seen for those values that are very dry, as they show the highest content in q_v^{init} . Comparing with the top right panels of Fig. 5.29, it is obvious that these values come from the second half of flight 310, which encountered an intrusion of upper tropospheric or stratospheric air at this time. It is interesting to note that this does not imply very low values in δD . These are encountered just after the intrusion (compare lower right panel of Fig. 5.27) and are to a large degree made up of q_v^{ocn} .

Another interesting signal is seen in the spike just above 200 ppm H_2O . While H_2O remains approximately constant at this value, the values in δD are dramatically variable, ranging from -600 to -450. While this spike has a similar shape and reaches values in δD similar to those discussed before, the

content in ocean evaporate is constant at about $R^{\text{ocn}} \approx 1 - R^{\text{init}} \approx 70\%$. It is worthwhile noting that the sample comes from (or goes to) $\{\text{H}_2\text{O}, \delta\text{D}\}$ values that closely follow Rayleigh fractionation. This demonstrates that ICON-ART-Iso is capable of capturing different non-Rayleigh processes including air mass mixing, which are necessary to reproduce this span of $\{\text{H}_2\text{O}, \delta\text{D}\}$.

This section has discussed the influence of q^{init} , q^{ocn} and q^{ind} on the samples of δD , as they are encountered along the flight tracks of the four CARIBIC flights. It has become clear that it is highly non-trivial to relate certain signals in δD to a certain origin of water. High ratios in q^{ind} do not show up specially in δD and certain special features seen in δD cannot be related to only one of the three origins. Of course, this discussion can be expanded by considering more model data, also along different transects. A detailed discussion like this is only possible due to the flexible nature of ICON-ART-Iso, which allows such an investigation with data consistently taken from a single model run.

5.8.5. The two cases in a larger context

The previous two sections have examined CARIBIC δD measurement data of four flights (305, 306, 309, 310) and model results interpolated onto the paths of these flights, focusing on different aspects. This section uses larger samples of measurements and model data to put this data in a larger context.

CARIBIC measurement data of flights 305 and 306 has been shown to be partially influenced by Hurricane Danielle, while flights 309 and 310 are partially influenced by Hurricane Igor (Christner, 2015). In order to use only data from locations influenced by these storms, data from the flight samples is only considered in $0^\circ\text{N} < \varphi < 30^\circ\text{N}$ here, compare Fig. 5.25 for the tracks of the hurricanes and flights. Model data is only considered in those locations where measurements are available, albeit this has little influence on the result.

The larger measurement sample is available from the totality of CARIBIC δD measurements. These are grouped by latitude φ into northern hemisphere extratropical ($23.5^\circ\text{N} < \varphi < 90^\circ\text{N}$) and tropical ($23.5^\circ\text{N} < \varphi < 23.5^\circ\text{N}$) data. These two samples have already been shown in Fig. 5.24. The isolines of probability are again shown in Fig. 5.31 (left panel). The isolines of flights 305-306 and flights 309-310 are also indicated. The tropical samples taken by CARIBIC are substantially more humid than those from mid and high latitudes. They are also less depleted in δD . This is not surprising, considering the relatively constant pressure altitude of the aircraft. Figure 5.31 shows all data, independent of the height relative to the local tropopause. As has been shown before (see Fig. 5.13) there is a strong dependence of δD on the distance to the local tropopause. In general, the distributions are limited by the detection limit of 40 ppm in H_2O .

The CARIBIC measurement data from the two storm samples also show different characteristics. While the range in H_2O is similar, Flights 309 and 310 indicate samples more depleted in HDO. The distribution of flights 305 and 306 shows more tropical characteristics, sampling more humid air and being less depleted in HDO. For flights 309 to 310 on the other hand, the humid branch is missing and δD is lower, overall more similar to the mid-latitude samples.

To create the larger sample of pairs of δD and H_2O from model data, a longer simulation of ICON-ART-Iso was used. This is the same simulation that was compared with IASI data in August 2014, see Sec. 5.7 (initialized on may 5, 2014 and run for almost four months). 30 output files were randomly chosen and from each file, 200 data points were randomly drawn within each of the latitudinal bins also used for CARIBIC (tropical and northern hemisphere extra-tropical). Data was only considered within the pressure range of $180\text{hPa} < p < 280\text{hPa}$. Together with the two samples along the paths of flights 305-306 and 309-310, the probability distribution are shown in the right panel of Fig. 5.31.

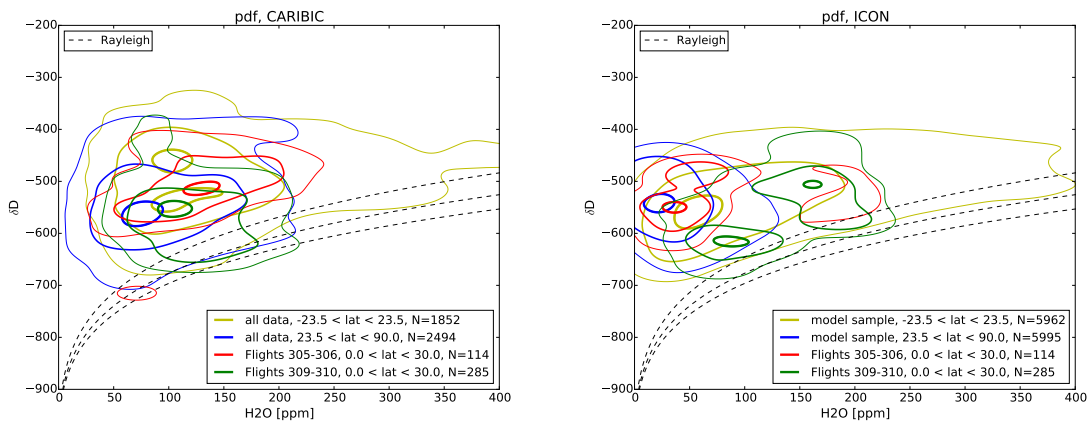


Fig. 5.31.: Probability contours (at 0.1, 0.4 and 0.9) of CARIBIC measurements (left) and ICON-ART-Iso model simulations (right) for larger samples and the two sets of CARIBIC flights (305-306 and 309-310). Model data is interpolated onto the paths of the CARIBIC flights and considered only in locations where there are also measurements. The larger model samples were created by randomly drawing data from a four months simulation, considering the limits in pressure ($180\text{hPa} < p < 280\text{hPa}$). The larger CARIBIC measurement samples are also on display in Fig. 5.24.

The tropical model sample has a similar distribution to that produced by all tropical CARIBIC measurements: There is swath of sparsely populated humid data and the upper limit in δD is roughly at -400 , while the lower limit is formed by the upper Rayleigh curve. But the sample also contains many drier value pairs, with the maximum density shifted to lower mixing ratios in H_2O than in the measurements. This is even more so for the mid-latitude sample, which shows the maximum density for values that are below the detection limit of CARIBIC δD measurements. This technical reason is enforced by the fact that the model sample contains more data from northern latitudes and also more stratospheric data.

The distribution for the four flights is also different in CARIBIC and ICON-ART-Iso, as has been discussed in the previous sections. If model data is only considered at latitudes with $\varphi < 30^\circ N$, a bimodal distribution shows up that was not seen before. This shows that the model was sampled in two distinctively different regions. Both are marked by similar values in δD but by different values in H_2O . This could be caused by the two branches of the Hadley cell, with humid air ascending in the tropics and

dry subsidence in the subtropics (Holton and Hakim, 2013). The effect of the aircraft crossing these two regions is also seen in the cross sections in Fig. 5.29 in the ratio of ocean evaporate to standard water, R^{ocn} with high values close to South America and lower values over subtropical Atlantic. But more data, again also taken along more transects, is needed to investigate the effects of this circulation. It would also have to be investigated in a longer model run, with the state of δD being fully developed, i.e. low values of R^{init} .

This section has shown compared larger mid-latitude and tropical samples of CARIBIC and ICON-ART-Iso data. The CARIBIC measurements are very valuable as a reference. But the detection limit for δD and the geographical coverage limit their representativeness for δD , as has already been pointed out in Sec. 5.8.1. It is remarkable that the tropical samples - i.e. those that are less influenced by the detection limit of the measurements - are quite similar in measurement and model data. The overall characteristics of the CARIBIC dataset are reproduced by the model, while details remain to be analyzed in future studies.

5.8.6. Simulation of the CARIBIC flights with COSMOiso

The previous sections compared data from two CARIBIC return flights to Caracas in 2010 with ICON-ART-Iso model simulations. This section compares the same flights with model simulations of COSMOiso. COSMOiso is a very different model, but it is interesting to compare results to ICON-ART-Iso, as the fractionation code of COSMOiso served as a reference for the development of ICON-ART-Iso. COSMO is also one of the predecessors of ICON in general.

COSMOiso is a regional model developed and first presented by Pfahl et al. (2012). Like ICON-ART-Iso, it is also non-hydrostatic, but the microphysics as well convection and advection are quite different. And since it is not a global model, values are needed at the lateral and vertical boundaries, also for the isotopes. In case of the simulations presented here, the boundary values are provided by the global, nudged isotope enabled model IsoGSM by Yoshimura et al. (2008) with yet different physics. Regional models, always being constrained by their boundaries, are, on the other hand, an ideal tool for case studies.

Two simulations were set up with COSMOiso. The domain is the same for both and is shown in Fig. 5.25. Boundary data was provided by Stephan Pfahl of ETH Zürich. The simulation for flights 305 and 306 was initialized on August 21, the simulations for flights 309 and 310 on September 12, 2010. Figure 5.32 shows the result as cross sections along the flight paths.

The range of values is similar to that simulated by ICON-ART-Iso (see Sec. 5.8.3) with surface values of approximately -50 and tropopause values reaching -720 in δD . In general, the tropopause seems more elevated in COSMOiso. Despite the fact that COSMOiso is a regional model, it does not do better at reproducing the measurements. This is not a statement about COSMOiso alone, but the error could also stem from IsoGSM, which sets the boundary values.

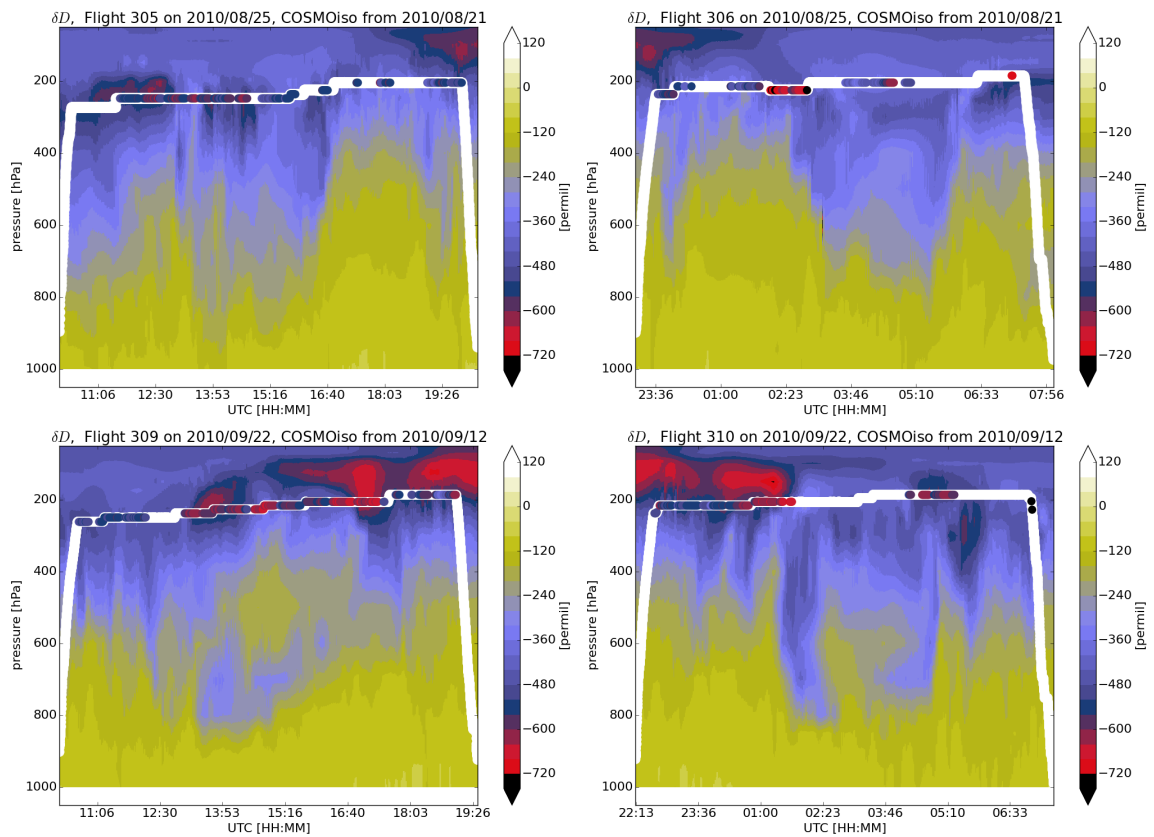


Fig. 5.32.: Crosssections of δD from two different COSMOiso simulations initialized on August 21, 2010 (top) and September 12, 2010 (bottom) on the domain indicated in Fig. 5.25. The output is interpolated onto the flight track of CARIBIC flights 305 and 306 (top) and 309 and 310 (bottom) during Hurricanes Danielle and Igor, respectively. Flight altitude is indicated in white, colored values inside the white line represent measurements.

The values are not only set at the lateral boundaries, but also at the model top. The Rayleigh damping layer of COSMOiso starts in model level 13 (counting from model top downwards), which is at around 220 hPa. Within this layer the model fields of COSMOiso are relaxed towards those of the driving model. The model data at flight altitude is therefore also directly influenced by IsoGSM. This is visible in cross sections of tagged water vapor. Similar to q^{ocn} and q^{land} in ICON-ART-Iso, the tagged water evaporates from ocean and land points inside the model domain. It reaches 11.26% for flights 305 and 306 and only 15.21% on average for flights 309 and 310 despite the longer lead time. As has been discussed in Sec. 5.8.4, ICON-ART-Iso reaches more than 50% ocean evaporate for flights 309 and 310. Cross sections of tagged water in COSMOiso show that there is a distinct upper boundary reached by the evaporate that is slightly below flight level. This underlines the strong influence of the driving model in the upper layers. Figure 5.33 exemplarily shows cross sections of the ratio q_v^{tag}/q_v for flights 306 and 310.

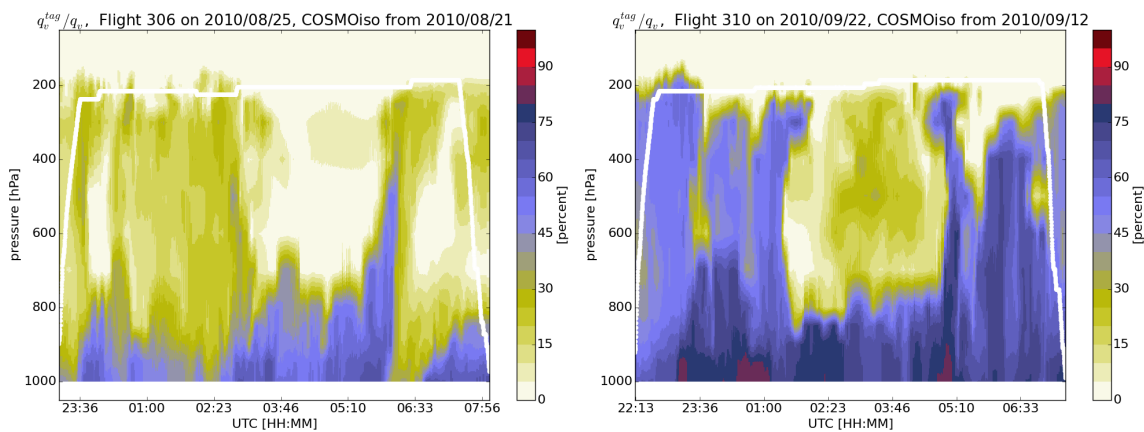


Fig. 5.33.: Ratio of q_v^{tag}/q_v along flight tracks 306 (left) and 310 (right) from simulations of COSMOiso. q_v^{tag} is vapor that evaporates from the ocean and land masses within the domain during the model simulation.

All these constraints make a direct comparison of ICON-ART-Iso and COSMOiso difficult. For a direct comparison of the model physics and in a future study, COSMOiso could be set up to use boundary values provided by ICON-ART-Iso. This has not been implemented for COSMOiso. The strong influence of the boundary model physics in the upper layers of COSMOiso also makes it difficult to use for comparison with CARIBIC data in the current setup. The model could be expanded in the vertical by using the layering presented by Eckstein et al. (2015).

5.8.7. Summary: CARIBIC and ICON-ART-Iso

This chapter presented a case study, in which simulations of ICON-ART-Iso are compared with in situ measurements of δD from the CARIBIC dataset, using data from four flights in August and September 2010. Because ICON-ART-Iso can only calculate forecasts at the moment - no nudging has been imple-

mented - the storms encountered by these flights were not simulated in a way to make a direct comparison with the measurements feasible.

This is demonstrated by comparing model simulations with different initialization dates. The high measurement uncertainty also leads to weak correlation coefficient. But the mean offset of model and measurement data is small, which is a promising result.

The following section investigated the situation within ICON-ART-Iso, examining the origin of the water vapor that is sampled along the flight track. Using different instances of water, it is shown that the attribution of pairs of δD and H_2O to a certain origin is not trivial. But different values of δD are simulated for similar H_2O mixing ratios at high ratios of ocean evaporate. This shows the potential of ICON-ART-Iso for investigating different processes.

The next section puts the samples from the four flights into a larger context, from the perspective of measurements and model data. The general characteristics of the CARIBIC δD dataset are reproduced by the model. But the detection and geographical limits in the CARIBIC dataset make a climatological investigation difficult.

The time periods of the flights were also simulated with the regional model COSMOiso. This model that served as a reference during the development of the fractionating code of ICON-ART-Iso, but it proved difficult to compare CARIBIC data with COSMOiso. The flight altitude is within the relaxation layer of the model and the simulated values along the flight paths are therefore strongly influenced by the driving model IsoGSM.

In all sections, it has become clear that the potential of ICON-ART-Iso is large to advance the understanding of the water cycle in the model. Measurements can be given a context, increasing what can be learned from them.

5.9. Summary and outlook

The intent of this chapter is twofold: Presenting the novel isotope enabled model ICON-ART-Iso and discussing the possibilities of using CARIBIC δD data to validate this model.

ICON-ART-Iso is the isotope enabled version of the atmospheric model ICON. It is shown to be a flexible model to simulate diagnostic instances of water, which can be set to resemble either H_2O or the stable isotopes HDO or $H_2^{18}O$. Simulating diagnostic H_2O allows to test the model stability and opens new applications as different evaporation regions can be set for different H_2O instances. These diagnostic instances are used for a first investigation of the water cycle in the model. The source regions for precipitating water over ocean and land surfaces in a winter and summer case are shown to vary by season and latitude.

The diagnostic instances of water can also be set to fractionate at phase changes to resemble HDO or $H_2^{18}O$. The different parameterizations that have been implemented for fractionation are explained in detail. Their influence is discussed, showing that fractionation at ice formation leads to the strongest depletion in the isotopes, while saturation adjustment has the smallest influence. The different processes during convection also have a strong effect on the distribution of the isotopes. The isotopes are initialized with mean measurement values. It is shown that the exact values of this initialization are increasingly irrelevant as the model simulation progresses in time and a consistent model state evolves.

The model results are then compared to pairs of δD and H_2O retrieved from IASI satellite data in a summer and winter case. The latitudinal dependence of these pairs is comparable to those from IASI retrievals. The annual cycle could not be examined because sea surface temperatures were kept constant during the simulations. The difference between land and ocean surfaces in the tropics and subtropics in the model is of similar magnitude in the measurements. The daily cycle that is seen in the satellite data is not reproduced in the model. Overall, the performance of ICON-ART-Iso is already similar to the isotope enabled climate model ECHAM5-wiso. Instances of H_2O which evaporate only from land and ocean only are shown to be a useful tool to characterize δD values.

A first comparison with in situ measurement data uses δD values from four CARIBIC flights transecting the Atlantic. A direct comparison with ICON-ART-Iso proves difficult. The model cannot yet be nudged to a meteorological analysis, so the model synoptics are different to the real situation. But the measurement uncertainty is also quite high, making an exact match to model simulations difficult. This is discussed with the help of simulations initialized on different dates prior to the flights. By analyzing the ICON-ART-Iso data alone, it is shown that the transects along the flight paths contain evidence of different, very localized processes. ICON-ART-Iso is able to reproduce the general features of full the CARIBIC dataset, while a comparison beyond case studies is difficult due to limitations of the measurement data. The performance of ICON-ART-Iso for these cases is similar to that of the regional model COSMOiso, which has its own technical shortcomings that make a comparison with CARIBIC data difficult.

This chapter documents the potential aircraft data have for validating models in case studies. The high temporal and spatial resolution outweigh the limitations set by the geographical coverage. Small scale processes become accessible that remain obscured in a comparison with data retrieved from satellite measurements.

ICON-ART-Iso itself is a promising tool for future investigations of the water cycle. It compares well with the other isotope enabled models ECHAM5-wiso on a seasonal and COSMOiso on a very local scale. For future applications, it would be interesting to implement a nudging towards meteorological analysis to make comparisons with measurements in case studies feasible. By implementing the newest features of ICON-ART, simulations with increased horizontal resolution in localized nests could be performed. Fractionation for different microphysical schemes should be implemented, which would make the model better applicable to climatological questions by increasing the speed of the model. Due to its flexible set up, it is ready to simulate instances of H₂¹⁷O or to be used for testing new microphysical parameterizations. In its current state already, the modeling system has the potential to increase the understanding about source regions and transport pathways in the hydrological cycle.

6. Conclusions

The aim of this thesis is to show the multitude of ways in which atmospheric models and aircraft measurements can benefit from one another. For this purpose, measurements from the IAGOS-CARIBIC dataset are compared with the output of model simulations for different purposes. The thesis is structured into three main parts: Chapter 3 uses IAGOS-CARIBIC measurements for a climatological validation of EMAC. The next chapter uses another integration of EMAC to investigate the climatological representativeness of the IAGOS-CARIBIC dataset. The third main chapter (Ch. 5) introduces the isotope enabled atmospheric model ICON-ART-Iso, which is validated with data from IAGOS-CARIBIC.

While each of these chapters can be considered a separate study, there are several linking subjects and lines of development. Figure 6.1 shows a schematic diagram which illustrates how the different subjects and chapters are related to one another.

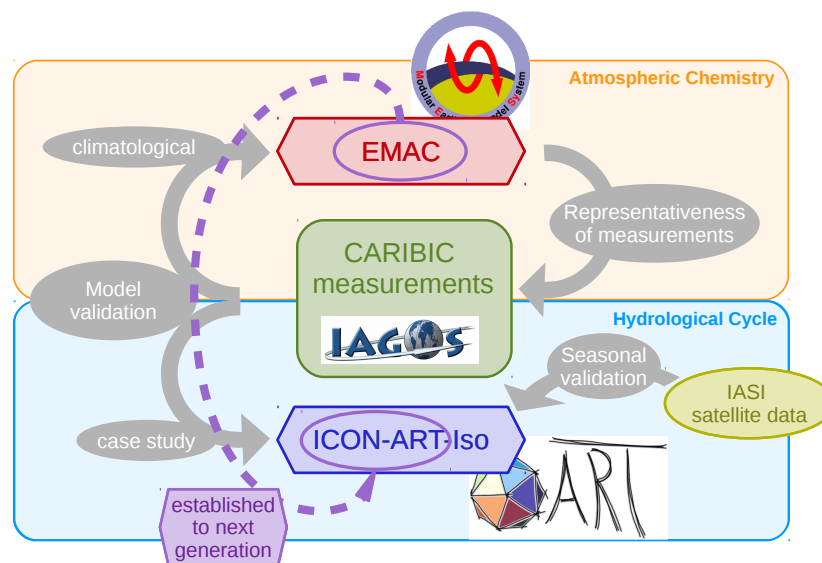


Fig. 6.1.: Schematic diagram to illustrate the connections between the different chapters and the lines of development traceable through the thesis. Chapters 3 and 4 use IAGOS-CARIBIC trace gas measurements and EMAC model simulations in reciprocal studies of climatological model validation and measurement representativeness in the scope of atmospheric chemistry. Chapter 5 shifts the scientific focus to the hydrological cycle and presents the new isotope enabled model ICON-ART-Iso. This model is validated on a seasonal time scale with IASI satellite data. IAGOS-CARIBIC data are used in a case study which considers four flights.

Chapter 3 uses IAGOS-CARIBIC measurements of O₃, CH₄, CO and acetone to validate climatological simulations of the chemistry-climate model EMAC performed within the ESCiMo project. While the model is able to reproduce the general feature of the climatologies of O₃, CH₄ and CO, the study reveals shortcomings in simulating acetone. This is an example how data from the long running measurement project IAGOS-CARIBIC can be used to validate models on a climatological time scale.

The examination of the climatologies of IAGOS-CARIBIC measurements and EMAC in Ch. 3 quickly leads to the climatological representativeness investigated in Ch. 4. Climatologies are easily compiled from the IAGOS-CARIBIC dataset, but it remains unclear whether they are representative of the mean seasonal cycle of the upper troposphere and lower stratosphere. This is investigated with a nudged climatological integration of EMAC. The IAGOS-CARIBIC sampled model data is compared to the mean model state and representativeness is given a sound mathematical definition. A separate section discusses under which conditions the conclusions from the model datasets can be applied to IAGOS-CARIBIC measurements. The climatological representativeness of IAGOS-CARIBIC measurements is then discussed and the limitations of the dataset in longitude and pressure are examined. The chapter demonstrates how a model simulation can add value to the IAGOS-CARIBIC dataset on climatological time scales. The general concept can be applied to similar questions, for which the model can take the role of a statistical database to test a hypothesis about a limited sample.

The last of the three main chapters presents ICON-ART-Iso, the new isotope enabled version of the general circulation model ICON. The physics to describe the fractionation of the isotopes are explained in detail. The results of the flexible modeling system are demonstrated to be self-consistent by examining fields of diagnostic water and the different fractionation parameterizations. But only the comparison with measurement data makes the model results meaningful. A comparison with IASI satellite data serves to validate the model on a seasonal time scale. These results are also compared to the isotope enabled climate model ECHAM5-wiso. In a case study, four IAGOS-CARIBIC flights are then used to validate ICON-ART-Iso. Its capability to capture small scale processes is demonstrated and the additional diagnostic water instances are shown to be of great value for the examination of the results. The results are also compared to COSMOiso, the isotope enabled version of the predecessor of ICON. This chapter returns to models profiting from the measurements, but on a very different scale to Ch. 3. Here, it is the high temporal and spatial resolution of IAGOS-CARIBIC that makes the dataset valuable.

The most obvious connection that carries through all chapters of this thesis is the IAGOS-CARIBIC dataset. Its value for validation on a climatological time scale and in case studies is demonstrated. This is only possible because it is a long running project and at the same time provides data at a high temporal and spatial resolution. The difference to satellite data is demonstrated by a validation of ICON-ART-Iso with IASI measurements.

Another development line can be traced through this thesis by considering the different models. EMAC is an established, state of the art chemistry climate model. By limitations due to the physics and numerical implementation of its base model, the horizontal resolution remains limited. ICON-ART is based on the

new model ICON which overcomes these limitations and can be applied for climatological studies as well as numerical weather prediction. This is demonstrated by comparing with data from ECHAM5-wiso, which uses the same base model as EMAC, and with data from the limited area model COSMOiso. ICON-ART-Iso compares well to both modeling systems.

The scientific scope of the first two chapters is the climatological analysis of atmospheric chemistry. While the last chapter moves on to the hydrological cycle, it also shifts the focus from climatological applications to case studies that serve to increase the understanding of small scale atmospheric processes. As the resolution of atmospheric models is becoming finer, the scientific focus is increasingly shifting to understanding small scales, while a correct climatological model state must be retained. ICON-ART-Iso is built on a modeling system that can serve both the climatological and the very local scale and is therefore ready for many future applications.

In different scientific fields and on different scales, this thesis demonstrates how aircraft measurements can be used to validate model developments and how a model integration can add value to the long running IAGOS-CARIBIC measurement project. Studying the complex system that forms the atmosphere requires both, measurements and model simulations. Only if the two are combined can we evaluate the meaning of measurements or be sure that models simulate realistic values. Together, models and high resolution measurements can become partners to advance our understanding of the atmosphere.

A. Climatological validation within the ESCiMo project: Additional figures

This section presents additional figures for Ch. 3. Two panels are presented for each of the species O₃, CO, CH₄ and acetone. The first panel shows the climatologies for each of the five model runs and for the measurements. The second panel shows all the relative differences between corresponding simulations. Ch. 3 gives a detailed interpretation.

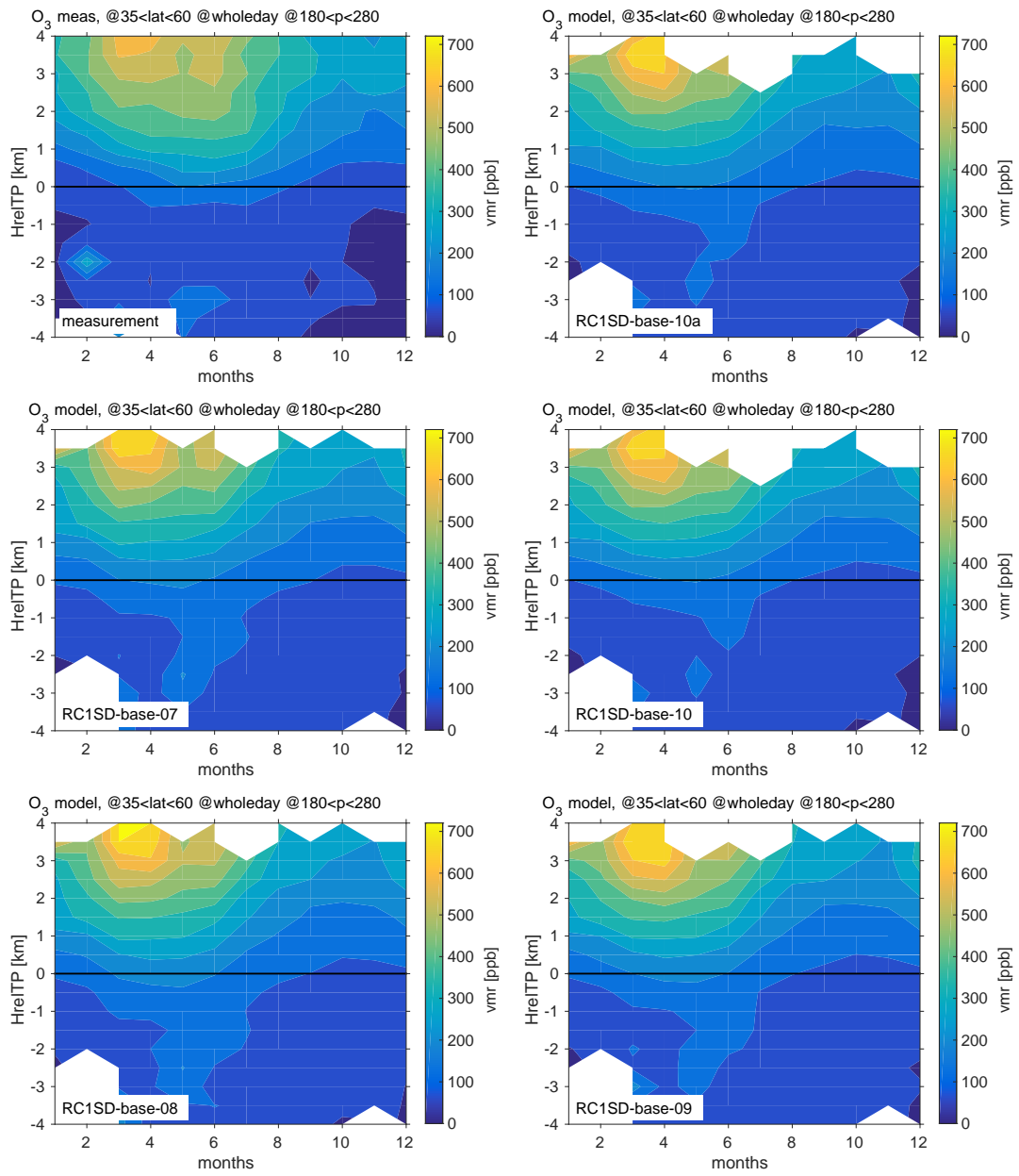


Fig. A.1.: Climatology for O₃ of CARIBIC measurements (top left) and all five model simulations.

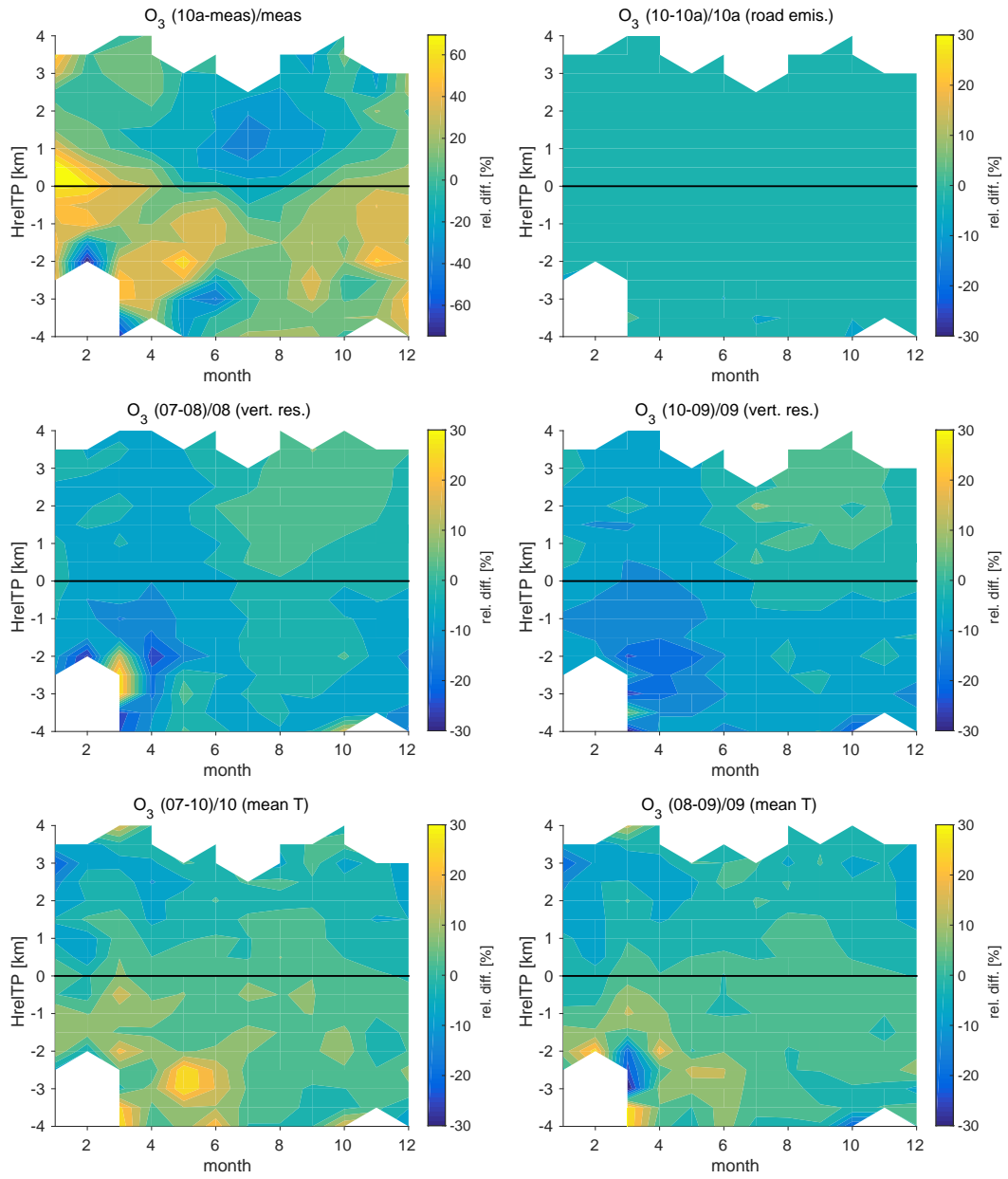


Fig. A.2.: Relative differences for O₃ of the measurements and model run *RCISD-base-10a* and all the corresponding pairs of model simulations.

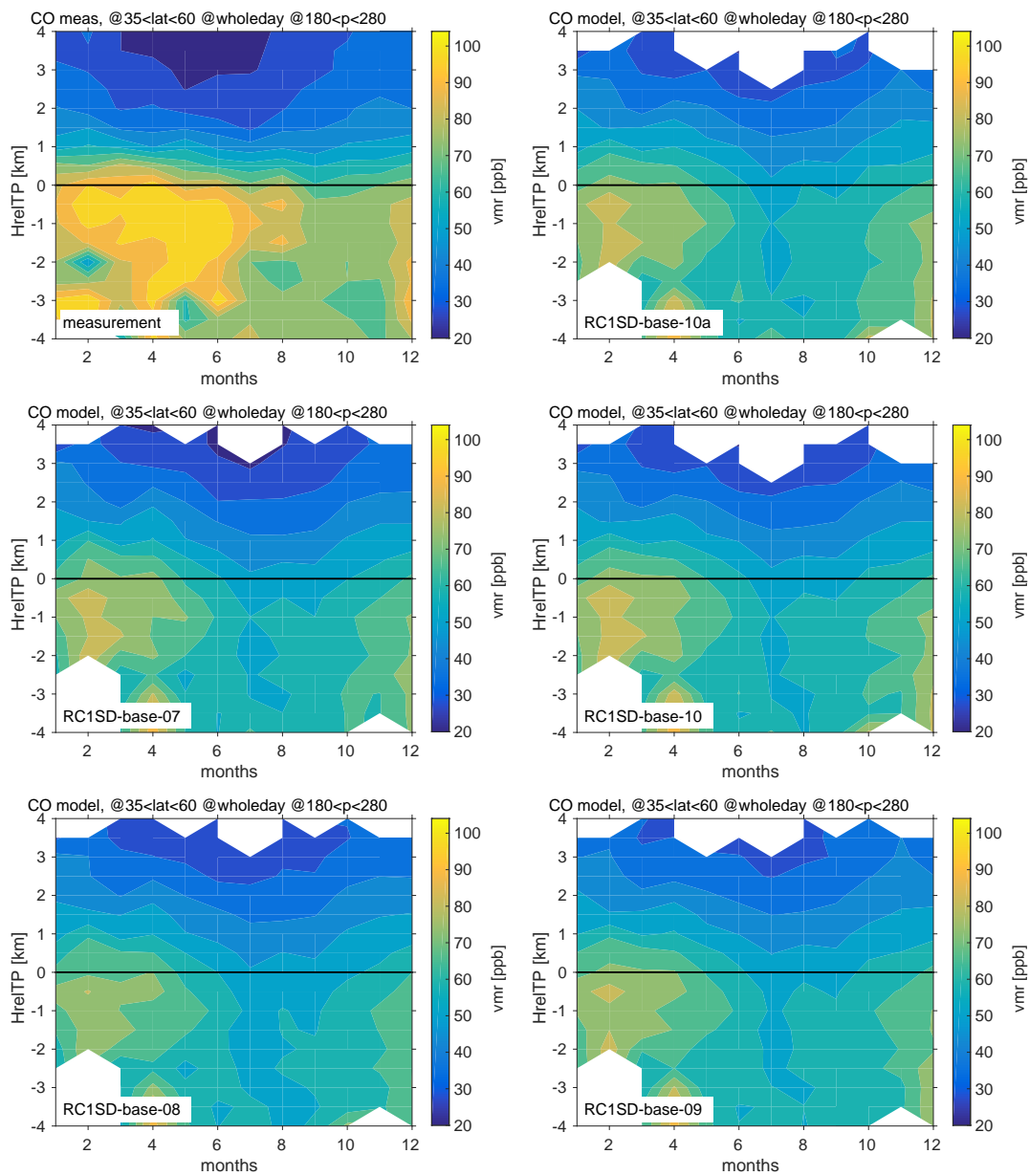


Fig. A.3.: As Fig. A.1, but for CO.

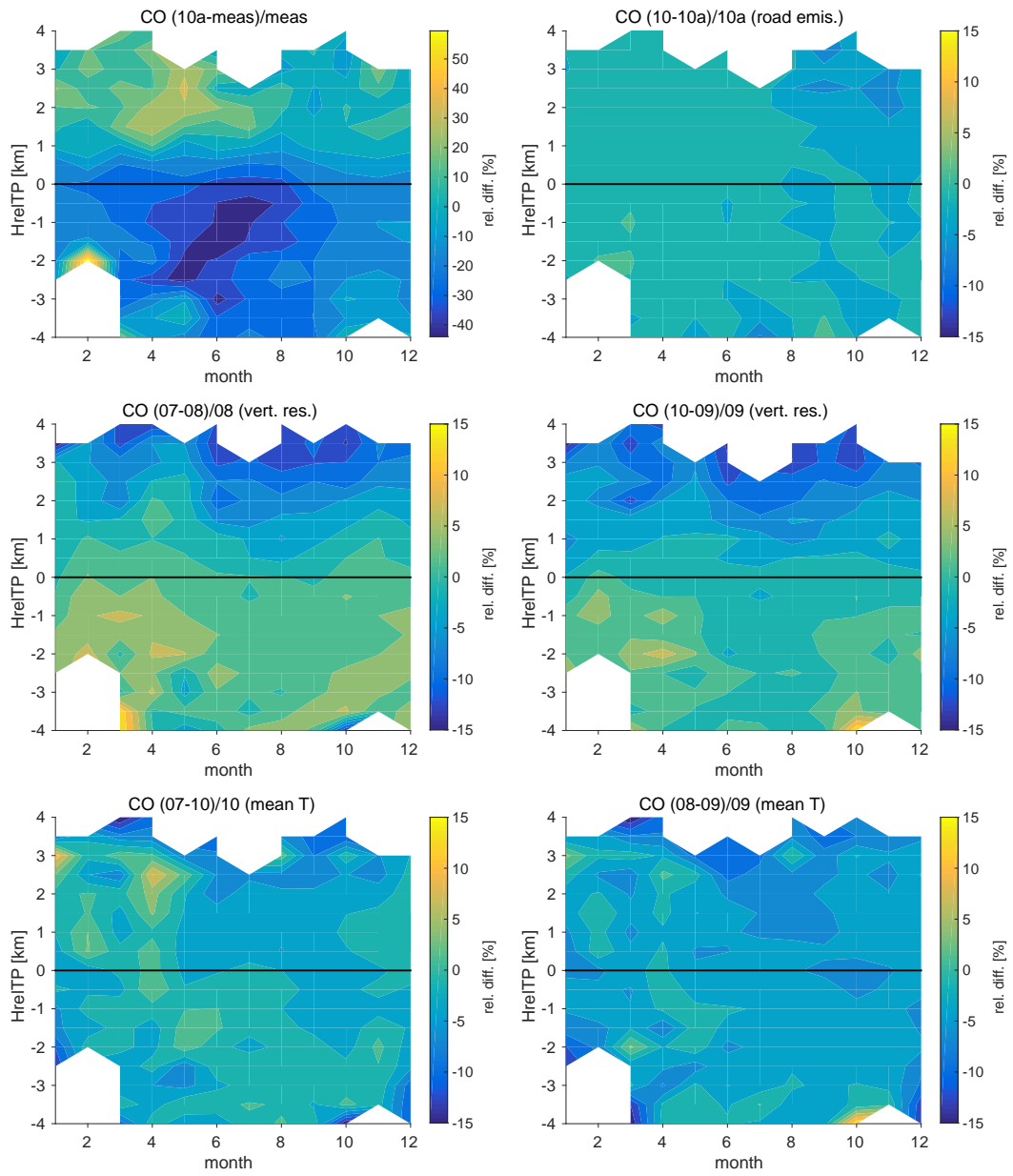


Fig. A.4.: As Fig. A.2, but for CO.

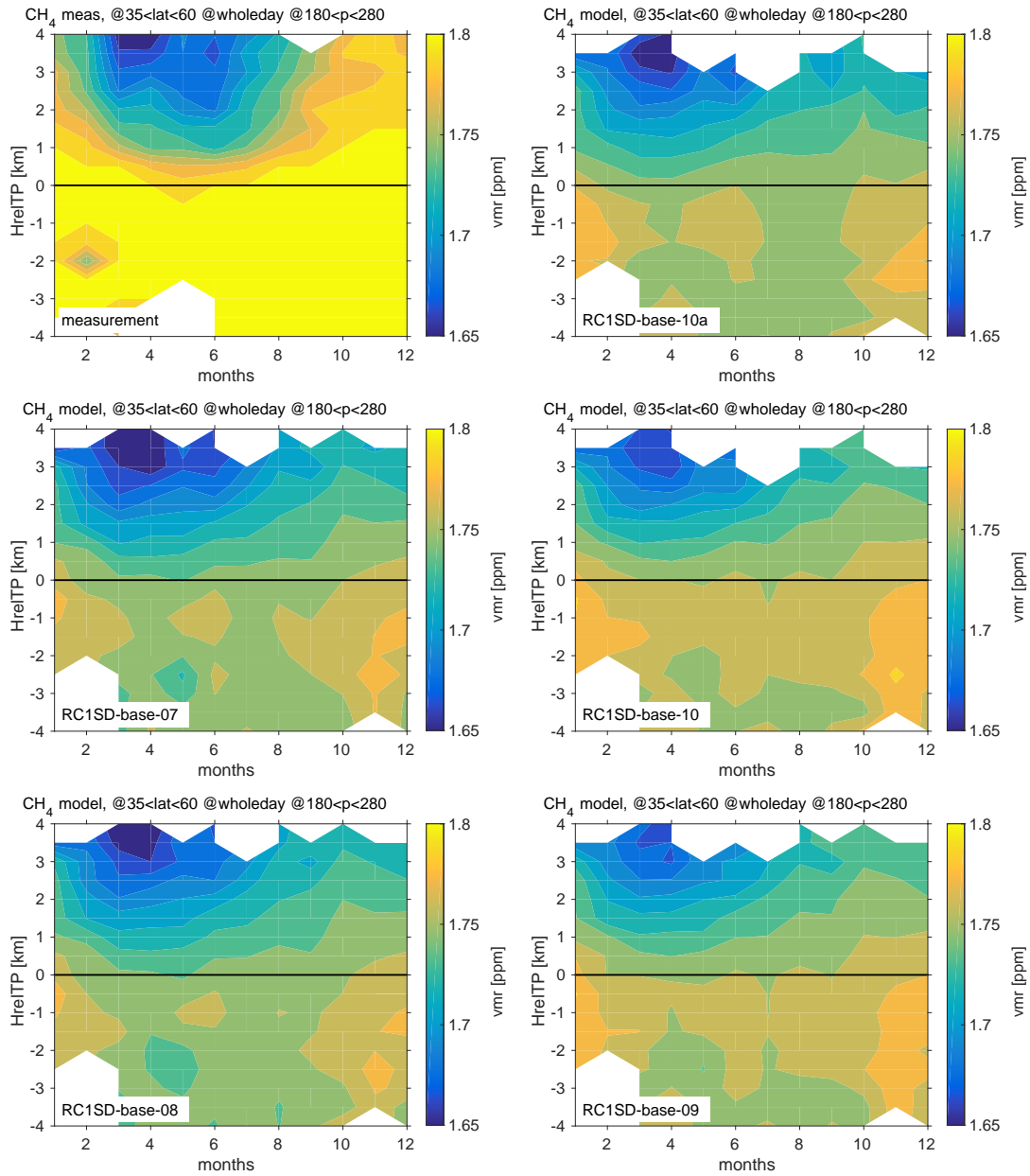


Fig. A.5.: As Fig. A.1, but for CH₄.

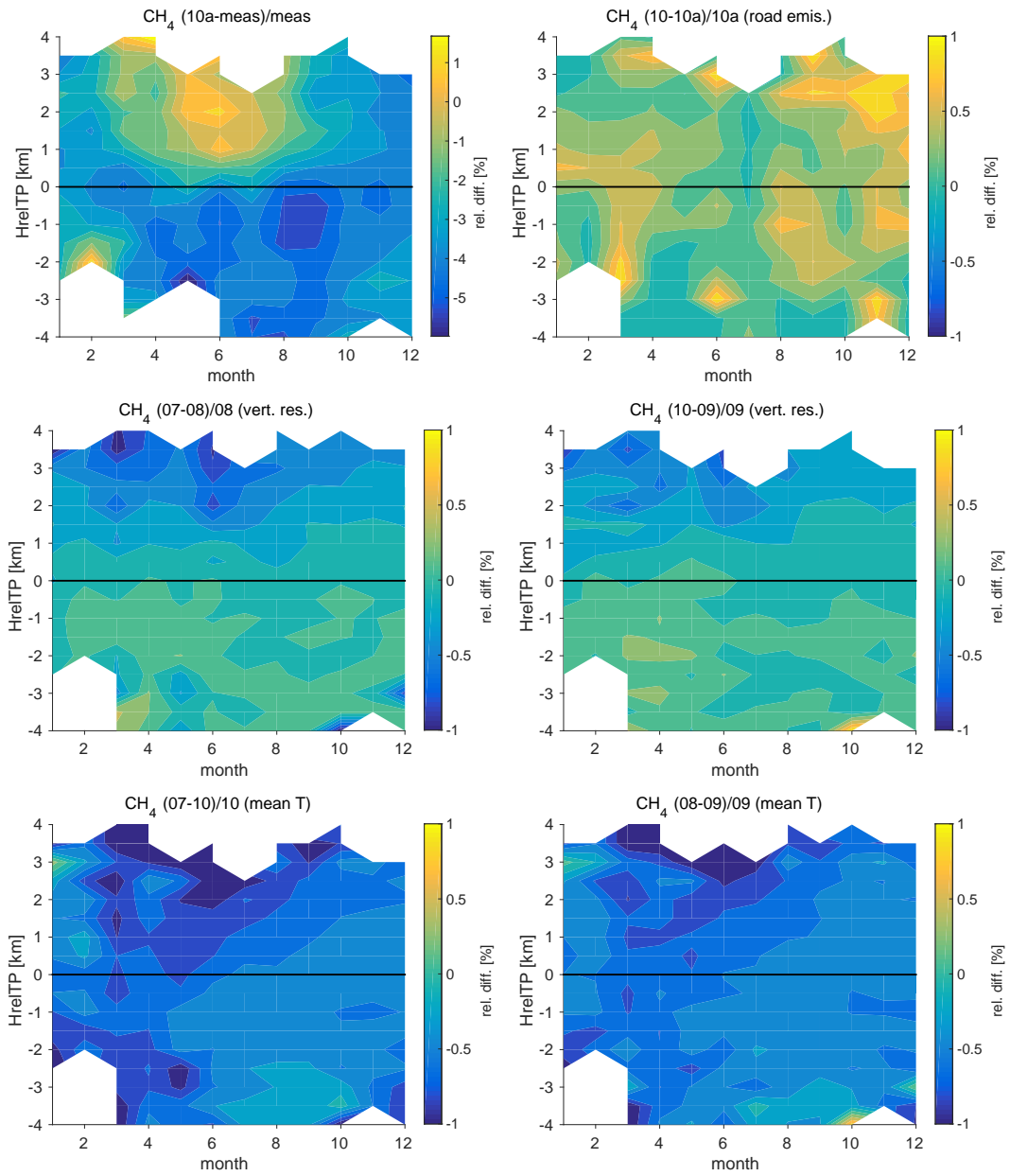


Fig. A.6.: As Fig. A.2, but for CH₄.

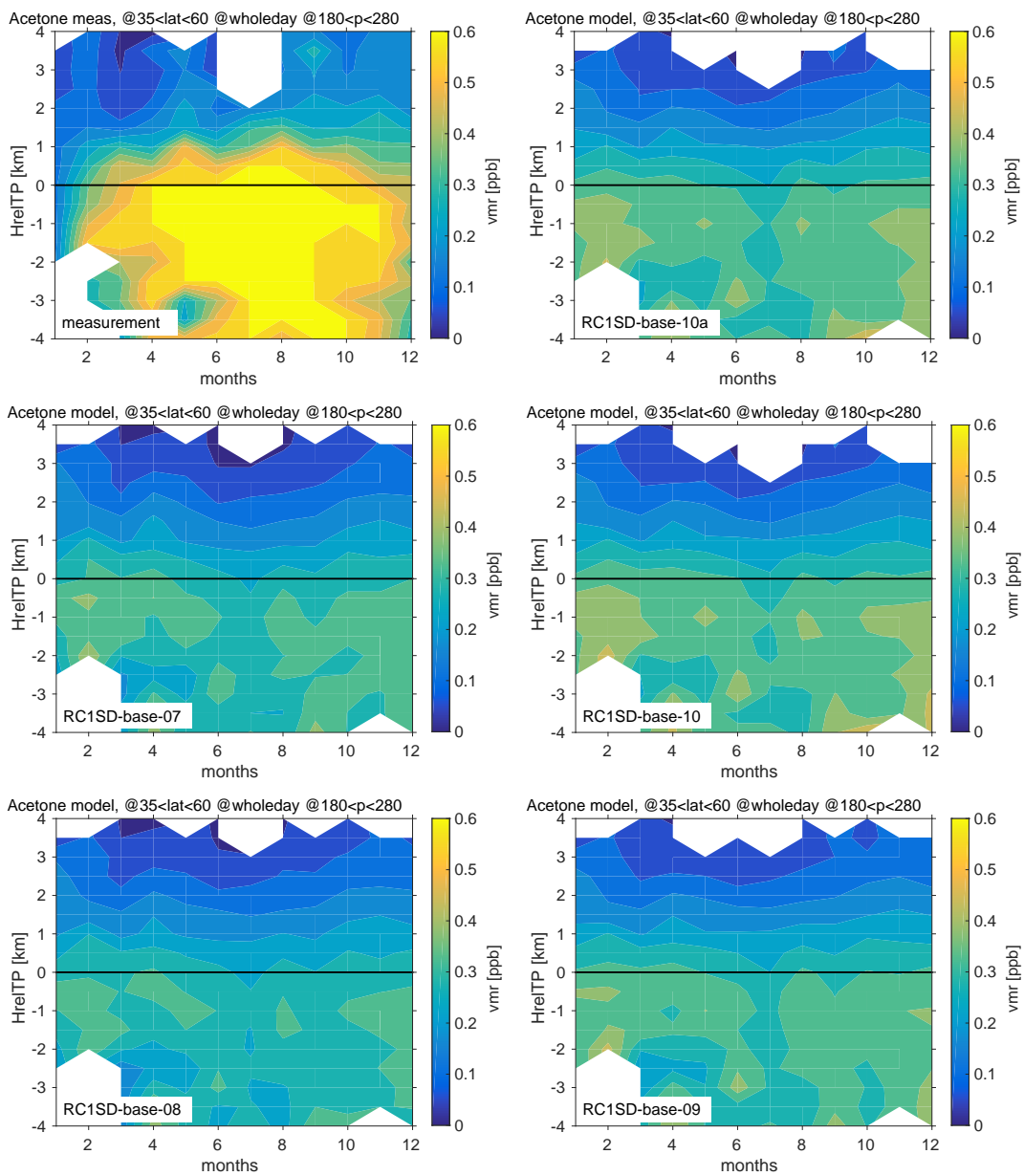


Fig. A.7.: As Fig. A.1, but for acetone.

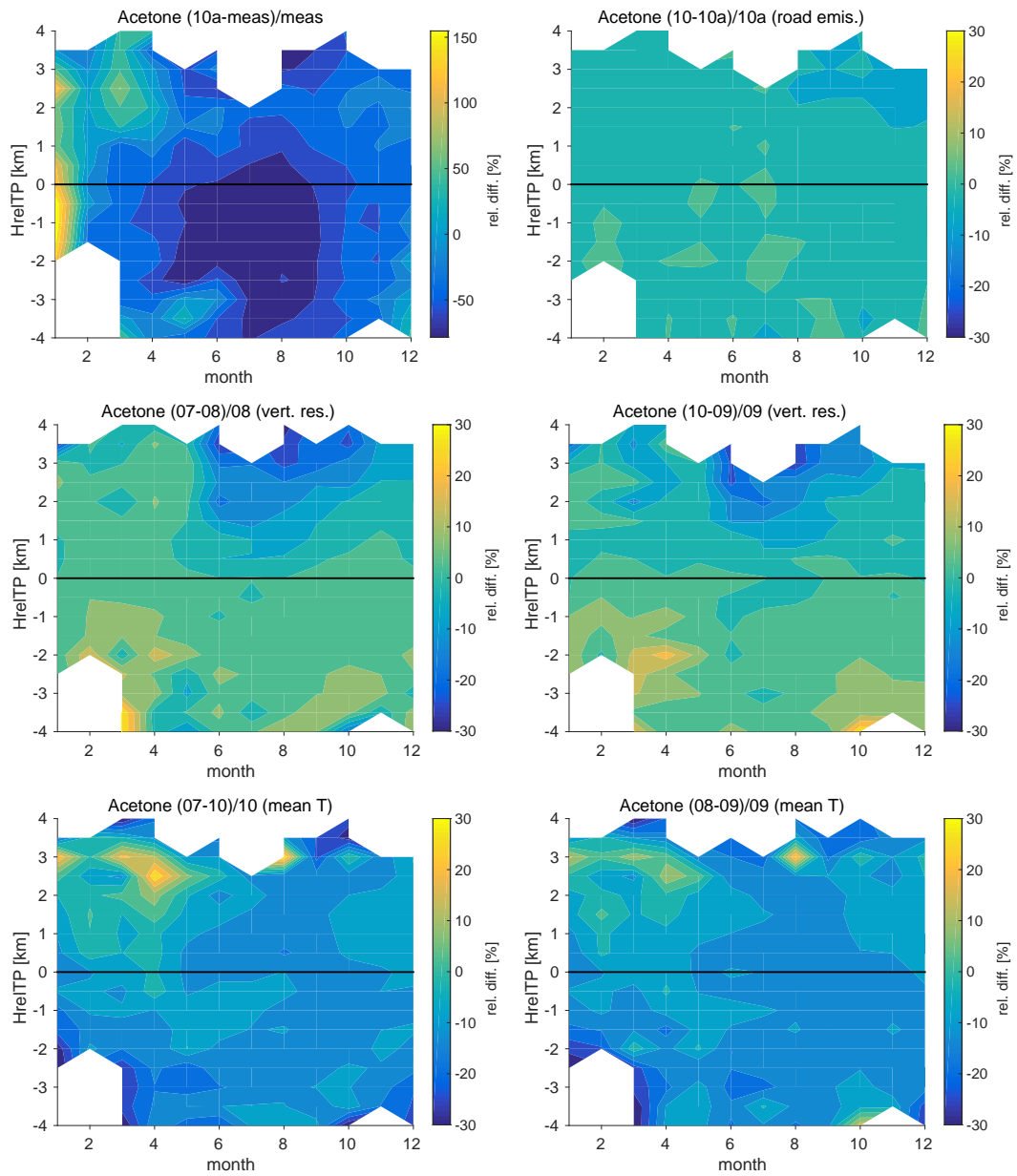


Fig. A.8.: As Fig. A.2, but for acetone.

B. Technical description of ICON-ART-Iso

This section of the appendix gives a technical description of the model ICON-ART-Iso. Section B.1 describes the necessary and possible settings in the namelist of ICON. As most settings for a simulation of ICON-ART-Iso are done in an XML table, this section also gives an example of possible, meaningful settings and gives a summary of all the possible entries that can be made to the XML table. Overall, Sec. B.1 could be considered a first draft of a user guide to the model, while it depends on the knowledge of the user about the model ICON and the ART extension.

Section B.2 gives a detailed technical overview. Each parameterization is technically explained, stating where and how it has been implemented in the code. Finally, Sec. B.3 describes a list of technical projects that could be implemented in the future. It also contains a list of ideas for larger development projects that would expand the possible applications of ICON-ART-Iso.

B.1. Namelist and XML settings

This section gives an overview over the settings that can be made regarding ICON-ART-Iso. These are set in the namelist file for ICON and in an XML file. While Sec. B.1.2 and B.1.3 explain namelist and XML settings in detail, Sec. B.1.1 gives an example of settings that can be made for first simulation of ICON-ART-Iso.

B.1.1. Example of settings

This section gives an example of settings that can be made to run ICON-ART-Iso and shortly explains the general idea behind each set of settings. The details of all settings are explained Sec. B.1 for namelist and XML file in the form of tables, while Sec. B.2 gives more details in free form, also discussing technical details. This section lists and shortly explains a reasonable example of settings. It is not a user guide to ICON or even ICON-ART, it rather builds on the userguide supplied with these two. Knowledge of them are prerequisite for running ICON-ART-Iso.

In the namelist, `lart_iso` has to be set to TRUE, while `cart_isotopes` contains the path to the XML file for the settings of the isotopes. `lart_ntracer` does not have to be set. All the other parameters can be set like for a regular simulation of ICON-ART, but adaptation of the two-moment scheme for ICON-ART has to be chosen, specified by `inwp_gscp = 6`.

All settings for ICON-ART-Iso itself are made in the XML file, for which Table B.1 gives an example. The settings given in the table will result in six different diagnostic water substances, called isotopes in

the following. The summarized meaning of the settings is shortly discussed in the following paragraphs.

id	H20tot	H20ini	H20lnd	H20ocn	HDO	H218O
isoflavor	1	1	1	1	2	3
equifrac_liq	1	1	1	1	201	301
equifrac_ice	1	1	1	1	201	301
iratio_diff	1	1	1	1	1	1
ratio_init	1.0	1.0	1.0	1.0	1.0	1.0
init	1	1	0	0	3	3
surf_land	1	0	1	0	2	2
surf_ocean	1	0	0	1	2	2
evap_land	1	2	2	2	3	3
evap_ocean	1	2	2	2	3	3
satad	1	1	1	1	2	2
gscp	1	1	1	1	2	2
gscp_evapfrac	0	0	0	0	1	1
gscp_icefrac	0	0	0	0	1	1
conv	1	1	1	1	1	1
conv_satad	0	0	0	0	1	1
conv_evapfrac_ddr	0	0	0	0	1	1
conv_evapfrac_flx	0	0	0	0	1	1
opt_idelta_style	2	1	1	1	-	-

Tab. B.1.: An example of settings for the XML file which is needed to run ICON-ART-Iso. `transport` should be set to `readiso` for all isotypes. The `id` is not an XML key but an attribute to `<isotype>`.

The isotype `H20tot` is a diagnostic that should always be equal to the ICON tracers: It is initialized with the values of ICON, and all processes that happen to water in ICON also affect this isotype, without considering fractionation. By setting `opt_idelta_style` to 2, the output of `group:ART-Iso_delta` will include differences to the ICON tracers correspondingly for this isotype.

The isotype `H20ini` is also initialized with ICON water and sees all processes, but surface values are set to zero and evaporation is set to be non-fractionating. The mixing ratios of the corresponding tracers will continuously drop and the water will precipitate out of the model domain or condense on the ground. The condensation on the ground is the reason to use non-fractionating evaporation instead of turning it off. This isotype serves to indicate the influence of the initialization. `H20lnd` and `H20ocn` on the other hand are initialized with zero. `H20lnd` evaporates only from land surfaces, while `H20ocn` evaporates only from ocean surfaces (they both condense without fractionation). By including these two,

the part of water that is influenced by land or surface evaporation can be determined. This is interesting, as land surface processes are not explicitly included in ICON-ART-Iso. `H2Oini`, `H2O1nd` and `H2Oocn` will write out ratios in percent of the ICON water tracers, as `opt_idelta_style` has been set to 1 (if `group:ART-Iso_delta` is given out).

Last but not least, the isotopes `HDO` and `H218O` simulate the distribution of H_2O and H_2^{18}O . They are initialized with climatological values and fractionate during evaporation, saturation adjustment, microphysics and convection. All fractionating options have been set to 1 (2 for `satad`), so the same parameterizations as in `COSMOiso` are used (Pfahl et al., 2012). Because `opt_idelta_style` is not set, correct δ values will be written out for each tracer if `group:ART-Iso_delta` is specified.

B.1.2. Namelist overview

This section gives a short overview on the namelist parameters that can be set to enable and alter simulations with ICON-ART-Iso. The namelist is commonly part of the file used to submit a simulation experiment. For an example, refer to `exp.testsuite.iso` in `art/runctrl_examples/run_ctrl/`. The namelist has limited options for ICON-ART-Iso. Since its goal is the simulation of a diagnostic water cycle, most settings are made in the other namelist blocks that determine the behaviour and setup of the ICON model itself. Of course, not all choices of ICON have been implemented in ICON-ART-Iso.

Necessary choices for a working simulation of ICON-ART-Iso are therefore given in Sec. B.1.2.1. Sec. B.1.2.2 then describes the few namelist switches that properly belong to ICON-ART-Iso. They are part of the ICON-ART namelist, `art_nml`. Sec. B.1.2.3 explains the output groups that are available. Most settings concerning the simulation of isotopologues are made separately for each isotopologue in an XML file. The possible settings in the XML file are explained in Sec. B.1.3.

B.1.2.1. ICON and ICON-ART namelist settings to run ICON-ART-Iso

The number of namelist settings that control the behavior of ICON-ART-Iso itself is very limited, see Sec. B.1.2.2. But not all namelist settings possible in ICON have been implemented in ICON-ART-Iso and some namelist settings for ICON-ART have to be made for ICON-ART-Iso to run properly. All these settings are explained in this section.

In the `nwp_phy_nml`, `inwp_gscp` has to be set to 6 to use the version of the 2 moment microphysical scheme that has been adapted to ICON-ART. All the other `inwp` switches have to be set to 1. `ldiff_qi` of `turbdiff_nml` (to turn on turbulent diffusion for ice) has been implemented for ICON-ART-Iso, as well as `ldetrain_conv_prec` of `nwp_phy_nml` (to use snow and rain tendencies from convection). In the `transport_nml`, `ihadv_tracer` has to be set to 52 for `qv` (the first entry) and 22 for the 13 other ICON tracers, while `itype_hlimit` has to be set to 3 for `qv` and 4 for the others. `ivadv_tracer` has to be set to 3 for all tracers.

In the `art_nml`, which contains the settings for ICON-ART, `lart_ntracer` does not have to be set. It can be left at 0 if only isotopes are simulated with ART.

`lart_diag` has to be set to `TRUE` if diagnostics of ICON-ART-Iso are to be used. These are the output groups (all starting with `group:Art-Iso_`), followed by the specifier `delta`, `precip` and `testing`, see Sec. B.1.2.3.

B.1.2.2. ICON-ART-Iso namelist settings

There are only three namelist switches that properly belong to ICON-ART-Iso. These are explained in Tab. B.2. All but the main switch are explained in their proper sections, the reference to which is also given in Tab. B.2. The main switch (`lart_iso`) turns ICON-ART-Iso on or off completely. It has to be set to `TRUE` for any simulation.

namelist entry	default	explanation	see Sec.
<code>lart_iso</code>	FALSE	Turns ICON-ART-Iso on or off.	B.1.2.2
<code>lart_iso_testing</code>	FALSE	Turns testing code on.	B.2.2.3
<code>cart_isotopes_xml</code>	–	Gives the path to XML file.	B.1.3

Tab. B.2.: List of ICON-ART-Iso namelist entries, their default values and a short explanation.

B.1.2.3. ICON-ART-Iso output groups

In order to facilitate the output, several output groups have been implemented. The `group:ART-Iso` will output the values of tracers. `group:ART-Iso_delta` will output the δ values of all tracers. Note that the exact definition of the δ values can be influenced by the optional XML key `opt_idelta_style`. The name of the output fields also changes from `delta` to `ratio` or `diff` if this key is set to 1 or 2, respectively. See Sec. B.2.1.2 for more details. The output group `group:ART-Iso_testing` is necessary for testing code. Note that this will result in 36 additional output fields for the first isotype (see Sec. B.2.2.3 for details on the testing code). The output group `group:ART-Iso_precip` will result in output of the precipitation diagnostics (see Sec. B.2.1.2 for details), eight two dimensional fields for each isotype. The same variables of the ICON water species can be added to output by the group `group:precip_vars`.

B.1.3. XML file overview

Almost all settings for ICON-ART-Iso are done in the XML (Extensible Markup Language) file. The path to this file is given in the namelist entry `cart_isotopes_xml`. Commonly, this file is saved is kept in `art/runctrl_examples/xml_ctrl`, like the other XML files defining tracers for the simulation of atmospheric chemistry or aerosols.

In contrast to these files, the XML file for ICON-ART-Iso does not define single tracers, but isotope types. The reason for this is a simple one: The simulation of chemistry uses different substances, and each corresponds to one tracer. In the case of ICON-ART-Iso, several tracers are needed to simulate one substance. Water in ICON is represented by several tracers, their exact number and definition depending on the microphysical scheme that has been chosen for a simulation. So each water isotope that is to be simulated also needs this number of tracers. The number of tracers that define one isotope are therefore not defined by ICON-ART-Iso, but by the settings in the ICON model. This is why the XML file defines isotope substances (called isotopes in the following) and not tracers like for the other implementations of ICON-ART.

Each entry for an isotope has several XML keys. These define the physical treatment of the isotope in the model. Parameterizations for processes can be chosen or processes can be turned off completely. The multitude of possibilities is large and care should be taken to set physically meaningful combinations.

The XML keys that define which processes act on an isotope may not be omitted in the XML file. All these non-optional parameters are explained in Tab. B.3. In addition, there are many optional parameters that can be set. If they are not given in the XML file, a default value is set at runtime. These optional parameters are mostly tuning parameters for the different parameterizations used to calculate fractionation. All optional parameters are listed in Table B.5. Some of the default values are determined by the `isoflavor`, a non-optional parameter that sets several physical constants at once. Default values that are determined by the `isoflavor` are listed in Table B.4. There are some optional parameters useful for testing the code, these are explained in Sec. B.2.2.

XML key	values	short explanation
<code>id</code>	<code>aNAME</code>	Name in output files, e.g. <code>mynewHDO</code> Is attribute to <code>isotype</code> in XML.
<code>transport</code> see Sec. B.2.1.4	<code>OFF</code> <code>ON</code> <code>stdiso</code> <code>readiso</code>	Advection schemes: <code>OFF</code> for no transport, <code>ON</code> for ICON-ART standard (<code>hadv = 22</code>) <code>stdiso</code> for fixed scheme (<code>hadv = 52</code>) <code>readiso</code> reads from corresp. ICON tracers.
<code>isoflavor</code> see Sec. B.2.1.2	1 2 3	Standard values for tuning parameters: 1 for H_2O , 2 for HDO 3 for H_2^{18}O
<code>equifrac_liq</code>	1	Equilibrium fractionation over liquid:

see Sec. B.2.1.2	201 202 301	1 for H ₂ O, 2* for HDO, 3* for H ₂ ¹⁸ O: 201 and 301 for Majoube (1971) 202 for Horita and Wesolowski (1994)
equifrac_ice see Sec. B.2.1.2	1 201 301	Equilibrium fractionation over ice: 1 for H ₂ O, 2* for HDO, 3* for H ₂ ¹⁸ O: 201 and 301 for Merlivat and Nief (1967)
iratio_diff see Sec. B.2.1.2	1 2	Diffusion constant ratio: 1 for Merlivat (1978), 2 for Cappa et al. (2003).
ratio_init	1.0	Ratio to initialize with.
init see Sec. B.2.1.3	0 1 2 3	Initialization: 0 to initialize with 0.0, 1 with ratio_init 2 to initialize with ratio_vsmow 3 for clim. state dep. on isoflavor
surf_land and surf_ocean see Sec. B.2.1.5	0 1 2	Surface ratio (land and ocean): 0 for 0.0, 1 for ratio_init 2 for ratio_vsmow
evap_land and evap_ocean see Sec. B.2.1.5	0 1 2 3 4	Surface evaporation (land and ocean): 0 to turn it off, 1 to use ratio_init 2 to use non-fractionating evaporation 3 to use Pfahl and Wernli (2009) 4 to use Merlivat and Jouzel (1979)
satad see Sec. B.2.1.7	0 1 2 3	Saturation adjustment: 0 to not consider isotope, 1 for non-frac. 2 for Blossey et al. (2010) of COSMOiso 3 for Blossey et al. (2010)
gscp see Sec. B.2.1.8	0 1	Microphysics: 0 to not consider isotope, 1 to consider it
gscp_evapfrac see Sec. B.2.1.8	0 1 2 3	Frac. during evap. in microphys.: 0 for no frac., 1 for Stewart (1975) 2 for Pruppacher and Klett (2012) derived 3 for Blossey et al. (2010)
gscp_icefrac see Sec. B.2.1.8	0 1 2	Frac. during ice form. in microphys.: 0 for no frac., 1 for Blossey et al. (2010) 2 for Pruppacher and Klett (2012) derived
conv see Sec. B.2.1.9	0 1	Convection: 0 to not consider isotope, 1 to consider it
conv_satad	0	Frac. during conv. sat. ad.: 0 for no frac.

see Sec. B.2.1.9	1	1 for Blossey et al. (2010) of COSMOiso
	2	2 for Blossey et al. (2010)
conv_evapfrac_ddd	0	Frac. during conv. evap. in downdrafts:
see Sec. B.2.1.9	1	0 for no frac., 1 for Pfahl et al. (2012)
conv_evapfrac_flg	0	Frac. during conv. evaporation in flux adj.:
see Sec. B.2.1.9	1	0 for no frac., 1 for Stewart (1975)

Tab. B.3.: Explanation of ICON-ART-Iso XML entries. These entries have to be made for each isotope.

XML key	H ₂ O	HDO	H ₂ ¹⁸ O
isoflavor	1	2	3
opt_molmass	18.0153	19.021442	20.015041
opt_ratio_vsmow	1.0	$1.5576 \cdot 10^{-4}$	$2.00520 \cdot 10^{-3}$
opt_diff_ratio	1.0	0.9755	0.9723
	1.0	0.9839	0.9691
opt_init_delta_bottom	1.0	-50.0	-7.0
opt_init_delta_tropo	1.0	-650.0	-80.0
opt_init_delta_top	1.0	-400.0	-50.0
opt_init_delta_offset	0.0	-100.0	-12.5

Tab. B.4.: Default values for optional XML entries that depend on the isoflavor. The default for the diffusion constant ratio depends on iratio_diff, the first of the two are defaults for iratio_diff=1 (Merlivat, 1978), the second for iratio_diff=2 (Cappa et al., 2003).

XML key	default	short explanation	see Sec.
opt_molmass	*	molar mass, is not used	B.2.1.2
opt_ratio_vsmow	*	VSMOW value	B.2.1.2
opt_diff_ratio	*	ratio of diffusion constants	B.2.1.2
opt_idelta_style	0	0 for δ , 1 for ratio, 2 for diff.	B.2.1.2
opt_epsilon	0.0	limits source in non-frac. tend.	B.2.1.2
opt_rlimit	2	limits ratio in non-frac. tend.	B.2.1.2
opt_init_delta_bottom	*	if init = 3: δ at lowest level	B.2.1.3
opt_init_delta_tropo	*	if init = 3: δ at tropopause	B.2.1.3
opt_init_delta_top	*	if init = 3: δ at top	B.2.1.3
opt_init_delta_offset	*	if init = 3: δ hydrom. offset	B.2.1.3
opt_evap_limit	10.0	Limit for ratio in evaporation.	B.2.1.5
opt_evap_windind_expk	0.28	Exp. for surface evap.	B.2.1.5
opt_turbdiff_off	0	1 to turn off turbulent diffusion	B.2.1.6
opt_gscp_ventfac_ice	1.0	Ventilation factor for ice.	B.2.1.8
opt_gscp_ventfac_snow	0.995	Ventilation factor for snow.	B.2.1.8
opt_gscp_ventfac_graupel	1.0	Ventilation factor for graupel.	B.2.1.8
opt_gscp_ventfac_hail	1.0	Ventilation factor for hail.	B.2.1.8
opt_gscp_stewart_ndiff	0.58	Exp. for microphy. evap.	B.2.1.8
opt_conv_stewart_ndiff	0.58	Exp. for conv. evap.	B.2.1.9
opt_conv_stewart_addequi	0.5	Additional conv. equil.	B.2.1.9
opt_conv_satad_lambdasupsat	0.004	Conv. sat. adj. supersat.	B.2.1.9
opt_bridge_adv	0	1 to bridge advection	B.2.2.4
opt_bridge_evap	0	1 to bridge evaporation	B.2.2.4
opt_bridge_turb	0	1 to bridge turbulence	B.2.2.4
opt_bridge_satad	0	1 to bridge satur. adjust.	B.2.2.4
opt_bridge_conv	0	1 to bridge convection	B.2.2.4
opt_bridge_gscp	0	1 to bridge microphysics	B.2.2.4
opt_bridge_gscpmain	0	1 to bridge microphysics core	B.2.2.4
opt_bridge_gscpsedi	0	1 to bridge sedimentation	B.2.2.4
opt_idev_test	0	to test new developments	B.2.2.5

Tab. B.5.: List of optional XML entries for ICON-ART-Iso. Default values are given. Those default values that depend on the isoflavor are marked with *, corresponding values are given in Table B.4.

B.2. Technical documentation of ICON-ART-Iso

ICON-ART-Iso uses the ICON-ART infrastructure to simulate a diagnostically doubled atmospheric water cycle. In ICON, water can be represented by different numbers of tracers, the exact number depending on the microphysical scheme that is chosen. The tracers then correspond to vapor, cloud water, ice, rain and snow, for example. So for a diagnostically doubled water cycle, the same number of tracers has to be added to the model. ICON transfers water from one tracer to another by different processes (e.g. melting of snow to rain during microphysics). All these processes also have to be applied to the diagnostic water of ICON-ART-Iso.

It has been said that ICON-ART-Iso simulates a doubled water cycle. This should not be misleading as the number of doubled instances is not limited. Each realization of a doubled water cycle is called an isotype. The different isotypes consist of a number of tracers (determined by the microphysical scheme) and may differ only slightly by some physical parameter setting. All settings are done separately for each isotype to retain maximum flexibility. These settings are done in an XML file. The number of namelist switches that control the behavior of ICON which are specific to ICON-ART-Iso is therefore very limited, while not all possible namelist settings of ICON itself are compatible with ICON-ART-Iso. All namelist switches and XML settings are explained in Sec. B.1.

This section discusses these settings in more details from a technical perspective. The physics behind those parts of ICON-ART-Iso that calculate fractionation are explained in Sec. 5.3.

B.2.1. Code structure

The code of ICON-ART-Iso is part of the project ICON-ART. All the routines that genuinely belong to ICON-ART-Iso are kept in `art/iso`. Whenever these need to be called from the ICON code, there is an interface layer. These interface routines are part of the ICON code but their main purpose is to call ICON-ART-Iso routines. The interface routines are kept in `art_interface`, the name of those that genuinely belong to ICON-ART-Iso starting with `mo_art_iso`. By programming in this way, the ICON model is less cluttered with statements that belong to ICON-ART-Iso. The interface in turn are also programmed in such a way that the ICON model will compile without the genuine ICON-ART-Iso routines. As ICON-ART-Iso is part of ICON-ART, there is no such interface layer in ICON-ART routines.

Within the model code of ICON and ICON-ART, all statements that belong to ICON-ART-Iso are surrounded by the statements `! iso code` and `! end iso code` on separate lines.

B.2.1.1. Meta data

Most processes that are treated by ICON-ART-Iso deal with more than one class of water, shifting mass from one tracer of the isotype to another. So conceptionally, the model does not treat separate tracers but separate isotypes. This is the reason why meta data is also saved for each isotype rather than for

each tracer. There are two Fortran derived types that store the metadata (`iso_meta` and `iso_tune`), both contain another derived type for each isotope. The names of the variables that make up each of these derived types resemble those given in the XML file and tables above, omitting an `opt_` or adding `i`. Some are transformed to logical values first. See Tables B.3 and B.5 for a list of all the XML keys.

`iso_meta` contains all the information needed for choosing which parts of the model to run. This includes all the non-optional XML keys from Table B.3 as well as `opt_turbdiff_off` and all those beginning with `opt_bridge` from Table B.5. In addition, `iso_meta` contains the indices of all tracer fields associated with this isotope and the indices in the convective and turbulent tendency fields. `iso_meta` also contains an array of all the indices of the ICON water classes in the derived type `qcclass`.

`iso_tune` on the other hand contains all the other optional parameters listed in Table B.5. If they are not set in the XML file, they are determined from default values, some depending on the `isoflavor`.

B.2.1.2. General isotope physics

There are some parameters, definitions and parameterizations that are used by many processes dealing with isotopes. These are explained in this section. The definition of these values and parameterizations makes up the module file `mo_art_iso_util.f90`. The default values for all physical parameterizations are kept in this routine.

The `isoflavor` Some values for physical parameters are determined en block by the non-optional XML key `isoflavor`. The flavor has to be chosen for each isotope and determines these values from a dictionary in the model. Most of these values can be overwritten by directly giving a value in the XML file. The values and their defaults are listed in Table B.4.

Two of the physical constants set by the `isoflavor` are of general nature (default values given in B.4) `opt_molmass` sets the molar mass of the isotope. This value is never used in the model.

`opt_ratio_vsmow` sets the value of R_{VSMOW} , the standard ratio used for the calculation of δ values (see Sec. B.2.1.2) and for setting initial (`init`) and surface ratios (`surf_land` and `surf_ocean`) if the corresponding keys are set to 2. R_{VSMOW} is the isotope ratio in the Vienna Standard Mean Ocean Water, the values of which are given for each `isoflavor` in Table B.4.

Diffusion constant and saturation vapor pressure The simulation of water isotopes requires that the model can stably simulate a constant fraction of water as a diagnostic variable. If this ratio changes, the process is said to be fractionating. This happens during phase changes. The differences in molar masses of the isotopes lead to differences in the diffusion constant and in the saturation vapor pressure. The differences in these two physical parameters are essentially the reason for fractionation during phase changes. The parameters are not used directly in the model code, but rather their values relative to that of standard water.

Several XML keys are used to set the the diffusion constant ratio. It can be set directly by giving a value to the optional key `opt_diff_ratio`. If no value is set here, there are two different literature sources that can be chosen by setting `iratio_diff`. Setting 1 will result in values given by Merlivat (1978), setting 2 in those by Cappa et al. (2003). The final value is determined from `isoflavor`. If a value is given directly by setting `opt_diff_ratio`, `iratio_diff` is reset to 0 to mark user input. Table B.4 lists the default ratios for the different values of `isoflavor` for both literature sources.

The ratio of the saturation vapor pressure is not constant but itself a function of temperature. This is the reason why no optional values can be set in the XML file. In addition, the ratio is different depending on whether the saturation vapor pressure is calculated over liquid water or over ice. This results in two XML keys that determine the two parameterizations to be used: `equifrac_liq` for liquid water and `equifrac_ice` for ice. Table B.3 lists the different settings and corresponding literature. When setting these values, care should be taken to make choices consistent with the `isoflavor` as this determines the diffusion ratio constant, the other parameter that mainly sets fractionation. The actual parameterizations are discussed in Sec. 5.2.2.1

δ values: Definition and output The δ notation is a common transformation of mass mixing ratios used for the notation isotopes of water. The definition of a ${}^h\delta_x$ value of a certain water class ${}^h q_x$ of the isotope h is given in Eq. B.1. Here, ${}^l q_x$ is the mass mixing ratio of standard water (i.e. the ICON value), while R_{standard} is the standard value of this isotope. Normally, R_{VSMOW} is used for R_{standard} . In ICON-ART-Iso, it is sometimes more meaningful to set a different standard ratio. If `init` is set to initialize with a constant ratio (by setting 1, `ratio_init` will be used), this initialization ratio is used for R_{standard} (unless `ratio_init` = 0, when R_{standard} is set to 1). The δ values of all isotope tracers can be added to the output by the output group `group:ART-Iso_delta`.

$${}^h\delta_x = \left(\frac{{}^h q_x / {}^l q_x}{R_{\text{standard}}} - 1 \right) \cdot 1000 \quad [\text{B.1}]$$

There are two more definitions that can be used to calculate δ values by setting the XML key `opt_idelta_style` to 1 or 2 (default is 0, using Eq. B.1). Setting 1 results in the pure ratio in percent, which is interesting when aiming at a fractions of ICON water: ${}^h\delta_x = {}^h q_x / {}^l q_x * 100$ (if ${}^l q_x > 0$, 0 otherwise). Setting 2 results in the difference to ICON water, which is convenient when testing the model: ${}^h\delta_x = {}^h q_x - \text{ratio_init} \cdot {}^l q_x$. In the output file, the field names change from `delta` to `ratio` and `diff` if `opt_idelta_style` is set to 1 or 2 respectively.

Non-fractionating tendencies i Two more optional XML keys can be specified that control the behavior of an isotope in general: `opt_epsilon` and `opt_rlimit`. To understand the meaning of these parameters, we return to what was said above: The main task of ICON-ART-Iso is to simulate a certain fraction of water as a diagnostic variable. In order to do so, the tendencies ${}^l S$ of water (${}^l q_x$) in ICON often have to be applied to the isotopes (${}^h q_x$) in the manner specified in Eq. B.2. The isotope fraction in the

source of the tendency is also the fraction applied to the tendency itself to calculate the tendency for the isotope. The tendency that is calculated is limited to be smaller than the source (${}^h q_x$) and positive definit. This is necessary to ensure model stability.

$${}^h S = {}^l S \cdot \frac{{}^h q_x}{{}^l q_x} \quad [\text{B.2}]$$

In this equation, ${}^l q_x$ can never be 0. So the calculation is accompanied by the condition ${}^l q_x > \varepsilon$ (otherwise, ${}^h S$ is set to 0). The optional XML key `opt_epsilon` sets a value for ε different to 0 in this condition, e.g. 10^{-15} . This can be interesting to test the stability of the code. The default value is 0.

The second parameter `opt_rlimit` also changes Eq. B.2. To enforce stability, it can be interesting to limit the ratio $\frac{{}^h q_x}{{}^l q_x}$ that is used to determine ${}^h S$. Due to some process in the model run, this ratio could become very large and it may be interesting to set a limit, e.g. 1, to this ratio. The default value is the 2. This also means that it is technically not meaningful to set a value higher than 2 for `ratio_init`.

Eq. B.2 is applied in convection, microphysics, saturation adjustment and surface evaporation. So `opt_epsilon` and `opt_rlimit` change the behavior of many parts of the code. Setting different values for these XML keys should therefore be done with care and not without testing the resulting effects. Both these parameters will mostly be changed during development when problems arise and further testing is needed.

Precipitation diagnostics In order to investigate precipitation at ground level, some precipitation diagnostics have been implemented. These can be added to output by the group `group:ART-Iso_precip`. All are summed up precipitation values given in [kg m^{-2}]. The following diagnostics are determined for each isotype: total precipitation (`tot_prec`), precipitation from microphysics (`_gsp_`) of rain, snow, ice, graupel and hail and convective precipitation (`_con_`) of rain and snow. The calculation of δ values in these summed up variables, increments, etc. have to be calculated in postprocessing. The same variables from ICON can be added to output by specifying `group:precip_vars` in the output namelist.

B.2.1.3. Initialization

There are four different ways to initialize the tracer fields ${}^h q_x$ of each isotype, which can be chosen with the XML key `init`. Setting 0, 1 or 2 use a constant ratio R_{init} to initialize each tracer depending on the corresponding ICON tracer (${}^l q_x$), see Eq. B.3. R_{init} can be set to 0 (`init = 0`), to `ratio_init` (`init = 1`) or to R_{VSMOW} defined by the `isoflavor` (`init=2`). In a default setup, the highest meaningful value for `ratio_init` is 2, as `opt_rlimit` defaults to 2, see Sec. B.2.1.2.

$${}^h q_x = R_{\text{init}} \cdot {}^l q_x \quad [\text{B.3}]$$

In addition to these more technical initializations, `init = 3` uses a climatological profile depending on the tropopause height. The exact shape of the profile can be influenced by the optional XML keys

`opt_init_delta`, specifying bottom, tropo (tropopause) and model top values. `offset` defines the offset for hydrometeors from the profile determined for vapor. This initialization is explained in more detail in the physics section, see Sec. 5.3.1. The tendency fields from advection, turbulence and convection are initialized with the same ratio as the corresponding tracer fields.

Different to the initialization of chemical and aerosol fields of ICON-ART, the initialization is called from `perform_nh_stepping` before the time loop of the model. This ensures that the values of all fields are set even for the first timestep. Together with those routines that allocate space for the calculation of the isotopes, the routine `art_init_iso_values` is part of the module and file `art/iso/mo_art_iso_init.f90`.

B.2.1.4. Advection

Advection calculates the grid scale transport of all tracers. As the isotopes cannot exist independently of the ICON water classes, it is essential for the simulation that the advection retains the isotope ratios. This is ensured by the different advection schemes implemented into ICON. These can be chosen in the namelist via a set of parameters (`ivadv_tracer`, `ihadv_tracer`, `itype_hlimit` and `itype_vlimit`). This list has to be filled with the schemes set as default by DWD and explained in Sec. B.1.2.1.

The transport scheme of the ICON-ART-Iso tracers is set by the XML key `transport`. It is recommended that `readiso` is set here, as this will read the values set for each corresponding tracer from the namelist. `ON` and `OFF` are standards provided by ICON-ART, while `stdiso` is an arbitrary set of choices (`ihadv_tracer = 52` for all tracers). All but `readiso` will result in settings different to those of the ICON tracers and will therefore result in different advection tendencies. This will change the isotope ratio by advection alone, which is unphysical and should therefore be avoided.

B.2.1.5. Evaporation

Evaporation and turbulent mixing are very closely linked in ICON-ART-Iso since the evaporative flux is used as a lower boundary during turbulent diffusion. The treatment of evaporation in turn depends on the surface. ICON-ART-Iso does not include all processes that happen to water in the land surface model. This is one of the main deficits of ICON-ART-Iso. For this reason, evaporation and surface parameterizations can be chosen separately for land and ocean points.

In ICON, the sum of all fluxes that make up evapotranspiration in the model is kept in the field `qhfl_s`. But this field alone does not contain all the information necessary to calculate fractionation. Four different parts of evapotranspiration are considered in ICON-ART-Iso: dewfall and riming, evaporation from open water and transpiration from plants. The first two describe a flux directed towards the surface, the second pair describes a flux away from the surface. These four parts sum up to `qhfl_s`. The correct sum can be tested in testing mode (see Sec. B.2.2.3).

The four parts have to be considered separately, as they fractionate differently. While dewfall and riming are considered to fractionate in equilibrium fractionation, transpiration is considered a non-fractionating process. For evaporation, two different implementations of a Craig-Cordon type model have been implemented: `evap_land` or `evap_ocean` can be set to 3 for Pfahl and Wernli (2009) and to 4 for Merlivat and Jouzel (1979). These two choices will consider the four summands of `qhfl_s` as described. Tiling of the land surface has also been implemented.

Setting `evap_land` or `evap_ocean` to 0 will turn evaporation off, setting 1 will use `ratio_init` 1q and setting 2 will use non-fractionating evaporation, calculating the isotope flux from the parts of `qhfl_s` and the isotope ratio in the source like for the calculation of hS in Eq. B.2.

In all these calculations, the surface isotope ratio plays an important role. Since no surface model has been implemented in ICON-ART-Iso, different constant values can be set for `surf_land` and `surf_ocean`. These choices are sufficiently explained in Table B.3.

The collection of the different parts of `qhfl_s` is taken care of by module and file `mo_art_isoevap_collect_interface.f90` while surface values are set during initialization by `art_init_iso_surface` of `mo_art_iso_init.f90`. Fractionation and actually setting the flux as the lower boundary of turbulence is done by `art_iso_surf_evaporation` of `mo_art_iso_evaporation.f90` called by `art_surface_value`, which in turn is called from `mo_art_turbdiff_interface.f90`.

B.2.1.6. Turbulence

For simulating turbulent diffusion, ICON-ART-Iso uses the corresponding ICON-ART interface. The only difference to the other ART tracers is that the lower boundary is defined to be a flux. This can be done by setting the switch (`fc` of the derived type `ptr`) to `TRUE`. In addition, the integration case (`update_ptr`) has been slightly altered to account for the fact that only water vapor and cloud water is effected by ICON turbulence. By setting the namelist switch `ldiff_qi` of `turbdiff_nml` `TRUE`, cloud ice can also be affected by turbulent diffusion. This is also implemented for ICON-ART-Iso.

One small change had to be made to the turbulence code itself. This was done in accordance with the author Matthias Raschendorfer of DWD. In the original version of the code, the calculation of vertical diffusion of vapor and temperature (original ICON code) uses a slightly different density than the vertical diffusion of other tracers. This would lead to differences between ICON water and a diagnostic field passed to turbulence. By generalizing one if-clause in the code, the vertical diffusion of ICON water now uses the same density and the differences disappear. A comment has been made about this in the code of the turbulence routine `src_turbdiff.f90`.

B.2.1.7. Saturation adjustment

The general saturation adjustment is one of the main processes to transform vapor (`qv`) to cloud water (`qc`) and vice versa. It is called directly from `mo_nh_interface_nwp.f90` or, in the case of an ICON-

ART-Iso simulation, from the `art_isosaturation_interface.f90`. Saturation adjustment in ICON itself is calculated iteratively. For calculating the isotope tendencies, this iteration is not redone, but the tendencies are calculated by comparing cloud water content before and after the call to saturation adjustment.

All choices for saturation adjustment are accessible through the XML key `satad`, see Table B.3. Besides turning it off (by setting 0) or using non-fractionating saturation adjustment (by setting 1), there are two options for fractionating saturation adjustment. These two options differ only slightly. Both build on the scheme described by Blossey et al. (2010). By setting `satad` to 2, the implementation from COSMOiso is used, while setting `satad` to 3 results the parameterization described by Blossey et al. (2010) directly. The two implementations differ only by a small factor, which is described in Sec. 5.3.4.

Despite its simplicity, the routine dealing with saturation adjustment is kept in the separate module file `art/iso/mo_art_iso_satad.f90`. For non-fractionating saturation adjustment, routines from `art_iso_gscp.f90` are used.

B.2.1.8. Microphysics

The calculation of thermodynamic effects on the water tracer fields that lead to phase changes and precipitation at grid scale is commonly referred to as microphysics and abbreviated as `gscp` (grid scale precipitation). Several microphysical schemes have been implemented in ICON. The 2-moment scheme by Seifert and Beheng (2006) has been adopted to ICON-ART to simulate interactions of these processes with a prognostically calculated aerosol. For ICON-ART-Iso, this scheme has been further adapted to its needs. The other microphysical schemes are currently not prepared for ICON-ART-Iso. If `gscp` is set to 0, the isotope will not see any changes by microphysics.

The scheme by Seifert and Beheng (2006) uses seven water classes (vapor, liquid cloud water, ice, rain, snow, graupel and hail). For all but vapor, it also calculates prognostic fields for the number density and in addition, there is one tracer field for the condensation nuclei. So in total, 14 tracers are needed for this scheme, seven of which represent water in its different physical states. These seven therefore also have to be included for each isotope in order to diagnostically double all the processes described by the microphysical scheme. The number concentrations do not need to be doubled, as the isotopes do not exist independently of the ICON water species.

The microphysical scheme by Seifert and Beheng (2006) has been implemented into ICON as a series of 39 box models that describe 62 processes, e.g. `ice_melting` that describes the melting of ice to cloud water and rain. Only those processes that involve water vapor have to consider fractionation. All the other processes are non-fractionating and therefore have to be applied to the isotopes in proportion to the isotope ratio in the source of the process, see Eq. B.2 (Pfahl et al., 2012). This implies that the processes have to happen in the same order as in the separate box models, which describe up to eight processes. The order has to be correct even if the tracer update technically happens after a call to a

routine that calculates one of the box models. It is this correct order that can make code maintenance tricky if there are changes to the scheme in the ICON code.

Fractionation happens when water vapor is involved in one the processes. This is the case during evaporation of rain, evaporation of melting ice (where ice can also mean snow, graupel and hail), deposition of vapor on one of these ice classes and homogeneous nucleation of ice. Ice is not considered to fractionate during sublimation.

For fractionation during evaporation (Sec. 5.3.3.1), three different schemes can be chosen. `gscp_evapfrac` can take values 0 (to turn fractionation off) to 3 correspondingly. Setting 1 will result in the parameterization of Stewart (1975). This is the scheme that is also applied in COSMOiso, see Pfahl et al. (2012). Setting 2 will result in a parameterization derived from Pruppacher and Klett (2012). Setting 3 will result in a direct implementation of the parameterization by Blossey et al. (2010).

For fractionation during the formation of ice, i.e. deposition of vapor on ice and the nucleation of ice (Sec. 5.3.3.2), two parameterizations are available. `gscp_icefrac` can be set to 0 to turn fractionation off. By setting it to 1, the scheme by Blossey et al. (2010) will be used. This is the scheme that is also used in COSMOiso (Pfahl et al., 2012). By setting `gscp_icefrac` to 2, a newly derived parameterization following Pruppacher and Klett (2012) will be used.

Since ICON-ART-Iso uses the interface of ICON-ART for the 2-moment scheme, there is no separate interface. All routines necessary for microphysics have been collected in the module and file `art/iso/mo_art_iso_gscp.f90`.

B.2.1.9. Convection

Those thermodynamic effects that are too small to be resolved by the model directly but lead to small-scale clouds with a strong influence on dynamics and heavy precipitation are covered by the convection parameterization. ICON uses the scheme by Tiedtke (1989), with improvements by Bechtold et al. (2014). For ICON-ART, this scheme transports tracers vertically in the convective systems. For ICON-ART-Iso, many more processes have to be considered as this is one of the three main processes that creates clouds and precipitation.

Convection in the model consists of an interface (`mo_nwp_conv_interface.f90`) which calls a master routine (`mo_cumaster.f90/cumastrn`). From here, the different processes are called that calculate ascent or descent, cloud formation or the effect on the wind fields.

Microphysics can be represented by a series of box models which depend on the physical state in each grid cell. There are no dynamics that need to be parameterized. This is different in convection. Here, the water vapor and the latent energy that heats the atmosphere upon condensation is one of the main drivers for the dynamics. This is why the code cannot simply use a tendency that is calculated within each subroutine. But it is also not possible to call each subroutine with the diagnosed water species in place of the ICON water. The much lower mixing ratios would result in very different dynamics, leading to very different atmospheric fields. This is why the code has to be examined line by line. Each line

that changes the fields of water must be doubled, while all lines that alter other fields (parameterized temperature, wind fields, etc.) must be called with the ICON water fields. As a general rule, factors in each line must be retained while all water species that appear as summands must be replaced.

In practice, this means that each subprocess of convection that alters the fields representing water must be called for each isotope. It is called with the ICON water fields as regular arguments and the corresponding fields for the isotope as additional input. This approach is implemented through the `mo_art_isoconvection_interface.f90`. In 21 cases, the ICON fields are first saved to local variables and then the corresponding subroutine is called for each isotope with additional arguments. Cases starting with 1 (101-104) are called from the NWP interface or from `nwp_nh_interface`. Cases starting with 2 (201-217) are called from `cumastrn` and serve as wrappers to the different subprocesses, as described above. In addition, there are two cases starting with 9 (901 and 902) which are used if `lart_iso_testing` is set to TRUE, see Sec. B.2.2.3.

Some processes (which are called from the `cumastrn` and `art_isoconvection` interfaces) require interaction with code that is specific to ICON-ART-Iso. This third layer of interaction (interface (cases 1), master (cases 2) and now processes (cases 3)) cannot be included in the `art_isoconvection_interface` as this would lead to circular dependencies. This is the reason why these cases have been moved to the `mo_art_isoconvproc_interface.f90`. These cases (numbering starting with 3) include all the calls to fractionating routines (cases starting with 31 and 32) and those lines needed to exclude the isotope tracers from convective transport (case 330). Convective transport affects all ART tracers but not the ICON water species, which is why the isotope tracers have to be excluded. Fractionation happens during convective saturation adjustment (cases 311 and 312) and during evaporation (cases 321 and 322). In addition, the `convproc` interface tests for the correct settings in cases whose numbers start with 30.

A real saturation adjustment is calculated twice in the convection code: During ascent (`cuascn`) and during the calculation of cloud base values (`cubasen`). For these the XML key `conv_satad` can be set to 0 for non-fractionating saturation adjustment or to 1 or 2 turn on convective saturation adjustment. Setting 1 results in the the implementation of Blossey et al. (2010) from COSMOiso, while 2 is a direct implementation of Blossey et al. (2010). The two differ only by a small factor. In contrast to general saturation adjustment (Sec. B.2.1.7), convective saturation adjustment also considers supersaturation for mixed phase clouds, the strength of which can be influenced by setting the optional XML key `opt_conv_satad_lambdasupsat`. See Sec. 5.3.5.1 for further details.

Evaporation of hydrometeors below cloud base happens in `cuf1xn`, for which fractionation is parameterized following Stewart (1975) if the XML key `conv_evapfrac_flg` is set to 1. Its behavior can be influenced by the optional XML keys `opt_conv_stewart_ndiff` and `opt_conv_stewart_addequi`. This parameterisation differs slightly from the one implemented for microphysics as an additional equilibration can be turned on. In addition, convection uses the tracer values themselves while microphysics calculate a tendency. This is why a second, different routine is necessary. Evaporation is also considered during calculation of saturated downdrafts, calling case 322 from `cud1fsn` and `cuddraf.n`. Because the

downdrafts are assumed to remain saturated, this is much simpler than the scheme by Stewart (1975). Fractionation is considered as in COSMOiso (Pfahl et al., 2012) if the XML key `conv_evapfrac_ddr` is set to 1. Evaporation during convection and the associated fractionation is explained in more detail in Sec. 5.3.5.3 for evaporation below cloud base and in Sec. 5.3.5.2 for saturated downdrafts.

All the routines necessary for calculating fractionation during convection have been collected in the module file `art/iso/mo_art_iso_convectio.f90`. Convection does not work on the tracer fields directly, but the result is a convective tendency (see Sec. B.2.1.10). All the intermediate fields are prepared for each isotope centrally in `iso_conv` of `p_art_data`. It should not go unnoticed that convection depends on the tendencies calculated by advection and turbulence, as these two sum up to moisture convergence before the call to `cumastrn`.

B.2.1.10. Integration of convective tendencies

As has been noted above, the final result of convection are tendencies. These tendencies are added to the tracer fields in `nh_update_tracer_phy`. The integration is accompanied by clipping and redistribution. All of this is done for the isotope fields in the `mo_art_iso_integrate_interface`. In addition, this interface takes care that the isotope fields do not see the standard ICON-ART convective tendencies (from vertical transport). It is also used to sum up diagnostic precipitation variables.

B.2.1.11. The `isoindlookup` interface

One interface remains that has not been documented by the sections above. The `art_isoindlookup_interface` is called while reading the ART namelist in `art_nml.f90`. When running ICON-ART, the number of tracers has to be specified by the namelist parameter `iaart_ntracer`. This is not necessary for ICON-ART-Iso. This number is looked up by the call to this interface, which checks the number of isotopes in the XML file and increases the number specified in `iaart_ntracer` accordingly.

B.2.2. Code maintenance and testing

This section explains where the model code is maintained and how the model can be tested during development.

B.2.2.1. Code maintenance

The code of ICON-ART-Iso is kept in the git repositories of ICON and ICON-ART as a branch of development, `icon-kit/icon-kit-isotop` in the case of the ICON repository, `isotop` in the case of the ART repository. This way, it is possible to keep up to date with new developments. But care should be taken when merging with new versions of ICON or ICON-ART. Not only will conflicts have to be solved, but changes made in one of the processes in the ICON code also have to be made to ICON-ART-

Iso code. This will not result in merge conflicts but is essential for ICON-ART-Iso to work properly. Therefore, merging with the ICON code can be a tedious task and definitely requires testing the model.

B.2.2.2. Testing the model

To a first approximation, the simulation of isotopes requires that the model can simulate constant ratios of water while passing water and the isotopes through all processes. The fractionation, which make the isotopes interesting for understanding physical processes, come on top of that. For that reason, it is important that each process maintains a constant ratio and that the model as a whole can simulate constant ratios. Because this functionality is an important prerequisite for the simulation of isotopes, certain testing mechanisms have been implemented into the model.

B.2.2.3. Testing single time steps

Each process can be tested separately by setting the namelist switch `lart_iso_testing` to `TRUE`, thereby turning on the testing code. If this switch is set, the first isotope of the XML file is used for testing. This implies that all processes should be turned on but fractionation for each process should be turned off. The `init_ratio` should set to a positive value smaller than 1. Setting 1 will not result in realistic testing results.

If testing is turned on, then the necessary fields of the tracers of the first isotope are filled with '`init_ratio · (ICON tracer value)`' right before each process. After each process, the difference '`(ICON-ART-Iso value) – init_ratio · (ICON value)`' is saved in a diagnostic field. These fields can be added to output with `group:ART-Iso_testing` in the `output_nml`. The following processes are tested: advection, turbulence, saturation adjustment, microphysics, convection and integration. The last of these is not a physical process but tests the part of the code that integrates convective tendencies in `art_isoindlookup_interface`. The output group will result in up to seven fields for each process. It should be kept in mind that these differences only test one timestep and that the output only represents the current timestep.

Testing the model in this way is an important tool during the development of ICON-ART-Iso. It is equally important when there are changes in the ICON code. These changes also have to be made to the ICON-ART-Iso code if they affect a doubled line of code. Only if the differences in the output of the testing code are small, i.e. smaller than the precision (currently 12 decimal places), can the code be used and considered to be working. Only if this is the case will changes in the isotope ratio actually be related to fractionation and not to errors in the code.

B.2.2.4. Testing the model during an integration

In addition to testing the model each time timestep separately, it can be interesting to test each process and its effects during a free running model integration. In order to activate this, an optional XML key is

available for each process. The default for each of the keys is 0, 1 has to be set to turn testing on. The optional keys are `opt_bridge_adv` for advection, `opt_bridge_evap` for evaporation, `opt_bridge_turb` for turbulence, `opt_bridge_satad` for saturation adjustment, `opt_bridge_conv` for convection and `opt_bridge_gscp` to test all of microphysics. `opt_bridge_gscpmain` tests only the box model core of microphysics and `opt_bridge_gscpsedi` tests sedimentation during microphysics.

For this testing procedure, the process for which a switch is set to 1 is bypassed for this isotype. At the end of each process, the tendencies of the ICON tracers are multiplied with `ratio_init` and added to or passed to the fields of the isotype, thereby overwriting whatever happened to the isotype during the process. In the case of turbulence and convection, only the tendencies need to be overwritten. `opt_bridge_evap` does not overwrite a process, but just uses the surface flux of ICON directly. By bridging the processes this way, the integrated effect of each process can be examined, which can aid in finding bugs in the code. This testing procedure is only worthwhile after the code has passed the tests of single timesteps.

B.2.2.5. Testing new developments

When working on the model code, it may be useful to use the XML key `opt_idev_test`. This is nothing but an integer value that is set to the value given in the XML file, the default being 0. This integer value can be used to turn parts of the code on or off for separate isotypes. In a regular model run, this value has no effect. It is only useful during development, but there it is as simple as powerful.

B.3. Possible future developments

This chapter lists and describes open issues regarding ICON-ART-Iso. Section B.3.1 lists open points that could be fixed in the near future. Section B.3.2 is a list of ideas for larger development projects that would expand the functionality of ICON-ART-Iso to include more physical processes or make use of more advanced features of ICON that have so far not been implemented.

B.3.1. Small open issues

This section lists some small issues that are open at the time of writing this document. They may be fixed quickly or be a hint of some deeper problem.

Land surface evaporation is not free of error. When fractionation is set to options 3 or 4, very high δ values (order of 5000) appear in some very localized spots. The last problem solved for land surface evaporation was a similar problem over lakes, for which the surface temperature was not set correctly in ICON-ART-Iso. Maybe this smaller scale problem has a similar cause. Remember that land surface evaporation also considers land surface tiles. There may also be a bug here.

The parameterization of fractionation at the evaporation of hydrometeors following to Pruppacher and Klett (2012) does not run stably. The fields of an isotope using this parameterization are quickly filled with non-numerical values. This is probably a question of the numerical implementation.

The model results do not seem to be completely reproducible. On rare occasions, the model does not run stably. Very high values (order of 10^6) then appear in any one of the isotopes that rapidly spread throughout the model domain. The model does not crash but the values are no longer realistic. Another run, sometimes using more memory, has so far always been a good work around.

So far, the model has mainly been run at a resolution of R2B06 (see Zängl et al. (2015) on the meaning of this code). R3B07 has been tested, but non-numerical values (inf or nan) appeared in an isotope after about two days of simulation in a standard setup given in Tab. B.1. Other resolutions like R2B04 should also be tested.

The model has been developed and tested on ic2 of KIT. It has also run on uc1, but other clusters have not been used so far. It has compiled with the intel compiler suit. At one point, a cray compiler was also successfully used.

B.3.2. Larger development projects

The following sections list different ideas for future developments. They would expand the functionality of ICON-ART-Iso, either by considering more physics or implementing advanced technical features of ICON.

B.3.2.1. Initialization

An initialization with external data needs to be considered. This may prove difficult, as water is also part of the initial data for ICON. The fields have to match in their geographic location. COSMOiso, being a regional model, is initialized with data from a global isotope model by Yoshimura et al. (2008).

B.3.2.2. Surface ratios and evaporation

The isotope ratio at the surface can so far only be prescribed by constant values. A first improvement would be the implementation of a climatology. There is a dataset for sea surface ratios available from NASA¹ (LeGrande and Schmidt, 2006), while GNIP data (Global network for isotopes in precipitation, Terzer et al. (2013)) could be used as an approximation of the ratio of land surface ground water.

A second idea by Emanuel Christner is to include one artificial layer of soil water for each isotope. Within this layer, precipitation could mix with soil water and evaporation could happen from this artificial mixed layer. Not the actual amount would be influenced, only the surface ratio could then dynamically evolve as the model integration progresses. The exact thickness would have to be determined by a sensitivity study.

The implementation of real-time, analysed ratios for a certain start date seems unrealistic, as the corresponding measurement data is not available, unless the model is started from another global isotope model that may include surface ratios.

B.3.2.3. Land surface processes

As in the first versions of COSMOiso, the land surface processes and the influence of ground water fluxes have been neglected in ICON-ART-Iso. This would require an extension of the TERRA module, which calculates all the corresponding processes in ICON. ICON-ART-Iso only crudely separates the surface flux of water vapor into evaporation, transpiration, dew and rime formation and calculates fractionation for these four parts. The isotope ratio of ground and surface water (and snow and ice) is assumed to be equal to the value given during the setup of the model for the surface points. The exclusion of ground and surface water processes in ICON-ART-Iso is the largest deficit in the model.

B.3.2.4. Microphysical schemes

So far, only the 2-moment microphysical scheme by Seifert and Beheng (2006) has been made available for ICON-ART-Iso. There are other simpler schemes available in ICON, which cannot be chosen when running ICON-ART-Iso. These are: the COSMO-EU scheme (2-category ice scheme), the COSMO-DE scheme (3-category ice) and an improved ice nucleation scheme (3-category). Making these schemes available by the implementation of a new ART interface to ICON could be a future project. This is

¹<http://data.giss.nasa.gov/o18data/grid.html>

interesting especially for long term simulations, as all these microphysical schemes are computationally cheaper than the 2-moment microphysics.

B.3.2.5. Nesting

One of the most prominent features of ICON is the possibility to include nests of a higher resolution within the global model domain. This functionality has not been tested in ICON-ART-Iso and may require some further work.

B.3.2.6. LES physics

When calling ICON with the LES (large eddy simulation) physics, they replace the NWP (numerical weather prediction) physics which have so far been used for the development of ICON-ART-Iso. A future project could include the expansion of ICON-ART-Iso to also run with ICON-LES. The surface scheme of the LES have to be expanded to also consider the tracers of ICON-ART-Iso. The main changes will be necessary in turbulence. Turbulent diffusion is calculated in a routine provided by the LES physics package. This routine will need to be expanded to also treat isotope tracers. In addition, the routine `update_tracer_les` will also need to be expanded. This is a short routine that limits the tracers and adds the tendencies to the field.

B.3.2.7. Simulating H₂¹⁷O

Due to the flexibility of the model, the simulation of H₂¹⁷O is also possible with only very few modifications. The possible values of `isoflavor` would have to be increased to 4 and all the parameters that depend on it researched in literature. This includes the diffusion ratio constant. In addition, parameterizations for equilibrium fractionation will have to be included. All the necessary changes would have to happen in `mo_art_iso_util.f90`.

C. Bibliography

- Balzani Lööv, J., S. Henne, G. Legreid, J. Staehelin, S. Reimann, A. Prévôt, M. Steinbacher, and M. Vollmer, 2008: Estimation of background concentrations of trace gases at the Swiss Alpine site Jungfraujoch (3580 m asl). *Journal of Geophysical Research: Atmospheres* (1984–2012), **113** (D22).
- Bechtold, P., N. Semane, P. Lopez, J.-P. Chaboureau, A. Beljaars, and N. Bormann, 2014: Representing equilibrium and nonequilibrium convection in large-scale models. *Journal of the Atmospheric Sciences*, **71** (2), 734–753.
- Blossey, P. N., Z. Kuang, and D. M. Romps, 2010: Isotopic composition of water in the tropical tropopause layer in cloud-resolving simulations of an idealized tropical circulation. *Journal of Geophysical Research: Atmospheres*, **115** (D24).
- Bony, S., C. Risi, and F. Vimeux, 2008: Influence of convective processes on the isotopic composition ($\delta^{18}\text{O}$ and δD) of precipitation and water vapor in the tropics: 1. Radiative-convective equilibrium and Tropical Ocean–Global Atmosphere–Coupled Ocean–Atmosphere Response Experiment (TOGA-COARE) simulations. *Journal of Geophysical Research: Atmospheres*, **113** (D19).
- Brenninkmeijer, C. A. M., P. Crutzen, F. Boumard, T. Dauer, B. Dix, R. Ebinghaus, D. Filippi, H. Fischer, H. Franke, U. Friß, J. Heintzenberg, F. Helleis, M. Hermann, H. H. Kock, C. Koepfel, J. Lelieveld, M. Leuenberger, B. G. Martinsson, S. Miemczyk, H. P. Moret, H. N. Nguyen, P. Nyfeler, D. Oram, D. O’Sullivan, S. Penkett, U. Platt, M. Pucek, M. Ramonet, B. Randa, M. Reichelt, T. S. Rhee, J. Rohwer, K. Rosenfeld, D. Scharffe, H. Schlager, U. Schumann, F. Slemr, D. Sprung, P. Stock, R. Thaler, F. Valentino, P. van Velthoven, A. Waibel, A. Wandel, K. Waschitschek, A. Wiedensohler, I. Xueref-Remy, A. Zahn, U. Zech, and H. Ziereis, 2007: Civil Aircraft for the Regular Investigation of the Atmosphere Based on an Instrumented Container: The new CARIBIC system. *Atmospheric Chemistry and Physics*, **7** (18), 4953–4976.
- Cappa, C. D., M. B. Hendricks, D. J. DePaolo, and R. C. Cohen, 2003: Isotopic fractionation of water during evaporation. *Journal of Geophysical Research: Atmospheres*, **108** (D16), 4525.
- Christner, E., 2015: Messungen von Wasserisotopologen von der planetaren Grenzschicht bis zur oberen Troposphäre zur Untersuchung des hydrologischen Kreislaufs. Ph.D. thesis, KIT, IMK-ASF, H.-v.-Helmholtz-Platz 1, 76344 Leopoldshafen.
- Craig, H., 1961: Isotopic variations in meteoric waters. *Science*, **133** (3465), 1702–1703.

- Craig, H. and L. Gordon, 1965: Deuterium and oxygen 18 variations in the ocean and marine atmosphere. *Stable Isotopes in Oceanographic Studies and Paleotemperatures*, Tongiogi, E., Ed., V. Lishi e F., Pisa, 9–130.
- Dansgaard, W., 1954: The O18-abundance in fresh water. *Geochimica et Cosmochimica Acta*, **6 (5-6)**, 241–260.
- , 1964: Stable isotopes in precipitation. *Tellus*, **16 (4)**, 436–468.
- Dee, D. P., S. M. Uppala, A. J. Simmons, P. Berrisford, P. Poli, S. Kobayashi, U. Andrae, M. A. Balmaseda, G. Balsamo, P. Bauer, P. Bechtold, A. C. M. Beljaars, L. van de Berg, J. Bidlot, N. Bormann, C. Delsol, R. Dragani, M. Fuentes, A. J. Geer, L. Haimberger, S. B. Healy, H. Hersbach, E. V. Hólm, L. Isaksen, P. Kållberg, M. Köhler, M. Matricardi, A. P. McNally, B. M. Monge-Sanz, J.-J. Morcrette, B.-K. Park, C. Peubey, P. de Rosnay, C. Tavolato, J.-N. Thépaut, and F. Vitart, 2011: The ERA-Interim reanalysis: configuration and performance of the data assimilation system. *Quarterly Journal of the Royal Meteorological Society*, **137 (656)**, 553–597.
- Diekmann, C., 2017: Simulation der polaren UT/LS im Winter 2015/16 mit ICON-ART. Master's thesis, IMK-ASF, KIT.
- Dyroff, C., D. Fütterer, and A. Zahn, 2010: Compact diode-laser spectrometer ISOWAT for highly sensitive airborne measurements of water-isotope ratios. *Applied Physics B*, **98 (2)**, 537–548.
- Dyroff, C., A. Zahn, S. Sanati, E. Christner, A. Rauthe-Schöch, and T. J. Schuck, 2014: Tunable diode laser in-situ CH_4 measurements aboard the CARIBIC passenger aircraft: instrument performance assessment. *Atmospheric Measurement Techniques*, **7 (3)**, 743–755.
- Eckstein, J., R. Ruhnke, A. Zahn, M. Neumaier, O. Kirner, and P. Braesicke, 2017: An assessment of the climatological representativeness of IAGOS-CARIBIC trace gas measurements using EMAC model simulations. *Atmospheric Chemistry and Physics*, **17 (4)**, 2775–2794.
- Eckstein, J., S. Schmitz, and R. Ruhnke, 2015: Reaching the lower stratosphere: validating an extended vertical grid for COSMO. *Geoscientific Model Development*, **8 (6)**, 1839–1855.
- Engel, A., H. Bönisch, D. Brunner, H. Fischer, H. Franke, G. Günther, C. Gurk, M. Hegglin, P. Hoor, R. Königstedt, M. Krebsbach, R. Maser, U. Parchatka, T. Peter, D. Schell, C. Schiller, U. Schmidt, N. Spelten, T. Szabo, U. Weers, H. Wernli, T. Wetter, and V. Wirth, 2006: Highly resolved observations of trace gases in the lowermost stratosphere and upper troposphere from the Spurt project: an overview. *Atmospheric Chemistry and Physics*, **6 (2)**, 283–301.
- Field, R. D., D. Kim, A. N. LeGrande, J. Worden, M. Kelley, and G. A. Schmidt, 2014: Evaluating climate model performance in the tropics with retrievals of water isotopic composition from Aura TES. *Geophysical Research Letters*, **41 (16)**, 6030–6036.

- Galewsky, J., H. C. Steen-Larsen, R. D. Field, J. Worden, C. Risi, and M. Schneider, 2016: Stable isotopes in atmospheric water vapor and applications to the hydrologic cycle. *Reviews of Geophysics*, **54** (4), 809–865.
- Gat, J. R., 1996: Oxygen and hydrogen isotopes in the hydrologic cycle. *Annual Review of Earth and Planetary Sciences*, **24** (1), 225–262.
- , 2010: *Isotope hydrology : a study of the water cycle*. Series on environmental science and management ; 6, Imperial College Press, London.
- Gottelman, A., P. Hoor, L. Pan, W. Randel, M. Hegglin, and T. Birner, 2011: The extratropical upper troposphere and lower stratosphere. *Reviews of Geophysics*, **49** (3).
- Gunson, M. R., M. Abbas, M. Abrams, M. Allen, L. Brown, T. Brown, A. Chang, A. Goldman, F. Irion, L. Lowes, et al., 1996: The Atmospheric Trace Molecule Spectroscopy (ATMOS) experiment: Deployment on the ATLAS space shuttle missions. *Geophysical Research Letters*, **23** (17), 2333–2336.
- Hegglin, M. I., A. Gottelman, P. Hoor, R. Krichevsky, G. L. Manney, L. L. Pan, S.-W. Son, G. Stiller, S. Tilmes, K. A. Walker, V. Eyring, T. G. Shepherd, D. Waugh, H. Akiyoshi, J. A. Añel, J. Austin, A. Baumgaertner, S. Bekki, P. Braesicke, C. Brühl, N. Butchart, M. Chipperfield, M. Dameris, S. Dhomse, S. Frith, H. Garny, S. C. Hardiman, P. Jöckel, D. E. Kinnison, J. F. Lamarque, E. Mancini, M. Michou, O. Morgenstern, T. Nakamura, D. Olivie, S. Pawson, G. Pitari, D. A. Plummer, J. A. Pyle, E. Rozanov, J. F. Scinocca, K. Shibata, D. Smale, H. Teyssèdre, W. Tian, and Y. Yamashita, 2010: Multimodel assessment of the upper troposphere and lower stratosphere: Extratropics. *Journal of Geophysical Research: Atmospheres*, **115** (D3).
- Henne, S., D. Brunner, D. Folini, S. Solberg, J. Klausen, and B. Buchmann, 2010: Assessment of parameters describing representativeness of air quality in-situ measurement sites. *Atmospheric Chemistry and Physics*, **10** (8), 3561–3581.
- Henne, S., J. Klausen, W. Junkermann, J. Kariuki, J. Aseyo, and B. Buchmann, 2008: Representativeness and climatology of carbon monoxide and ozone at the global GAW station Mt. Kenya in equatorial Africa. *Atmospheric Chemistry and Physics*, **8** (12), 3119–3139.
- Holton, J. R. and G. J. Hakim, 2013: *An introduction to dynamic meteorology*. 5th ed., Elsevier Academic Press, Amsterdam.
- Holton, J. R., P. H. Haynes, M. E. McIntyre, A. R. Douglass, R. B. Rood, and L. Pfister, 1995: Stratosphere-troposphere exchange. *Reviews of geophysics*, **33** (4), 403–439.
- Horita, J. and D. J. Wesolowski, 1994: Liquid-vapor fractionation of oxygen and hydrogen isotopes of water from the freezing to the critical temperature. *Geochimica et Cosmochimica Acta*, **58** (16), 3425 – 3437.

- Jacob, D. J., 1999: *Introduction to atmospheric chemistry*. Princeton Univ. Press, Princeton, NJ [u.a.].
- Jacob, D. J., B. D. Field, E. M. Jin, I. Bey, Q. Li, J. A. Logan, R. M. Yantosca, and H. B. Singh, 2002: Atmospheric budget of acetone. *Journal of Geophysical Research: Atmospheres*, **107** (D10).
- Jöckel, P., R. Sander, A. Kerkweg, H. Tost, and J. Lelieveld, 2005: Technical Note: The Modular Earth Submodel System (MESSy)-a new approach towards Earth System Modeling. *Atmospheric Chemistry and Physics*, **5** (2), 433–444.
- Jöckel, P., H. Tost, A. Pozzer, C. Brühl, J. Buchholz, L. Ganzeveld, P. Hoor, A. Kerkweg, M. G. Lawrence, R. Sander, B. Steil, G. Stiller, M. Tanarhte, D. Taraborrelli, J. van Aardenne, and J. Lelieveld, 2006: The atmospheric chemistry general circulation model ECHAM5/MESSy1: consistent simulation of ozone from the surface to the mesosphere. *Atmospheric Chemistry and Physics*, **6** (12), 5067–5104.
- Jöckel, P., H. Tost, A. Pozzer, M. Kunze, O. Kirner, C. A. M. Brenninkmeijer, S. Brinkop, D. S. Cai, C. Dyroff, J. Eckstein, F. Frank, H. Garny, K.-D. Gottschaldt, P. Graf, V. Grewe, A. Kerkweg, B. Kern, S. Matthes, M. Mertens, S. Meul, M. Neumaier, M. Nützel, S. Oberländer-Hayn, R. Ruhnke, T. Runde, R. Sander, D. Scharffe, and A. Zahn, 2016: Earth System Chemistry integrated Modelling (ESCiMo) with the Modular Earth Submodel System (MESSy) version 2.51. *Geoscientific Model Development*, **9** (3), 1153–1200.
- Johnson, D. G., K. W. Jucks, W. A. Traub, and K. V. Chance, 2001: Isotopic composition of stratospheric water vapor: Implications for transport. *Journal of Geophysical Research: Atmospheres*, **106** (D11), 12 219–12 226.
- Joussaume, S. and J. Jouzel, 1993: Paleoclimatic tracers: An investigation using an atmospheric general circulation model under ice age conditions: 2. Water isotopes. *Journal of Geophysical Research: Atmospheres*, **98** (D2), 2807–2830.
- Joussaume, S., R. Sadourny, and J. Jouzel, 1984: A general circulation model of water isotope cycles in the atmosphere. *Nature*, **311**, 24–29.
- Jouzel, J. and L. Merlivat, 1984: Deuterium and oxygen 18 in precipitation: Modeling of the isotopic effects during snow formation. *Journal of Geophysical Research: Atmospheres*, **89** (D7), 11 749–11 757.
- Jouzel, J., L. Merlivat, and E. Roth, 1975: Isotopic study of hail. *Journal of Geophysical Research*, **80** (36), 5015–5030.
- Junge, C. E., 1974: Residence time and variability of tropospheric trace gases. *Tellus*, **26** (4), 477–488.

- Kimberlain, T. B., 2010: Tropical Cyclone Report Hurricane Danielle (AL062010). Tech. rep., National Hurricane Center.
- Köppe, M., M. Hermann, C. Brenninkmeijer, J. Heintzenberg, H. Schlager, T. Schuck, F. Slemr, D. Sprung, P. van Velthoven, A. Wiedensohler, et al., 2009: Origin of aerosol particles in the mid-latitude and subtropical upper troposphere and lowermost stratosphere from cluster analysis of CARIBIC data. *Atmospheric Chemistry and Physics*, **9** (21), 8413–8430.
- Kraus, H., 2004: *Die Atmosphäre der Erde : eine Einführung in die Meteorologie*. 3d ed., Springer, Berlin.
- Kunz, A., C. Schiller, F. Rohrer, H. Smit, P. Nedelec, and N. Spelten, 2008: Statistical analysis of water vapour and ozone in the UT/LS observed during SPURT and MOZAIC. *Atmospheric Chemistry and Physics*, **8** (22), 6603–6615.
- Laj, P., J. Klausen, M. Bilde, C. Plass-Duelmer, G. Pappalardo, C. Clerbaux, U. Baltensperger, J. Hjorth, D. Simpson, S. Reimann, et al., 2009: Measuring atmospheric composition change. *Atmospheric Environment*, **43** (33), 5351–5414.
- Lange, H.-J., 2002: *Die Physik des Wetters und des Klimas : ein Grundkurs zur Theorie des Systems Atmosphäre*. Reimer, Berlin.
- Larsen, M. L., C. A. Briner, and P. Boehner, 2014: On the Recovery of 3D Spatial Statistics of Particles from 1D Measurements: Implications for Airborne Instruments. *Journal of Atmospheric and Oceanic Technology*, **31** (10), 2078–2087.
- Lary, D. J., 2004: Representativeness uncertainty in chemical data assimilation highlight mixing barriers. *Atmospheric Science Letters*, **5** (1-4), 35–41.
- Lee, X., S. Sargent, R. Smith, and B. Tanner, 2005: In Situ Measurement of the Water Vapor 18O/16O Isotope Ratio for Atmospheric and Ecological Applications. *Journal of Atmospheric and Oceanic Technology*, **22** (5), 555–565.
- LeGrande, A. N. and G. A. Schmidt, 2006: Global gridded data set of the oxygen isotopic composition in seawater. *Geophysical Research Letters*, **33** (12).
- MacLeod, M., A. Kierkegaard, S. Genualdi, T. Harner, and M. Scheringer, 2013: Junge relationships in measurement data for cyclic siloxanes in air. *Chemosphere*, **93** (5), 830–834.
- Majoube, M., 1971: Fractionnement en oxygène 18 et en deutérium entre l'eau et sa vapeur. *Journal de Chimie Physique et de Physico-Chimie Biologique*, **68** (10), 1423.

- Matsueda, H., T. Machida, Y. Sawa, Y. Nakagawa, K. Hirokuni, H. Ikeda, N. Kondo, and K. Goto, 2008: Evaluation of atmospheric CO₂ measurements from new flask air sampling of JAL airliner observations. *Pap. Met. Geophys.*, **59**, 1–17.
- Meinshausen, M., S. J. Smith, K. Calvin, J. S. Daniel, M. Kainuma, J. Lamarque, K. Matsumoto, S. Montzka, S. Raper, K. Riahi, et al., 2011: The RCP greenhouse gas concentrations and their extensions from 1765 to 2300. *Climatic change*, **109** (1-2), 213–241.
- Merlivat, L., 1978: Molecular diffusivities of H₂¹⁶O, HD¹⁶O, and H₂¹⁸O in gases. *The Journal of Chemical Physics*, **69** (6), 2864–2871.
- Merlivat, L. and J. Jouzel, 1979: Global climatic interpretation of the deuterium-oxygen 18 relationship for precipitation. *Journal of Geophysical Research: Oceans*, **84** (C8), 5029–5033.
- Merlivat, L. and G. Nief, 1967: Fractionnement isotopique lors des changements d'état solide-vapeur et liquide-vapeur de l'eau à des températures inférieures à 0 c. *Tellus*, **19** (1), 122–127.
- Mook, W. G., 2001: *Environmental isotopes in the hydrological cycle, Principles and Applications*, Vol. 2. International Atomic Energy Agency, UNESCO, Paris.
- Moss, R. H., J. A. Edmonds, K. A. Hibbard, M. R. Manning, S. K. Rose, D. P. Van Vuuren, T. R. Carter, S. Emori, M. Kainuma, T. Kram, et al., 2010: The next generation of scenarios for climate change research and assessment. *Nature*, **463** (7282), 747–756.
- Moyer, E. J., F. W. Irion, Y. L. Yung, and M. R. Gunson, 1996: ATMOS stratospheric deuterated water and implications for troposphere-stratosphere transport. *Geophysical Research Letters*, **23** (17), 2385–2388.
- Nappo, C., J. Caneill, R. Furman, F. Gifford, J. Kaimal, M. Kramer, T. Lockhart, M. Pendergast, R. Pielke, D. Randerson, et al., 1982: Workshop on the representativeness of meteorological observations, June 1981, Boulder, Colorado. *Bull. Am. Meteorol. Soc.*, **63** (7).
- Neumaier, M., R. Ruhnke, O. Kirner, H. Ziereis, G. Stratmann, C. A. M. Brenninkmeijer, and A. Zahn, 2014: Impact of acetone (photo)oxidation on HO_x production in the UT/LMS based on CARIBIC passenger aircraft observations and EMAC simulations. *Geophysical Research Letters*, **41** (9), 3289–3297.
- Pasch, R. J. and T. B. Kimberlain, 2011: Tropical Cyclone Report Hurricane Igor (AL112010). Tech. rep., National Hurricane Center.
- Petzold, A., V. Thouret, C. Gerbig, A. Zahn, C. A. M. Brenninkmeijer, M. Gallagher, M. Hermann, M. Pontaud, H. Ziereis, D. Boulanger, J. Marshall, P. Nédélec, H. G. J. Smit, U. Friess, J.-M. Flaud, A. Wahner, J.-P. Cammas, A. Volz-Thomas, and I. TEAM, 2015: Global-scale atmosphere monitoring

- by in-service aircraft – current achievements and future prospects of the European Research Infrastructure IAGOS. *Tellus B: Chemical and Physical Meteorology*, **67 (1)**, 28–452.
- Pfahl, S. and H. Wernli, 2009: Lagrangian simulations of stable isotopes in water vapor: An evaluation of nonequilibrium fractionation in the Craig-Gordon model. *Journal of Geophysical Research: Atmospheres*, **114 (D20)**.
- Pfahl, S., H. Wernli, K. Yoshimura, and M. Dubey, 2012: The isotopic composition of precipitation from a winter storm—a case study with the limited-area model COSMO iso. *Atmospheric Chemistry & Physics*, **12 (3)**.
- Pinet, P. R., 1993: *Oceanography : an introduction to the planet oceanus*. 2d ed., West Publishing, St. Paul.
- Pozzer, A., P. Jöckel, H. Tost, R. Sander, L. Ganzeveld, A. Kerkweg, and J. Lelieveld, 2007: Simulating organic species with the global atmospheric chemistry general circulation model ECHAM5/MESy1: a comparison of model results with observations. *Atmospheric Chemistry and Physics*, **7 (10)**, 2527–2550.
- Pozzer, A., J. Pollmann, D. Taraborrelli, P. Joeckel, D. Helmig, P. Tans, J. Hueber, and J. Lelieveld, 2010: Observed and simulated global distribution and budget of atmospheric C₂–C₅ alkanes. *Atmospheric Chemistry and Physics*, **10 (9)**, 4403–4422.
- Pruppacher, H. R. and J. D. Klett, 2012: *Microphysics of Clouds and Precipitation: Reprinted 1980*. Springer Science & Business Media.
- Ramsey, C. A. and A. D. Hewitt, 2005: A methodology for assessing sample representativeness. *Environmental Forensics*, **6 (1)**, 71–75.
- Ravishankara, A. R., S. Solomon, A. A. Turnipseed, and R. F. Warren, 1993: Atmospheric Lifetimes of Long-Lived Halogenated Species. *Science*, **259 (5092)**, 194–199.
- Rieger, D., M. Bangert, I. Bischoff-Gauss, J. Förstner, K. Lundgren, D. Reinert, J. Schröter, H. Vogel, G. Zängl, R. Ruhnke, et al., 2015: ICON-ART 1.0—a new online-coupled model system from the global to regional scale. *Geoscientific Model Development*, **8 (6)**, 1659–1676.
- Riese, M., F. Ploeger, A. Rap, B. Vogel, P. Konopka, M. Dameris, and P. Forster, 2012: Impact of uncertainties in atmospheric mixing on simulated UTLS composition and related radiative effects. *Journal of Geophysical Research: Atmospheres (1984–2012)*, **117 (D16)**.
- Risi, C., S. Bony, F. Vimeux, and J. Jouzel, 2010: Water-stable isotopes in the LMDZ4 general circulation model: Model evaluation for present-day and past climates and applications to climatic interpretations of tropical isotopic records. *Journal of Geophysical Research: Atmospheres*, **115 (D12)**.

- Risi, C., D. Noone, J. Worden, C. Frankenberg, G. Stiller, M. Kiefer, B. Funke, K. Walker, P. Bernath, M. Schneider, S. Bony, J. Lee, D. Brown, and C. Sturm, 2012: Process-evaluation of tropospheric humidity simulated by general circulation models using water vapor isotopic observations: 2. Using isotopic diagnostics to understand the mid and upper tropospheric moist bias in the tropics and subtropics. *Journal of Geophysical Research: Atmospheres*, **117** (D5).
- Roeckner, E., G. Bäuml, L. Bonaventura, R. Brokopf, M. Esch, M. Giorgetta, S. Hagemann, I. Kirchner, L. Kornbluh, E. Manzini, A. Rhodin, U. Schlese, U. Schulzweida, and A. Tompkins, 2003: The atmospheric general circulation model ECHAM5 Part I. Tech. Rep. 349, Max-Planck-Institut für Meteorologie.
- Roeckner, E., R. Brokopf, M. Esch, M. Giorgetta, S. Hagemann, L. Kornbluh, E. Manzini, U. Schlese, and U. Schulzweida, 2006: Sensitivity of simulated climate to horizontal and vertical resolution in the ECHAM5 atmosphere model. *Journal of Climate*, **19** (16), 3771–3791.
- Rohrer, F. and H. Berresheim, 2006: Strong correlation between levels of tropospheric hydroxyl radicals and solar ultraviolet radiation. *Nature*, **442** (7099), 184–187.
- Sachs, L. and J. Hedderich, 2009: *Angewandte Statistik : Methodensammlung mit R*. 13th ed., Springer, Berlin.
- Sander, S. P., J. Abbatt, J. R. Barker, J. B. Burkholder, R. R. Friedl, and D. M. Golden, 2011: Chemical Kinetics and Photochemical Data for Use in Atmospheric Studies, Evaluation No. 17. Tech. rep., Jet Propulsion Laboratory, California Institute of Technology.
- Scharffe, D., F. Slemr, C. A. M. Brenninkmeijer, and A. Zahn, 2012: Carbon monoxide measurements onboard the CARIBIC passenger aircraft using UV resonance fluorescence. *Atmospheric Measurement Techniques*, **5** (7), 1753–1760.
- Schmid, H., 1997: Experimental design for flux measurements: matching scales of observations and fluxes. *Agricultural and Forest Meteorology*, **87** (2), 179–200.
- Schmidt, G. A., R. A. Ruedy, R. L. Miller, and A. A. Lacis, 2010: Attribution of the present-day total greenhouse effect. *Journal of Geophysical Research: Atmospheres*, **115** (D20).
- Schneider, M., C. Borger, A. Wiegele, F. Hase, O. E. García, E. Sepúlveda, and M. Werner, 2017: MUSICA MetOp/IASI H_2O , δd pair retrieval simulations for validating tropospheric moisture pathways in atmospheric models. *Atmospheric Measurement Techniques*, **10** (2), 507–525.
- Schneider, M. and F. Hase, 2011: Optimal estimation of tropospheric H_2O and δD with IASI/METOP. *Atmospheric Chemistry and Physics*, **11** (21), 11 207–11 220.

- Schneider, M., A. Wiegele, S. Barthlott, Y. González, E. Christner, C. Dyroff, O. E. García, F. Hase, T. Blumenstock, E. Sepúlveda, G. Mengistu Tsidu, S. Takele Kenea, S. Rodríguez, and J. Andrey, 2016: Accomplishments of the MUSICA project to provide accurate, long-term, global and high-resolution observations of tropospheric H₂O,δD pairs – a review. *Atmospheric Measurement Techniques*, **9** (7), 2845–2875.
- Schroeter, J., D. Rieger, C. Stassen, M. Weimer, S. Werchner, J. Förstner, D. Reinert, F. Prill, H. Vogel, G. Zängl, R. Ruhnke, B. Vogel, P. Braesicke, and M. Giorgetta, 2017: ICON-ART 2.1 - The concept of a flexible tracer model framework for numerical weather forecasting and climate simulations. *Geoscientific Model Development*, **(in preparation)**.
- Schutgens, N. A. J., D. G. Partridge, and P. Stier, 2016: The importance of temporal collocation for the evaluation of aerosol models with observations. *Atmospheric Chemistry and Physics*, **16** (2), 1065–1079.
- Seemann, S. W., E. E. Borbas, R. O. Knuteson, G. R. Stephenson, and H.-L. Huang, 2008: Development of a Global Infrared Land Surface Emissivity Database for Application to Clear Sky Sounding Retrievals from Multispectral Satellite Radiance Measurements. *Journal of Applied Meteorology and Climatology*, **47** (1), 108–123.
- Seifert, A., 2002: Parametrisierung wolkenmikrophysikalischer Prozesse und Simulation konvektiver Mischwolken. Ph.D. thesis, KIT, IMK-TRO, H.-v.-Helmholtz-Platz 1, 76344 Leopoldshafen.
- Seifert, A. and K. Beheng, 2006: A two-moment cloud microphysics parameterization for mixed-phase clouds. part 1: Model description. *Meteorology and atmospheric physics*, **92** (1-2), 45–66.
- Sherwood, S. C., S. Bony, and J.-L. Dufresne, 2014: Spread in model climate sensitivity traced to atmospheric convective mixing. *Nature*, **505** (7481), 37–42.
- Stassen, C., 2015: Simulation von chemischen Tracern mit ICON-ART. Master's thesis, IMK-ASF, KIT.
- Steinwagner, J., M. Milz, T. v. Clarmann, N. Glatthor, U. Grabowski, M. Höpfner, G. Stiller, and T. Röckmann, 2007: HDO measurements with MIPAS. *Atmospheric chemistry and physics*, **7** (10), 2601–2615.
- Stevenson, D. S., R. M. Doherty, M. G. Sanderson, W. J. Collins, C. E. Johnson, and R. G. Derwent, 2004: Radiative forcing from aircraft NO_x emissions: Mechanisms and seasonal dependence. *Journal of Geophysical Research: Atmospheres*, **109** (D17).
- Stewart, M. K., 1975: Stable isotope fractionation due to evaporation and isotopic exchange of falling waterdrops: Applications to atmospheric processes and evaporation of lakes. *Journal of Geophysical Research*, **80** (9), 1133–1146.

- Stiller, O., 2010: A flow-dependent estimate for the sampling error. *Journal of Geophysical Research: Atmospheres*, **115** (D22).
- Stroebe, M., M. Scheringer, and K. Hungerbühler, 2006: Effects of multi-media partitioning of chemicals on Junge's variability–lifetime relationship. *Science of the total environment*, **367** (2), 888–898.
- Terzer, S., L. Wasenaar, L. Araguás-Araguás, and P. Aggarwal, 2013: Global Isoscapes for $\delta^{18}\text{O}$ and $\delta^2\text{H}$ in precipitation: improved prediction using regionalized climatic regression models. *Hydrology and Earth System Sciences*, **17**, 1–16.
- Tiedtke, M., 1989: A comprehensive mass flux scheme for cumulus parameterization in large-scale models. *Monthly Weather Review*, **117** (8), 1779–1800.
- Washington, P., (Ed.) , 2006: *Rumi Poems*. Everyman's Library Pocket Poets, Alfred A. Knopf, Randomhouse, New York.
- Weimer, M., 2015: Simulation of volatile organic compounds with ICON-ART. Master's thesis, IMK-ASF, KIT.
- Weimer, M., J. Schröter, J. Eckstein, K. Deetz, M. Neumaier, G. Fischbeck, L. Hu, D. B. Millet, D. Rieger, H. Vogel, B. Vogel, T. Reddmann, O. Kirner, R. Ruhnke, and P. Braesicke, 2017: An emission module for ICON-ART 2.0: implementation and simulations of acetone. *Geoscientific Model Development*, **10** (6), 2471–2494.
- Werner, M., P. M. Langebroek, T. Carlsen, M. Herold, and G. Lohmann, 2011: Stable water isotopes in the ECHAM5 general circulation model: Toward high-resolution isotope modeling on a global scale. *Journal of Geophysical Research: Atmospheres*, **116** (D15).
- Wiegele, A., M. Schneider, F. Hase, S. Barthlott, O. E. García, E. Sepúlveda, Y. González, T. Blumenstock, U. Raffalski, M. Gisi, and R. Kohlhepp, 2014: The MUSICA MetOp/IASI H_2O and δD products: characterisation and long-term comparison to NDACC/FTIR data. *Atmospheric Measurement Techniques*, **7** (8), 2719–2732.
- WMO, 2010: *Scientific Assessment of Ozone Depletion: 2010, Global Ozone Research and Monitoring Project–Report No. 52*. World Meteorological Organization.
- Worden, J., K. Bowman, D. Noone, R. Beer, S. Clough, A. Eldering, B. Fisher, A. Goldman, M. Gunson, R. Herman, S. S. Kulawik, M. Lampel, M. Luo, G. Osterman, C. Rinsland, C. Rodgers, S. Sander, M. Shephard, and H. Worden, 2006: Tropospheric Emission Spectrometer observations of the tropospheric $\text{HDO}/\text{H}_2\text{O}$ ratio: Estimation approach and characterization. *Journal of Geophysical Research: Atmospheres*, **111** (D16).

- Yoshimura, K., M. Kanamitsu, D. Noone, and T. Oki, 2008: Historical isotope simulation using Reanalysis atmospheric data. *Journal of Geophysical Research: Atmospheres*, **113** (D19).
- Zahn, A., E. Christner, P. F. J. van Velthoven, A. Rauthe-Schöch, and C. A. M. Brenninkmeijer, 2014: Processes controlling water vapor in the upper troposphere/lowermost stratosphere: An analysis of 8 years of monthly measurements by the IAGOS-CARIBIC observatory. *Journal of Geophysical Research: Atmospheres*, **119** (19), 11,505–11,525.
- Zahn, A., J. Weppner, H. Widmann, K. Schlote-Holubek, B. Burger, T. Kühner, and H. Franke, 2012: A fast and precise chemiluminescence ozone detector for eddy flux and airborne application. *Atmospheric Measurement Techniques*, **5** (2), 363–375.
- Zängl, G., D. Reinert, P. Rípodas, and M. Baldauf, 2015: The ICON (ICOsahedral Non-hydrostatic) modelling framework of DWD and MPI-M: Description of the non-hydrostatic dynamical core. *Quarterly Journal of the Royal Meteorological Society*, **141** (687), 563–579.

Acknowledgements

I would like to thank my advisors Roland Ruhnke, Andreas Zahn and Peter Braesicke for uncountable rounds of reading text, discussing the interpretation of data and figures and the encouraging words that let me finish this thesis. I also feel indebted to Stephan Pfahl for providing the code of COSMOiso, without which the development of ICON-ART-Iso would have been incomparably more difficult.

I would also like to take the chance to thank my colleagues of the two working groups and at the institute for the good times we spent, in the office or on trips to here or there.

Not naming all the other people who stood by me during my time as PhD student, I would foremost like to thank my wonderful wife Silvia for bearing with me in these past years.

I declare that I have developed and written the enclosed thesis completely by myself, and have not used sources or means without declaration in the text.

Karlsruhe, July 25, 2017

.....

(Johannes Eckstein)